Star Formation and the Interstellar Medium in M33

Thesis by

Christine Diana Wilson

In Partial Fulfillment of the Requirements

for the Degree of

Doctor of Philosophy

California Institute of Technology

Pasadena, California

1990

(Submitted May 9, 1990)

Acknowledgements

If my advisor Nick Scoville had not approached me at the beginning of my second year to encourage me to try a project with the Owens Valley Millimeter-Wave Interferometer, my thesis topic would probably have been very different. I thank Nick for introducing me to the (relatively) weather-insensitive joys of millimeter radio astronomy, for letting me work at my own pace without constant supervision, and for putting up with what must have seemed an incessant stream of papers and thesis chapters over the last year. I also thank him for paying for many distant observing runs and conferences during my stay at Caltech, as well as for helping to make them both fun and instructive.

Wendy Freedman is also partially responsible for my choice of thesis topic, since it was the work I was doing with her my first summer here on the Cepheids in M33 that made me think of looking at M33 with the interferometer. I thank Wendy for many helpful discussions in the reduction and analysis of optical photometry and for the use of the MicroVax on which the optical data in this thesis was reduced. I also thank both Wendy and Barry Madore for letting me use some of their observing time at the CFHT to obtain data for my thesis.

I would not have safely negotiated the various stresses and pitfalls of Caltech without the friendship and support of the other graduate students. I thank all the students in the Astronomy department, as well as my friends from astrophysics and infrared/submillimeter astronomy, for making Caltech a more humane place. In particular, I would like to thank my classmates Rich and Alain. It has been very helpful to have two friends who were going through the various courses, exams and other hurdles at the same time as I was. Senior students (by one year) Steve, Blaise, and Chuck were always willing to share their expertise in the intricacies of radio and optical observing. Watching Steve's thesis agonies over

the last year may have helped me avoid the same fate. I thank Debbie and Karl for organizing several P.J. fund trips, which provided excellent opportunities to see bits of California other than Pasadena. Helen and Chris helped with the astronomical infiltration of Caltech's choral music program as well contributing to many discussions (astronomical or otherwise) in the student lounge and at the Ath.

I thank all the staff at the Owens Valley Radio Observatory for helping to make my once-a-month trips there so enjoyable and productive. I also thank the staff at Palomar Observatory for their help and support during my several observing runs there.

The academic and social atmosphere of the department has been strengthened by the presence of post-doc Neill Reid (honorary student?). I thank Neill for always being ready to listen to my latest enthusiasms about blobs or stars, as well as for a whirl-wind guided tour of England and Scotland after the Tenerife conference.

I thank Julie Moses for putting up with me as a house-mate over the last five years. Her friendship and enthusiasm have made my stay at Caltech more fun, as well as helping me through the occasional personal crisis.

The various sporting and musical activities I have participated in at Caltech provided a much needed break from the rigors of observing and data reduction. Thank you to the members and directors/coaches of the Women's and Men's Glee Clubs, the Sweet Adelines, the Chamber Singers, the Caltech Women's Volleyball team, and the various Astronomy intramural teams. I thank in particular the members of the *Cantores Atri Mortis* (Rachel, Cathy, Jen, Barbara, Helen, Bryan, Chris, Donnie, Joel, Neill, and Roger) for lots of good singing and fun.

My family has always been very supportive. I thank my parents for their interest in what I am doing, for their support in times of crisis, and for their love and encouragement. I especially thank my brother Arthur for helping convince me to come to Caltech in the first place.

Finally, I thank Joe for his love and support.

Abstract

New millimeter-wave and optical data are used to study high-mass star formation and its relationship with the interstellar medium in the inner 4′ radius of the nearby spiral galaxy M33. The total mass of molecular hydrogen in this region is 3.4×10^7 $M_\odot$, roughly twice the mass in atomic hydrogen. The predicted atomic hydrogen column density from atomic mantles of molecular clouds is similar to the observed mean atomic hydrogen column density. Thus probably only a small fraction of the atomic hydrogen is in a diffuse component not directly associated with molecular clouds.

The properties of 38 individual molecular clouds in M33 (velocity widths, diameters, peak brightness temperatures, and masses) are very similar to those of Galactic molecular clouds. Masses derived from the virial theorem and from the integrated CO fluxes agree to within 10%, which implies that the value of the conversion factor from CO flux to H_2 column density, α, is the same in M33 and the Galaxy. This is the first direct measurement of the value of α in an external galaxy.

The mass distribution of clouds in M33 is consistent with that derived in the Galaxy for $M = 0.8 - 4 \times 10^5$ $M_\odot$, but shows a total lack of clouds with masses greater than 4×10^5 $M_\odot$. A simple model is proposed to explain the high-mass cutoff to the mass distribution as arising from the competing processes of cloud growth through accretion and cloud destruction due to star formation. Comparison of the flux detected with the interferometer with single dish data indicates that 50% of the molecular gas resides in structures less massive than 0.8×10^5 $M_\odot$, in contrast to the Galaxy where only 15% of the molecular gas mass is in these smaller structures.

41 OB associations each containing at least ten blue stars have been identi-

fied in this region of M33. The associations have mean radii of 40 pc, masses in stars of mass > 20 $M_\odot$ of 600 $M_\odot$, and ages of 8×10^6 yr. No evidence is found for a gradient in the ratio of blue to red supergiants in the inner two kiloparsecs of M33, despite a factor of two decrease in the metallicity over this range of radius. The blue luminosity function for stars in the field is deficient at bright magnitudes relative to the luminosity function for stars in associations. In addition, the associations in the northern arm contain no stars more massive than 20 $M_\odot$ while associations in the southern arm contain several stars with masses of 60 $M_\odot$. These differences may be due to a sudden cessation of star formation resulting in a larger mean age for the stars or to a smaller upper mass cutoff to the initial mass function in the field and the northern arm.

The offset between the molecular and atomic gas peaks in the southern spiral arm is consistent with streaming motions expected as the gas enters a spiral density wave. In addition, the OB associations in the southern spiral arm show a weak age gradient perpendicular to the arm, consistent with the presence of a density wave. However, the northern arm has an age gradient running along the arm, as would be expected for a stochastic star formation arm.

A comparison of the spatial distributions of the Hα, CO, and HI emission peaks indicates that the atomic gas is probably formed via photo-dissociation of the molecular gas by recent high-mass star formation. Roughly two-thirds of the molecular clouds with $M > 0.5 \times 10^5$ $M_\odot$ contain recent massive star formation with inferred high-mass star formation rates for individual clouds ranging from 5×10^{-6} to 5×10^{-4} $M_\odot$ yr^{-1}. The photo-dissociating flux produced by these stars is sufficient to produce the amount of atomic gas near the molecular clouds if the molecular clouds have a clumped structure.

The high-mass star formation rate and efficiency are measured by combining

optical, far-infrared, and millimeter data. The high-mass star formation rate calculated from the Hα emission is 0.007 $M_\odot$ yr^{-1} over an area of 5 kpc^2, which corresponds to a total star formation rate of 0.04 $M_\odot$ yr^{-1}. The star formation rate obtained from the far-infrared emission agrees with the rate obtained from the Hα emission to within a factor of two. A lower limit to the high-mass star formation rate obtained from number counts of blue stars is consistent with the rates obtained from Hα and far-infrared emission. The southern spiral arm and the molecular complexes have similar star formation efficiencies to regions of the galaxy containing little molecular gas. Thus the large amount of star formation occurring in the spiral arms of M33 is due to the presence of large amounts of molecular gas and not to an increased star formation efficiency.

Table of Contents

CHAPTER 1

Introduction and Review of Previous Work

I. Introduction

How star formation proceeds in galaxies has important consequences for understanding the structure and evolution of galaxies. Massive stars are important sources of kinetic energy for interstellar gas through both strong stellar winds and HII regions occurring early in the star's lifetime and red giant mass loss and supernova explosions at the end of the star's life, which return most of the material in the star to the interstellar medium. High-mass stars are also a primary source of gas enriched with elements heavier than lithium. How much longer galaxies will continue to form stars is determined by the star formation rate and the total reservoir of interstellar gas. Thus blue dwarf galaxies and starburst galaxies are apparently forming stars at a much greater rate now than their average past rate, since otherwise they would exhaust their gas supply in a relatively short time ($10^8 - 10^9$ yr). Finally, the prominence of spiral arms in disk galaxies is produced by the presence of many young, high-mass stars. The mechanism by which these massive stars form is thus important for understanding spiral structure in galaxies.

Many basic questions concerning the details of how star formation occurs remain poorly understood. For example, what causes the star formation rate to vary so dramatically between normal and starburst galaxies and even between adjacent arm and interarm regions within the same galaxy? Such issues can best be addressed through detailed, high resolution studies of the stellar content and interstellar medium in nearby galaxies. Studies of individual stars are limited to

the high-mass stars, since stars with masses less than 10 $M_{\odot}$ cannot be resolved from the background light except in the Magellanic Clouds. However, since these stars have a disproportionately large effect on the heating, ionization, and dynamics of the gas, the study of them is most important for understanding the interrelation between star formation, the interstellar medium, and galactic structure.

The critical issues addressed in this thesis are the interaction of high-mass stars with the interstellar medium and how the star formation rate and efficiency vary between different regions of a single galaxy. In Galactic studies, our position within the plane of the Galaxy makes it difficult to separate objects at different distances along the line of sight. In addition, obscuration by dust limits many optical studies to areas within 2 kpc of the Sun. In addition, the locations of the spiral arms in our Galaxy are not well known, which makes comparative studies of arm and interarm regions difficult. Therefore, the face-on spiral galaxy M33, which at a distance of 0.8 Mpc is one of the closest spiral galaxies, was chosen for this study.

This study differs in important ways from previous similar studies of M31 (Walterbos 1986) and M33 (Deul 1989). In both studies, the molecular gas component was neglected in favor of a global mapping of atomic hydrogen and little detailed analysis of the stellar populations was done. These are serious defects since molecular clouds are probably the main sites of star formation and the young stars dominate much of the optical morphology. In the present study, the molecular gas distribution has been mapped at both high and low resolution. In addition, the properties of the stellar associations and HII regions have been analyzed. Thus all the components involved in the star formation process are included: the high-mass stars and the molecular, atomic, and ionized hydrogen

gas. High spatial resolution observations are used for all components, which allows individual star-forming regions to be studied. A large contiguous region centered on the nucleus is used in this thesis to avoid biasing the results towards regions of active star formation.

Previous work on M33 is reviewed in Section II of this chapter and related work on our own Galaxy and M31 is discussed in Section III. Chapter 2 describes the single dish CO map of M33. The radial profile of the molecular hydrogen surface density is calculated and compared with the atomic hydrogen distribution (Deul and van der Hulst 1987). The large structures seen in the CO map are discussed and their positions are compared with the positions of the optically identified spiral arms. This chapter has already been published (Wilson and Scoville 1989a).

Chapter 3 describes optical broadband UBV photometry of individual high-mass stars in M33. The mean reddening of the stars by interstellar dust is calculated. The OB associations are re-identified using an objective grouping algorithm and their properties are discussed. The luminosity function of stars in associations is compared with that of field stars. The relative numbers of red to blue supergiants, a possible tracer of chemical abundance variations and a discriminator of stellar evolution models, are calculated as a function of radius. The ages of the OB associations are used to test spiral structure theories.

Chapter 4 describes interferometric CO observations of individual molecular clouds. The properties of the clouds are compared with those of Galactic giant molecular clouds. The mass of molecular gas contained in small clouds below our sensitivity limit is calculated by comparing the interferometer and single dish fluxes. The mass distributions of clouds in M33 and the Galaxy are compared and a model for the upper mass cutoff to the cloud mass function is presented.

Chapter 5 compares the interferometric CO observations with optical Hα data and the atomic hydrogen map. High-mass star formation rates are calculated for individual clouds using the Hα emission. The offset between the atomic and molecular gas peaks in the southern spiral arm is used to constrain the cycle between these two phases of the interstellar medium. The amount of atomic hydrogen that can be produced by the high-mass stars via photo-dissociation is calculated for each cloud. The observed atomic hydrogen surface density is compared with the expected surface density from atomic mantles around molecular clouds in order to understand the relationship between the atomic and molecular phases.

Chapter 6 combines the entire data set to obtain high-mass star formation rates and efficiencies for different regions of M33. Star formation rates calculated from Hα and far-infrared observations are compared with rates obtained directly from number counts of young stars. Star formation efficiencies in regions with abundant molecular gas are compared with efficiencies for regions with no detected molecular gas. The dust properties of M33 are discussed briefly. Chapter 7 summarizes the conclusions from the previous chapters and outlines areas of future research.

II. Previous Work on M33

M33 is a small Sc-type spiral galaxy in the Local Group. Its inclination angle is 57^o (Deul and van der Hulst 1987) and thus projection effects are less severe in this galaxy than in M31 ($i = 79^o$). It has high-mass star formation occurring throughout the disk and flocculent spiral arms (Sandage and Humphreys 1980). The two inner spiral arms are more regular and the southern arm in particular has been suggested to be generated by a spiral density wave (Humphreys and Sandage 1980).

The amount of molecular and atomic gas must be known to determine star formation efficiencies and to develop a complete picture of the star formation cycle. The molecular gas component is especially important since star formation is thought to occur in molecular clouds. Despite prominent star formation in M33, there have been very few observations in the CO J=1-0 line, the primary tracer of molecular hydrogen gas. The weak CO flux of the nucleus suggested that M33 contained relatively little molecular gas (Young and Scoville 1982) and the steeply declining CO radial profile supported this interpretation (Young 1987). Of six large HII regions in M33, only NGC 604 and NGC 595 have been detected in CO (Blitz 1985). The inferred amount of molecular gas is surprisingly small given the large numbers of young stars in M33. However, observations with the Owens Valley Millimeter-Wave Interferometer of NGC 604 (Boulanger *et al.* 1988) and the nucleus (Wilson *et al.* 1988) in the early stages of this thesis detected several clouds with properties very similar to those of Galactic clouds.

The spatial distribution of the atomic hydrogen gas is important for determining the cycle between the molecular and atomic phases of the interstellar medium. The atomic distribution has been well studied in M33 (for a summary of previous HI observations see Newton 1980). The most recent maps of atomic hydrogen in M33 reveal a network of HI holes that correlate well with the positions of OB associations (Deul and van der Hulst 1987, Deul and den Hartog 1990). The large holes correspond to interarm cavities, with the OB associations and HII regions on the edges of the holes, while the smaller holes are probably created via supernova explosions. The HI-derived inclination angle of 57^o and position angle of 22^o (Deul and van der Hulst 1987) are used throughout this thesis.

The spatial distribution of warm dust can identify the dominant source of

dust heating, either radiation from young stars or from the general interstellar radiation field. The dust distribution in M33 has been measured with the IRAS satellite (Rice *et al.* 1989). The global far-infrared properties of M33 are similar to those of the Galaxy, with half of the luminosity generated by large HII complexes (Deul 1989; Rice *et al.* 1990). M33 also has a steep radial decrease in the dust-to-atomic-gas ratio.

High-mass stars can be identified using broadband optical photometry, narrowband Hα photometry, or, for regions with high extinction, radio free-free emission. HII regions in M33 were identified from photographic plates (Courtes *et al.* 1987), but without quantitative measurements of their fluxes. A 1.4 GHz survey revealed 112 radio sources associated with Hα emission (Viallefond *et al.* 1986). These radio HII regions have substantial internal extinction (Viallefond and Goss 1986), which implies that star formation rates calculated from optical data may be underestimated. The HII regions are usually found in areas of the galaxy with high atomic hydrogen surface densities. Star formation efficiencies calculated using the atomic hydrogen gas mass vary by only a factor of three. Since this study did not include the molecular gas component, the relevance of the calculated star formation efficiencies is unclear.

The total amount of star formation estimated from the high-mass star formation rate depends heavily on the assumed form of the initial mass function. The luminosity function of blue stars has been used to study the high-mass end of the initial mass function. The luminosity functions of ten nearby galaxies all have a similar slope (Freedman 1985a). In addition, no variation in the slope of the luminosity function as a function of radius was found in M33 (Freedman 1985a).

The relative numbers of red and blue supergiants is predicted to depend on

the chemical abundance, since the amount of mass, which has a large effect on post-main sequence evolution, depends on the metallicity. The high-mass stellar content of M33 has been studied using blue and red photographic plates and a gradient in the ratio of blue-to-red supergiants was found that traced the known abundance gradient (Humphreys and Sandage 1980). However, a later study found no significant gradient in the blue-to-red ratio as a function of radius (Freedman 1985b).

Wolf-Rayet stars are important tracers of the high-mass stellar population (Massey 1985) since they are relatively easy to identify and are all high-mass stars ($M \sim 40$ $M_{\odot}$). They are also the end product of stellar evolution and thus provide a strong discriminator for evolutionary models, which vary widely in their predicted post-main sequence evolution (de Loore 1988). M33 has been surveyed for Wolf-Rayet stars using narrowband filters to identify candidates and follow-up spectroscopy to determine sub-types (Massey and Conti 1983; Massey *et al.* 1987; Massey, Conti, and Armandroff 1987). A total of 150 Wolf-Rayet candidates are now known in this galaxy, of which 95 have been confirmed spectroscopically.

Variations in the chemical abundance are predicted to have large effects on stellar evolution, dust-to-gas ratios, and the proportionality constant used to obtain molecular hydrogen gas masses from CO fluxes. M33 has a fairly steep abundance gradient, varying from near solar in the nucleus to a factor of four lower at the radius of NGC 604, the largest HII region (Pagel *et al.* 1979; Kwitter and Aller 1981; McCall, Rybski, and Shields 1985; Blair and Kirshner 1985; Vilchez *et al.* 1988). The large radial gradient in M33 provides a potentially powerful laboratory in which to test the predicted effects of chemical abundance variations.

The distance of M33 can be determined using its Cepheid variable stars. 35

Cepheids in M33 were first catalogued by Hubble (1926). These data were corrected for a scale error using photoelectric photometry (Sandage 1983) to obtain a distance of 1.2 Mpc, in good agreement with the distance obtained from new Cepheids identified at larger galactic radii (Sandage and Carlson 1983). However, recent CCD photometry (Christian and Schommer 1987; Wilson, Freedman, and Madore 1990) shows that the scale error in the photographic photometry was probably over-corrected. Freedman (1985c) used BVRI CCD photometry to correct for differential reddening of the Cepheids and obtained a distance of 0.66 Mpc from single phase observations. Madore *et al.* (1985) using H-band aperture photometry obtained a distance of 0.72 Mpc. Finally, Freedman, Wilson, and Madore (1990) have used phased magnitudes of nine Cepheids to simultaneously solve for both the reddening and the distance and obtain a distance of 0.79 Mpc. This value for the distance to M33 is used throughout this thesis.

To summarize, many of the components which are important for characterizing high-mass star formation have been studied in detail in M33. In particular, the distributions of the atomic gas and dust, the Wolf-Rayet stars, and the radio HII regions are all fairly complete and the abundance gradient in M33 is determined accurately using a variety of objects. However, very little is known about the molecular gas in M33, which is crucial to developing a complete picture of the star formation process. Also, quantitative Hα photometry as well as accurate optical CCD photometry are lacking. Thus this thesis supplies the data required for a complete study of high-mass star formation in the inner 1-2 kpc of M33.

III. Related Work on the Galaxy and Other Nearby Galaxies

The high spatial resolution that can be achieved in nearby galaxies such as M33 enables a direct comparison with our own Galaxy. For example, the molecular cloud population can be compared directly with Galactic giant molecular

clouds and used to constrain models of cloud growth and destruction. A comparison of gas-to-dust ratios can distinguish between different models for dust opacity. The advantage of Galactic studies is that detailed information can be obtained due to the proximity of the objects, while global variations are more easily identified in other galaxies.

Since star formation occurs in molecular clouds, it is important to know the properties of molecular clouds in detail. The first large survey of Galactic molecular clouds was presented in Sanders, Scoville, and Solomon (1985). The clouds have diameters of 20-100 pc, masses of $\sim 10^5 - 10^6$ $M_\odot$, and molecular hydrogen densities of 100-200 cm^{-3}. The velocity widths are proportional to the cloud diameters to the 0.6 power and the mean density varies as $D^{-0.75}$, which implies a cloud mass spectrum $N(M) \propto M^{-1.6}$. Over 90% of the molecular mass in our Galaxy is in clouds with diameters bigger than 20 pc.

Clouds with HII regions have higher peak CO brightness temperatures than clouds without HII regions and are distributed in the spiral arms (Scoville *et al.* 1987). Molecular clouds containing HII regions have higher peak 60/100 μm color temperatures and higher infrared luminosity to mass ratios than clouds without HII regions (Scoville and Good 1989). In addition, the virial mass and the infrared-luminosity-to-mass ratio correlate only weakly, which implies that the star formation efficiency does not depend strongly on the mass of the cloud.

Models of the evolution of the molecular cloud population can be tested by observing clouds in different environments. High resolution studies of molecular clouds in other galaxies were first attempted in M31. Four clouds with masses similar to Galactic molecular clouds were identified in a spiral arm of M31 (Lada *et al.* 1988). High-resolution observations of one cloud showed it to be very similar to the Orion molecular clouds (Vogel, Ball, and Boulanger 1987).

Molecular hydrogen masses are obtained from CO fluxes by adopting a conversion factor between CO flux and H_2 column density. This conversion factor, α, has only been reliably determined for our own Galaxy, $\alpha = 3 \pm 1 \times 10^{20}$ cm^{-2} (K km s^{-1})$^{-1}$ (Scoville and Sanders 1987; Bloemen *et al.* 1986; Strong *et al.* 1988). For clouds with different densities and temperatures, α scales as $T/\sqrt{\rho}$ (cf. Scoville and Sanders 1987; Dickman, Snell, and Schloerb 1987). In addition, α may have a strong dependence on metallicity (Maloney and Black 1988). Recent CO observations of the LMC, which has a metallicity four times less than solar, claim to have found such a systematic effect (Cohen *et al.* 1988). However, these data suffer from a low spatial resolution of $\sim$ 140 pc, larger than the typical sizes of Galactic molecular clouds, and thus the higher value of α may not be reliable.

There have been recent claims of variations in the slope of the initial mass function for OB stars in our Galaxy. Many more O stars are found in the direction of the Galactic center than in the direction of the anti-center, resulting in a slope of -1.3 inside the solar circle and -2.1 outside (Garmany, Conti, and Chiosi 1982). However, incompleteness may be a serious problem in this study, especially for the fainter B stars (Humphreys and McElroy 1984). A recent study of two OB associations in the LMC (Massey *et al.* 1989) has obtained a slope of -1.8, as well as revealing evidence of sequential star formation. The importance of obtaining spectra of these high-mass stars is emphasized in a study of the SMC association NGC 346 (Massey, Parker, and Garmany 1989), where the slope of the initial mass function is found to be -2.5 using only multicolor photometry and -1.8 using spectra to place the stars in the theoretical H-R diagram.

The other Local Group spiral galaxy M31 has recently been the subject of several interstellar medium studies. Most of the far-infrared emission can be

attributed to a cool dust component with relatively little emission from warm dust (Walterbos and Schwering 1987). This cool dust associated with atomic clouds is heated by the interstellar radiation field and is not directly related to recent star formation. However, M31 has an especially low abundance of molecular hydrogen relative to atomic hydrogen and these results may not be relevant for more active star-forming galaxies. There is also a strong radial decrease in the ratio of infrared luminosity to atomic hydrogen. The disk light is bluer at larger radii, which may be due to the abundance gradient or to recent interarm star formation at large radii (Walterbos and Kennicutt 1988). A dust-to-atomic-gas ratio similar to the solar neighbourhood value is obtained from measurements of the absorption in two major dust lanes.

In summary, the properties of molecular clouds are fairly well understood in our own Galaxy, but no large samples of individual clouds are available for other galaxies. Studies of the initial mass function in the Galaxy are confused by completeness problems and limited to a fairly small region near the Sun. M31 is forming stars at a low rate compared to the Galaxy (Walterbos 1986) and thus the star formation process in this galaxy may not be typical of more active star-forming galaxies. By including data on the molecular gas component in a nearby galaxy for the first time, this thesis provides for a detailed comparison between the star-forming characteristics of M33 and our own Galaxy.

CHAPTER 2

The Molecular Gas Content of the Nuclear Region of M33

(C. D. Wilson and N. Scoville 1989, *Ap. J.* **347**, 743)

I. Introduction

A knowledge of the amount of molecular gas in a galaxy is required for calculating the star formation efficiency. Early observations of the M33 nucleus (Young and Scoville 1982) and of the two largest HII regions (Blitz 1985) suggested that the molecular gas content of this galaxy was low. Nevertheless, interferometric studies have recently detected molecular clouds with properties similar to Galactic giant molecular clouds (GMCs) (Boulanger *et al.* 1988; Wilson *et al.* 1988). The spatial resolution in M33 achievable with single dish telescopes can distinguish between arm and interarm regions, which provides a quantitative basis for studies of star formation and the interstellar medium in a wide range of galactic environments. In addition, M33 is one of the few galaxies where the molecular gas distribution can be resolved on scales similar to the nuclear ring and rotating disk seen in the center of the Milky Way Galaxy (Oort 1977). Thus the kinematics of the molecular gas provide a clue as to whether M33, like our Galaxy, shows evidence of some kind of nuclear activity.

In this chapter we present a completely sampled map of the CO J=1-0 emission to elucidate the distribution of the molecular gas in the nuclear region of M33 out to a 3.5′ radius. The observations and the data reduction are discussed

in Section II. The spatial distribution of the CO emission is compared with the distribution of the atomic gas and the positions of the spiral arms in Section III. The mass of molecular gas and the radially averaged H_2 column density are calculated in Section IV. The velocity field and a simple model for the mass distribution in the inner kiloparsec of M33 are discussed in Section V and the molecular gas content of M33 is compared with that of the Galaxy in Section VI. The chapter is summarized in Section VII.

II. Observations and Data Reduction

The nuclear region of M33 was mapped with the NRAO 12m telescope[1] (half power beam width = 55″) in the CO J=1-0 transition during two observing runs of four days each in June and July 1988. Observations were made at 30″ spacing resulting in a fully sampled map. Two five-minute scans were taken for most positions, although as many as six scans were taken at large airmasses or under poor weather conditions. Typical system temperatures referred to outside the atmosphere were 900-1500 K (SSB). The 500 kHz and 1 MHz 256 channel filter banks were configured in parallel mode to detect both polarizations. Only the 1 MHz data (2.6 km s^{-1}) were used in the analysis. The data obtained in June were calibrated by observations of Orion (T_R^*(peak)=80 K), while during the second run one strong position in M33 was re-observed each day to check that the flux scale was consistent with the first observing run. During both runs, the integrations on source and on the hot load were slightly contaminated due to the hot load not moving quickly enough into and out of the beam. This resulted in system temperature measurements roughly 30% higher than normal. Thus

[1] The National Radio Astronomy Observatory is operated by Associated Universities, Inc., under cooperative agreement with the National Science Foundation.

the raw data have been scaled down by a factor of 0.75 and the resulting fluxes are estimated to be accurate to about 20%.

Spectra were obtained at 161 points within the inner 3.5′ radius of M33. The individual scans on each position were summed and separated into the two polarizations. The data were smoothed by a 4 km s^{-1} Gaussian filter and the two polarizations averaged to produce the total spectrum. Each spectrum was fitted with a first or second order baseline, which resulted in an rms noise σ of 0.01 to 0.04 K in the final, smoothed spectrum. The integrated intensity, peak temperature, velocity width, and central velocity of the line were obtained by fitting the line with a Gaussian profile. In the few cases where two lines appeared to be present in one spectrum, these parameters were measured directly from the spectrum. For positions with peak antenna temperatures less than 3σ, an upper limit to the amount of emission was obtained by integrating over 60 km s^{-1} centered on the predicted velocity for this position. The predicted velocity was estimated from the velocity field of the galaxy determined from positions with obvious lines. The uncertainty in the integrated flux of any individual observation is typically less than 0.5 K km s^{-1} and is given by $4\sigma\sqrt{N_{line}}\sqrt{1+N_{line}/N_{base}}$ where N_{line} is the number of channels over which the line was integrated, and N_{base} is the number of channels used in determining the baseline. The factor of 4 in front is the velocity resolution of 4 km s^{-1} for the smoothed data. The peak brightness temperatures of the lines range from 0.07 to 0.26 K and the integrated intensities range from 0.6 to 4.0 K km s^{-1}. The line widths (full-width half-maximum) range from 8 to 36 km s^{-1}.

III. The CO Emission

The map of the integrated CO emission is shown in Figure 1 where it is immediately apparent that the strongest emission peaks off of the optical nu-

cleus. Thus the weak nuclear emission (Young and Scoville 1982) gives a rather misleading picture of the molecular gas content in the nucleus of the galaxy. The peak surface brightness ($\sim$ 4 K km s^{-1}) in our map of M33 is similar to that of M101 (Solomon *et al.* 1983). However, if the M33 map is degraded to the same linear resolution ($\sim$ 1.8 kpc) as the data for M101, which is eight times further away, the mean surface brightness is four times lower in M33. The structures seen in Figure 1 have diameters of 200-400 pc, comparable to our instrumental resolution of 230 pc; they are therefore much larger than individual GMCs but smaller than the large structures seen in the spiral arms of M51 (Vogel, Kulkarni, and Scoville 1988). Interferometer observations for most of the M33 structures resolve them into individual clouds with properties similar to Galactic GMCs (Chapter 4). Thus, the structures seen in Figure 1 are either associations of individual GMCs or GMCs embedded in a more tenuous H_2 gas.

Most of the large CO complexes lie along the two main spiral arms of M33 that have been traced in integrated blue light (Sandage and Humphreys 1980). The three large complexes east of the nucleus lie along the massive southern spiral arm (SI in their notation), while the complex due west of the nucleus and the emission on the northwest edge of our map lie near the northern spiral arm (NI). However, the emission in the southwest corner of our map is not associated with one of the previously identified optical arms, although it is associated with a large HI complex, HII emission, and OB association 48. This region may be a fragmentary arm coming off the southern arm or an extension of one of the northern arms (NIV or NV). A string of OB associations running southwest from this region is prominent in blue optical photographs (Humphreys and Sandage 1980; Chapter 3).

The atomic hydrogen distribution in M33 has recently been mapped at high

spatial resolution ($12'' \times 24''$) using the Westerbork Array (Deul and van der Hulst 1987). The spatial distributions of the CO and HI emission are compared in Figure 2. The CO and HI emission appear fairly well correlated in this figure and major peaks in both distributions fall on or near the two spiral arms. The ratio of the flux in the strongest line to that of the weakest detected line (the contrast) in the CO map is 7 to 1, more than twice that in the HI map smoothed to a similar resolution. This CO contrast is a lower limit since CO emission is not detected at many positions, while HI emission is observed over the entire region. Many of the CO complexes contain HI maxima of similar spatial extent. A notable exception is the large CO complex to the northeast of the nucleus which is deficient in HI gas relative to the other CO complexes. Only a few small HI peaks are seen in this region. The weaker CO peak due south of the nucleus is also deficient in HI emission. In general, the brightest peaks in the HI emission follow the spiral arm pattern as well as do the CO peaks.

The correlation between CO and HI was tested objectively by computing the cross-correlation function of the two intensities, with the HI map rebinned to the CO resolution. The cross-correlation analysis was used to look for translations and rotations about the center of the CO map to $\pm 30^o$ from the intrinsic coordinate system. No peaks in the cross-correlation were found more than two sigma above the average. The intrinsic coordinate system (no translation offsets) is a two-sigma peak for rotations from $-5^o \leq \theta \leq 5^o$, but several offset coordinate frames have peaks that are almost as strong. Thus although the emission in the two maps appears well correlated on casual inspection, more rigorous analysis shows that the *global* spatial distributions of the atomic and molecular gas are only weakly correlated.

One explanation for the apparent discrepancy between a visual inspection of

Figure 2 and the cross-correlation analysis is that the HI and CO emission peaks generally lie near each other but the separation vectors between the peaks are oriented randomly. This situation could arise if the atomic gas formed via dissociation of molecular gas or if the molecular clouds condensed out of large atomic complexes with no global symmetries such as spiral density waves to establish a preferred direction for the separation vectors. To examine this possibility, we identified the positions of eleven peaks in the rebinned HI map. Random positions for ten CO peaks were generated and the average distance to the nearest HI peak was calculated. For random distributions of CO peaks, the mean distance o the nearest HI peak is $50\pm6''$, while the mean peak separation in the data is 30-40″, depending on whether the CO peaks that lie on the edges of our map are included. Thus the CO and HI peaks are spatially correlated at the 2-3σ level, despite the lack of a significant global correlation.

IV. The Molecular Gas Mass

The mass of molecular hydrogen can be calculated from the integrated CO emission by assuming a conversion factor α between the CO line flux and the column density of H_2. For a point source, the conversion factor from antenna temperature to Janskys is 34 Jy K^{-1} for the NRAO antenna. Adopting $\alpha = 3 \times 10^{20}$ cm^{-2} (K km s^{-1})$^{-1}$ and a coupling factor $\eta_c = 1$ for Galactic GMCs (cf. Scoville *et al.* 1987; Wilson *et al.* 1988), we find

$$M_{H_2} = 7390 \int S_{Jy} dV_{km\ s^{-1}}\ M_\odot \qquad (1)$$

The uncertainty in the value of the Galactic conversion factor is a factor of 2 (Strong *et al.* 1988; Scoville and Sanders 1987; MacLaren, Richardson, and Wolfendale 1988). In the region of M33 covered by this survey the metallicity decreases by only a factor of two from a nuclear value of roughly solar (Pagel

1985; McCall, Rybski, and Shields 1985), so α is unlikely to be very different from the Galactic value due to a difference in metallicity. In addition, interferometer measurements of individual molecular clouds in M33 show good agreement between the molecular and virial masses (Chapter 4).

For extended sources, the source-beam coupling factor, which depends on the flux distribution of the source, is required to calculate the true flux from the observed antenna temperature. For a uniform source with a diameter equal to the width, the apparent flux computed by assuming a point source at the beam center (i.e., 34 Jy K^{-1}) is smaller by a factor of 1.4 than the true flux because of the Gaussian fall-off of the primary beam. Adopting a source-beam coupling factor of 1.4, the amount of molecular gas in our map of M33 is 3.4×10^7 $M_\odot$. The formal error due to the uncertainties in the fluxes is 10%; however, systematic errors exist in the source-beam coupling factor and the conversion factor α.

The molecular masses (including helium) of the individual structures seen in the map range from 3-10 $\times10^6$ $M_\odot$. The virial mass of the complex at ($\Delta\alpha = 2.5$, $\Delta\delta = -0.5$) is $\sim 2\times10^7$ $M_\odot$, while the molecular mass is 4×10^6 $M_\odot$. A similar discrepancy is found for all the other features except for the complex due west of the nucleus where the virial and molecular masses agree. The uncertainties in the masses (roughly $\pm40\%$) are not enough to resolve this discrepancy. The region surveyed is very close to the nucleus of M33, and thus tidal forces may have a large effect on these structures. The minimum mass required for a cloud with radius R_c at a distance R_g from the center of the galaxy to be tidally stable is $M_c > 2M_g(R_c/R_g)^3$ where M_c is the mass of the cloud and M_g is the mass of the galaxy within radius R_g. The molecular masses of all the complexes are 3-7 times *smaller* than the minimum tidally stable mass, which suggests that these structures are transient and not gravitationally bound.

This result is not surprising if we compare the properties of these structures with those of Galactic GMCs (cf. Sanders, Scoville, and Solomon 1985). A simple extension of the Galactic velocity-diameter relation to these structures predicts velocity widths 50% greater than what is observed. These structures are also much larger in diameter than the largest Galactic GMC (D$\sim$100 pc). Finally, the peak brightness temperatures seen in M33 are typically 0.2-0.3 K, a factor of ten smaller than what is seen for individual Galactic GMCs. Thus if the molecular gas in M33 resides primarily in molecular clouds with properties similar to Galactic GMCs, the area-filling factor by these clouds in our beam is $\sim$ 10%. Individual clouds will escape from the unbound complex in roughly one crossing time $t_{cross} = R/\sigma$, where R is the radius of the complex and σ is the three-dimensional velocity dispersion of the clouds. The crossing times are 1-2$\times 10^7$ yr, roughly 10-20% of the time required to complete one orbit around M33.

The CO emission was integrated over elliptical annuli to obtain the radial profile of H_2 in the central disk of M33. The resulting average column density perpendicular to the plane of the galaxy is shown in Figure 3. The average column density ($2N_{H_2}$) is roughly constant at 1.1×10^{21} cm^{-2} out to a radius of 1 kpc. The data points at 0.8 and 1 kpc have a larger uncertainty, since we have observed less than 50% of the area of the annulus. It is interesting that a strong decrease in the column density as a function of radius is not yet seen. In particular, if the molecular hydrogen had the same scale length as the far-infrared emission (5.3′-8.5′, Rice *et al.* 1990), the column density at 1 kpc should be lower than the central column density by roughly a factor of 2. These data therefore suggest that the molecular gas has a larger scale length than the far-infrared emission. In view of the highly irregular CO distribution seen in

our fully sampled map, it is clear that CO radial profiles obtained by sampling only along one or two strips (e.g., the M33 profile given by Young 1987) can be unreliable.

The radial profile of the atomic gas shows a central depression in the inner kiloparsec and a mean column density of $\sim 10^{21}$ atoms cm^{-2} from 1 to 6 kpc (Deul and van der Hulst 1987). A central hole in the atomic hydrogen distribution is often seen in spiral galaxies (e.g., Rogstad and Shostak 1972, Bosma 1978). The average HI column density in the inner 3.5′ of M33 is $\sim 4 \times 10^{20}$ cm $^{-2}$, about one-third that of the molecular gas. This difference is small compared to more luminous late-type galaxies for which the central molecular hydrogen column density may be more than ten times that of the atomic hydrogen (Young 1987). The average HI column density per CO single dish beam is plotted versus the molecular hydrogen column density in Figure 4. There is no correlation between the two column densities and no significant difference in the HI column densities between positions with and without CO lines. This result is not unexpected, given the mean separation of the HI and CO peaks calculated above.

V. The CO Velocity Field

The central velocity of the CO lines is plotted as a function of position in Figure 5. The velocity field of the molecular hydrogen gas is very similar to that of the atomic gas (Deul and van der Hulst 1987) and the systemic velocity of -181 km s^{-1} (V_{LSR}) derived from the HI gas is in good agreement with that of the molecular gas at the optical center. In Figure 6, the true rotation velocity of the molecular gas (corrected for inclination by sin$i$) is plotted versus radius, where points within 30^o of the minor axis have been excluded. If the CO data are fit with an R$^\beta$ power law, the χ^2 of the individual fits are equally good for $0.5 \leq \beta \leq 1$. Also plotted in Figure 6 are four points taken from the HI rotation

curve of Newton (1980). Including these points constrains the fit to be closer to β=0.5, which is consistent with the potential at 1-8′ radius being dominated by a uniform density disk. The total mass within 800 pc derived from this rotation curve is 5.4×10^8 $M_\odot$ and thus the mass of the molecular gas within this radius is 4% of the total mass in the disk. The optical rotation curve derived from H_α emission shows a constant velocity of ~23 km s^{-1} in the inner 250 pc of the galaxy (Rubin and Ford 1985). This flat rotation curve may reflect a spheroidal distribution with $\rho \propto R^{-2}$ or a disk with $\Sigma \propto R^{-1}$.

The observed H_α, CO, and HI rotation velocities suggest a two-component model for the density distribution in the inner part of M33. For R < 300 pc the potential may be dominated by a spheroid with a R^{-2} density distribution and a total mass of 3.5×10^7 $M_\odot$. It is tempting to identify this region with the bulge of M33, although previous measurements of the bulge of M33 (Boulesteix *et al.* 1979) yielded a somewhat lower mass (1.5×10^7 $M_\odot$ within a 630 pc radius). For R > 500 pc the observed rotation velocities may be produced by a uniform density disk, with a total surface density of 270 $M_\odot$ pc^{-2}. The region 300 < R < 500 pc is presumably a transition zone where both mass components are important. Other models are also possible (e.g., no spheroid and a disk with a density profile which varies with radius) and measurements of the integrated light distribution are required to conclusively identify the mass distribution.

No difference is seen in the velocities between the northern and southern halves of the galaxy. Two adjacent positions in our map show a difference in the central velocity of 30 km s^{-1} (open circles in Figure 4). The peak line temperatures in both spectra are 4σ above the noise, and the integrated fluxes are 3-4σ detections. The two positions are near OB association 64, an HII region, and a ridge of atomic hydrogen emission and thus the molecular gas may have

been disturbed by nearby high-mass star formation. Other regions in our map that have similar concentrations of HII and HI emission and lie within 30° of the minor axis are excluded from the rotation curve analysis. However, none of them shows such a large difference in the central velocity between adjacent positions.

VI. Comparison with the Milky Way Galaxy

We see no evidence in M33 for a nuclear ring of molecular gas similar to that seen in the Milky Way Galaxy (Scoville 1972; Bania 1977). Such a ring with a radius of ~200 pc and mass of 3×10^8 $M_\odot$ would be marginally resolved in our map and would be very much brighter than our observed central emission. We also see no evidence for large noncircular velocities similar to the expansion velocities of 140 km s^{-1} seen in the Galactic center. Given the rms noise of our maps, we can set a limit of $\leq 10^6$ $M_\odot$ for any broad feature ($\Delta V \sim 200$ km s^{-1}) in this area of the galaxy with size ≤ 200 pc. In addition, the masses of atomic and molecular gas are more nearly equal in M33, compared to the factor of 10-50 contrast in the Galactic center (Oort 1977). Thus the nuclear region of M33 is very different from that of the Galaxy, both in its total mass of molecular gas, its H_2-to-HI ratio, and its energetics.

The difference between the two galaxies may be related to the smaller total mass of M33. The total mass of the Galaxy in the central kiloparsec is 1.6×10^{10} $M_\odot$ (Oort 1977) while the total mass in the same region of M33 (from our rotation curve) is $\sim 8\times10^8$ $M_\odot$. The fractions of the central mass in the form of molecular hydrogen are 10% and 4% for the Galaxy (Oort 1977) and for M33, respectively, while the total gas mass fractions are 11% and 6%. Thus the weak CO emission of M33 is not so much due to a *relative* scarcity of interstellar matter as to the smaller overall mass of the galaxy, since the gas mass fractions in the two galaxies are comparable. The very different atomic to molecular gas ratios may be due to a

surface density threshold for the formation of molecular gas. If similar HI surface densities are required to form molecular gas in both galaxies, the molecular to atomic gas ratio will be much lower in M33 since the total gas surface density is so much lower. Finally, the noncircular motions observed in the Galaxy are likely due to its low-level nuclear activity, which is presumably lacking in M33.

VII. Conclusions

The inner 3.5′ radius of M33 is found to contain 3.4×10^7 $M_\odot$ of molecular hydrogen in structures with sizes of 200-400 pc and masses of $3\text{-}10\times10^6$ $M_\odot$. The diameters, velocity widths, and peak brightness temperatures of these structures are inconsistent with their being an extension to larger diameters of a Galactic-type molecular cloud population. In addition, these structures are neither tidally nor virially bound and must therefore be transient agglomerations of smaller bound systems. Most of these CO complexes are associated with the inner spiral arms. The HI and CO emission are spatially correlated, but without an overall global pattern. The radially averaged H_2 column density is approximately constant within this region, i.e., no evidence is seen for an exponential decrease with radius out to 3.5′. The average column density of molecular hydrogen is roughly three times the column density of atomic hydrogen and is sufficient to remove the central hole seen in the radial HI profile. The rotation velocity of the CO emission agrees well with previous determinations and gives a total mass of 5×10^8 $M_\odot$ and a molecular gas mass fraction of 4% within a radius of 800 pc. The weak CO emission in M33 is mainly due to its small total mass, while the observed approximately circular motions may be due to the absence of the low-level nuclear activity which is seen in our own Galaxy.

Figure Captions

Fig. 1 – The map of the integrated CO emission for the inner region of M33. The lowest contour is at 1.1 K km s^{-1} and contours increase by 0.4 K km s^{-1}. The (0,0) position corresponds to $\alpha(1950) = 01^h31^m03.0^s$, $\delta(1950) = +30^o23'54''$ and the optical nucleus is indicated by the cross at ($\Delta\alpha = -0.3, \Delta\delta = 0.35$). The two inner spiral arms are indicated by dashed lines (Humphreys and Sandage 1980).

Fig. 2 – The CO emission contours of Figure 1 are overlaid on a grey-scale plot of the HI emission in the nucleus of M33. Peaks in the HI emission show up as dark areas on the grey-scale plot.

Fig. 3 – The radial profile of the H_2 column density perpendicular to the plane of the galaxy, averaged over elliptical annuli, is indicated by the solid line. The HI column density from Deul and van der Hulst (1987) is indicated by the dashed line.

Fig. 4 – HI column density versus H_2 column density, both measured perpendicular to the plane of M33 at 60″ resolution.

Fig. 5 – The observed velocity field (V_{LSR}) of M33 as traced by the CO line.

Fig. 6 – Rotation velocity versus radius for M33. Points from the northern half of the galaxy are indicated by dots and points from the southern half by triangles. The four squares are taken from the HI rotation curve (Newton 1980) and the open circles are for the two positions near OB association 64 (see text). The line is a fit to these points with velocity assumed proportional to $R^{0.5}$. The cross-hatched area indicates the region covered by the optical data (Rubin and Ford 1985).

Figure 1

Integrated CO Emission in M33

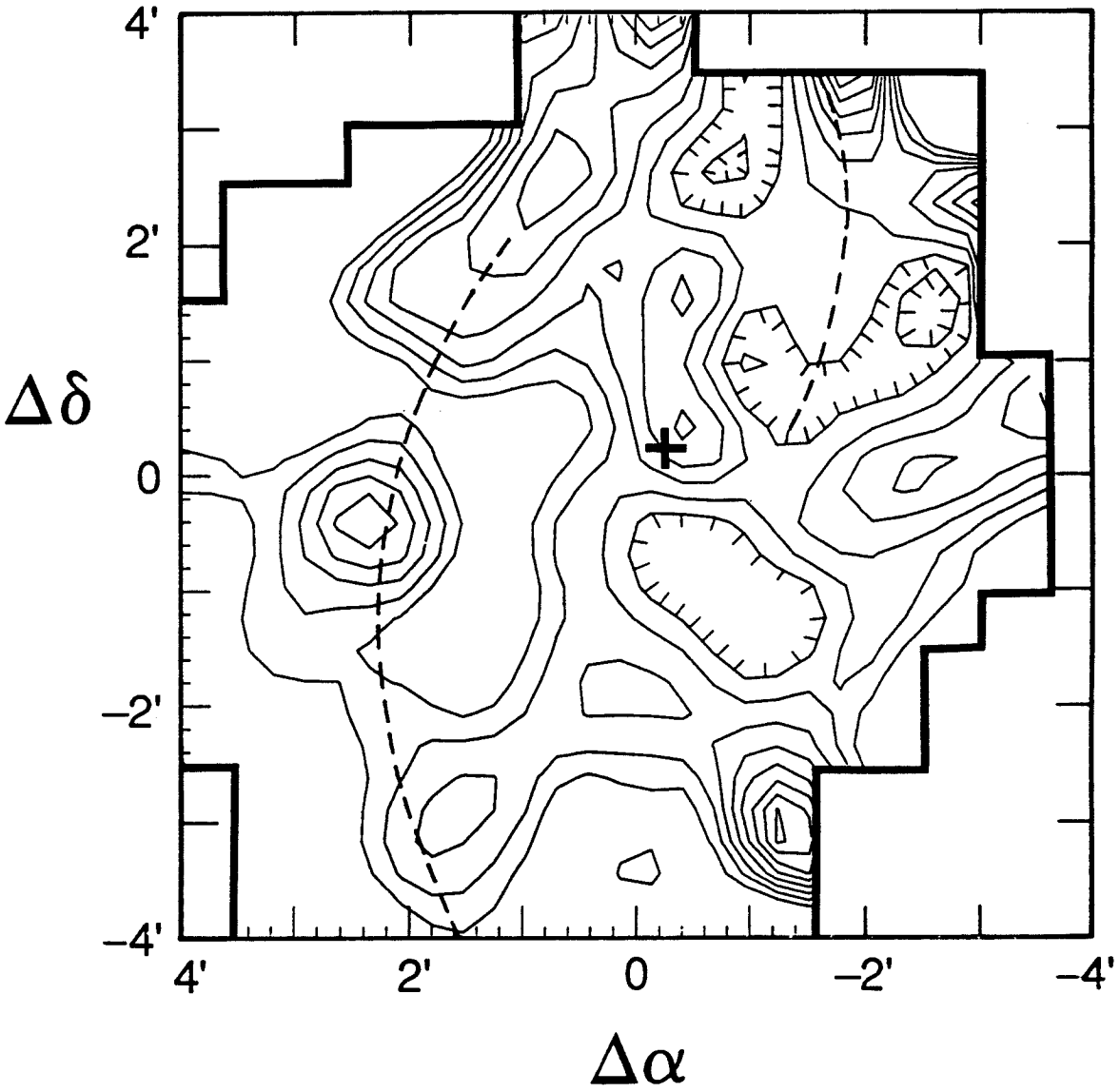

Figure 2

CO and HI Emission in M33

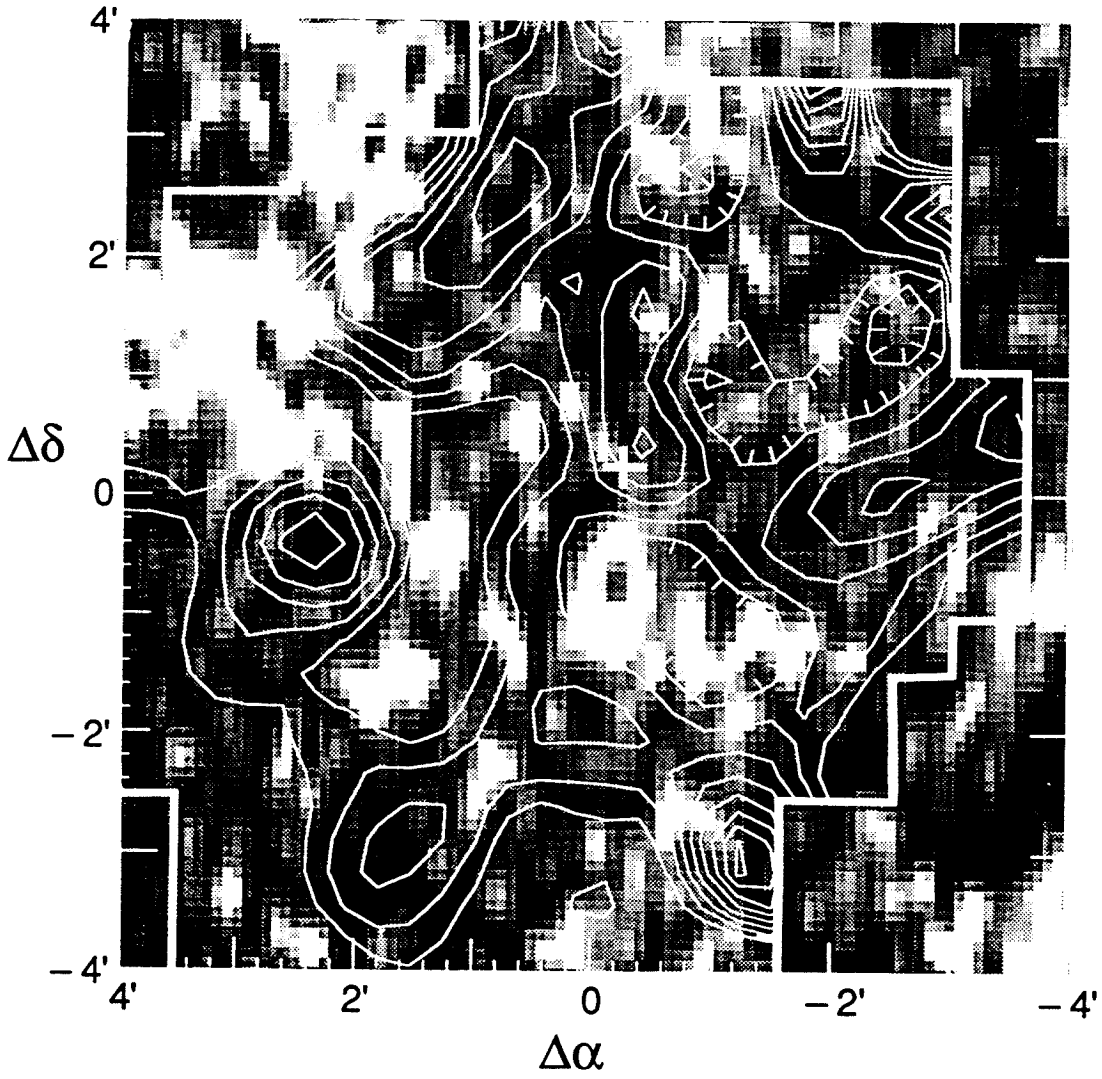

Figure 3

H_2 and HI Column Density Radial Profiles

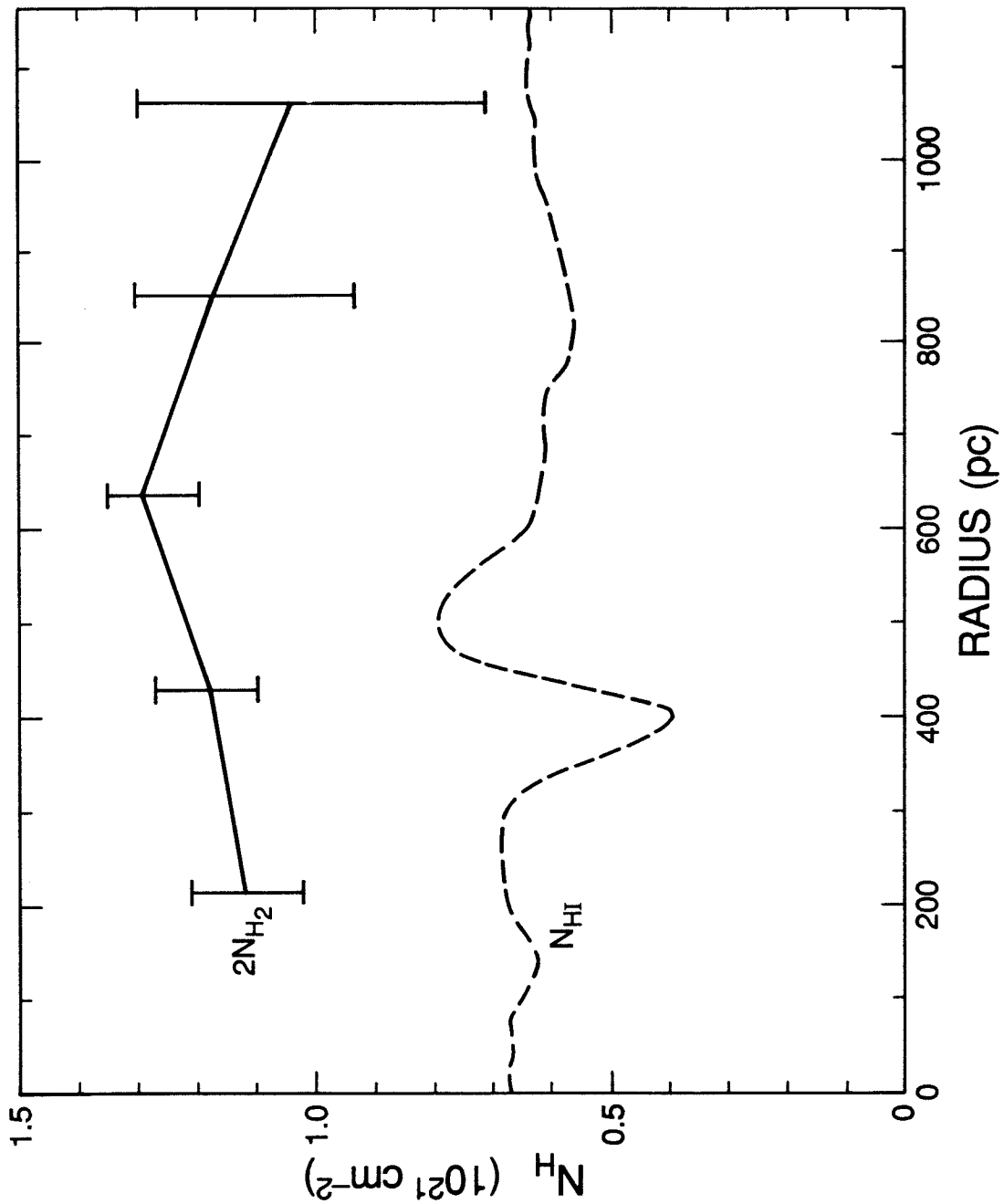

Figure 4

HI versus H_2 Column Density

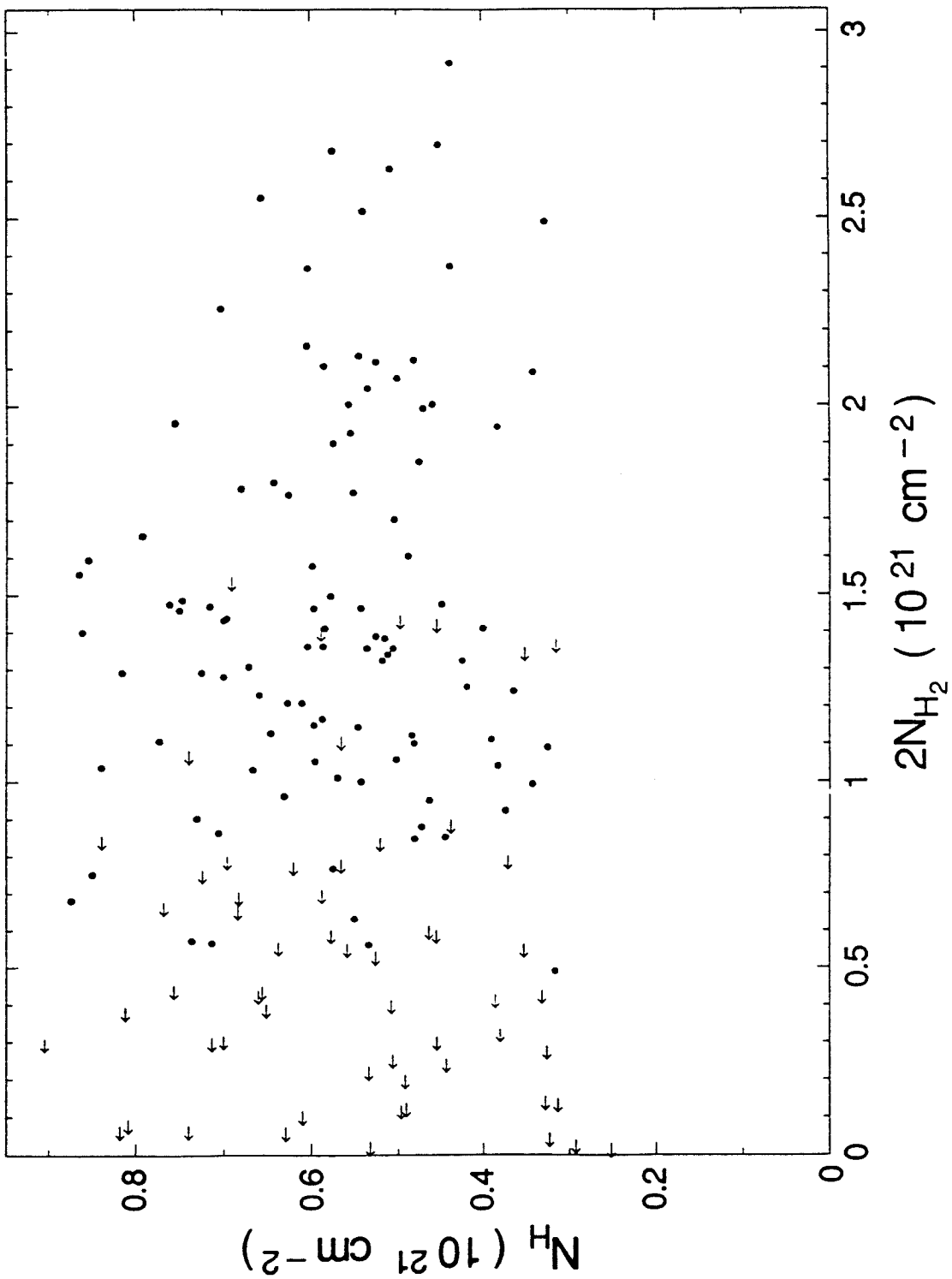

Figure 5

CO Velocity Field

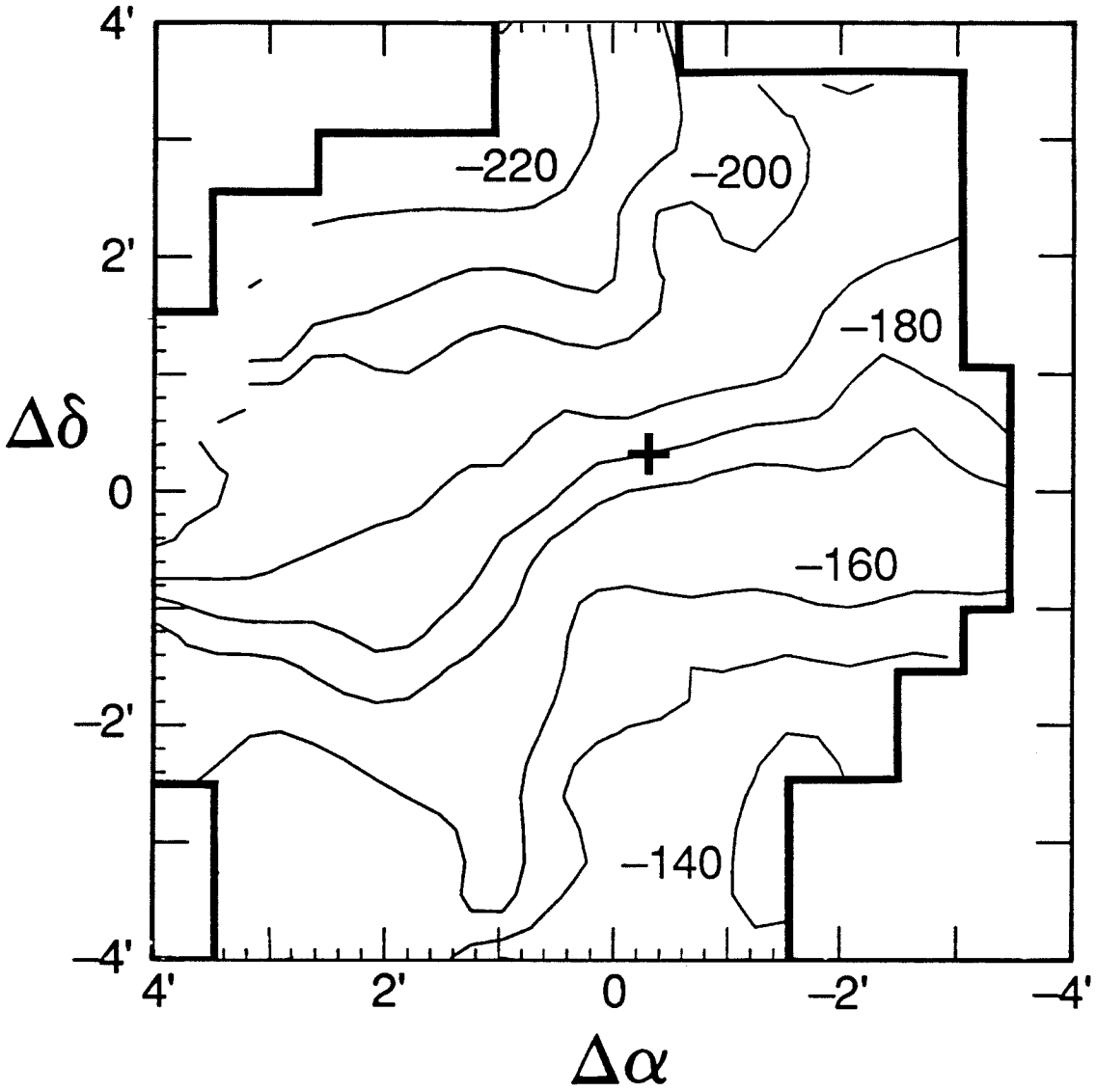

Figure 6

CO Rotation Velocity

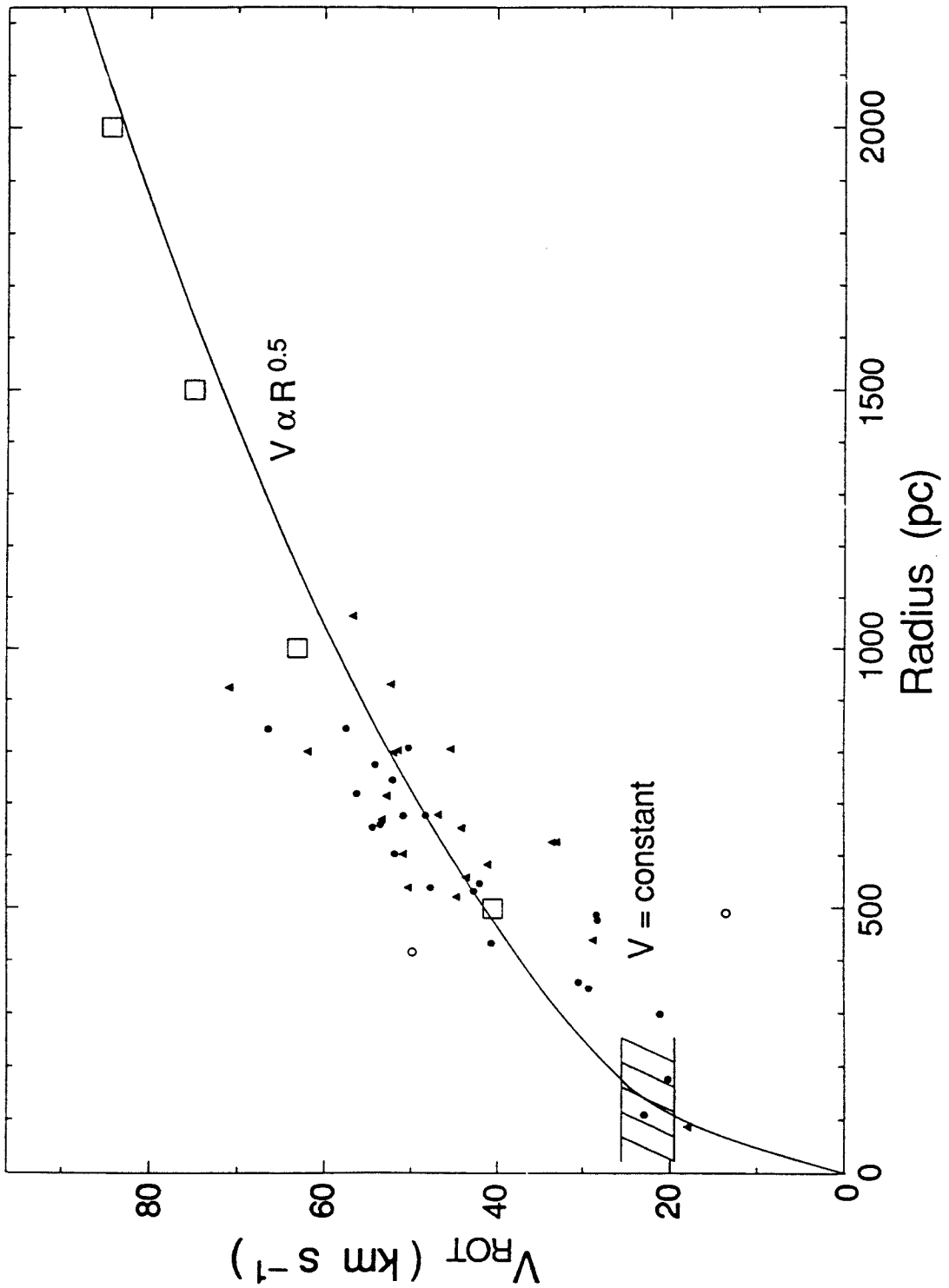

CHAPTER 3

OB Associations in the Inner Two Kiloparsecs of M33

I. Introduction

The properties of OB associations are important for addressing a number of questions relating to star formation and spiral structure in galaxies. The ages of associations in spiral arms constrain theories of spiral structure. For example, an age gradient across the arms indicates the presence of a spiral density wave, whereas an age gradient running along the arms may indicate the presence of stochastic, propagating star formation. The large numbers of OB stars outside spiral arms reveals that high-mass star formation is not limited to spiral arms, since these young stars must have formed near their present location (Madore 1979).

OB stars and associations provide a direct means of probing changes in the initial mass function and the star formation rate in external galaxies, since they are the only stars that can be studied individually in galaxies more distant than the Magellanic Clouds. High-mass stars also have a large effect on the interstellar medium, enriching the chemical composition and providing kinetic energy through stellar winds, HII regions, and supernova explosions. However, the study of these stars is complicated by their degeneracy in U-B and B-V color, requiring spectroscopy to place these stars accurately in a theoretical H-R diagram (Massey 1985). In addition, evolution along the main sequence occurs at roughly constant color, resulting in large uncertainties in transforming from a luminosity function to an initial mass function or in calculating masses of

individual stars. Photometric studies are useful nevertheless to identify blue stars for follow-up spectroscopic studies and to identify the OB associations.

OB associations in M33 have been identified by eye from photographic plates (Humphreys and Sandage 1980; Kunchev and Ivanov 1984). These associations are typically twice as large as OB associations in our own Galaxy (Humphreys 1979). Comparisons of association properties between individual galaxies are difficult unless similar quality plate material is available for all galaxies and the same person has identified the associations in all galaxies (Hodge 1986). Such subjectivity in association properties is unsatisfactory, since biasing the results could lead to significant errors in the derived star formation properties. An objective method of identifying associations in external galaxies could provide a powerful tool for studying high-mass star formation.

In this chapter we present new UBV CCD photometry for 9 x 12′ centered on the nucleus of M33. These data reach ~1 mag fainter than earlier photographic surveys and thus extend roughly a factor of two lower in mass along the main sequence. The observations and the data reduction are described in Section II. The global properties are discussed in Section III. The identification of the OB associations using an automated grouping algorithm is discussed in Section IV. The results are compared with earlier photographic studies and systematic biases remaining in this selection algorithm are discussed in detail. The properties of the OB associations such as size, mass, age, and location relative to spiral arms are discussed in Section V. The chapter is summarized in Section VI.

II. Observations and Data Reduction

A total of twelve overlapping CCD fields in the nucleus of M33 were observed through *UBV* filters in two observing runs in the fall of 1988. Four fields were observed in B and V at the Canada-France-Hawaii telescope on 9 August 1988

with the RCA2 double density CCD chip (chip scale 0.205 $''$ pixel^{-1}). The seeing was $\sim$ 0.8$''$ and the night was not photometric. These CCD frames were flat-fielded using dome flats. The remaining fields and filters were observed at the Palomar 60$''$ telescope during 9-13 October 1988. A Tektronix CCD chip (CCD 6) that is extremely sensitive to blue light was used for these observations. The chip scale is 0.235 $''$ pixel^{-1}. The seeing varied from 1.2-1.9$''$ in U and from 1-1.5$''$ in B, and V and the first night was photometric. The V data were flat-fielded using morning dome flats taken each day. Medianed sky flats were used to flat-field the U and B data, since the flat-fielding lamp did not produce good dome flats in these bands.

The data were reduced using the data reduction program DAOPHOT (Stetson 1987), which uses point-spread function fitting to groups of stars to achieve more accurate photometry in crowded fields. NSTAR magnitudes were obtained for all the frames. Aperture corrections to correct for the light from the star beyond the fitting radius were calculated using images from which all but the brightest, unsaturated, and relatively isolated stars had been subtracted (see Freedman 1988 for details). These corrections were calculated using between two and ten stars, with most frames having at least five stars, and formally are accurate to 0.007-0.027 mag.

The data were calibrated using standards in NGC 7790 and M92 (Christian *et al.* 1985) for B and V and Landolt standards for U (Landolt 1983) observed on the night of October 9. Standards for which a faint star was included within the aperture were eliminated, as were standards near the few bad columns on the chip. For the U standards, three exposures of each star were taken per frame, moving the telescope between exposures. The magnitudes of these three observations disagreed by up to 0.09 mag and so an average magnitude with

the appropriate uncertainty was used to calculate the transformation. The most likely explanation for these variations is problems in flat-fielding the U frames or small variations in the sky background caused by the multiple exposure technique. The transfer solution and the calibration of the data were calculated using programs written by Peter Stetson. The final transformations are given in Table 1.

Fields not observed on the photometric night were calibrated using overlap regions with fields that could be independently calibrated. The zero-point shift in the instrumental magnitudes between the two frames was calculated using stars in the overlap region. Only stars with good χ values from the NSTAR fits ($\chi < 1.8$ for CFHT frames, $\chi < 1.3$ for Palomar frames) were used to calculate the zero-point shift. For frames obtained at Palomar, no stars within 50 pixels of the edge of the chip were used in calculating the shift, since the flat-fielding is not reliable for this chip near the edges. The stars were weighted by their NSTAR uncertainties in calculating the fit. The uncertainties in the final zero-point shifts range from 0.01 to 0.06 mag, with a typical uncertainty of 0.03 mag.

In order to check that the first night of the Palomar run was photometric, we compared calibrated B and V magnitudes for Field 5 with magnitudes from Field 2 of Wilson, Freedman, and Madore (1990). Using only stars brighter than 21 mag, the mean difference between this data set and that of Wilson, Freedman, and Madore is 0.012±0.01 mag in B and -0.063±0.014 mag in V. These zero-point shifts lie within the uncertainties in the photometric transformations of the two different data sets. Thus we conclude that the first night of the Palomar run was indeed photometric.

Some large zero-point shifts between frames remain in the calibrated U data and thus these magnitudes are more uncertain than the B and V magnitudes.

Some of the scatter in the U magnitudes may be attributed to the same source as the scatter in the magnitudes of the Landolt standards. The average magnitude difference between the left and right sides of the chip seen in the standard stars is 0.066±0.019 mag. Thus the U magnitudes have an additional uncertainty of ±0.04 mag due to the variation in instrumental magnitudes over the surface of the chip. We cannot estimate easily the effect of this variation on the other filters because we do not have multiple observations of a single standard star at the same airmass, but it should not be larger than the effect seen in the U data.

Table 2 (Appendix 1) gives UBV magnitudes for all stars with V < 21 mag and either B-V < 0.4 or U-B < -0.5 mag. The aperture correction and instrumental transformation uncertainties have been added in quadrature to the NSTAR uncertainties. For stars observed in more than one frame, a flux-averaged magnitude and uncertainty were calculated from the independent measurements. Measurements within 50 pixels of the edge of the CCD frame were not included. Since the U frames do not go as deep as the B and V frames and have poorer seeing, the B and V data were matched independently. Stars found only in these two filters are also included in Table 2. The right ascension and declination of the stars were calculated using the astrometric positions for nine bright Cepheids in these fields (Freedman, Wilson, and Madore 1990) and are accurate to $\pm 0.1^s$ in right ascension and $\pm 1''$ in declination. The mean uncertainties as a function of magnitude are given in Table 3. Including the uncertainties in the aperture corrections for B and V, the systematic uncertainties in our calibration are ±0.15 mag in U, ±0.05 mag in B, and ±0.04 mag in V.

III. Global Properties

Color-magnitude and color-color diagrams for the entire data set are presented in Figure 1. The major feature of both color magnitude diagrams is the

blue plume of the main sequence, running vertically at B-V$\sim$0 and U-B$\sim$-0.9 mag. The width of this feature above V=21 mag is about 0.5 mag in both B-V and U-B, somewhat larger than the two-sigma photometric uncertainties. Red supergiants are also visible in the V versus B-V color magnitude diagram at 19 $<$ V $<$ 21 and B-V$\sim$1.5 mag.

The average reddening can be calculated by comparing the color of the blue plume to the expected unreddened color of the zero-age main sequence, $B-V = -0.3$ mag (Flower 1970). The reddening for the entire data set was estimated from the modal B-V color of all stars with $19 < V < 21$ and $-0.4 < B-V < 0.4$ mag, binned to a resolution of 0.1 mag. This method gives an average reddening E(B-V) = 0.35 mag. The reddening can also be calculated from the color-color diagram of Figure 1c. All the main sequence stars we observe have roughly the same B-V and U-B colors and thus a fit of the main sequence colors to the data is not justified. Instead, the centroid colors were calculated for the concentration of stars with $-0.25 < B-V < 0.15$ and $-1.2 < U-B < -0.7$ mag, yielding mean colors of B-V=-0.04 and U-B=-0.92 mag. Adopting intrinsic colors for O stars of -0.3 and -1.2, respectively, the color excesses are E(B-V)=0.25 and E(U-B)=0.30 mag. These color excesses are not formally consistent with a normal reddening law, E(U-B)=0.72E(B-V). However, given the large uncertainty of $\pm$0.15 in the zero-point of the U photometry, these colors cannot be taken as evidence for a different reddening law in M33. Averaging the E(B-V) results from the color-magnitude and color-color diagrams gives a mean reddening of E(B-V)=0.3 mag.

The data were examined for radial variations in the average reddening. Reddenings were calculated using the modal B-V color in four elliptical annuli spaced by 500 pc in radius. No evidence for a significant reddening gradient was found. This is consistent with a uniform dust-to-gas ratio, since the HI and CO radial

profiles are both quite flat (Chapter 2). Reddenings were also calculated for the northern and southern halves of the galaxy and again no difference in the mean reddening was found.

The blue luminosity function is plotted in Figure 2. Stars were selected using a B-V cutoff of 0.0 or a U-V cutoff of -0.9. A straight line with a slope of 0.65 (Freedman 1985a) has been overlaid on the luminosity functions and is consistent with our number counts for V < 19.5. A turnover in both luminosity functions occurs below V=21 mag. No attempt has been made to correct our data for incompleteness at the faint end. Assuming that the slope of the luminosity function is constant to V=21 mag, our data are incomplete by 30% for 19.5 < V < 20, 55% for 20 < V < 20.5, and 65% for 20.5 < V < 21.

IV. Identifying the OB Associations

OB associations are identified using a "friends of friends" method. All the stars brighter than a given cutoff in V magnitude and bluer than a given B-V or U-B cutoff were identified. The mean surface density of blue stars, Σ, was used to calculate a mean separation radius, $R_o = \sqrt{1/\pi\Sigma}$. For each blue star, the list of bright, blue stars was searched to identify any other stars lying within one search radius of the program star. Any stars identified in this way were in turn checked for new stars lying within the search radius. In this way, all blue stars were placed in groups, varying in size from a single star to a few hundred stars. This process was carried out for a range of V, B-V, and U-B cutoffs and for search radii of $R_o/\sqrt{2}$, R_o, and $\sqrt{2}R_o$ to estimate the dependence of the group properties on the search radius, magnitude, and color cutoffs. The color cutoffs were selected to range from the center to the red edge of the blue plume. (B-V = 0, 0.2, 0.4; U-B = -0.9, -0.7, -0.5). The faintest limiting magnitude used was V=21 mag, since the uncertainties in magnitudes and colors are large at

fainter magnitudes. In addition, the Palomar frames are more incomplete than the CFHT frames at V < 21 mag, which would produce a nonuniformity in the properties of groups identified using a fainter cutoff.

The main source of subjectivity in our method is the choice of search radius, illustrated in Figure 3. The search radius varies by a factor of two across the three panels, dramatically changing the size and appearance of the groups identified. A large search radius produces large, low surface density groups, while a small search radius identifies only small, tight knots of blue stars. A larger search radius also decreases the percentage of groups containing less than three stars and increases the percentage containing more than ten stars, as well as decreasing the total number of groups found. No effort was made to vary the search radius to compensate for the background star density, since the mean density of blue stars is very uniform if the contribution of the large group near the nucleus is ignored.

Another option is to use all stars with B and V magnitudes or only stars with U photometry to identify the groups. The U photometry has lower background levels near the nucleus while the B and V data have considerably better seeing and smaller systematic uncertainties in the photometric calibration. The groups identified with the UBV data set are shown in Figure 3d. There is good agreement between the statistics of the BV- and UBV-identified groups, but some variations (naturally) exist in the exact definition of a given group. Changing the color and magnitude cutoffs does not change the group properties very much. The main effect of using a brighter magnitude cutoff or a bluer color cutoff is to decrease the number of stars to be grouped, reducing the number of large groups found with a given search radius.

To test whether the data are significantly more clumped than a random

distribution, the size distribution of the groups was compared with that obtained from a random distribution of the same number of stars. Most of the smaller groups in our sample are not statistically significant, i.e., similar numbers of small groups are found in the random distribution. Figure 4 compares the observed size distribution with that of a random distribution for three different search radii. Depending on the search radius, the smallest group that is significant compared to a random distribution varies from 9 stars for the smallest radius to about 20 stars for a radius twice as large. Thus in studying the properties of the OB associations we exclude the smaller groups, since we do not know if they are physically meaningful associations or simply chance superpositions of stars.

The "friends of friends" algorithm has been compared with another method commonly used to identify groups, that is, the identification of regions of above average stellar density. Figure 5 shows a contour plot of stellar surface density binned to a resolution of 50 pixels compared with the positions of groups with at least 10 stars identified using the "friends of friends" algorithm. The two methods agree very well, with 80% of the groups identified with an individual density peak that is two sigma above the mean level and most of the rest of the groups sharing a single extended two-sigma peak.

It is interesting to compare our method and data with previous identifications of the M33 associations. OB associations have been identified using a limiting V magnitude of 20, a B-V cutoff of 0.4, and a search radius of 55.4 pixels ($\sqrt{2}R_o$) to try to match the associations identified photographically (Humphreys and Sandage 1980; Kunchev and Ivanov 1984). In general, there is good agreement with the associations of Humphreys and Sandage (1980) except near the nucleus of the galaxy where the high background density makes it difficult to identify stars on photographic plates. We also identify most of the Kunchev and

Ivanov associations in this region. However, we do not identify associations for three of their groups (147, 150, and 151), although there are some blue stars scattered through these regions. This comparison shows that the photographic studies identified OB associations with reasonably uniform selection criteria across the inner part of the galaxy.

V. The Properties of the OB Associations

a) Parameters Used to Define Association Properties

The properties of OB associations in our own Galaxy have been reviewed by Blaauw (1964). Eleven associations within 1 kpc of the Sun have diameters ranging from 2 to 200 pc and contain between 1 and 60 O-B2 stars. Many associations are made up of sub-groups containing 10 to 20 OB stars. The mean age of the associations is 8×10^6 yr. Humphreys (1979) estimated a mean linear size of 125 pc for 57 Galactic OB associations and noted that the associations in M33 are larger than Galactic associations.

We have identified associations using a limiting V magnitude of 21 (for which our data is reasonably uniform across the whole area surveyed) and color cutoffs that include the whole width of the blue plume (B-V $<$ 0.4 and U-B $<$ -0.5). Some evolved stars may be included in this sample, but such stars have left the main sequence fairly recently and are also high-mass stars. Since the time between the end of core hydrogen burning and the end of core carbon burning is roughly 15% of the main sequence lifetime (Maeder and Meynet 1988), the contamination by evolved stars within the adopted color limits is small.

The association properties were analyzed using both the BV- and the UBV-identified groups to estimate the uncertainties in the derived association properties from the choice of data set. A search radius R_o was used for both data

sets, corresponding to 24.5 pixels (22 pc) for the BV data and 33.4 pixels (30 pc) for the UBV data. These radii are reasonably well matched to the mean radii of 40 pc of OB associations in the LMC and the SMC (Hodge 1986) and the mean radii of 60 pc estimated for Galactic OB associations (Humphreys 1979). No systematic differences were found in the association properties and so only the BV associations are discussed in detail below. *It must be emphasized that the choice of the search radius is arbitrary and directly affects the diameters and masses of the associations identified.* However, the automated grouping algorithm allows the identification of associations in different galaxies using the same search radius and thus enables a fair comparison between association properties in different galaxies.

The center of an association was defined to be the centroid of the stars that define the boundary of the association, the smallest convex figure that can be drawn around the association. The association radius was then defined to be the mean distance of these boundary stars from the center. For six associations with at least 20 stars in the range $19 < V < 21$ and $-0.4 < B - V < 0.4$, the reddening was determined for each association using the modal color method of Section III, while the mean reddening of the entire data set was adopted initially for smaller associations. The resulting overlay of evolutionary tracks in the H-R diagram was used to adjust the reddening interactively for eight associations that appeared to have slightly less foreground extinction, i.e., the adopted reddening resulted in many stars lying significantly blueward of the main sequence.

Red-to-blue ratios were calculated using the formalism of Meylan and Maeder (1982) with a limiting dereddened V magnitude of 20 instead of 21.2, since our data usually do not go deep enough to use the fainter magnitude cutoff. Using dereddened colors, stars with B-V < 0 are assigned spectral type OB, $0 <$

B-V < 0.2 type A, 0.2 < B-V < 1.2 type FG, and 1.2 < B-V type KM. For associations that lie in fields observed at the CFHT, the ratios were also calculated using the fainter V cutoff. Ratios were also calculated for the entire data set using V cutoffs of 18, 19, and 20 to determine whether a faint cutoff biases the results against red stars. Changing the V cutoff produced no significant differences in the red-to-blue ratios. The red-to-blue ratios also do not vary significantly when the input reddening is changed by ±0.1 mag.

The above properties of the OB associations (radii, number of blue stars, red-to-blue ratios) are derived directly from the observations. Both the mean number of blue stars per association and the mean radius vary with the search radius. Thus the adopted search radius has a large influence on the resulting association properties; there is no way to avoid this systematic affect. However, both the mass and the age of an association are calculated using theoretical evolutionary tracks to obtain masses from the observed colors and magnitudes. The uncertainties in this procedure are difficult to estimate and thus the adopted procedures are discussed in detail below.

b) Calculating Stellar Masses

The most important problem in estimating stellar masses from photometry is the degeneracy in the colors and magnitudes of high-mass stars. The transformation from effective temperature to photometric colors is also uncertain. A recent study of the SMC association NGC 346 that used both photometry and spectroscopy to place stars in the theoretical color-magnitude diagram revealed that masses obtained from photometry alone are systematically underestimated compared to masses obtained from spectroscopy (Massey, Parker, and Garmany 1989). Many stars more massive than 25 $M_\odot$ are shifted down into the 25 and 15 $M_\odot$ bins, which causes a systematic flattening of the initial mass function

obtained from the photometric data.

Other sources of uncertainty in estimating masses such as bolometric corrections and reddening affect both spectroscopic and photometric measurements. For example, the two-sigma systematic uncertainty in our B-V colors and thus in the mean reddening is ±0.1 mag, which changes the placement of the evolutionary tracks in the color-magnitude diagram and introduces an uncertainty in the mass of ~30%. In addition, evolutionary tracks calculated using different assumptions for mass loss and convective overshooting show large disagreements in the late stages of stellar evolution (de Loore 1988). However, the agreement along the main sequence is better than ±0.2 mag and ±0.05 in $\log(T_{eff})$, so this is probably not a large source of uncertainty in obtaining main sequence masses.

The evolutionary tracks of Maeder and Meynet (1988) are used to calculate the masses of the stars in the OB associations. The tracks were transformed from effective temperature and luminosity to V magnitudes and B-V colors using the equations for bolometric correction and effective temperature as a function of B-V color given in Massey, Parker, and Garmany (1989). The U-B colors were then estimated from the B-V colors using the data given by Fitzgerald (1970) for luminosity classes Iab, III, and V. Stars more massive than 20 $M_{\odot}$ were assumed to be luminosity class Iab once core hydrogen was exhausted, while stars with masses 20 $M_{\odot}$ and less were assumed to be luminosity class III. These evolutionary tracks were then reddened using $A_v = 3E(B-V)$, $E(U-B) = 0.72E(B-V)$, and the mean E(B-V) of 0.3 mag calculated earlier.

The most obvious problem in estimating stellar masses in this way is the degeneracy of the evolutionary tracks along the main sequence. Figure 6 shows the evolutionary tracks for stars from 9 to 85 $M_{\odot}$ plotted in the theoretical plane and transformed to both B-V and U-B color. *Stellar masses along the main*

sequence estimated from photometry alone are uncertain by at least 50% due to the constant color of the upper main sequence and the vertical evolution of stars in the color magnitude diagram until the end of core hydrogen burning. For this reason, we have chosen to work in the observational plane rather than transforming from observed magnitudes to luminosities and effective temperatures, which would spread out the main sequence due to insignificant differences in color and disguise this important problem.

The mass of the association was obtained by interpolating between the evolutionary tracks and counting the number of stars in each mass region. The ends of the bins were extrapolated to the blue at constant V magnitude in order to assign masses to stars that lie blueward of the evolutionary tracks. Only stars with dereddened V magnitudes brighter than 20 were used to calculate association masses, which corresponds to a main sequence mass cutoff of 20 $M_{\odot}$. The lowest mass for which we have complete coverage of the main sequence evolution is 40 $M_{\odot}$. The derived masses need to be corrected upward for photometric incompleteness at faint V magnitudes and incomplete coverage of the main sequence for masses between 20 and 40 $M_{\odot}$. To correct for photometric incompleteness, the number of stars with $20 < V < 20.5$ was scaled up by a factor of 1.4 and the number of stars with $20.5 < V < 21$ was scaled up by a factor of 2.2 (see Section III). The coverage of the main sequence was estimated from the evolutionary tracks by assuming that stars travel at a uniform rate up the evolutionary track while on the main sequence. Thus counts of 25 $M_{\odot}$ and 20 $M_{\odot}$ stars on the main sequence are 70% and 40% complete, respectively. The mass corrected for incomplete main sequence coverage and incomplete photometry for $V > 20$ is $M_{corr}(\geq 20\,M_{\odot}) = 1.6M(\geq 20\,M_{\odot})$. Adopting the modified Miller-Scalo initial mass function $N(M) \propto M^{\alpha}$ (Kennicutt 1983) with α = -1.4

for 0.1 < M < 1 and -2.5 for 1 < M < 100, the total mass of the association is $M(\geq 0.1\,M_{\odot}) = 12 M_{corr}(\geq 20\,M_{\odot})$.

c) Calculating Association Ages

Association ages are estimated from the V magnitudes of the brightest main sequence stars. High-mass stars evolve with constant color and continually increasing V magnitude while burning hydrogen in their cores. When core hydrogen is exhausted, the star brightens and reddens, rapidly evolving out of the main sequence region. Stars with larger masses reach a brighter limiting main sequence V magnitude than do stars of lower mass, allowing us to assign a *minimum* mass to a star based on its V magnitude. This method will only work up to 60 $M_{\odot}$, since more massive stars have fainter maximum V magnitudes than 60 $M_{\odot}$ stars. Thus the main sequence lifetime of the most massive star in an association defines an upper limit to the age of the association.

Other physical effects can be confused with age variations. For example, if the upper mass cutoff to the initial mass function is not constant across the galaxy, it would be impossible to determine ages in this way. Also, small associations may not contain a very massive star. Adopting the modified Miller-Scalo initial mass function (Kennicutt 1983), an association containing 300 $M_{\odot}$ of stars more massive than 20 $M_{\odot}$ should contain at least one star with M > 60 $M_{\odot}$. Thus statistical effects due to small numbers of stars are not important for associations with $M(> 20\,M_{\odot}) > 300$ $M_{\odot}$.

The age of each OB association was estimated using the three brightest stars lying within ± 0.15 mag (2σ) of the reddened zero-age main sequence. The three brightest stars were used to define a mean age rather than using the single brightest star in order to reduce the effects of small number statistics. Each star was assigned a mean minimum mass taking into account the 2σ uncertainty in V

magnitudes (0.15 mag) and shifting the mean reddening by 0.1, 0, and -0.1 mag. The age of the association was calculated from the average mass of the three stars by interpolating between the terminal main sequence ages (Maeder and Meynet 1988). The masses, V magnitude cutoffs, and ages for the theoretical tracks are given for convenience in Table 4.

Because there are only five different evolutionary tracks covering the mass range from 15 to 60 $M_\odot$, the resolution in age along the main sequence corresponds to uncertainties in the ages of $\pm 10^6$ yr for ages $< 5 \times 10^6$ yr, $\pm 2 \times 10^6$ yr for $5 - 9 \times 10^6$ yr, and $\pm 3 \times 10^6$ yr for $9 - 12 \times 10^6$ yr. The uncertainty due to random errors in the photometry should be much less than this, since the peak magnitudes of the different mass tracks are separated by at least six times the 1σ photometric uncertainties. The uncertainty from using small numbers of stars is difficult to estimate. Ages estimated using U magnitudes instead of V magnitudes were $(0.7 \pm 0.9) \times 10^6$ yr younger on average than the V ages. Adopting this age difference as the uncertainty due to small numbers of stars, the total uncertainty in the ages is $\pm 2 \times 10^6$ yr for ages $< 9 \times 10^6$ yr, and $\pm 3 \times 10^6$ yr for larger ages.

d) Results

A total of 41 associations each containing at least 10 bright, blue stars have been identified. The properties of these associations are given in Table 5 and the positions of the associations are overlaid on blue CCD frames in Figure 7. The radii range from 10 to 120 pc, with a mean radius of 40 pc. The masses $M(\geq 20\, M_\odot)$ range from 200 to 5000 $M_\odot$, with a mean mass of 600 $M_\odot$, excluding the four most massive associations. The ages range from 3.6×10^6 yr to 1.4×10^7 yr, with a mean age of 8×10^6 yr. Half of the associations lie along the northern and southern spiral arms (Sandage and Humphreys 1980), but the spiral pattern

of M33 cannot be traced unambiguously using these OB associations (Figure 3b), a conclusion consistent with previous studies. Six associations lie in a region of active star formation in the southwest corner of our map that may be another spiral arm (Kunchev and Ivanov 1984).

The luminosity function of stars in these associations is compared with the luminosity function for the remaining blue stars (field stars) in Figure 8. For the BV data, there are 580 field stars and 440 stars in associations, while for the UBV data the number of stars in each sample are 380 and 280, respectively. Despite somewhat fewer stars, the associations contain roughly twice as many stars brighter than V=18 than the field. The difference in the total number of bright stars is marginally significant given the small number of stars involved (10 versus 4 stars for the BV data, 8 versus 5 for the UBV data). This difference cannot be due to a larger reddening of the field stars, since the mean reddening of the two data sets is the same. One possible explanation for the different numbers of bright stars is that the upper mass cutoff to the initial mass function is smaller in the field. However, due to the degeneracy in the magnitudes of stars at the high mass end, some 60 $M_{\odot}$ stars could be fainter than V=18 mag. Spectroscopic observations of the brightest association and field stars would provide more accurate masses.

Another possible explanation is that field stars are older than stars in associations, that is, field stars are members of old associations that are sufficiently dispersed that they are not identified. More stars would have evolved off the main sequence, which would produce an excess number of red supergiants in the field. The red-to-blue ratios for the entire data set (Table 6) do show a higher number of FG supergiants than the ratios in the associations. This excess is real unless the foreground contamination (Ratnatunga and Bahcall 1985) has been

underestimated by a factor of six.

The relative numbers of red and blue supergiants can be used to test stellar evolution models. In particular, regions with lower metallicity are observed to have larger numbers of red supergiants, perhaps from decreased mass loss rates (Meylan and Maeder 1982). A steep gradient in the ratio of red (B-V $>$ 1.9) to blue (B-V $<$ 0.5) stars was observed in the inner part of M33 that appeared correlated with the metallicity gradient (Humphreys and Sandage 1980). However, the study suffered from small numbers of associations in the inner kiloparsec and in addition galactic radii were calculated in the plane of the sky, not deprojected to the true plane of M33. This result has been challenged in the photographic study of Freedman (1985b) and in a recent study of four CCD fields (Wilson, Freedman, and Madore 1990) that, however, did not extend into the nucleus of the galaxy. Our new data, which completely cover the inner part of the galaxy and go significantly fainter than earlier photographic studies, provide a definitive measurement of red-to-blue ratios in M33.

The number of supergiants of different spectral types (Meylan and Maeder 1982) were calculated for each of fourteen associations with at least 20 bright stars (Table 6). The associations were binned according to their deprojected radius and average ratios calculated in each of four radial bins. No radial gradient in the distribution of supergiant types is found within the inner two kiloparsecs of M33. In particular, the red-to-blue ratio, N_{KM}/N_{OBA}, shows very little variation from one association to another. The metallicity in this region varies by a factor of two, falling steeply from a value of 12 + log(O/H) = 9.0 near the nucleus to 8.7 at R = 1500 pc (Vilchez *et al.* 1988). Thus there is no variation in the relative numbers of red and blue supergiants as a function of metallicity in this region of M33, in agreement with other recent studies of M33. This conclusion disagrees

with the comparative study of the Galaxy and the Magellanic Clouds by Meylan and Maeder (1982). Data on OB associations in M33 at larger radii and lower metallicity could strengthen this conclusion.

Three associations have supergiant distributions that are significantly different from the mean. Association 34 is deficient in stars redder than spectral type OB. This association is probably a young cluster in which post-main sequence evolution is just beginning. Association 39 contains only one red star and is also probably a very young cluster in which little significant post-main sequence evolution has occurred. In contrast, Association 6 contains an excess number of red stars. The color-magnitude diagram shows one bright, very red star and a fairly even distribution of stars with -0.2 < B-V < 1.0 and 20 < V < 21 without a clearly defined blue plume. The fitted color excess is E(B-V) = 0.45, yielding an age of 8.5×10^6 yr. However, if the mean color excess for the galaxy is adopted, the age rises to 1.1×10^7 yr. Thus this association is probably the oldest large association in this region of the galaxy.

The spiral structure in the inner disk of M33 has been modelled using density wave theory (Roberts, Roberts, and Shu 1975). If the two inner arms are due to density waves, OB associations should be distributed with the younger associations on the inside (upstream) edges of the arms. Conversely, spiral structure generated by propagating star formation should produce age gradients running along the arms. The southern spiral arm contains prominent dust lanes (Humphreys and Sandage 1980) and a string of small HII regions (Boulesteix *et al.* 1974), while the northern arm is less regular in appearance. This difference between the northern and southern arms is also evident in the atomic hydrogen distribution (Newton 1980) and in the relative numbers of massive stars (Boulesteix, Dubout-Crillon, and Monnet 1981). Humphreys and Sandage

(1980) found no age gradients along or across the two inner arms of M33.

There are two regions in each arm where associations ages can be used to test the density wave hypothesis. Two regions in the southern arm at $\Delta\alpha = 1.9$, $\Delta\delta = -0.3$ and $\Delta\alpha = 1.7$, $\Delta\delta = 3.9$ (Figure 9) contain six associations each with masses ranging from 300 to 1500 $M_\odot$. Four pairs of associations show an age gradient across the arm with the younger association lying upstream of the older association and an average age difference of 3×10^6 yr. Thus the ordering of ages for these eight associations are weak evidence for the presence of a density wave in the southern spiral arm. However, two other associations run counter to this trend, since they are young but lie on the downstream side of the arm.

The situation in the northern spiral arm is quite different. The two regions at $\Delta\alpha = -2.3$, $\Delta\delta = -1.3$ and $\Delta\alpha = -1.4$, $\Delta\delta = 2.2$ contain three and five associations, respectively, with none younger than 8.5×10^6 yr. The masses of the associations range from 350-500 $M_\odot$, somewhat smaller than those of the southern arm, but still large enough to contain massive stars. One association in each region is $\sim 2 \times 10^6$ yr younger than the others and lies further up the arm in the direction of the nucleus. This age pattern is more consistent with a spiral arm generated by self-propagating star formation.

Why do the associations in the northern and southern arms look so different? The youngest northern associations contain no stars more massive than $\sim$20 $M_\odot$, while several associations of the southern arm contain stars as massive as 60 $M_\odot$. The lack of high-mass stars cannot be due to the smaller number of stars in the northern arm, since Association 1 has a similar number of stars to the northern arm associations and contains several 60 $M_\odot$ stars. One possible explanation is that no OB associations have formed in the northern arm during the last $\sim 8 \times 10^6$ yr. Thus the northern arm of M33 is currently at a special time in its

evolution when massive star formation throughout the arm has recently ceased. Another possibility is that the upper mass cutoff to the initial mass function is different in the northern and southern arms. In this case the ages of the northern associations would be over-estimated, since the high-mass stars would be missing due to this cutoff and *not* due to evolution.

VI. Conclusions

We have presented new CCD UBV photometry for stars in the inner 9′ x 12′ of M33. The average reddening for this region of M33 determined from the position of the blue plume in the V versus B-V color-magnitude diagram and from the U-B versus B-V color-color diagram is 0.3±0.1 mag. No evidence is found for a radial gradient in the average reddening. The slope of the luminosity function for V $\leq$ 19.5 is consistent with previous determinations and indicates that our data are 70% complete at V=20 mag.

The data have been used to re-identify OB associations using an objective, automated "friends of friends" algorithm. The major remaining source of subjectivity in this method is the search radius used to identify the associations. Comparison of this method with earlier photographic studies shows that previous assignments of association boundaries used a fairly uniform selection criteria, although the blue photographic study of Humphreys and Sandage (1980) was incomplete near the center of the galaxy. Photographic surveys in the U band (Kunchev and Ivanov 1984) perform better in regions with high background densities.

Associations were identified using stars with V < 21, B-V < 0.4, and a search radius of 24.5 pixels and correspond to 2σ deviations from the mean stellar surface density. A total of 41 associations were identified, with mean radii of 40 pc, masses of 600 $M_{\odot}$, and ages of 8×10^6 yr. These associations show a

remarkable uniformity in their distribution of supergiants of different spectral types. Thus we find, in agreement with Freedman (1985b), that M33 does not have a significant gradient in the ratio of blue-to-red stars as had been previously claimed (Humphreys and Sandage 1980, Walker 1964).

The luminosity functions for association and field stars show a marginally significant difference at the bright end in that the associations contain more bright stars than the field. This may be due to a difference in the upper mass cutoff to the initial mass function between associations and field stars. Alternately, field stars may be older on average than stars in associations. Spectra of the brightest blue stars in both the field and the associations are required to conclusively demonstrate that this mass difference is real.

There is weak evidence for a gradient in the OB association ages across the southern spiral arm in the sense expected to be produced by a density wave. However, the northern arm shows a weak age gradient along the arm. The properties of the OB associations in the two arms are significantly different, in that the associations in the northern arm do not contain any stars more massive than $\sim 20\ M_{\odot}$. The associations in the northern arm may all be significantly older than the southern arm associations and thus high-mass star formation has recently ceased or paused in the northern arm. Alternatively, the upper mass cutoff to the initial mass function may be substantially smaller in the northern arm than in the southern arm.

TABLE 1

Calibration for 1988 October 9

Filter	α	β	γ	additional observational scatter
U	0.488±0.115	-0.121±0.015	0.724±0.090	0.005
B	-0.338±0.033	0.009±0.013	0.326±0.018	0.026
V	-0.263±0.031	-0.042±0.012	0.230±0.018	0.025

B and V data are calibrated using $m = M + \alpha + \beta \times (B - V)_o + \gamma \times \chi$, where m is the observed magnitude, M is the standard magnitude, and χ is the extinction. U data are calibrated using $m = M + \alpha + \beta \times (U - B)_o + \gamma \times \chi$.

TABLE 2

UBV Photometry of Blue Stars in M33

(See Appendix)

TABLE 3

Mean Random Uncertainties as a Function of Magnitude

Filter Magnitude	σ_V	σ_B	σ_U
14-14.99	0.06	0.08	0.04
15-15.99	0.04	0.04	0.04
16-16.99	0.03	0.03	0.04
17-17.99	0.04	0.04	0.04
18-18.99	0.04	0.04	0.04
19-19.99	0.05	0.04	0.05
20-20.99	0.06	0.05	0.06
21-21.99	0.10	0.07	0.10
22-22.99	0.16	0.11	0.20

TABLE 4

Maximum V Magnitude and Main Sequence Lifetime

Mass ($M_\odot$)	Bright V cutoff (mag)	Main Sequence Age (10^6 yr)
60	16.74	3.6
40	17.16	4.8
25	18.52	7.1
20	19.05	8.8
15	19.75	12.1
12	20.25	17.4
9	20.95	28.7

TABLE 5

OB Association Properties

ID Number	$\Delta\alpha$ (′)	$\Delta\delta$ (′)	R (pc)	E(B-V) (mag)	$M(>20\,M_\odot)$ ($M_\odot$)	N_{blue}	N_{total}	Age (10^6 yr)
1	0.2	-0.7	120	0.25[a]	5050	132	222	3.6
2	-0.5	-0.5	40	0.30	400	11	21	13.9
3	-0.8	-1.0	10	0.30	400	11	11	8.5
4	-1.0	-2.7	20	0.30	610	13	16	10.1
5	-0.3	-0.2	40	0.30	720	22	33	7.1
6	-0.3	-1.1	40	0.45[b]	1020	21	48	8.5
7	0.3	-1.7	30	0.30	420	12	19	9.5
8	-2.0	2.3	20	0.20[b]	400	12	12	10.1
9	-1.0	2.0	30	0.40[b]	380	12	24	10.1
10	-1.7	2.0	30	0.30	340	11	12	10.1
11	-1.5	2.0	30	0.30	380	10	10	9.5
12	-1.0	3.1	20	0.20[b]	380	10	10	8.5
13	-2.1	1.6	30	0.30	440	12	14	8.5
14	-2.0	-1.2	30	0.30	450	12	15	10.8
15	-2.4	-1.2	20	0.30	430	10	10	10.8
16	-2.4	-1.5	20	0.10[b]	510	13	13	8.8
17	-3.4	-0.9	30	0.30	860	15	17	5.3
18	-1.2	-3.2	30	0.30	810	15	16	5.6
19	-2.3	-3.9	100	0.20[b]	2210	73	106	7.8
20	-3.7	-3.3	20	0.30	690	12	12	5.7
21	-2.9	-4.3	40	0.20[b]	290	11	12	13.9
22	-1.0	-4.8	30	0.30	990	20	23	6.6
23	-2.3	-4.7	50	0.25[a]	760	27	37	8.1
24	2.7	2.4	40	0.30	650	19	46	7.8
25	1.8	0.3	60	0.35[a]	1190	29	123	7.8

TABLE 5 (continued)

ID Number	$\Delta\alpha$ (′)	$\Delta\delta$ (′)	R (pc)	E(B-V) (mag)	$M(>20\,M_\odot)$ ($M_\odot$)	N_{blue}	N_{total}	Age (10^6 yr)
26	2.1	0.2	30	0.30	330	13	41	11.4
27	0.8	0.9	30	0.30	640	19	44	7.4
28	2.4	-1.8	20	0.30	340	11	16	8.1
29	2.2	-2.3	30	0.30	560	16	30	8.8
30	1.7	-0.3	40	0.30	310	15	55	8.8
31	2.4	-0.9	30	0.30	440	15	35	6.6
32	1.5	-0.8	20	0.40[b]	540	15	31	7.1
33	2.1	-0.4	30	0.30	540	16	32	10.1
34	2.3	-3.2	30	0.45[a]	1500	29	53	4.5
35	2.4	-3.7	50	0.30	580	23	91	8.1
36	1.8	-3.9	30	0.30	320	16	49	10.8
37	1.7	-4.2	40	0.30	520	18	44	5.9
38	1.3	-4.1	20	0.30	430	12	25	8.5
39	0.7	-4.2	30	0.20[b]	1020	23	27	6.2
40	0.1	0.3	30	0.30	750	18	26	7.1
41	0.0	1.3	50	0.35[a]	1140	38	111	6.9

[a] The reddening was obtained from the modal B-V color of the group.

[b] The reddening was adjusted by hand, since the mean or fitted reddening resulted in the main sequence plume being significantly offset from the reddened zero-age main sequence of the evolutionary tracks.

TABLE 6

Red to Blue Ratios for Groups with > 20 Bright Stars

ID Number	Radius (kpc)	E(B-V) (mag)	N_{bright}	N_{OB}	N_A/N_{OB}	N_{FG}/N_{OB}	N_{KM}/N_{OB}	N_{AFGKM}/N_{OB}	N_{KM}/N_{OBA}
1	0.24	0.25	129	107	0.08±0.03	0.10±0.03	0.02±0.01	0.21±0.05	0.02±0.01
5	0.28	0.30	23	19	0.05±0.05	0.16±0.10	0.00±0.00	0.21±0.12	0.00±0.00
6	0.41	0.45	43	26	0.23±0.10	0.42±0.15	0.00±0.00	0.65±0.20	0.00±0.00
19	1.08	0.20	68	49	0.16±0.06	0.16±0.06	0.06±0.04	0.39±0.10	0.05±0.03
23	1.24	0.25	26	18	0.17±0.10	0.17±0.10	0.11±0.08	0.44±0.19	0.10±0.07
24	1.01	0.30	21	14	0.21±0.14	0.21±0.14	0.07±0.07	0.50±0.23	0.06±0.06
25	0.71	0.35	39	30	0.10±0.06	0.17±0.08	0.03±0.03	0.30±0.11	0.03±0.03
27	0.31	0.30	21	14	0.36±0.19	0.07±0.07	0.07±0.07	0.50±0.23	0.05±0.05
32	0.70	0.40	20	16	0.13±0.09	0.06±0.06	0.06±0.06	0.25±0.14	0.06±0.06
34	1.47	0.45	34	30	0.07±0.05	0.07±0.05	0.00±0.00	0.13±0.07	0.00±0.00
35	1.60	0.30	23	17	0.24±0.13	0.00±0.00	0.12±0.09	0.35±0.17	0.10±0.07
39	1.21	0.20	21	20	0.00±0.00	0.05±0.05	0.00±0.00	0.05±0.05	0.00±0.00
40	0.08	0.30	21	18	0.06±0.06	0.11±0.08	0.00±0.00	0.17±0.10	0.00±0.00
41	0.30	0.35	44	36	0.08±0.05	0.14±0.07	0.00±0.00	0.22±0.09	0.00±0.00

TABLE 6 (continued)

ID Number	Radius (kpc)	E(B-V) (mag)	N_{bright}	N_{OB}	N_A/N_{OB}	N_{FG}/N_{OB}	N_{KM}/N_{OB}	N_{AFGKM}/N_{OB}	N_{KM}/N_{OBA}
...	<0.5	...	281	220	0.11±0.02	0.15±0.03	0.01±0.01	0.28±0.04	0.01±0.01
...	0.5-1.0	...	59	46	0.11±0.05	0.13±0.06	0.04±0.03	0.28±0.09	0.04±0.03
...	1.0-1.5	...	170	131	0.12±0.03	0.13±0.03	0.05±0.02	0.30±0.05	0.04±0.02
...	>1.5	...	23	17	0.24±0.13	0.00±0.00	0.12±0.09	0.35±0.17	0.10±0.07
all groups	...	...	533	414	0.12±0.02	0.14±0.02	0.03±0.01	0.29±0.03	0.03±0.01
all stars[a]	...	...	3141	2058	0.17±0.01	0.26±0.01	0.05±0.01	0.48±0.02	0.04±0.01

[a] Corrected for foreground contamination (Ratnatunga and Bahcall 1985).

Figure Captions

Fig. 1 – (a) V versus B-V color-magnitude diagram for the entire data set. (b) V versus U-B color-magnitude diagram. (c) U-B versus B-V color-color diagram for stars with V < 21, $\sigma_{B-V} < 0.2$, and $\sigma_{U-B} < 0.3$.

Fig. 2 – (a) The V luminosity function for all stars with B-V < 0. The plotted uncertainties are $\sqrt{N}$. The straight line with a slope of 0.65 is given for reference and is not a fit to the data. (b) V luminosity function for all stars with U-V < -0.9.

Fig. 3 – OB associations identified using three different search radii and two different data sets. The axes are labelled with offsets in arcminutes relative to the optical center of the galaxy ($\alpha(1950) = 01^h\ 31^m\ 01.6^s$, $\delta(1950) = 30^o\ 24'\ 14''$. Stars with B-V < 0.4 and V < 21 were used to define the groups. The mean stellar surface density corresponds to a search radius R_o = 24.5 pixels. Only groups with at least ten stars are plotted. (a) Groups identified using a search radius of $R_o/\sqrt{2}$. (b) Groups identified using a search radius of R_o. (c) Groups identified using a search radius of $\sqrt{2}R_o$. Groups with less than 20 stars are not significantly different from a random distribution. (d) Groups identified using stars with U-B < -0.5 and V < 21 and a search radius of 33.4 pixels (R_o).

Fig. 4 – Percentage of groups containing a given number of stars compared with the distribution obtained from a random distribution of the same number of stars. The comparisons are made for three different search radii and stars with B-V < 0.4 and V < 21 are used to identify the groups. Crosses indicate the observed distribution of groups and squares the predicted distribution for a random set of stellar positions. (a) Groups identified using a search radius of $R_o/\sqrt{2}$. Groups with more than 5-8 stars are significant relative to a random distribution. (b) Groups identified using a search radius of R_o. Groups with more than 8-11 stars

are significant relative to a random distribution. (c) Groups identified using a search radius of $\sqrt{2}R_o$. Groups with more than 20-27 stars are significant relative to a random distribution.

Fig. 5 – (a) OB associations identified using "friends of friends" method. Axes are labelled as in Figure 3. Stars with B-V < 0.4 and V < 21 were grouped using a search radius of 24.5 pixels. Only groups with at least ten stars are plotted. (b) Regions of high blue star density. Stars with B-V < 0.4 and V < 21 were binned to a 50 pixel resolution. The mean density per pixel is $1\pm$ 2 stars. The first contour level is five stars per pixel (2σ) and the contours increase by two stars per pixel (1σ). Note the good agreement between the groups in (a) and regions with an over-density of at least 2σ.

Fig. 6 – Evolutionary tracks for stars of 9, 12, 15, 20, 25, 40, 60, and 85 $M_\odot$ from Maeder and Meynet (1988) are plotted in both the theoretical and observational planes. See Section Vb for details of the transformation from the theoretical to the observational H-R diagram. (a) Evolutionary tracks in the $\log(L_\odot)$-$\log(T_{eff})$ plane. (b) Evolutionary tracks in the V versus B-V plane. (c) Evolutionary tracks in the V versus U-B plane.

Fig. 7 – The OB associations identified in this study are outlined on the blue CCD images. Stars with B-V < 0.4 and V < 21 were used to identify the associations and are marked by white dots. A search radius of 24.5 pixels (R_o) was used. The x,y coordinates of the upper right corner are given for each figure to aid in identifying stars from Table 2. X increases down the page and Y increases to the left. Fields 1-3 and 6 are 558 x 698 pixels, while the remaining fields are 800 x 800 pixels. (a) Field 1 (-576,598) (b) Field 2 (-15,602) (c) Field 3 (551,601) (d) Field 4 (589,-10) (e) Field 5 (1,1) (f) Field 6 (-570,28) (g) Field 7 (-1130,599) (h) Field 8 (-1140,47) (i) Field 9 (1153,-519) (j) Field 10 (-567,-541)

(k) Field 11 (0,-550) (l) Field 12 (585,-581).

Fig. 8 – (a) The V luminosity function for stars in associations is compared with the luminosity function for field stars. A B-V cutoff of 0.0 was used. Large open circles denote the association luminosity function and small filled circles give the field luminosity function. The association luminosity function has been normalized to the same number of stars as the field luminosity function. (b) Same as in (a), but with stars selected using a U-V cutoff of -0.9.

Fig. 9 – The 41 associations plotted in Figure 7 are outlined on a schematic plot of the entire region surveyed. The axes are labelled as in Figure 3. The two inner spiral arms (Sandage and Humphreys 1980) are indicated by the heavy lines. Association ages in 10^6 yr (Table 6) are printed near each association outline. Dashed lines are drawn around pairs of associations discussed in Section Vd.

Figure 1

Color-Magnitude and Color-Color Diagrams

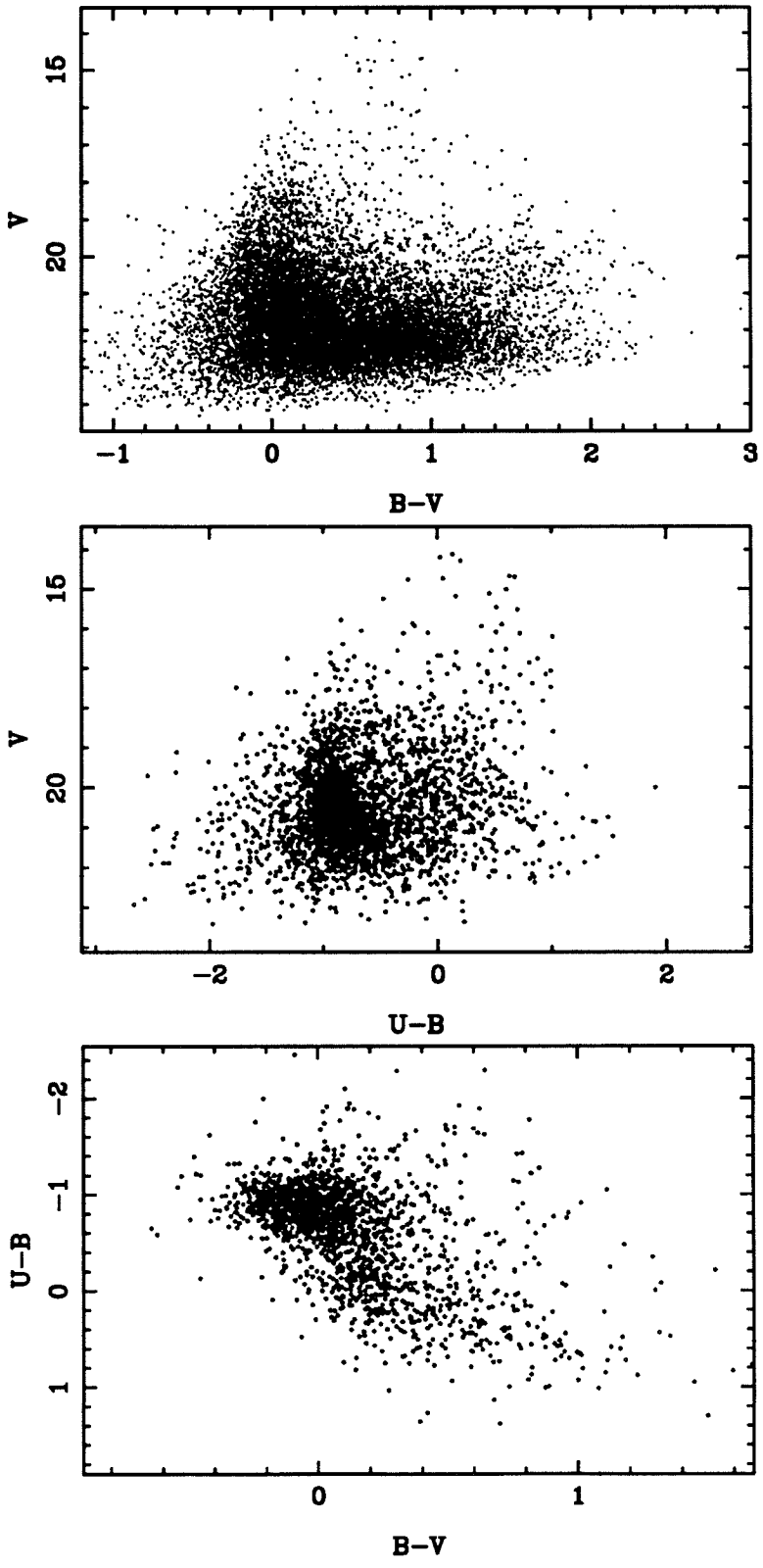

Figure 2

Blue Luminosity Functions

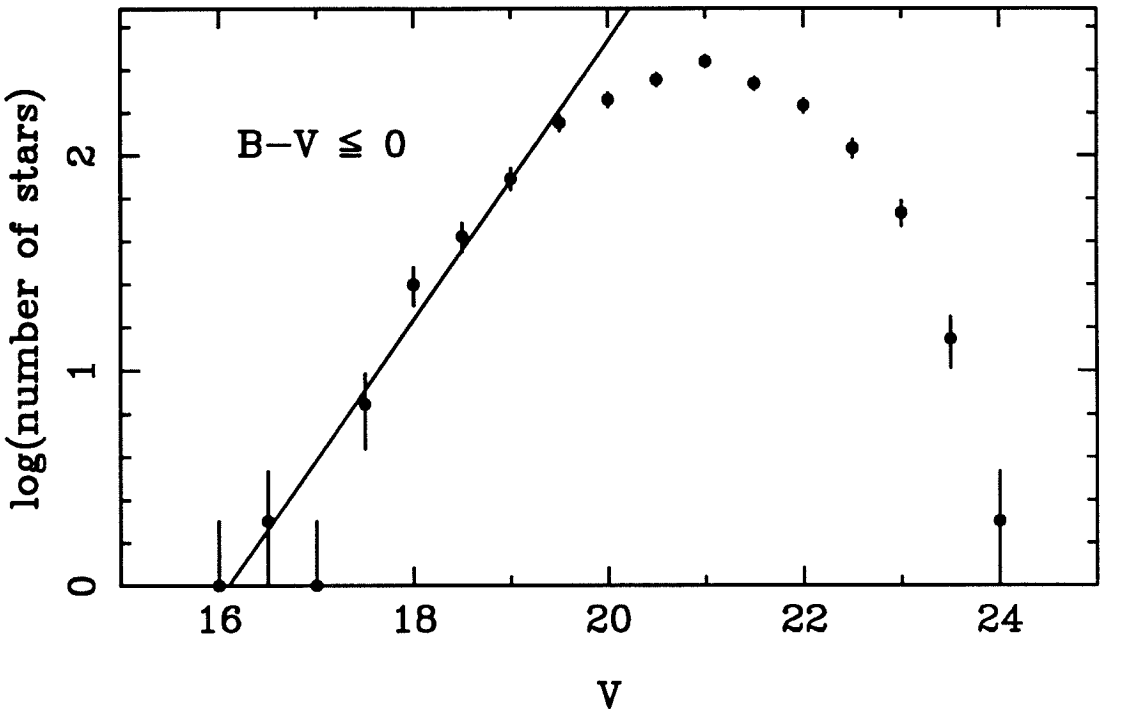

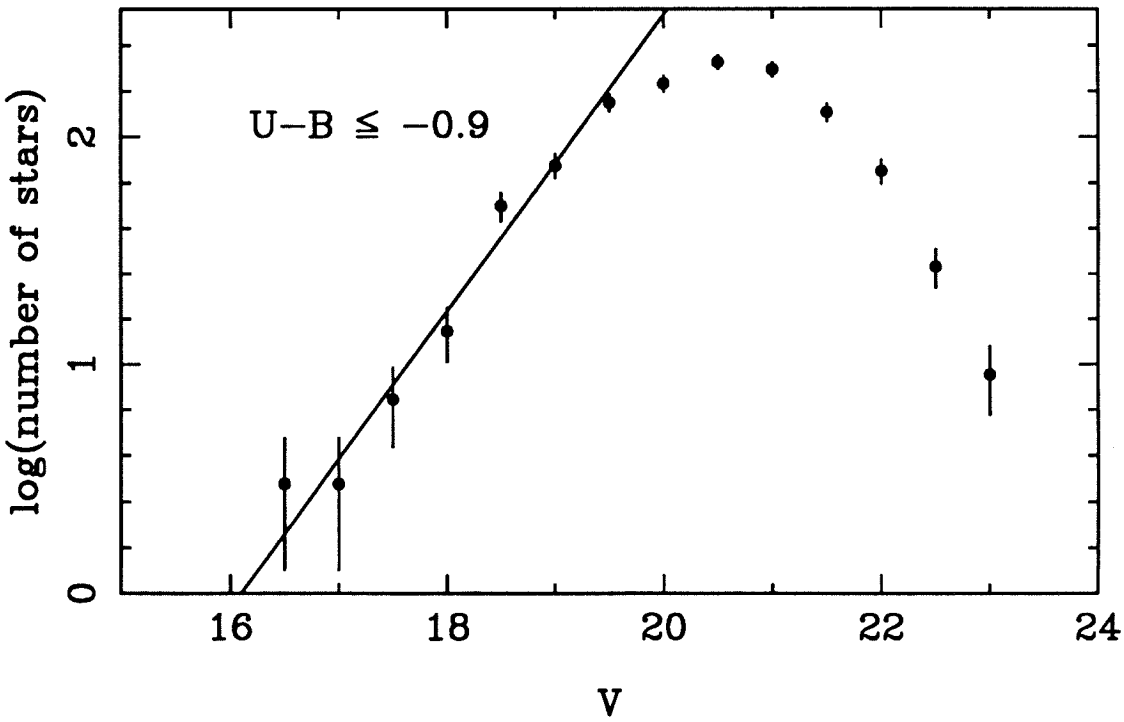

Figure 3a-b

Influence of Search Radius on Associations

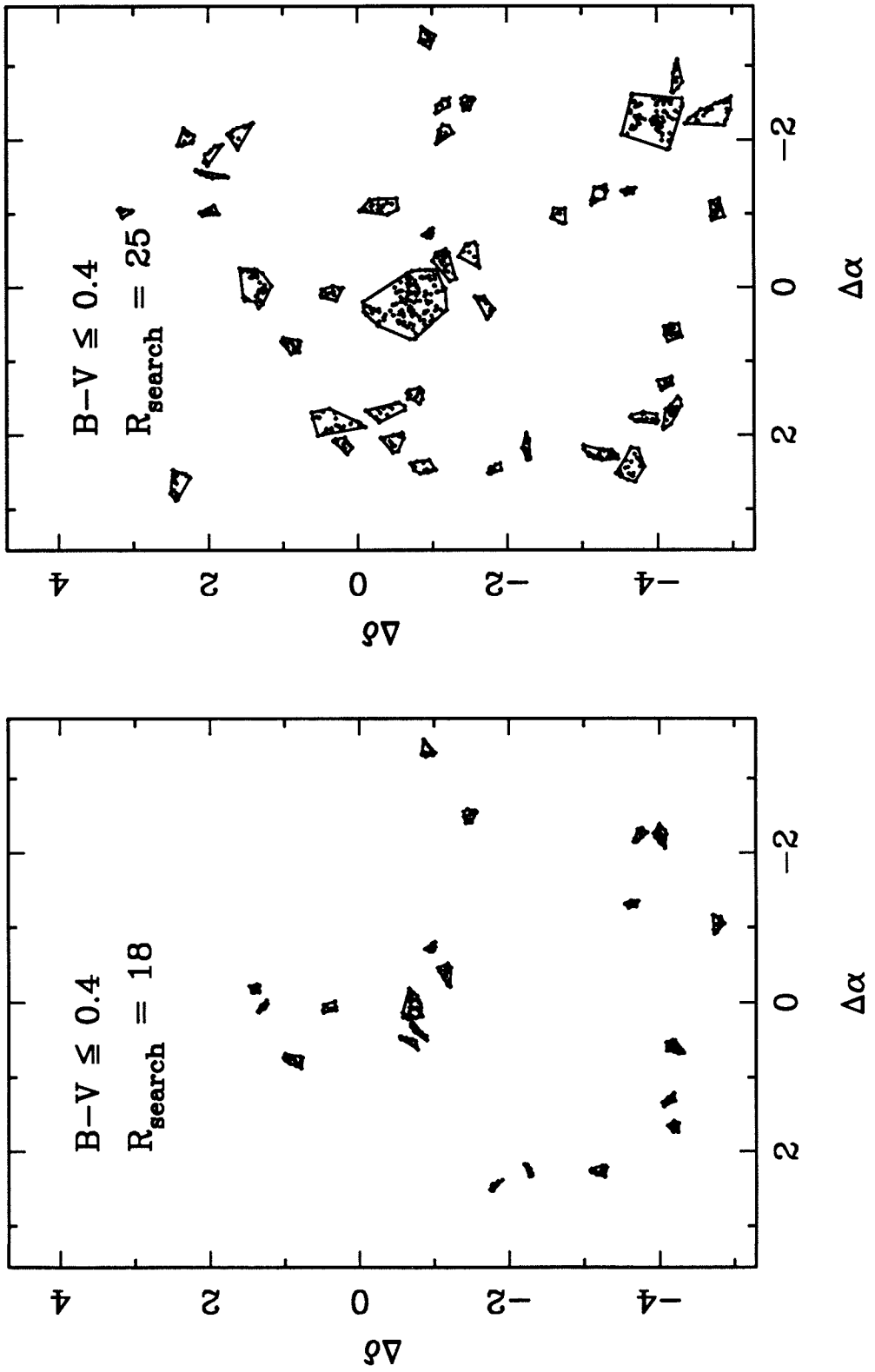

Figure 3c-d

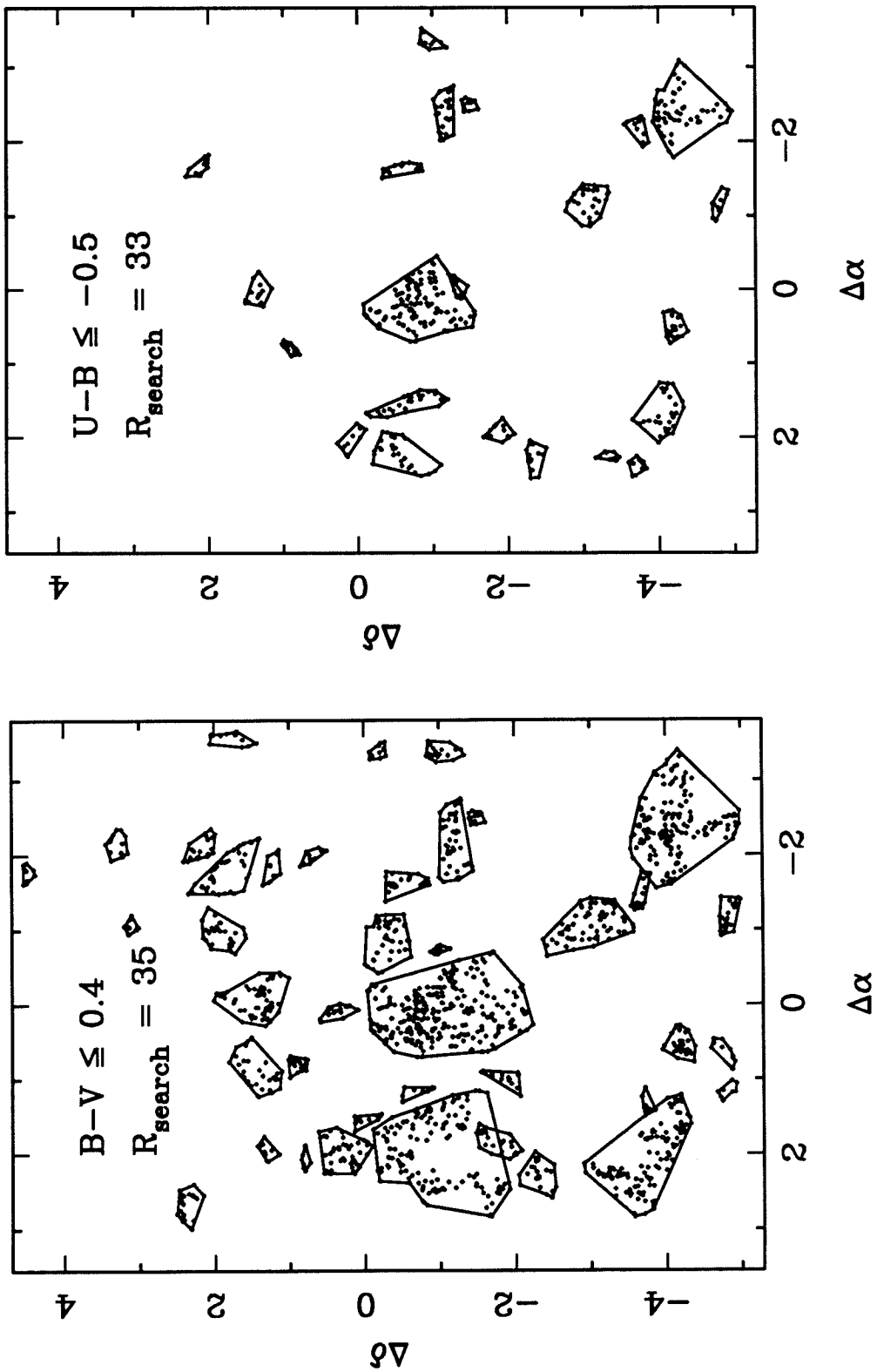

Figure 4

Observed Groups Compared with Random Distribution

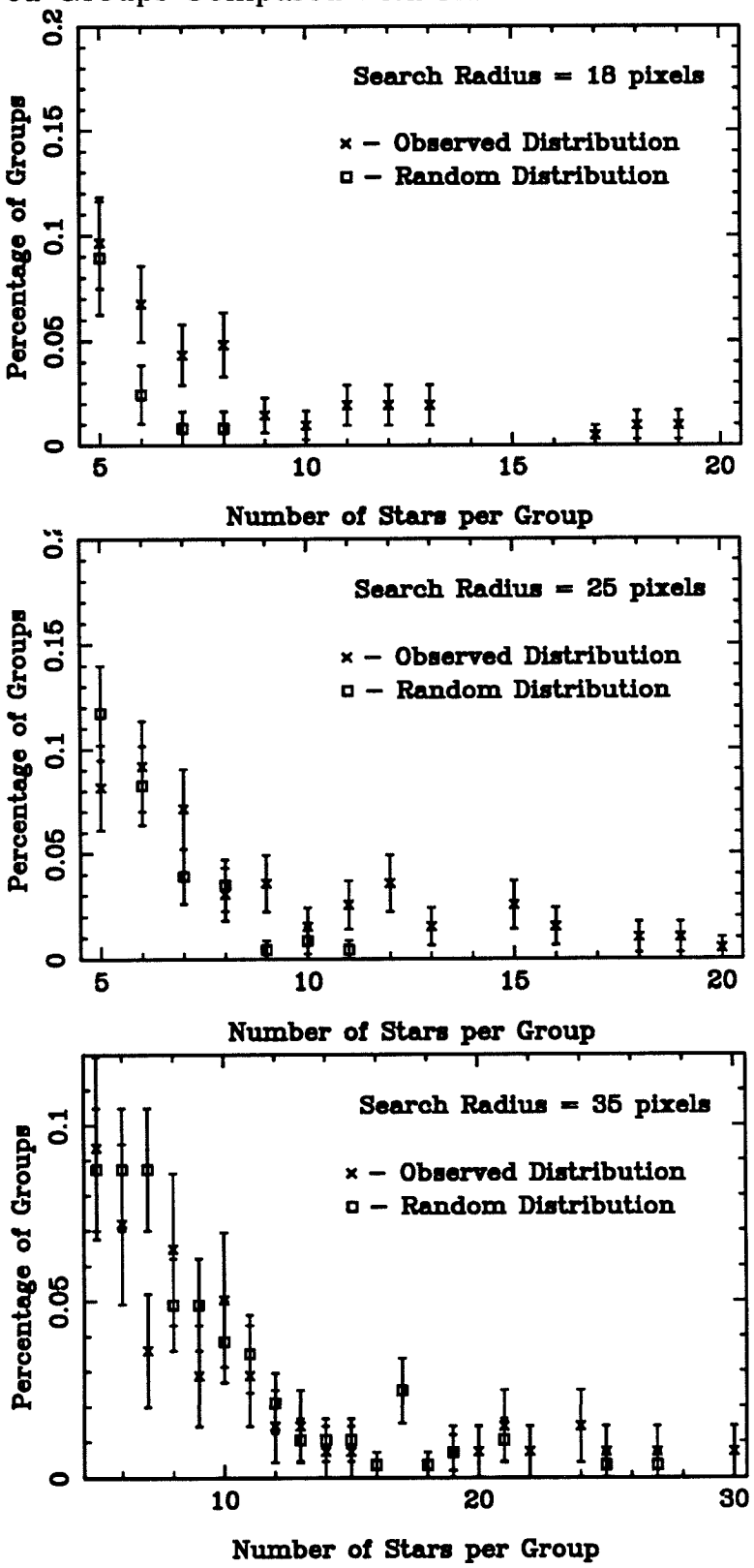

Figure 5

"Friends of Friends" versus "Overdensity" Method

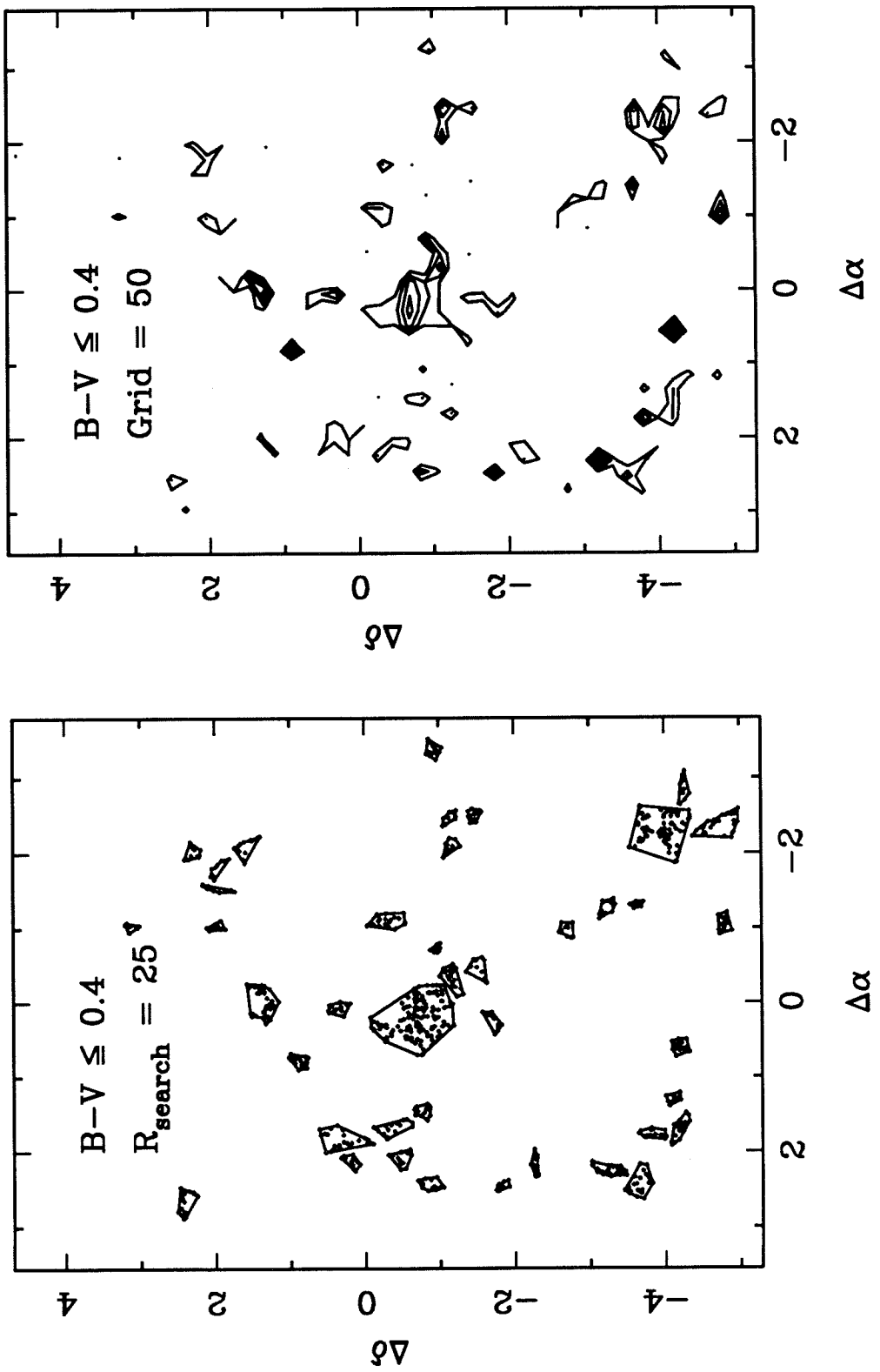

Figure 6

Evolutionary Tracks of Massive Stars

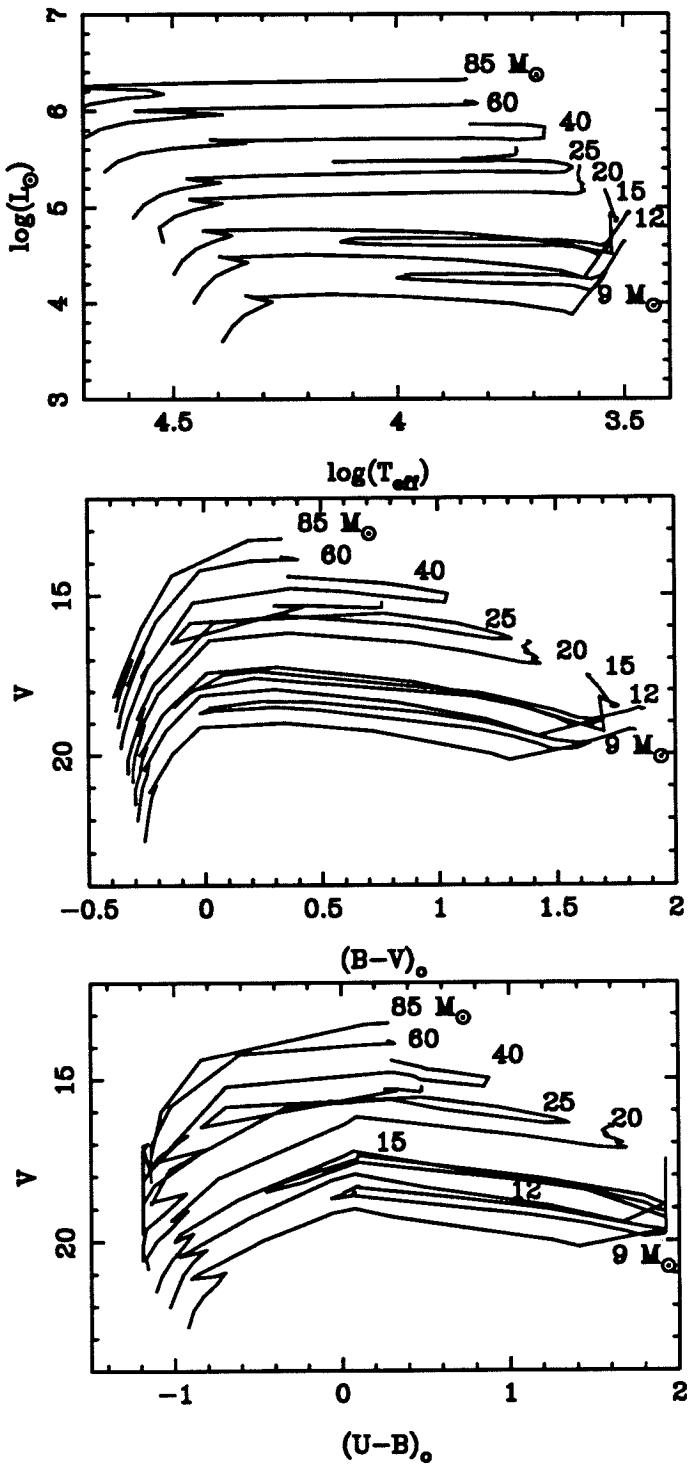

Figure 7a

OB Associations in M33

NORTH

EAST

Figure 7b

NORTH

EAST

Figure 7c

NORTH

EAST

Figure 7d

NORTH

EAST

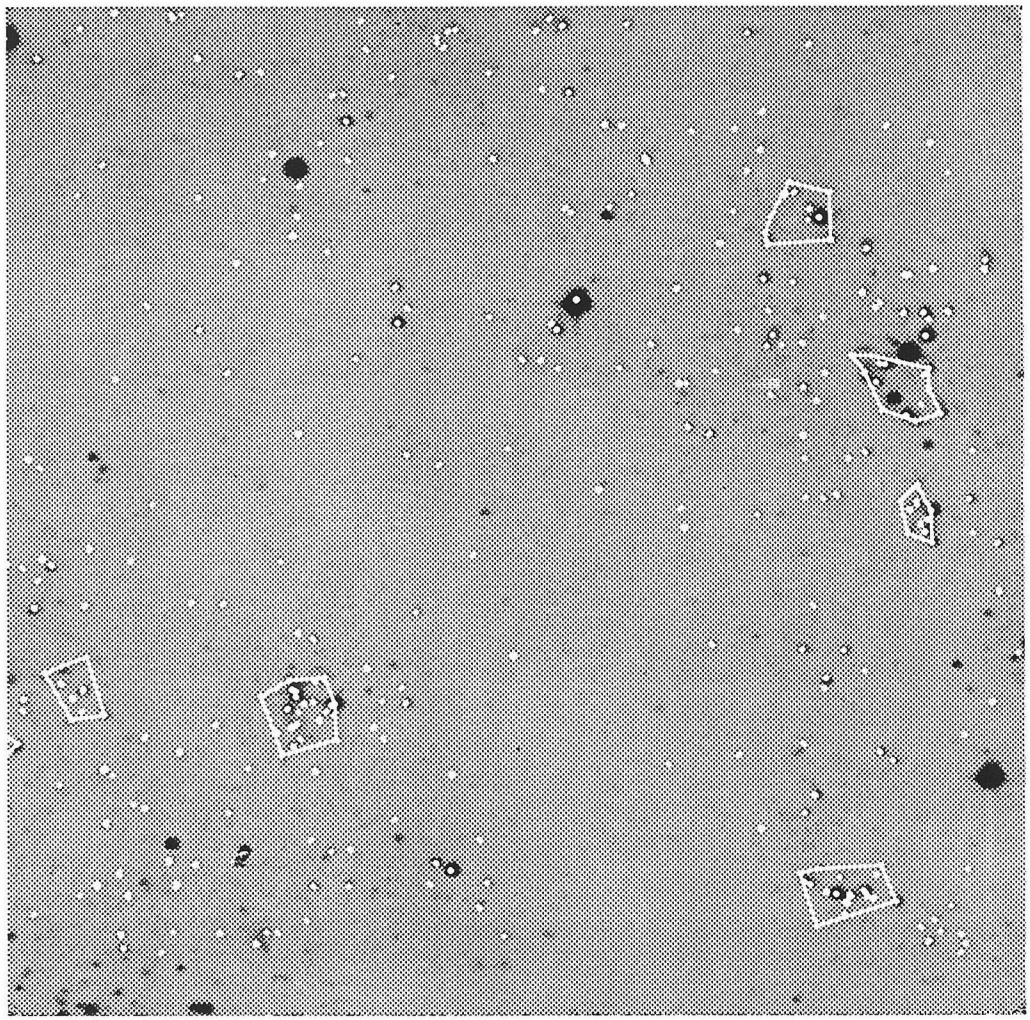

Figure 7e

NORTH

EAST

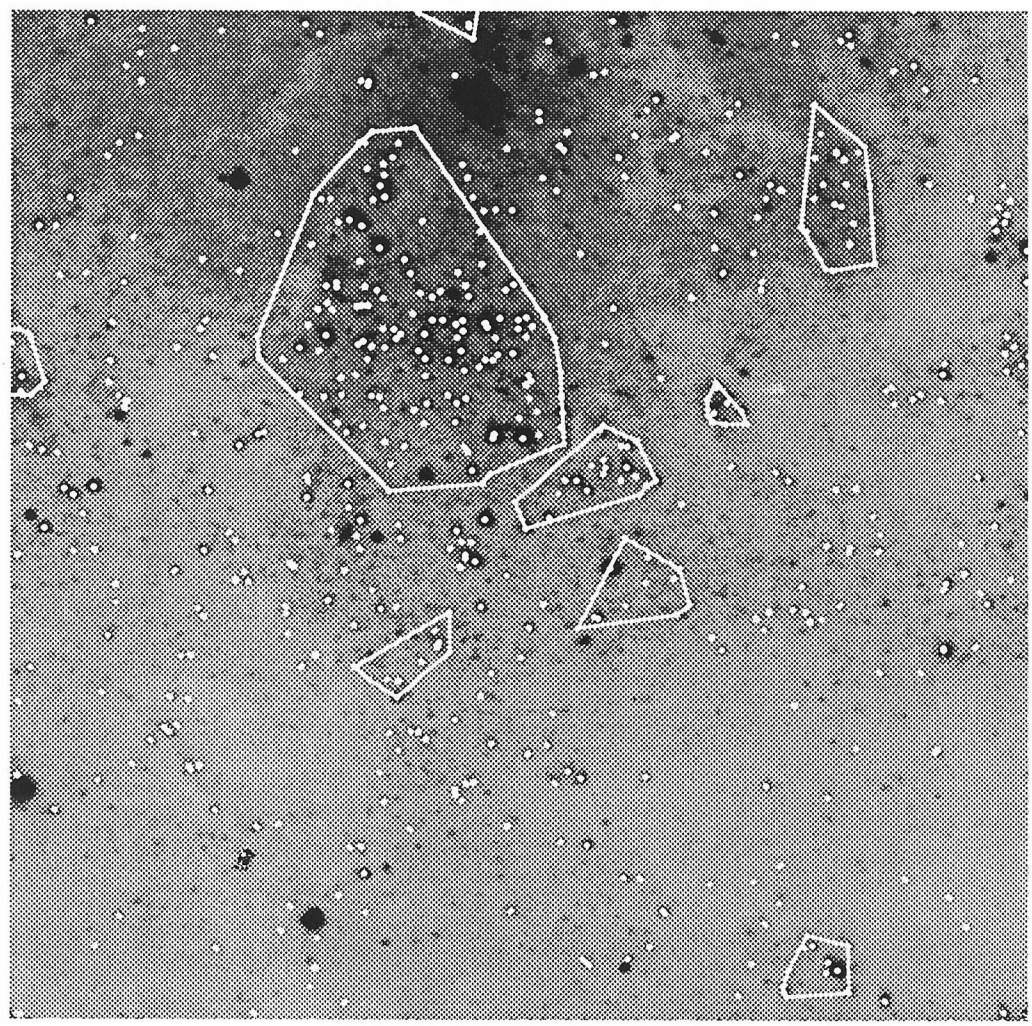

Figure 7f

NORTH

EAST

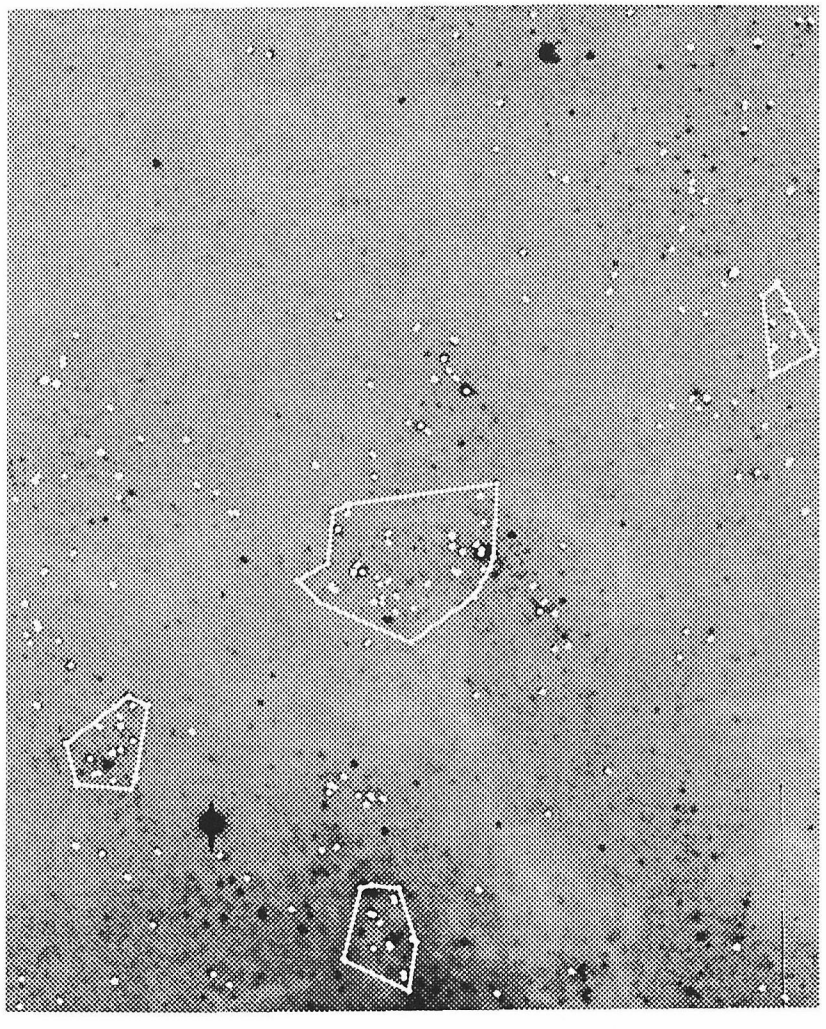

Figure 7g

NORTH

EAST

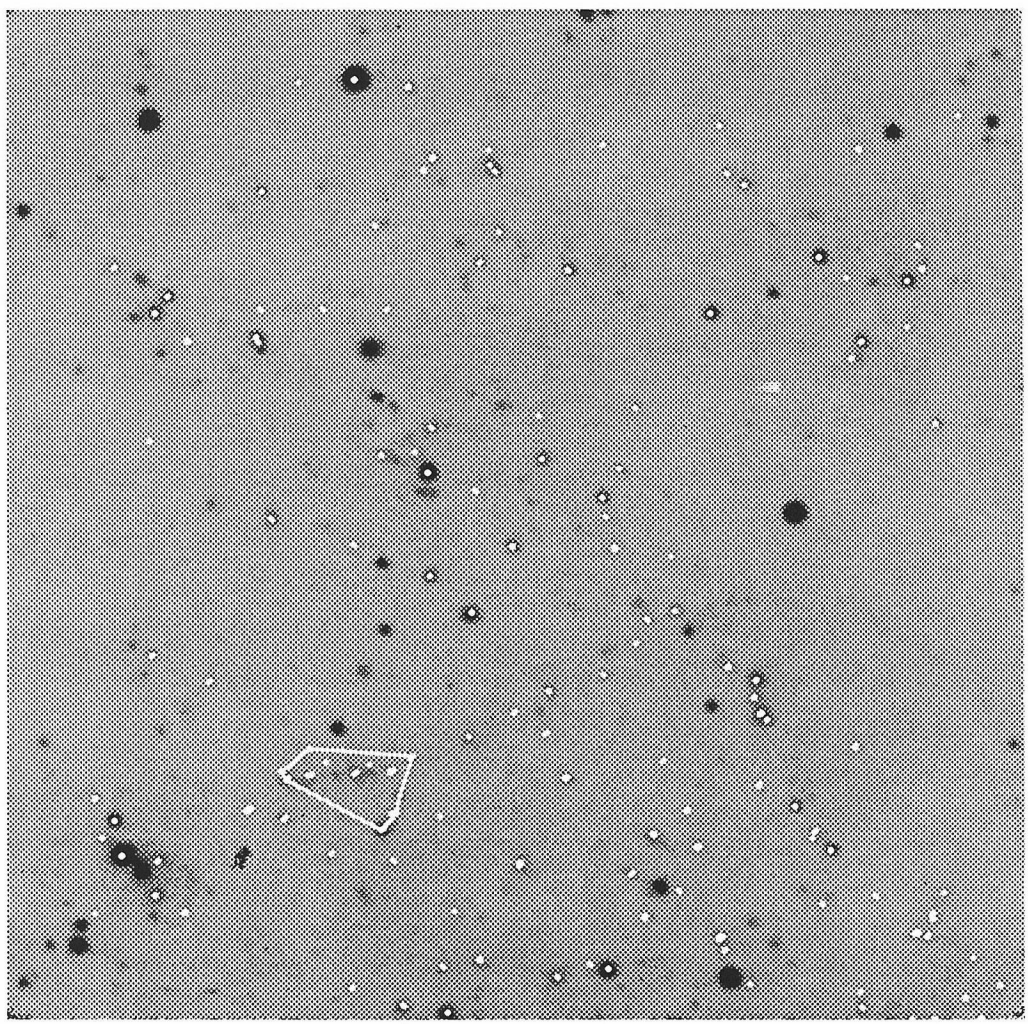

Figure 7h

NORTH

EAST

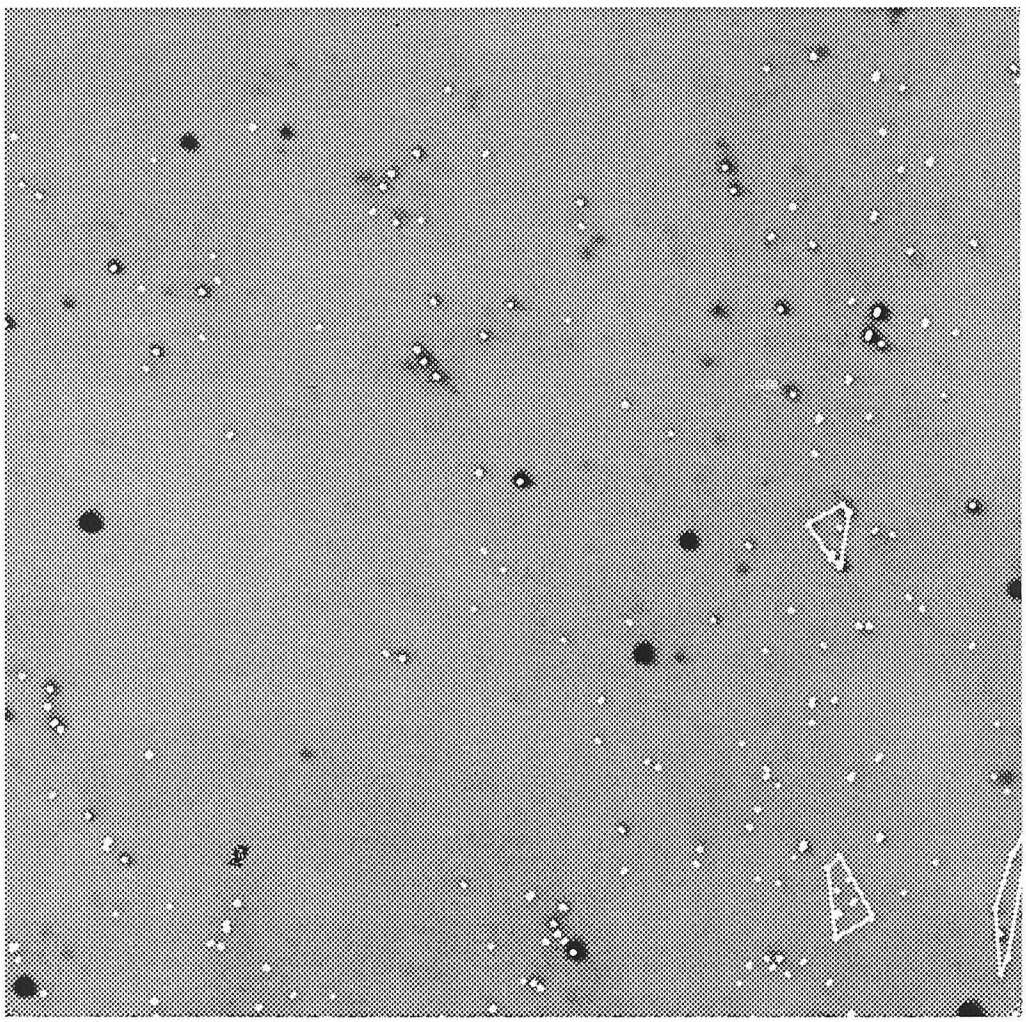

Figure 7i

NORTH

EAST

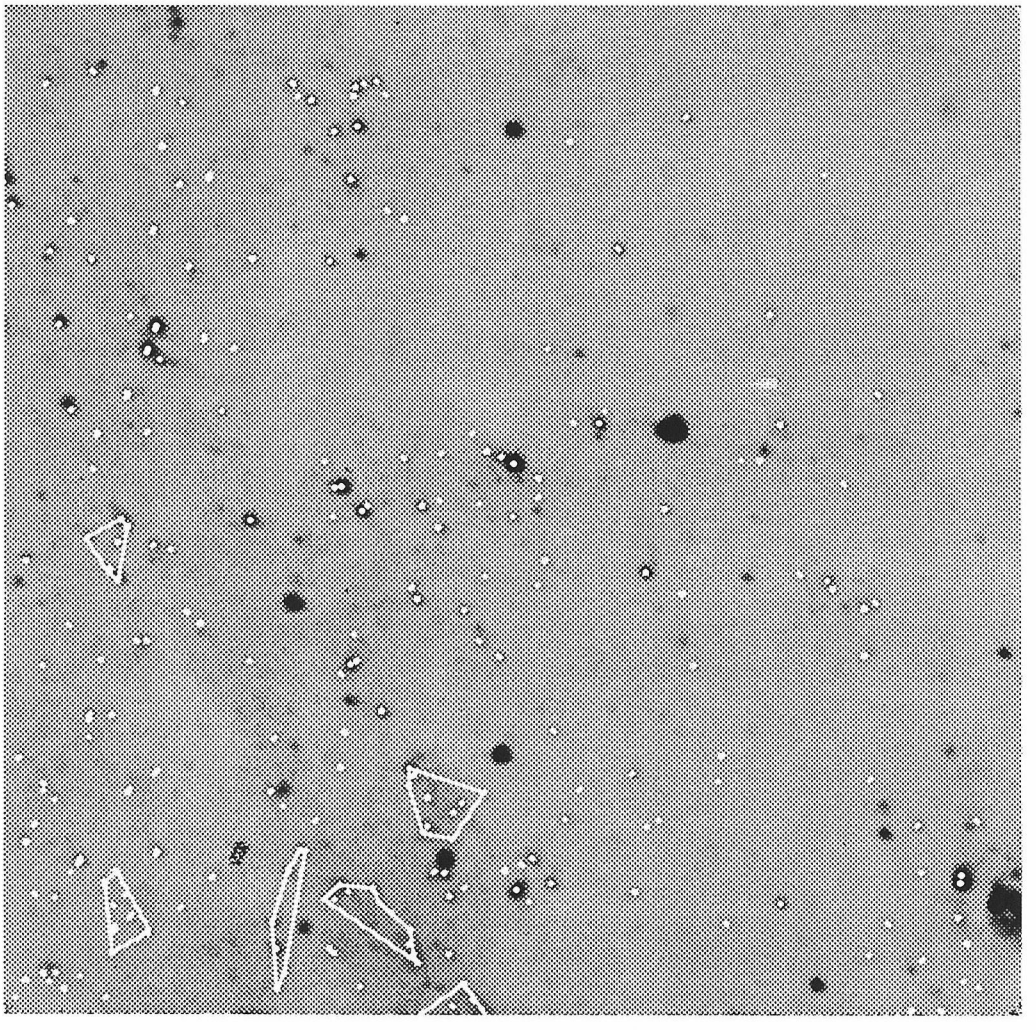

Figure 7j

NORTH

EAST

Figure 7k

NORTH

EAST

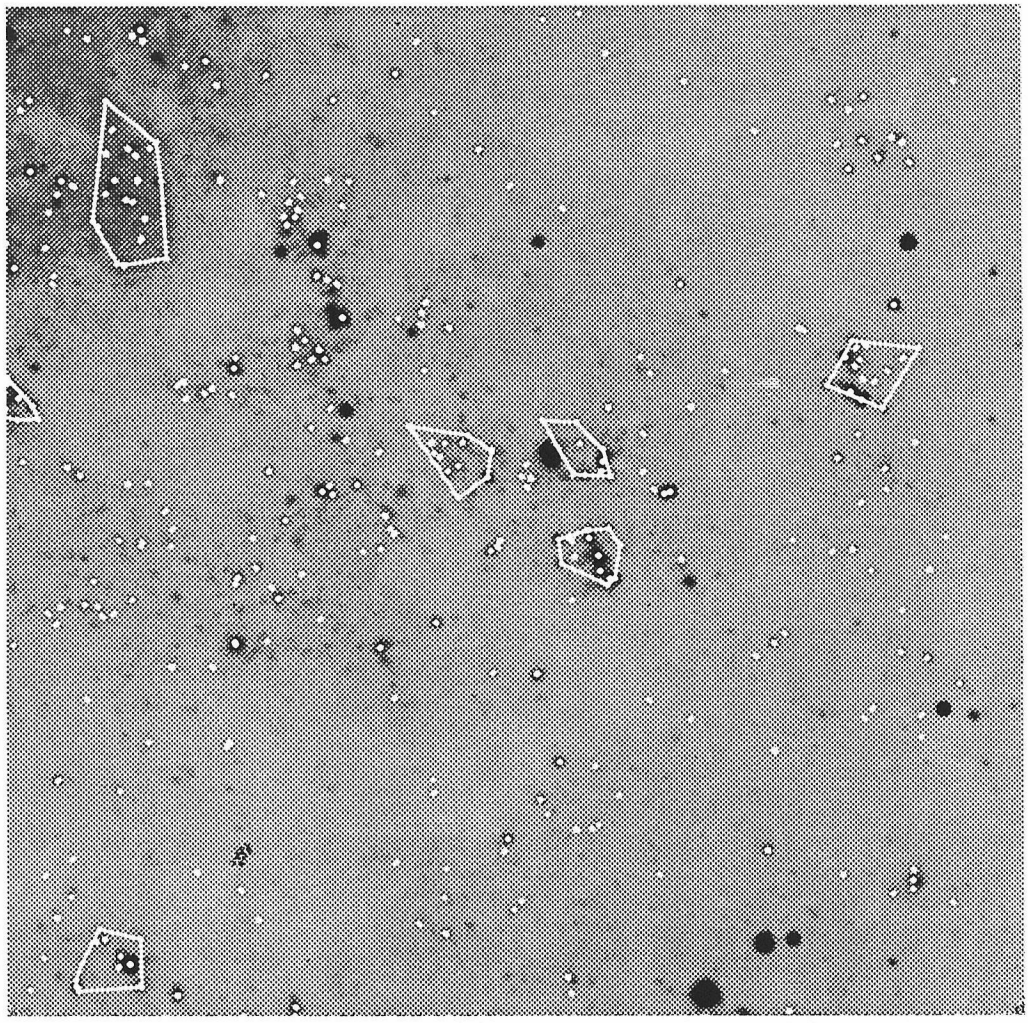

Figure 7l

NORTH

EAST

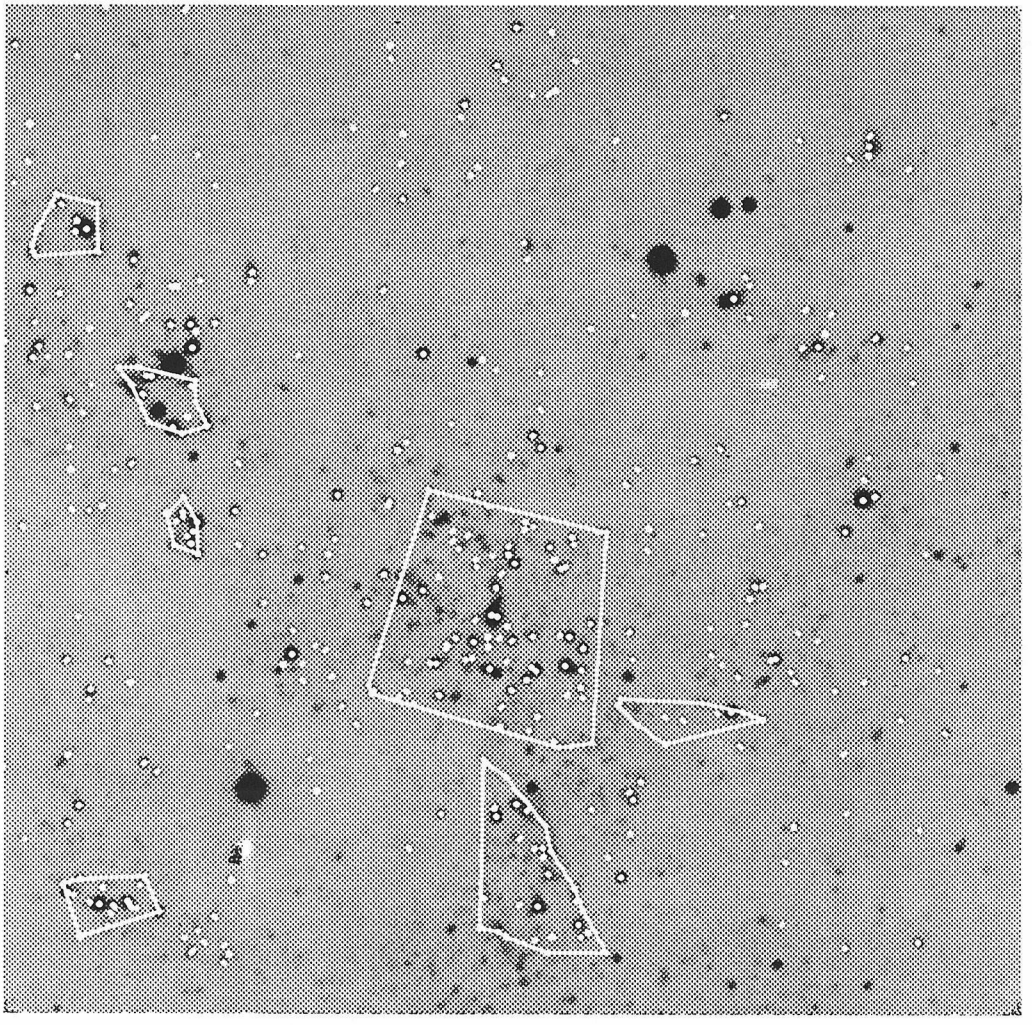

Figure 8

Field and Association Luminosity Functions

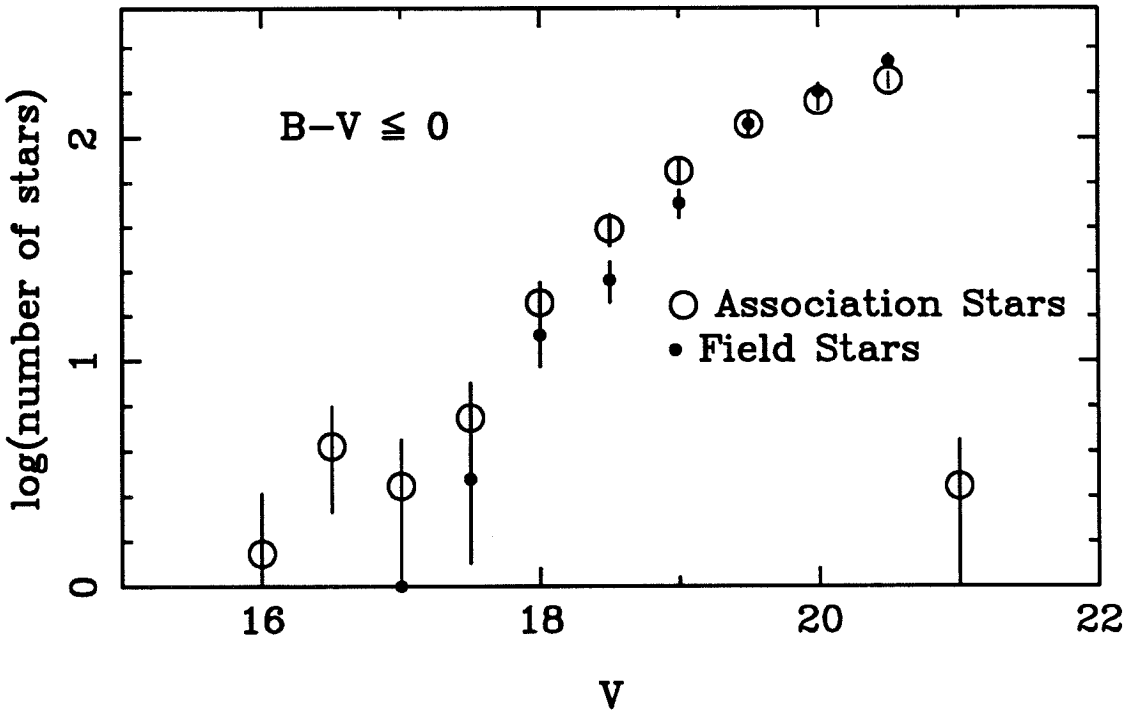

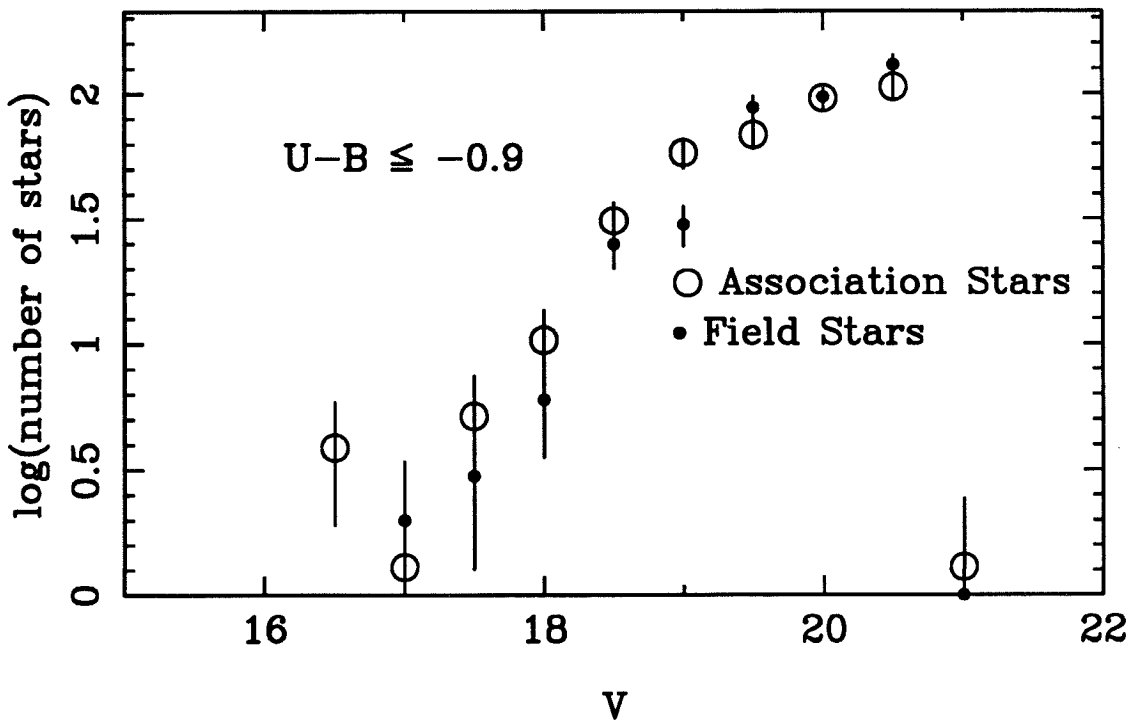

Figure 9

Association Ages and Spiral Structure

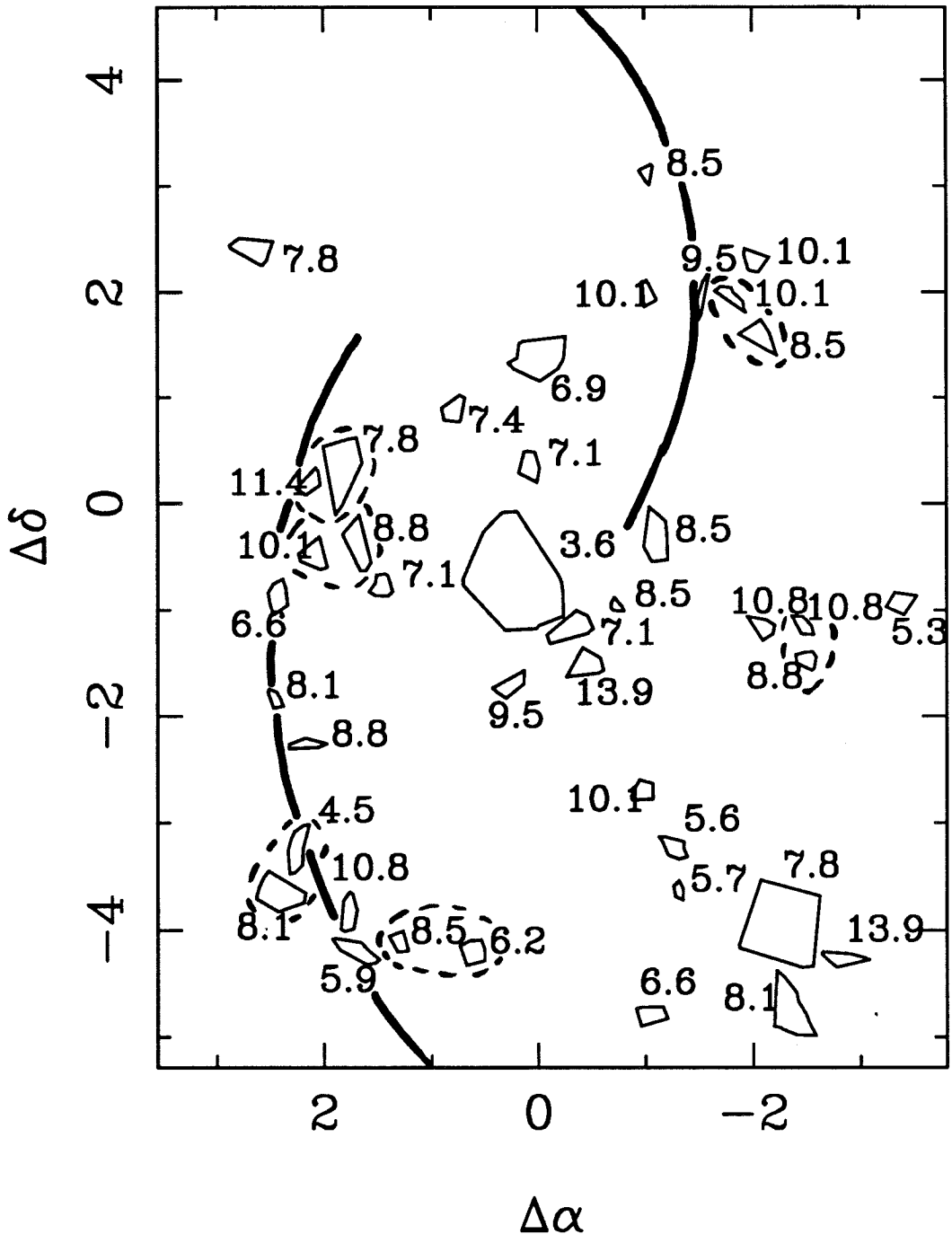

CHAPTER 4

The Properties of Individual Giant Molecular Clouds in M33

I. Introduction

The molecular component of the interstellar medium in our own Galaxy has been studied in great detail since the advent of millimeter astronomy. In particular, the properties of the giant molecular clouds (GMCs) that contain most of the molecular gas in the Galaxy have been the subject of numerous surveys (Sanders, Scoville, and Solomon 1985; Solomon *et al.* 1987; Scoville *et al.* 1987). The recently completed southern hemisphere survey (Bronfman *et al.* 1988) results in a fairly complete picture of the molecular gas distribution in the Galaxy. The detailed information in these surveys has sparked numerous theoretical studies to explain the observed cloud properties, such as the mass spectrum (Kwan 1979), the internal velocity dispersions (Myers and Goodman 1988), and the cloud-cloud velocity dispersion (Jog and Ostriker 1988).

By providing information on molecular clouds in different physical conditions than in the Milky Way, studies of molecular clouds in other galaxies provide important constraints on theoretical models. Due to the low resolution of early millimeter telescopes, surveys in nearby external galaxies on the scale of individual GMCs were not possible until the construction of millimeter interferometers and large single dish telescopes. Observations with the Nobeyama 45 m telescope in a spiral arm of M31 revealed four peaks in the CO emission with masses similar to large Galactic GMCs (Lada *et al.* 1988), while two large clouds of $\sim 10^6$ $M_\odot$

have been mapped with the IRAM 30 m telescope (Casoli, Combes, and Stark 1987; Casoli and Combes 1988). The first interferometer map of M31 resolved a single cloud similar in size to the Orion molecular cloud (Vogel, Boulanger, and Ball 1987). Observations in M33 of both the nucleus (Wilson *et al.* 1988) and the giant HII region NGC 604 (Boulanger *et al.* 1988) detected five molecular clouds similar to Galactic GMCs.

To provide a meaningful comparison of the properties of molecular clouds in another galaxy with Galactic GMCs a large number of clouds must be observed. This chapter reports the results of a survey of the inner disk of the Local Group spiral galaxy M33 using the Owens Valley Millimeter-Wave Interferometer. Six unbound molecular gas complexes with masses of 2-10$\times 10^7$ $M_\odot$ have been detected with single dish CO observations in the inner kiloparsec of M33 (Chapter 2); most of these complexes are mapped in the interferometer survey presented here.

The observations and the data reduction, including the method of identifying cloud candidates, are discussed in Section II. The properties of the clouds are compared with those of Galactic GMCs and the conversion factor between CO flux and H_2 column density in M33 is obtained in Section III. The cloud mass spectrum and a theoretical analysis of the cloud upper mass cutoff are discussed in Section IV. The interferometer observations are compared with the single dish CO map in Section V. The chapter is summarized in Section VI. Preliminary results from this survey were given in Wilson and Scoville (1989b).

II. Observations and Analysis

a) Observations

A total of 19 fields within a 4′ radius of the center of M33 were observed

with the Owens Valley Millimeter-Wave Interferometer between October 1986 and June 1989 in the CO J=1-0 line using the 1 MHz (2.6 km s^{-1}) 32 channel filterbank. Maps in the first two observing seasons were centered on the nucleus and areas of high optical extinction. In the third observing season, fields were selected in the molecular gas complexes (Chapter 2). Each field was observed in three configurations, except for the nuclear region that was observed in five configurations (Wilson *et al.* 1988). Typical double-sideband system temperatures at the zenith were 600-800 K in 1986-1987, 400-600 K in 1987-1988, and 200-400 K in 1988-1989. The instrumental sensitivity was sufficiently improved in the 1988-1989 observing season that two fields were observed per transit. The field center coordinates, central velocity (V_{LSR}), synthesized beam size, and rms noise per 1 MHz channel (σ) are listed for each field in Table 1.

Mars, Uranus, and 3C84 were observed for amplitude calibration and the resulting uncertainty in the flux scale is $\sim$10% primarily due to pointing errors. The quasar 0133+476 was used as a phase calibrator and also as a check on the amplitude calibration. The uncertainties in the phase calibration are typically $\pm 20^o$. Passband calibration was obtained from observations of 3C84, with typical uncertainties of $\pm$10% in amplitude and $\pm 5^o$ in phase. Cleaned maps with 1.5″ pixels were made using the routine MXMAP in the AIPS software package for each of the 1 MHz channels individually. The FLUX parameter was set to 1.5σ to keep from cleaning too far down into the noise. In most fields the cleaned area was 60″ on a side, but if structure was seen on the edges of the map the cleaning was extended to 90″. The maps from the 1986-1987 and 1987-1988 observing seasons were made with natural weighting to increase the sensitivity, while the maps in the 1988-1989 season were made with uniform weighting.

b) Cloud Identification

Initial candidate molecular clouds were identified using the individual 1 MHz channel maps. Two criteria were used to select clouds for the final sample: (1) the emission had to exceed 3σ ($\sim$0.6 Jy) in at least two adjacent channel maps and (2) in the spectrum of the feature (obtained by integrating over the pixels within the cloud boundary), the emission peak had to exceed three times the noise in the spectrum measured at high and low velocity channels. The first criterion provides a sample of clouds for which the line widths are at least marginally resolved so that velocity dispersions can be estimated. The second criterion is necessary to ensure adequate signal-to-noise for the CO line flux when the cloud includes more than one beam area. The final maps for each cloud were constructed by integrating over *only* the range of channels in which significant flux from the cloud was seen in the spectrum. For fields containing several clouds, separate maps were constructed including different ranges of channels to highlight each cloud. The spectrum and total flux for each cloud were measured in a box with sides 1.4 times the full-width half-maximum extents in right ascension and declination. Experiments with a range of box sizes showed that a box of this size contains $\geq$90% of the flux (see also discussion below). Of the 55 clouds selected using the first criterion, 17 were eliminated from the final sample by the second criterion.

Figure 1 shows outlines of the CO clouds overlaid on a continuum subtracted H_α CCD image of M33 (Chapter 5); the integrated intensity maps for the 38 clouds are shown in Figure 2. For fields where more than one cloud is present, the maps in Figure 2 are montages of the individual integrated intensity maps for each cloud. This montaging technique was used since creating one integrated intensity map using the entire range of channels would dilute the emission of

the weaker clouds by noise in channels with no significant emission. Figure 3 shows the spectra of the clouds. Table 2 gives the measured parameters for the final sample of clouds. The table gives the cloud identification, the right ascension and declination of the cloud center, the velocity of the peak flux, the full-width half-maximum velocity, the integrated intensity of the cloud and the peak brightness temperature (corrected for the response of the primary beam), and the deconvolved diameter, if the cloud is resolved by the synthesized beam. Some regions are sufficiently confused that it is difficult to determine whether the structures seen in the maps are one cloud or two, and these regions are noted in the table.

c) Cloud Masses

Cloud masses were calculated from both the CO line flux and application of the virial theorem. The virial mass M_{vir} was calculated for clouds that are sufficiently large that a deconvolved diameter can be determined. For the virial mass calculation a density profile $\rho \propto 1/r$ was assumed, giving

$$M_{vir} = 99 V_{FWHM}^2 D_{pc} \;\; M_\odot \tag{1}$$

where V_{FWHM} is the full-width velocity at half-maximum intensity in km s^{-1} and D_{pc} is the cloud diameter in parsecs. Since the coefficient in Equation (1) is 110 for a uniform density cloud, the form of this equation is only weakly dependent on the adopted density profile $\rho(r) = \rho_o(R_o/r)^\alpha$ for $0 \leq \alpha \leq 1$. However, the virial mass depends linearly on the conversion from R_{FWHM} to R_o, where R_o is the true radius of the cloud. The full-width half-maximum radius is related to the true radius by $R_o = 1.15 R_{FWHM}$ for α=0, $R_o = 1.4 R_{FWHM}$ for α=0.3, and $R_o = 2 R_{FWHM}$ for α=0.5. This relation cannot be calculated for the $\alpha = 1$ profile, since the central density and hence the peak line flux is infinite. We used

1.4 times the deconvolved diameter of the cloud in calculating the virial mass, since this diameter was found empirically to contain most of the flux of the cloud. However, the uncertainty in converting R_{FWHM} to R_o introduces a systematic uncertainty in our calculation of virial masses.

Using the Galactic value for the conversion factor between CO flux and molecular hydrogen column density, $\alpha = (3 \pm 1) \times 10^{20}$ cm^{-2} / (K km s^{-1}) (Strong *et al.* 1988; Scoville and Sanders 1987), the molecular mass M_{mol} is related to the integrated CO flux S_{CO} by

$$M_{mol} = 1.61 \times 10^4 d_{Mpc}^2 S_{CO} \ \ M_\odot \tag{2}$$

(Wilson *et al.* 1988; Chapter 2) where S_{CO} is in Jy km s^{-1} and d_{Mpc} is the distance in megaparsecs. The uncertainty in M_{mol} is primarily the calibration uncertainty (20%), with a possible systematic error due to the assumed value of α. The uncertainties in V_{FWHM} and the deconvolved diameter are taken to be 1.3 km s^{-1} (i.e., one half the channel resolution) and 7 pc (~25% of the synthesized beam diameter). These uncertainties should be appropriate for the large resolved clouds, while the uncertainties are larger for smaller clouds with diameters similar to the beam size and line emission in only 2-3 channels.

III. The Ensemble Properties and Comparison with Galactic GMCs

In this section the properties of individual clouds in M33 (diameter, velocity width, and mass) are compared with those of Galactic GMCs. A subset of the clouds, which are well resolved (both spatially and kinematically), lie in unconfused regions, and have good signal-to-noise ratios, are used in the analysis of sections a) and b). This sample of 9 clouds is indicated by a + in Table 2.

a) The Velocity-Diameter Relation

The velocity width is plotted versus diameter in Figure 4a for the refined

sample of nine clouds. The velocity width, diameter, and virial mass are plotted versus the molecular mass in Figure 4b-d. For each of these four combinations, the presence of a correlation was established by calculating the Spearman rank-order correlation coefficient. In all cases the two quantities are correlated, with only a 1-6% probability that the data points are drawn from an uncorrelated set.

A power law fit to the relation between velocity and diameter yields

$$V_{FWHM} = (5.4^{+0.8}_{-0.5})(D_{pc}/20\ pc)^{0.5\pm0.2} \tag{3}$$

where the uncertainties are one-sigma uncertainties derived from the fit. This result agrees within the errors with the observed relation for Galactic GMCs, $V_{FWHM} = (0.88 \pm 0.16)D_{pc}^{0.62\pm0.05}$ (Sanders, Scoville, and Solomon 1985). The relationship between mean cloud density and diameter depends on the assumed profile for the density distribution within a single cloud. Assuming a density profile of the form $\rho = \rho_o R_o/r$ (as in Sanders, Scoville, and Solomon 1985) and using the virial theorem, the mass-weighted three-dimensional velocity dispersion $\langle\sigma\rangle$ is given by

$$\langle\sigma\rangle = (\frac{8\pi}{25}G\rho_o)^{1/2}D \tag{4}$$

where Equation (4) is in cgs units. The full-width half-maximum velocity is given by $V_{FWHM} = 2\sqrt{2ln2/3}\langle\sigma\rangle$ and the mean cloud density is $1.5\rho_o$, which yields

$$V_{FWHM} = 0.019\sqrt{\langle n_{H_2}\rangle}D_{pc} \tag{5}$$

where $\langle n_{H_2}\rangle$ is the mean density of the cloud in H_2 cm^{-3} and a factor of 1.36 has been removed to account for the helium abundance. Combining this with Equation (3), we obtain

$$\langle n_{H_2}\rangle = 200^{+60}_{-30}(D_{pc}/20pc)^{-1.0\pm0.4} \tag{6}$$

This result agrees with the study by Solomon *et al.* (1987), which found a similar dependence of mean cloud density on cloud diameter. Note that this result does not depend on the assumed conversion factor between CO flux and molecular hydrogen column density. For a constant density cloud, the coefficient in Equation (6) is 230, while for a cloud with a density profile $\rho \propto 1/r^2$ it is 130.

A power law fit to the diameters and molecular masses yields $D_{pc} = 35 \pm 6 \times (M_{mol}/10^5\ M_\odot)^{0.3\pm0.1}$, while a fit to the velocities and molecular masses yields $V_{FWHM} = 3.3^{+01.2}_{-2.3}(M_{mol}/10^5\ M_\odot)^{0.4\pm0.1}$. These results are consistent within the errors with the velocity-diameter relation derived above. Some of these fits are not particularly stable, since fitting mass as a function of diameter does not yield an equation which is the inverse of that given above. The velocity-diameter relation also suffers from this. The most stable relation in this sense is that between velocity and mass, since the results of fitting each variable against the other agree within the errors. However, the disadvantage of using this relationship to relate mean density and diameter is that it depends on the assumed value of α (see Section IIIb).

b) The CO Flux to H_2 Mass Ratio in M33

By resolving individual clouds in M33, we can test the universality of the Galactic value of α, the conversion factor between CO flux and molecular hydrogen column density, by independently deriving cloud masses using the virial theorem. The value of α is fairly well determined in our own Galaxy, with a mean value of about $3 \pm 1 \times 10^{21}$ cm^{-2} (K km s^{-1})$^{-1}$ (Strong *et al.* 1988; Scoville and Sanders 1987). However, theoretical studies suggest that α could vary significantly with excitation temperature, density, and metallicity (Dickman, Snell, and Schloerb 1987; Maloney and Black 1988).

The virial mass is plotted versus the molecular mass in Figure 4d for the

resolved clouds. Fitting a straight line to these data yields

$$M_{vir} = (1.1 \pm 0.1) M_{mol} \quad (7)$$

The χ^2 of the fit was improved significantly by excluding the cloud MC3, and so this cloud was dropped from the fit (it is the only cloud with a molecular mass that is larger than its virial mass). Most of the clouds lie within the error bars of the best fit line. *The excellent agreement between the molecular and virial masses provides the first direct confirmation that the Galactic conversion factor from CO flux to molecular column density is valid in an external galaxy.* The high spatial resolution obtained with the interferometer is crucial to this result, since single dish observations with a resolution of ~200 pc if taken alone give a significantly larger value for α (Chapter 2). It is very important to have enough spatial resolution in studies of external galaxies to resolve objects similar in size to Galactic GMCs if α is to be measured successfully. The metallicity in this region does not vary by more than a factor of two (Chapter 3) and thus these data do not provide much information on the dependence of α on metallicity, which may be important in dwarf galaxy environments such as the LMC.

The effect of excitation temperature on α ($\alpha \sim 1/T_{ex}$) may be an important uncertainty in determining the molecular gas mass in the nuclei of starburst galaxies (Dickman, Snell, and Schloerb 1987; Maloney and Black 1988). The three clouds near the nucleus have brightness temperatures which are roughly 50% higher than average (but still within the range observed for Galactic GMCs) and are the only clouds with flux-based masses significantly larger than their virial masses, which is consistent with the model predictions. The small cloud MC5 in the central region also has a higher than average brightness temperature for its size. These high temperatures are likely due to an increased ultraviolet radiation field in the vicinity of the nucleus.

The clouds near the giant HII region NGC 604 have brightness temperatures of 6-8 K (Boulanger *et al.* 1988), significantly higher than any clouds in our sample. NGC 604 is the largest HII region in M33 and therefore should have one of the strongest ultraviolet radiation fields. The data on NGC 604 thus support our conclusion that the high brightness temperatures observed for the nuclear clouds are due to an increased ultraviolet radiation field. The low temperatures observed for the clouds MC6-10, which lie significantly off the southern spiral arm, may then be due to a lower ultraviolet radiation field in this interarm region.

There are 18 weak emission features in our maps which typically extend over only two channels and have spectra with peak fluxes roughly three times the rms spectrum noise. Most of these clouds have peak brightness temperatures around 1 K and masses of 0.2-0.6$\times 10^5$ $M_\odot$. Since they are all unresolved, the low peak brightness temperatures are probably due to beam dilution. A cloud with a diameter of 20 pc and a true peak brightness temperature of 2 K would have a peak brightness temperature of 0.5 K if observed with an 8″ diameter synthesized beam.

c) The Cloud-Cloud Velocity Dispersion

The cloud-cloud velocity dispersion was obtained by comparing the radial velocity of an individual cloud with the central velocity of the single dish line at the same position (Table 1; single dish data from Chapter 2). The single dish velocity is required to remove galactic rotation from the individual cloud velocities. For the 27 clouds more massive than 0.5×10^5 $M_\odot$, the cloud-cloud one-dimensional velocity dispersion is 5 ± 1 km s^{-1}. The cloud-cloud velocity dispersion for Galactic GMCs is between 3 km s^{-1} (Clemens 1985) and 7 km s^{-1} (Stark and Brand 1989).

Jog and Ostriker (1988) have recently explained the Galactic cloud-cloud velocity dispersion by examining the sources of energy in the GMC system. In their model, the primary energy input into the GMC system is viscosity from the gravitational interactions among GMCs located in a differentially rotating galactic disk. The one-dimensional cloud-cloud velocity dispersion $\langle\sigma_{1D}\rangle$ is then given by

$$\langle\sigma_{1D}\rangle^3 = 0.33\Big(\frac{GM}{R_o}\Big)\kappa H \tag{8}$$

where κ is the epicyclic frequency and H is the total vertical cloud scale height (Jog and Ostriker 1988). If the average masses and radii of M33 GMCs are similar to Galactic GMCs, and we assume that the scale heights of the two systems are similar, then the ratio of the one-dimensional velocity dispersions depends only on the cube root of the ratio of the epicyclic frequencies. Jog and Ostriker (1988) use κ=35 km s^{-1} kpc^{-1} locally in the Galaxy. For the inner kiloparsec of M33, the value of κ can be calculated from the CO rotation curve (Chapter 2), giving $\kappa = 88/\sqrt{r}$ km s^{-1} kpc^{-1} where $r \leq 1$ kpc is the distance from the center of the galaxy in kiloparsecs. Thus κ ranges from 278 km s^{-1} kpc^{-1} for r=0.1 kpc to 88 km s^{-1} kpc^{-1} for r=1 kpc. The values of κ in the two galaxies imply that the velocity dispersion in M33 should be 1.5-2 times larger than that of the Galaxy. This is consistent with the lower estimates for the value of the Galactic velocity dispersion. (Note that Jog and Ostriker adopted a typical Galactic GMC mass of 6×10^5 $M_\odot$, while the typical mass of a cloud in M33 is closer to 10^5 $M_\odot$. This difference in the average cloud size reduces the predicted velocity dispersion in M33 by a factor of 1.3.)

IV. The Cloud Mass Spectrum

a) The Observed Distribution

The distribution of cloud masses (M_{mol}) for the entire sample of clouds is given in Table 3 and compared to the Galactic distribution in Figure 5. In the mass range 0.8-4$\times10^5$ $M_\odot$, the mass distribution in M33 is consistent with the distribution $N(M) \propto M^{-1.6}$ derived for Galactic GMCs. However, the M33 distribution departs strongly from the single power law at higher and lower masses. No clouds less massive than 0.2$\times10^5$ $M_\odot$ or more massive than 4$\times10^5$ $M_\odot$ are detected in M33. The turnover in the number of clouds below 0.7$\times10^5$ $M_\odot$, which corresponds to a diameter of roughly 20 pc, suggests that our sample is incomplete below this mass, consistent with our sensitivity and selection criteria (see below).

The lack of very large clouds in our sample is quite different from the Galactic GMC population which contains clouds up to 2$\times10^6$ $M_\odot$. Clouds more massive than 4$\times10^5$ $M_\odot$ make up 25% by number of the Galactic population of clouds with masses greater than 0.8$\times10^5$ $M_\odot$. Assuming the same mass function for both galaxies, a total of eight clouds should be seen in the three highest mass bins given our observed sample of 38 clouds. In addition, since a 10^6 $M_\odot$ cloud will produce a flux of 3 K km s^{-1} in the single dish observations and only one such position in the single dish map of Chapter 2 has not been mapped in this survey, we cannot be missing more than one large cloud in this region of M33. Thus the inner region of M33 is clearly deficient in the largest GMCs.

The deficiency of clouds with masses less than 0.7$\times10^5$ $M_\odot$ can be understood in terms of the two selection criteria used to identify clouds. These criteria based on the sensitivity and resolution of the interferometer data can be translated into mass limits using Equations (1 - 3). The most stringent criterion is

that requiring a 3σ detection in at least two adjacent 1 MHz channels, i.e., a flux of ≥ 0.6 Jy is required for $\Delta V \geq 5.2$ km s^{-1}. This velocity width corresponds to a cloud diameter greater than 20 pc and a mass greater than 0.5×10^5 $M_\odot$. The second criterion, that the flux in the spectrum of the cloud exceed 3σ (0.6 Jy), is easily satisfied for clouds of this mass, which produce a peak flux of 1.4 Jy. In summary, we expect our sample to be reasonably complete down to diameters of 20 pc or masses of 0.5×10^5 $M_\odot$, but for smaller clouds the small line widths will preclude detection over the required 5.2 km s^{-1} velocity range.

The interferometer is not sensitive to structure on very large scales, which might truncate our sample at the high-mass end. The largest Galactic GMCs have diameters $\sim$100 pc (Sanders, Scoville, and Solomon 1985). To estimate our sensitivity to clouds of this size, the AIPS program was used to simulate the observing process using model clouds with Gaussian brightness profiles and full-width half-maximum diameters ranging from 5-75 pc (1-20″). The true diameter of the cloud was assumed to be 1.4 times the full-width half-maximum diameter. The models were multiplied by a Gaussian with a full-width half-maximum diameter of 66″ to simulate the primary beam response. This combination was Fourier transformed to the UV plane, sampled by a model of our UV coverage, Fourier transformed back to the image plane, and finally cleaned using the Fourier transform of the modelled UV coverage as the dirty beam. The diameters of the clouds in the cleaned map agree very well with the input model. Thus this survey is sensitive to clouds with diameters up to $\sim$100 pc and the dirth of large clouds in M33 is not an artifact of the observing procedure.

b) Discussion

The upper mass cutoff to the cloud mass distribution may reflect an equilibrium between cloud growth and destruction processes. A cloud grows by accretion

of HI or H_2 as it moves through the interstellar medium and may lose material that is dissociated and ionized by high-mass stars forming within the cloud. The cloud also loses mass that is locked up in newly-formed stars of all masses. The balance between these three processes may provide a natural limit to the size of the clouds that may be different in different environments.

The rate of accretion of material by the cloud is given by

$$dM_c/dt = \pi R^2 \sigma_v \overline{n}_H m_H (1 + \frac{GM_c}{R\sigma_v^2}) \qquad (9)$$

where M_c is the mass of the cloud, R is the radius of the cloud, σ_v is the cloud-cloud velocity dispersion, $\overline{n}_H$ is the mean gas density (molecular + atomic) of the interstellar medium, and m_H is the mass of the hydrogen atom. The second term in Equation (9) is the increase in the effective cross section of the cloud due to gravitational focussing. Assuming a total star formation efficiency β_T (the mass rate of star formation per unit mass of H_2 gas), the rate of cloud mass loss due to star formation is

$$dM_c/dt = -\beta_T M_c \qquad (10)$$

To estimate the rates of molecular dissociation and ionization, the number of stars in or near the cloud at any given time must be known. Once molecular hydrogen has been dissociated to atomic hydrogen, the star will rapidly ionize the surrounding region. We assume here that only ionized gas is lost when the HII region breaks free of the cloud, since this material is at a much higher pressure than the neutral atomic mantle. Assuming a constant star-formation efficiency β_i for stars of mass M_i, the rate of cloud mass loss due to ionization is given by the star formation rate (by number) times the mass of ionized gas $M_{f,i}$ produced by a star of mass M_i, $dM_c/dt = -\sum_i \beta_i M_c M_{f,i}/M_i$, The mass of ionized gas produced by a star is

$$M_{f,i} = 2.3 \times 10^4 (\frac{\tau}{1.5 \times 10^{14} s})^{9/7} (\frac{Q}{2.4 \times 10^{49} s^{-1}})^{4/7} (\frac{2\langle n_{H_2} \rangle}{10^3 cm^{-3}})^{-1/7} \qquad (11)$$

(Whitworth 1979), where $M_{f,i}$ is in $M_\odot$, Q is the number of ionizing photons per second produced by the star, $2\langle n_{H_2}\rangle$ is the mean density of hydrogen atoms in the cloud, and $\tau = R/\langle\sigma\rangle$ is the average amount of time a star spends within the cloud. For a typical cloud with $R = 20$ pc and $V_{FWHM} = 7$ km s^{-1}, $\tau \sim 3 \times 10^6$ yr, comparable to the lifetime of a 100 $M_\odot$ star (Maeder 1980). We have used τ in Equation (11) rather than the main sequence lifetime originally used by Whitworth, since most of the stars will spend a large fraction of their main sequence lifetime far from the cloud.

The number of ionizing photons produced by a star of mass M_i is given by $Q = \epsilon M_i^{2.75}$ with $\epsilon = 4.1 \times 10^{44}$ s^{-1} $M_\odot^{-2.75}$ (McKee 1989), yielding

$$dM_c/dt = -6.9 \times 10^{-17} \tau^{9/7} \langle n_{H_2}\rangle^{-1/7} \beta_T M_c \sum_i \frac{\beta_i}{\beta_T} M_i^{0.6} \qquad (12)$$

The value of $\sum_i \beta_i M_i^{0.6}/\beta_T$ depends on the slope and the upper and lower mass limits of the initial mass function. Adopting the modified Miller-Scalo initial mass function (Kennicutt 1983; Chapter 3) $\sum_i \beta_i M_i^{0.6}/\beta_T = 1.07$ $M_\odot^{0.6}$.

Combining Equations (9), (10), and (12) and setting $dM_c/dt = 0$ yields an expression for the equilibrium cloud mass when gas accretion is balanced by gas losses,

$$dM_c/dt = \pi R^2 \sigma_v \overline{n}_H m_H (1 + \frac{GM_c}{R\sigma_v^2}) - \beta_T M_c - 7.4 \times 10^{-17} \tau^{9/7} \langle n_{H_2}\rangle^{-1/7} \beta_T M_c = 0 \qquad (13)$$

The empirical relationship between velocity width and diameter (Equation (3)) can be combined with the virial mass (Equation (1)) to calculate the cloud radius as a function of mass, and hence the dependence of the mean density on cloud mass through Equation (6). This allows us to write Equation (13) as a function of cloud mass only. We rewrite Equation (3) as $V_{FWHM} = \delta_A D_{pc}^{0.5}$ and Equation

(6) as $\langle n_{H_2} \rangle = n_o / D_{pc}$, where $\delta_A \simeq 1.2$ km s^{-1} pc$^{-0.5}$ and $n_o = 3800$ cm^{-3} pc^{-1} for M33. Thus, $R = 3.32\sqrt{M}/\delta_A$, $\tau = 2.5 \times 10^4 M_c^{0.25}/\sqrt{\delta_A}$, and $\langle n_{H_2} \rangle = 4.53 \times 10^{21} n_o \delta_A / \sqrt{M}$ with M, τ, R, and $\langle n_{H_2} \rangle$ in cgs units. Substituting these into Equation (13) and setting $dM_c/dt = 0$, we obtain a numerical expression for the equilibrium mass of the cloud,

$$5.77 \times 10^{-23} \frac{\overline{n_H} \sigma_v}{\delta_A} + 5.20 \times 10^{-14} \frac{\overline{n_H}}{\sigma_v \delta_A} \sqrt{M_c} - \beta_T - 0.3 \frac{\beta_T M_c^{0.4}}{n_o^{1/7} \delta_A^{0.8}} = 0 \qquad (14)$$

where M is now in M$_\odot$, δ_A and n_o are in the units given above, and the other variables are in cgs units.

In this model, the upper mass cutoff decreases with increasing star formation efficiencies and increases with increasing interstellar medium densities. One interesting result is that the range of β_T for which an upper mass cutoff exists is fairly small. For low values of β_T the cloud does not form stars quickly enough to use up the accreted material and its growth is not halted by this mechanism. For large values of β_T the cloud forms stars faster than it accretes new material. The upper mass cutoff is also extremely sensitive to the exact value of β_T, with variations of 10% in β_T changing the upper mass cutoff by a factor of two. Thus numerical values for the upper mass cutoff must be viewed with a hearty skepticism, although it is interesting to see if the observed cutoff can be produced with reasonable assumptions for the other parameters in this model.

The amount of molecular hydrogen in the Galaxy between 2 kpc < R < 10 kpc is 1-2×10^9 M$_\odot$ (Clemens, Sanders, and Scoville 1988; Bronfman *et al.* 1988). Adopting a disk thickness of 140 pc and a mass of 2×10^9 M$_\odot$, the mean hydrogen volume density $\overline{n}_H$ is 2 cm^{-3}. The cloud-cloud velocity dispersion is 3-7 km s^{-1} and we adopt $\sigma_v = 5$ km s^{-1}. We use the same density-radius relation in the Galaxy as in M33 and adopt $\delta_A = 1$. The total star formation rate in the Galaxy is quite uncertain, ranging from 2-10 M$_\odot$ yr^{-1} (Mezger and Smith

1977). The observed mass cutoff is obtained if a low total star formation rate of 0.7 $M_\odot$ yr^{-1} or $\beta_T = 1.1 \times 10^{-17}$ s^{-1} is adopted. Thus this model is not entirely satisfactory since it requires an unusually low star formation efficiency to produce the observed mass cutoff in the Galaxy.

The central kiloparsec of M33 contains 3.2×10^7 $M_\odot$ of molecular gas and has a molecular-to-atomic-gas ratio of 2:1 (Chapter 2). However, the atomic hydrogen volume density in the plane of the galaxy should be small compared to the molecular hydrogen volume density, since the scale height for the atomic gas is probably greater than that of the molecular gas. Assuming a molecular disk thickness of 140 pc, the mean hydrogen volume density is ~ 3 cm^{-3}. Thus the observed upper mass cutoff in M33 of 5×10^5 $M_\odot$ can be obtained if a total star formation efficiency of 1.75×10^{-17} s^{-1} is assumed. The total star formation efficiency is proportional to the ratio of the far-infrared luminosity to the molecular hydrogen mass L_{IR}/M_{H_2}. This ratio is 3.8 $L_\odot$ $M_\odot^{-1}$ in the inner kiloparsec of M33 (Chapter 6) and 2.8 $L_\odot$ $M_\odot^{-1}$ for Galactic GMCs between 2 kpc $<$ R $<$ 10 kpc (Scoville and Good 1989). Thus a slightly higher star formation efficiency than that be predicted from the L_{IR}/M_{H_2} ratios of the two galaxies is required to obtain the observed mass cutoff in M33.

This model provides a natural explanation for the difference between the clouds seen in the center of M33 and GMCs in the center of our own Galaxy. The surface density of molecular gas in the inner 100 pc of M33 is not significantly higher than average (Chapter 2) and the clouds seen in the nucleus are similar in mass and diameter to clouds at larger radii. In contrast, the Galactic nucleus has ten times the gas density of the disk (cf. Scoville and Sanders 1987). The ratio L_{IR}/M_{H_2} for the Galactic center is 3.5 (Scoville and Good), only 25% higher than that of molecular clouds in the disk. Thus the clouds in the nucleus are accreting

mass too quickly for star formation to limit their growth. The maximum size of clouds in the Galactic center may thus be only tidally limited.

V. The Large Scale Distribution of Molecular Gas

It is useful to compare the interferometric and single dish fluxes, since the single dish map contains all of the CO flux while the interferometer resolves out emission extended on scales $> 30''$ (the first fringe spacing). A *direct* comparison of the single dish and interferometer fluxes indicates that the interferometer has detected 10-90% of the single dish flux in the different fields. However, the interferometer maps are only cleaned out to the half-power point of the primary beam, while single dish measurements are sensitive to flux out to roughly twice the half-power beam-width. Half the power detected with a single dish telescope from a large uniform source comes from beyond the half-power point. Thus a fairer method of comparing the two systems is to compare the interferometer flux to one-half the corresponding single dish flux. This approximation is correct if most of the CO flux in M33 is distributed uniformly on fairly large scales and will not be strictly correct when there are small, high intensity sources located just beyond the half-power point.

To more precisely estimate the amount of flux that is missed by the interferometer, we adopt a model for the molecular gas distribution in M33 that consists of the observed clouds plus a smooth unresolved background. This background could be either diffuse gas or a fairly uniform distribution of clouds too weak to be detected individually with the interferometer. Thus the contribution of the smooth component *within* the half-power beam of the interferometer is given by

$$I^S = 0.5(I^N - I^I - I^B) \tag{15}$$

where I^I is the flux detected by the interferometer and I^N is the total flux detected with the NRAO 12 m telescope. The contribution of strong sources

beyond the half-power point but within the primary beam is removed by subtracting the term I^B, where I^B is the response to the strong, compact source(s). The percentage of the total flux within the half-power beam detected by the interferometer is then given by

$$\frac{I^I}{I^I + I^S} = \frac{I^I}{0.5I^I + 0.5I^N - 0.5I^B} \tag{16}$$

Table 4 lists the observed fluxes from interferometer and single dish measurements, the smooth component calculated using Equation (15), and the percentage of the total flux detected by the interferometer. On average, the flux in the smooth component is equal to the flux detected with the interferometer. (We have excluded Region 5 from this analysis, since both the very high single dish fluxes and the appearance of the HI map suggest that there is a large molecular cloud lying to the west of this region that we have not mapped.) Two fields that have a negligible smooth component are Field 1A and Field 3G. Field 1A is extremely close to the nucleus of the galaxy and a diffuse component or small clouds may not be able to survive in the strong radiation field and energetic kinematics of this region. The single dish flux in Field 3G may be in error, since a measurement at this position made with the NRAO 12 m telescope in October 1987 detected ~50% more flux.

It is interesting that M33 appears to have a substantial fraction of its molecular gas contained in either very small clouds ($\sim 10^4$ $M_\odot$) or a diffuse component. This distribution of molecular gas is fundamentally different from that in our own Galaxy, where 85% of the mass resides in clouds larger than 10^5 $M_\odot$. In comparison, M33 appears to contain only 40% of its molecular gas in clouds larger than $\sim 10^5$ $M_\odot$. However, the published surveys of Galactic GMCs have not attempted to compare the flux in the large, resolved GMCs with the total flux detected in the same volume of space. While it is possible that a significant

amount of molecular gas in our own Galaxy resides in small clouds or a diffuse component, it seems unlikely that a fraction as large as 50% could have been missed in previous studies.

The velocity dispersion of the M33 GMCs resolved with the interferometer is significantly smaller than the single dish line widths, which range from 8 to 36 km s^{-1} (Chapter 2). The rapid radial variation of rotation velocity in this region broadens the single dish lines by 5-12 km s^{-1}, excluding positions within $1'$ of the center of the galaxy. Adopting a uniform gas distribution and weighting by the Gaussian beam response, the single dish velocity width due to rotational broadening was estimated for each position observed in the single dish map. The velocity dispersion of the smooth component $(\Delta V_s)^2$ is then given by

$$(\Delta V_s)^2 = (\Delta V_{obs})^2 - (\Delta V_{rot})^2 - (\Delta V_{GMC})^2 - (\Delta V_{int})^2 \qquad (17)$$

where ΔV_{obs} is the observed velocity width, ΔV_{rot} is the predicted velocity width due to rotation, ΔV_{GMC} is the cloud-cloud velocity dispersion, and ΔV_{int} is the average internal velocity dispersion of the massive GMCs. The average velocity dispersion of the smooth component calculated is 11 ± 1 km s^{-1}, much higher than the internal velocity dispersion of the GMCs. Thus the smooth component is a kinematically distinct component and cannot be due to large envelopes around the observed GMCs. If this smooth component is a distribution of low-mass molecular clouds, the increased velocity dispersion is consistent with the Jog and Ostriker model discussed in Section IIIc.

VI. Conclusions

We have observed 19 fields in the nearby spiral galaxy M33 with the Owens Valley Millimeter Interferometer at $\sim$30 pc resolution. A total of 38 individual molecular clouds were detected in the region surveyed. The velocity widths,

diameters, peak brightness temperatures, and masses are very similar to those of Galactic GMCs. Many of the observed clouds are crowded or show confused structure, but nine of the clouds are sufficiently isolated that their properties can be determined with some confidence. The main results are listed below.

(1) The velocity widths and diameters of these nine clouds are related by $V_{FWHM} = (5.4^{+0.8}_{-0.5})(D_{pc}/20\ pc)^{0.5\pm0.2}$. This agrees within the errors with the velocity-diameter relation obtained for Galactic GMCs. The mean density of the clouds as a function of radius is $\langle n_{H_2} \rangle = 200^{+60}_{-30}(D_{pc}/20pc)^{-1.0\pm0.4}$.

(2) Eighteen of the clouds have very weak emission, with masses of 0.2-0.6$\times10^5$ $M_\odot$ and peak brightness temperatures of $\sim$1 K. These clouds are not resolved and the low brightness temperatures are probably due to beam dilution. The clouds within 200 pc of the nucleus have higher than average brightness temperatures, possibly due to an increased ultraviolet radiation field. This conclusion is supported by published observations of clouds in NGC 604 that also show increased brightness temperatures and observations in an interarm region, where the brightness temperatures are significantly lower than average.

(3) The virial and molecular masses for the clouds agree to within 10%. This implies that the value of α in this region of M33 is similar to that of our own Galaxy. This is the first direct confirmation that the Galactic value of α is appropriate to an external galaxy.

(4) The mass distribution of the M33 clouds is in good agreement with the Galactic mass distribution, but shows a cutoff at masses greater than 4×10^5 $M_\odot$. This can be explained in terms of a simple model where the rate of accretion of material by a cloud is balanced by the rate of dissociation of molecular gas by stars within the cloud. This upper mass cutoff depends quite sensitively on the input parameters such as the total star formation rate, the mean density of

hydrogen in the interstellar medium, and the adopted initial mass function.

(5) A comparison of the interferometric and single dish data reveals that M33 has a significant amount of molecular gas distributed in a smooth component. Roughly half of the molecular gas is in structures less massive than 0.8×10^5 $M_\odot$, in contrast to the Galaxy where only 15% of the mass is in these smaller structures. The missing flux could be distributed in either a smooth diffuse component or in clouds less massive than $\sim 0.5 \times 10^5$ $M_\odot$.

TABLE 1

Fields in M33 Mapped with the OVRO Interferometer

Field ID	$\alpha(1950)$ ($^h\ ^m\ ^s$)	$\delta(1950)$ ($^\circ\ '\ ''$)	V_{LSR} (km s^{-1})	beam ($''$)	σ (Jy beam^{-1})	weighting
1A	01 31 03.0	30 23 54	-168	5.2×5.2	0.17	natural
2A	01 31 16.2	30 23 12	-188	7.7×7.1	0.18	uniform
2B	01 31 14.4	30 23 56	-200	7.0×6.8	0.14	uniform
2C	01 31 12.7	30 23 13	-185	7.3×7.2	0.16	natural
3A	01 31 14.0	30 25 18	-214	8.0×6.8	0.18	uniform
3B	01 31 12.2	30 26 04	-213	7.5×6.7	0.17	uniform
3C	01 31 08.8	30 26 04	-218	7.3×6.9	0.19	uniform
3D[a]	01 31 07.0	30 25 18	-199	7.2×7.2	0.22	uniform
3E[a]	01 31 15.7	30 26 05	-216	7.6×5.6	0.17	uniform
3F	01 31 15.7	30 26 50	-223	7.6×5.7	0.16	uniform
3G	01 31 10.5	30 25 20	-209	8.5×6.5	0.10	natural
4A	01 31 09.8	30 20 29	-154	7.3×7.2	0.10	natural
4B	01 31 07.7	30 21 23	-168	9.3×6.5	0.15	natural
4C	01 31 03.0	30 21 54	-150	8.5×7.7	0.14	natural
5A	01 30 58.3	30 20 54	-140	6.4×5.6	0.13	uniform
5B	01 30 58.3	30 21 39	-144	6.6×5.4	0.13	uniform
6A	01 30 53.7	30 23 52	-166	7.5×7.0	0.10	uniform
6B	01 30 50.2	30 23 52	-167	7.2×7.1	0.14	uniform
7A[a]	01 31 03.0	30 27 54	-220	8.1×7.3	0.10	natural

[a] No clouds were detected in this field.

TABLE 2

Properties of Molecular Clouds in M33

Cloud	$\alpha(1950)$ (^{h} ^{m} ^{s})	$\delta(1950)$ ($^\circ$ $'$ $''$)	V_{peak} (km s^{-1})	V_{FWHM}[a] (km s^{-1})	T_B (K)	S_{CO}[a] (Jy km s^{-1})	$\overline{D}$[a,b] (pc)	M_{vir}[a] (10^5 M$_\odot$)	M_{mol}[a] (10^5 M$_\odot$)
MC1[c]	01 31 03.0	30 23 56	-171	9.9	4.1	11.9	...	...	1.2
MC2[+]	01 31 03.7	30 23 57	-166	4.9	4.4	20.1	23.0	0.8	2.0
MC3[+]	01 31 04.0	30 23 41	-150	5.6	5.5	14.5	19.5	0.8	1.5
MC4[+,c]	01 31 02.8	30 24 03	-168	6.2	3.8	11.7	16.5	0.9	1.2
MC5	01 31 02.1	30 24 02	-158	6.5	2.8	5.2	...	...	0.5
MC6[+]	01 31 03.7	30 22 21	-159	6.9	1.6	17.2	39.1	2.6	1.7
MC7[d]	01 31 03.6	30 21 38	-151	8.8	1.3	19.0	55.3	5.9	1.9
MC8	01 31 03.6	30 22 09	-154	6.1	1.3	6.7	...	...	0.7
MC9	01 31 04.0	30 21 54	-154	9.9	0.9	7.3	...	...	0.7
MC10[+]	01 31 01.1	30 22 05	-149	7.1	2.0	21.5	39.4	2.8	2.2
MC11	01 31 07.9	30 21 20	-166	7.7	1.8	16.0	...	...	1.6
MC12	01 31 07.9	30 21 40	-166	6.5	1.4	7.5	...	...	0.8
MC13	01 31 10.3	30 20 40	-151	5.4	3.4	19.2	...	...	1.9
MC14	01 31 09.2	30 20 08	-144	7.9	0.8	4.1	...	...	0.4
MC15	01 31 09.3	30 20 22	-133	5.7	0.9	3.7	...	...	0.4
MC16	01 31 12.5	30 23 17	-186	10.3	2.2	9.9	...	...	1.0
MC17	01 31 13.4	30 23 18	-181	7.4	2.5	11.0	...	...	1.1
MC18	01 31 15.0	30 23 17	-186	6.6	2.2	10.6	...	...	1.1
MC19[d]	01 31 13.4	30 23 52	-202	8.0	2.2	27.1	60.1	5.3	2.7
MC20[+]	01 31 10.9	30 25 24	-209	10.7	3.1	45.1	37.0	5.9	4.6
MC21[e]	01 31 10.3	30 25 41	-220	8.4	0.9	5.9	27.8	2.7	0.6
MC22	01 31 09.2	30 25 37	-186	10.6	0.9	3.7	...	...	0.4
MC23	01 31 12.5	30 25 00	-186	4.4	1.1	5.3	...	...	0.5
MC24[e]	01 31 14.8	30 25 13	-217	7.2	1.2	6.4	30.1	2.2	0.6
MC25	01 31 13.0	30 25 56	-206	6.2	1.3	4.5	...	...	0.5
MC26	01 31 15.7	30 26 50	-214	4.9	1.6	6.1	...	...	0.6
MC27[+,f]	01 31 10.6	30 26 08	-222	6.6	2.0	19.6	39.6	2.4	2.0
MC28[f]	01 31 10.0	30 26 14	-217	6.4	1.9	8.0	...	...	0.8
MC29[d]	01 31 06.7	30 26 02	-217	8.2	2.1	28.3	63.2	5.9	2.9
MC30	01 31 07.9	30 25 41	-217	6.5	2.1	9.8	...	...	1.0

TABLE 2 (continued)

Properties of Molecular Clouds in M33

Cloud	α(1950) (^{h} ^{m} ^{s})	δ(1950) ($^\circ$ $'$ $''$)	V_{peak} (km s^{-1})	V_{FWHM}[1] (km s^{-1})	T_B (K)	S_{CO}[a] (Jy km s^{-1})	$\overline{D}$[a,b] (pc)	M_{vir}[a] (10^5 M$_\odot$)	M_{mol}[a] (10^5 M$_\odot$)
MC31[+]	01 30 48.6	30 24 01	-166	7.2	1.7	16.3	24.5	1.8	1.6
MC32[+]	01 30 51.8	30 23 52	-164	9.8	3.6	45.9	44.6	5.9	4.5
MC33	01 30 54.1	30 23 29	-190	4.3	1.0	2.3	...	...	0.2
MC34	01 30 53.9	30 23 32	-177	6.3	0.8	2.9	...	...	0.3
MC35	01 30 54.8	30 23 49	-166	8.8	1.2	6.7	...	...	0.7
MC36	01 30 53.2	30 24 19	-172	4.1	1.3	2.9	...	...	0.3
MC37	01 30 58.2	30 20 35	-141	2.6	1.9	1.9	...	...	0.2
MC38	01 30 58.3	30 21 46	-143	4.4	1.7	5.9	...	...	0.6

A distance to M33 of 0.79 Mpc is assumed throughout.

[a] The typical errors are: $\overline{D}$ ±5 pc. V_{FWHM} ±1.3 km s^{-1}, I_{CO} ±20%, M_{mol} ±30%, M_{vir} $^{+30}_{-40}$%.

[b] $\overline{D}=(D_\alpha + D_\delta)/2$. where D_α and D_δ are the deconvolved full-width half-maximum diameters in the right ascension and declination directions.

[c] MC1 and MC4 were treated as one cloud in Wilson *et al.* (1988) where clouds were identified from a single integrated intensity map over 12 channels. If the two are treated as a single cloud, the virial mass for the system is eight times the flux-based mass.

[d] This cloud shows considerable structure and may in fact be two clouds. It was therefore not included in the refined sample of clouds for comparison with Galactic GMCs.

[e] This cloud was not included in the refined sample of clouds, since the emission is weak and the cloud is only marginally resolved.

[f] These clouds lie very close together and might be considered to be one cloud. For the two clouds taken together, the virial mass is three times larger than the flux-based mass.

TABLE 3

Number of Clouds per Unit Logarithmic Mass Interval

log M ($M_\odot$)	Number of Clouds
4.2-4.4	2
4.4-4.6	4
4.6-4.8	7
4.8-5.0	7
5.0-5.2	6
5.2-5.4	8
5.4-5.6	2
5.6-5.8	2

TABLE 4

Comparison of the Single Dish and Interferometer Fluxes in M33

Field ID	NRAO Flux (Jy km s^{-1})	OVRO Flux (Jy km s^{-1})	Smooth Flux (Jy km s^{-1})	Fraction Detected with OVRO
1A	64	58	3	1.0
2A	95	9	31[a]	0.2[a]
2B	122	24	41[a]	0.4[a]
2C	112	26	34[a]	0.4[a]
3A	65	6	18[b]	0.2[b]
3B	129	4	44[c]	0.1[c]
3C	141	44	37[b]	0.5[b]
3D	88	0	26[c]	0.0[c]
3G	88[d]	54	10[d]	0.8[d]

TABLE 4 (continued)

Comparison of the Single Dish and Interferometer Fluxes in M33

Field ID	NRAO Flux (Jy km s^{-1})	OVRO Flux (Jy km s^{-1})	Smooth Flux (Jy km s^{-1})	Fraction Detected with OVRO
4A	78	24	27	0.5
4B	82	22	30	0.4
4C	92	52	20	0.7
6A	143	41	51	0.4
6B	143	47	48	0.5

[a] The contribution of the other clouds in Region 2 was removed.

[b] The contribution of the cloud MC20 was removed.

[c] The contribution of the clouds MC20, MC27, and MC28 was removed.

[d] The NRAO flux measured in October 1987 was 50% higher.

Figure Captions

Fig. 1 – The nineteen fields observed with the Owens Valley Interferometer are shown on a continuum-subtracted H_α image obtained at the Palomar 60″ telescope. The positions of the 38 molecular clouds found in this survey are outlined. Detailed maps of individual clouds are given in Figure 2.

Fig. 2 – Contour plots of each of the sixteen fields mapped with the interferometer that contains molecular clouds. For maps containing more than one cloud, integrated flux maps were made for each cloud over the range of channels in which emission from that cloud was seen, and the resulting maps were combined to produce the final figures. The maps have not been corrected for the attenuation of the primary beam. (a) Field 1A – contour levels 2, 3, ... 9× 1.06 Jy beam^{-1} km s^{-1} (b) Field 4C – contour levels 2, 3, ... 9× 0.56 Jy beam^{-1} km s^{-1} (c) Field 4B – contour levels 1, 2, ... 10× 0.78 Jy beam^{-1} km s^{-1} (d) Field 4C – contour levels 1, 2, ... 10× 0.87Jy beam^{-1} km s^{-1} (e) Field 2C – contour levels 1, 2, ... 10× 1.02 Jy beam^{-1} km s^{-1} (f) Field 2A – contour levels 2, 3, ... 10× 0.67 Jy beam^{-1} km s^{-1} (g) Field 2B – contour levels 2, 3, ... 10× 0.59 Jy beam^{-1} km s^{-1} (h) Field 3G – contour levels 0.25, 0.5, 0.75, 1, 2, 3, ... 10× 1.90 Jy beam^{-1} km s^{-1} (i) Field 3A – contour levels 3, 4,... 10× 0.32 Jy beam^{-1} km s^{-1} (j) Field 3B – contour levels 2, 3, ... 10× 0.34 Jy beam^{-1} km s^{-1} (k) Field 3F – contour levels 2, 3, ... 10× 0.34 Jy beam^{-1} km s^{-1} (l) Field 3C – contour levels 2, 3, ... 10× 0.52 Jy beam^{-1} km s^{-1} (m) Field 6B – contour levels 1, 2, ... 10× 1.27 Jy beam^{-1} km s^{-1} (n) Field 6A – contour levels 0.5, 1, 2, 3, ... 10× 0.99 Jy beam^{-1} km s^{-1} (o) Field 5A – contour levels 3, 4, ... 10× 0.20 Jy beam^{-1} km s^{-1} (p) Field 5B – contour levels 2, 3, ... 10× 0.30 Jy beam^{-1} km s^{-1}.

Fig. 3 – Spectra of each of the 38 clouds detected in our survey, integrated over

the area of the cloud.

Fig. 4 – (a) Velocity width plotted versus diameter for our sample of 9 large, well-isolated clouds. The line shown is least squares fit of a power law to the data. (b) Full-width half-maximum velocity, (c) deconvolved diameter, and (d) virial mass plotted versus molecular mass for the same sample of clouds. The cloud MC3 was excluded from the fit of virial mass to molecular mass. It is the only cloud with a virial mass significantly smaller than its molecular mass and the χ^2 of the fit was significantly reduced by excluding this cloud.

Fig. 5 – The function g(m) (Kwan 1979), the number of molecular clouds per unit logarithmic mass interval, is shown as the solid line for the M33 clouds. The corresponding distribution for Galactic clouds from Sanders, Solomon, and Scoville (1985) is the dashed line.

Figure 1

Positions of OVRO Fields

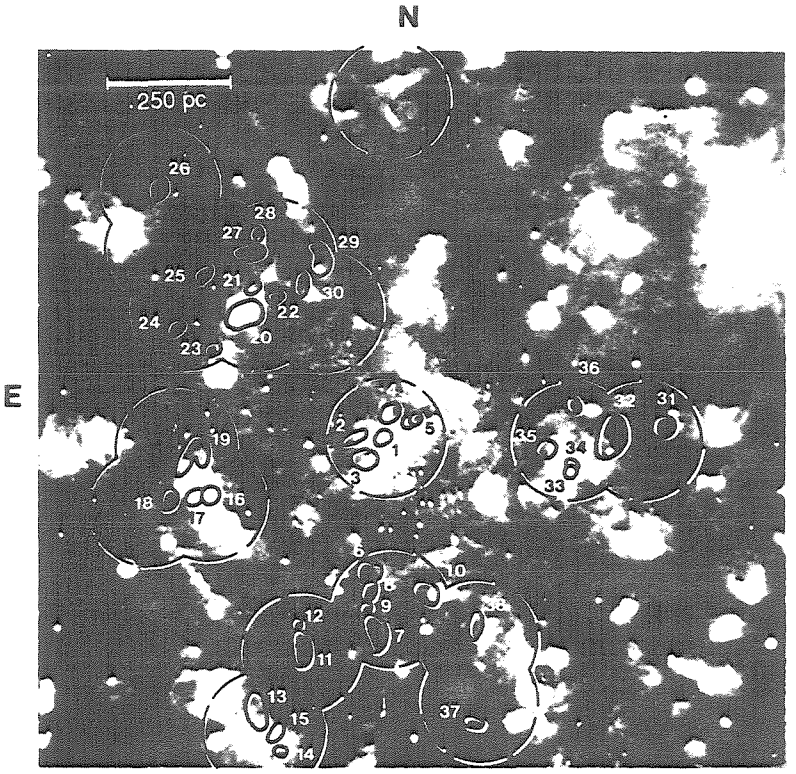

Figure 2a-d

Maps of Molecular Clouds

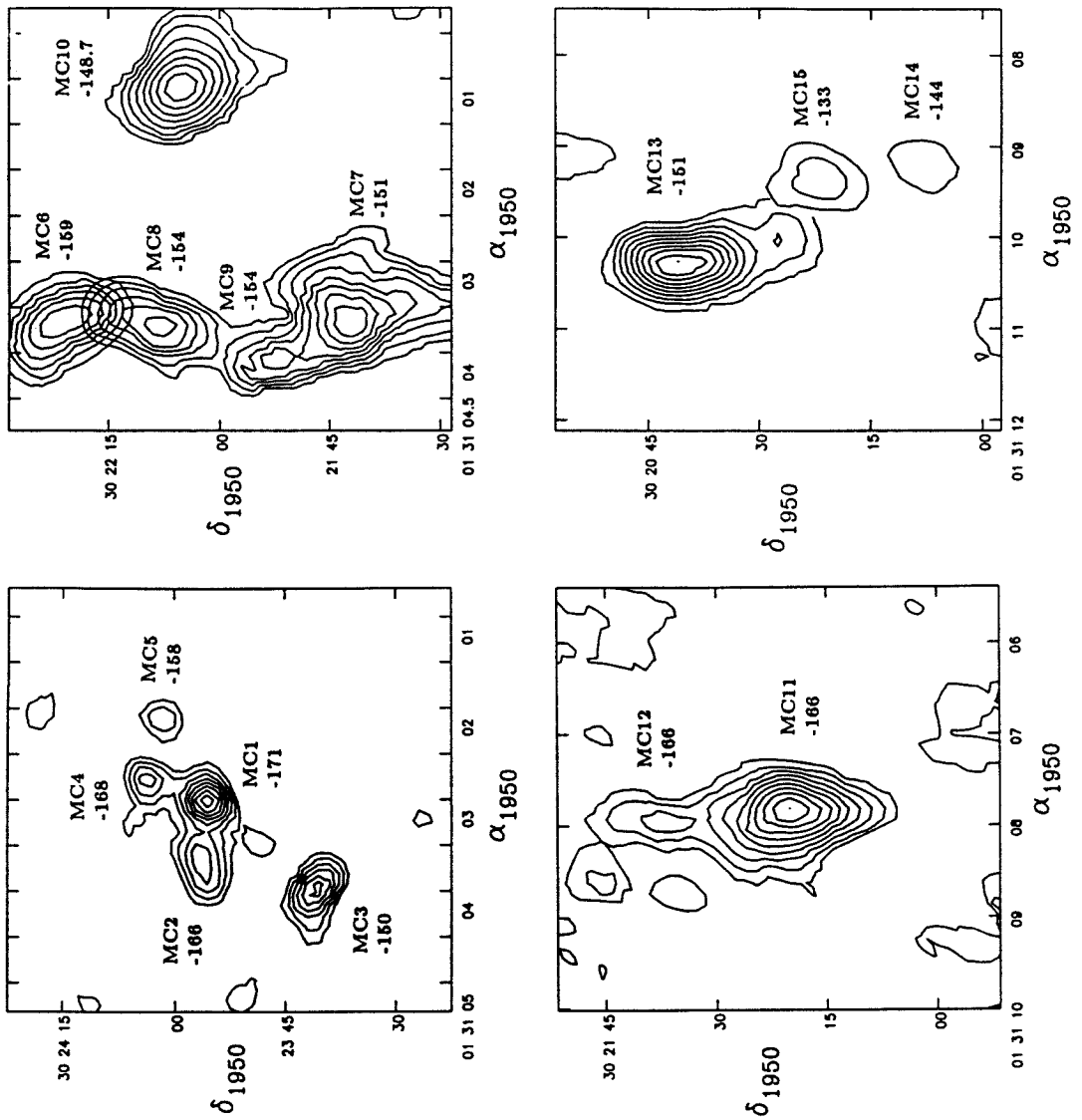

Figure 2e-h

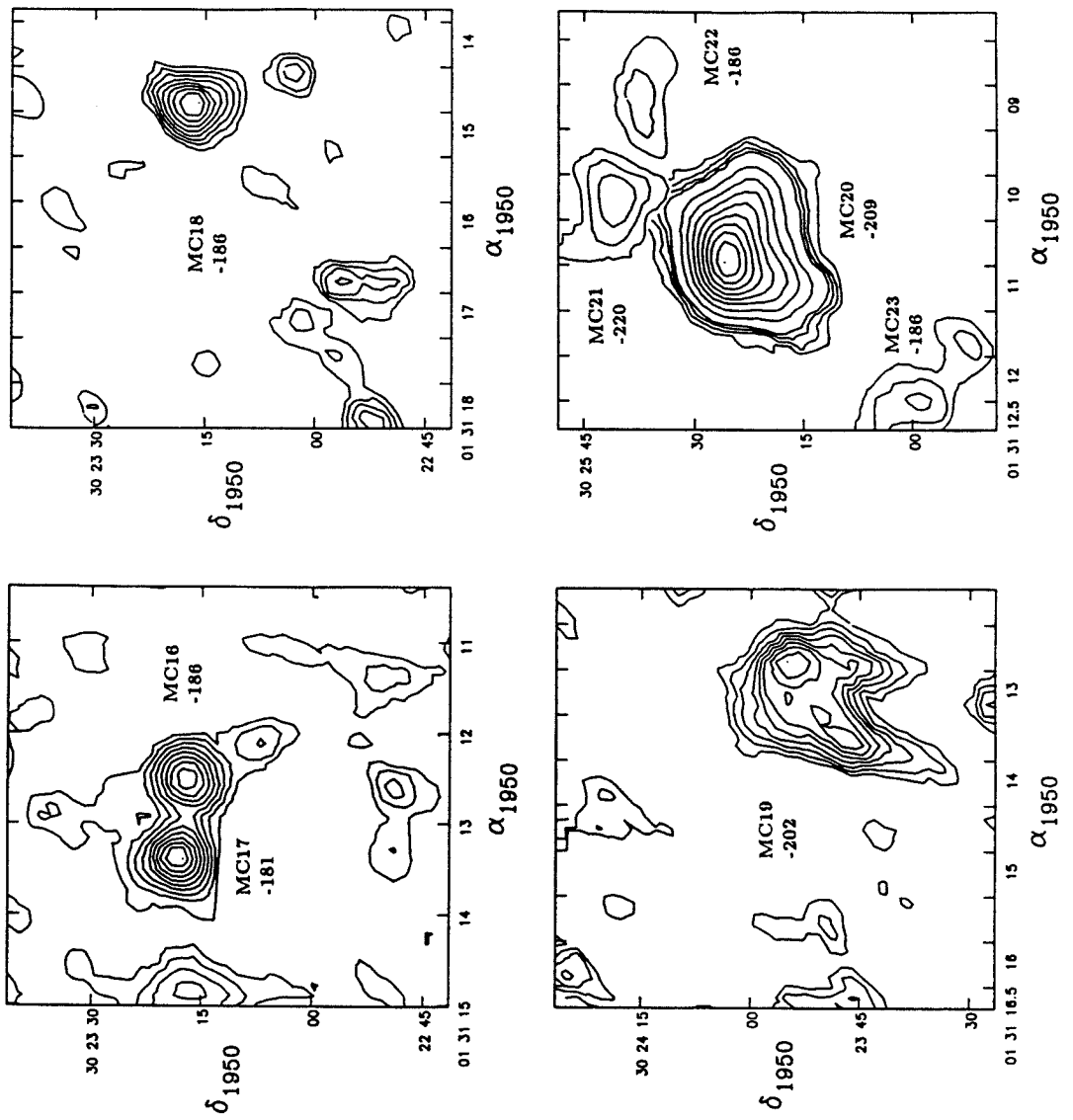
MC16
-186
MC17
-181
MC18
-186
MC19
-202
MC20
-209
MC21
-220
MC22
-186
MC23
-186
α_{1950}
δ_{1950}

Figure 2i-l

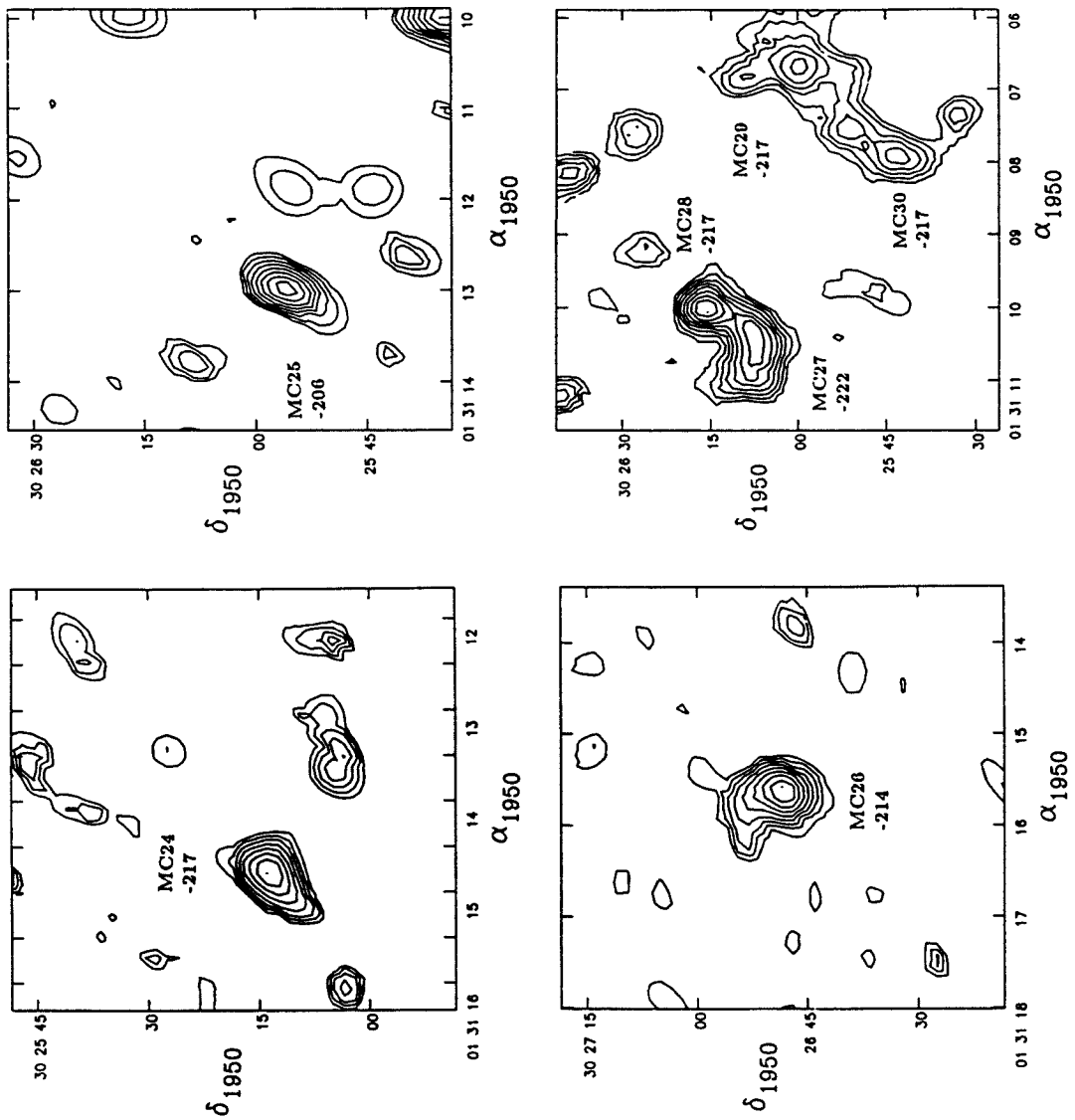
MC24
-217
MC25
-206
MC26
-214
MC27
-222
MC28
-217
MC29
-217
MC30
-217
δ_{1950}
α_{1950}

Figure 2m-p

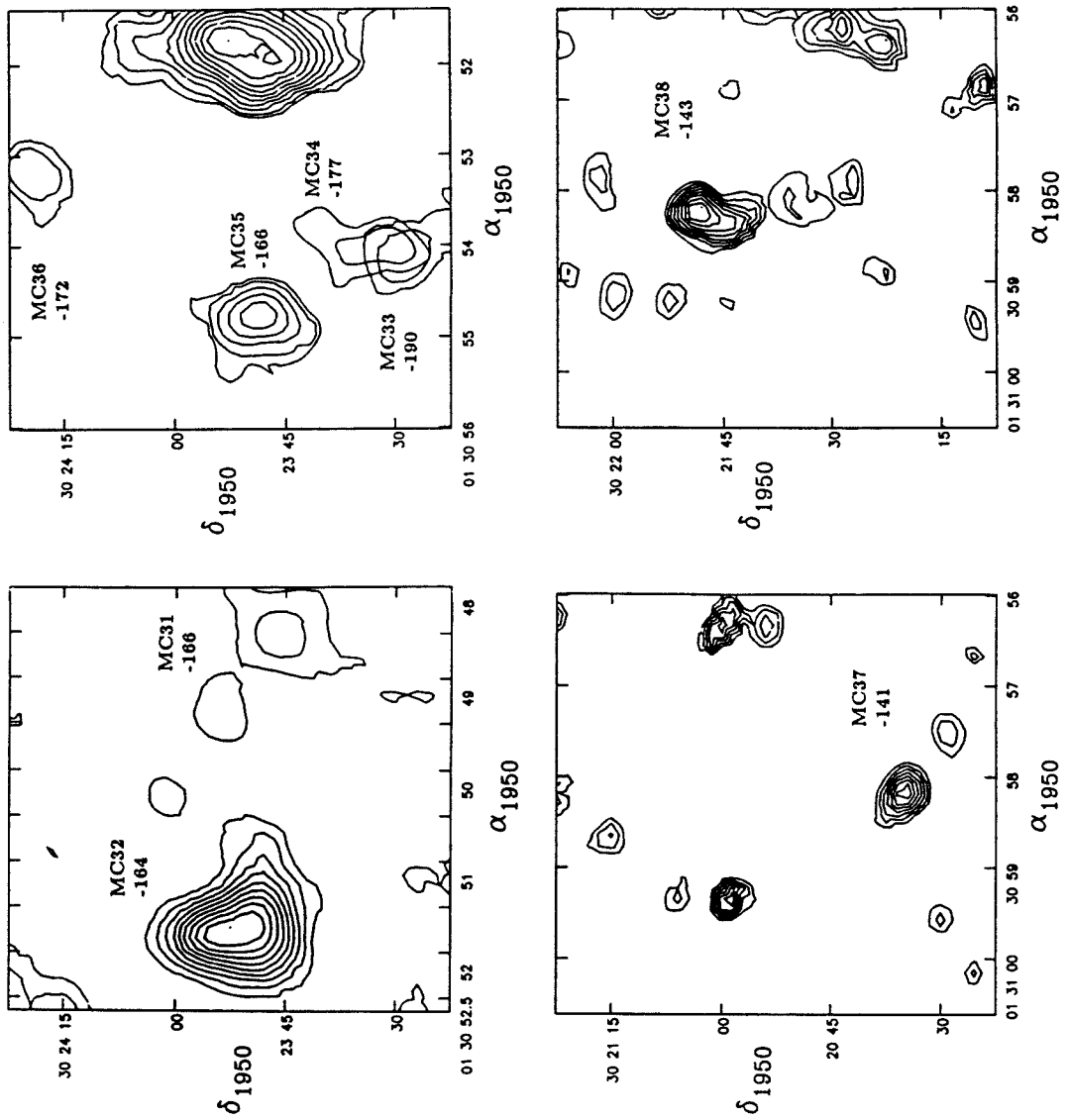
MC36
-172
MC35
-166
MC34
-177
MC33
-190
MC38
-143
MC32
-164
MC31
-166
MC37
-141
δ_{1950}
α_{1950}

Figure 3

Spectra of Molecular Clouds

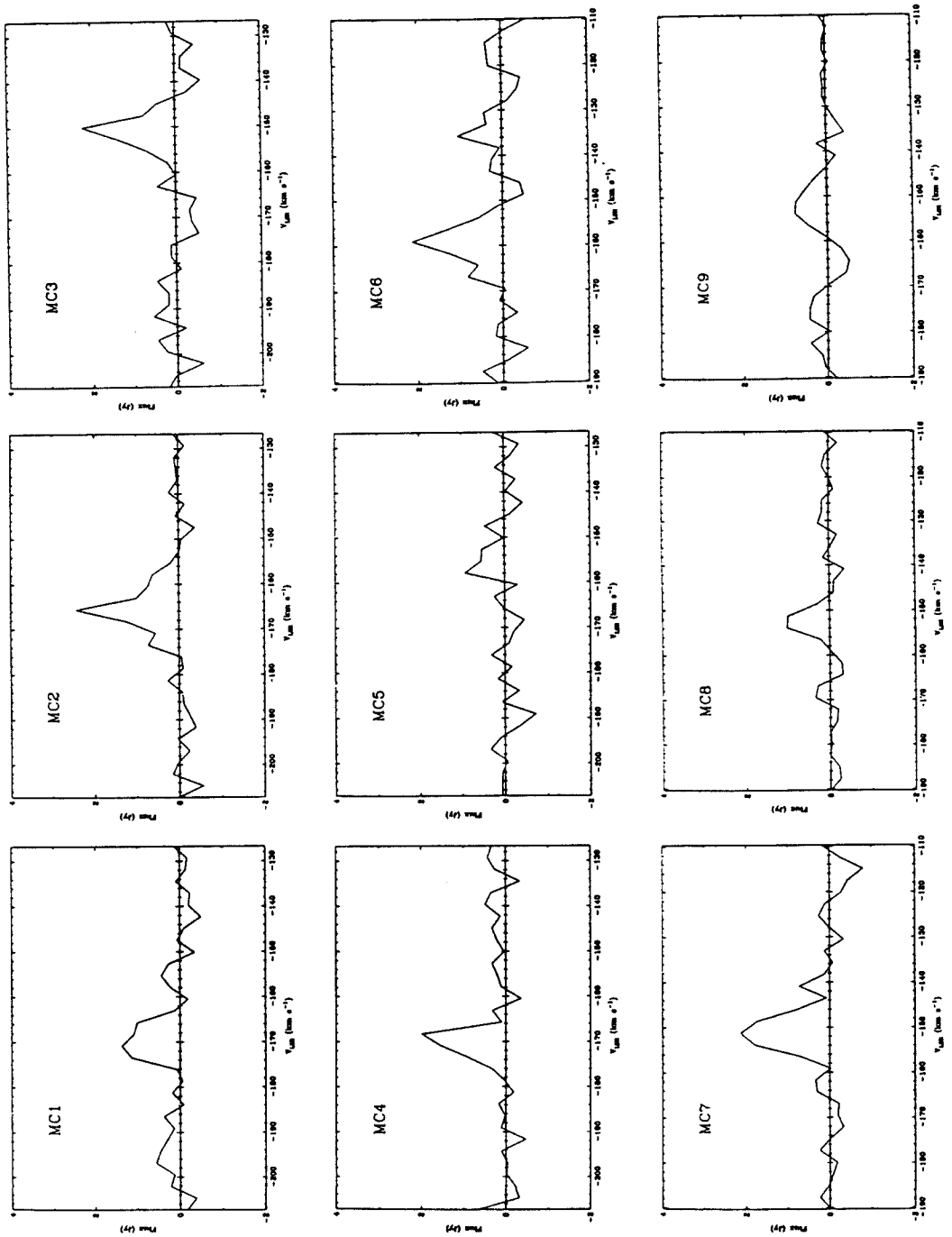

Figure 3 (continued)

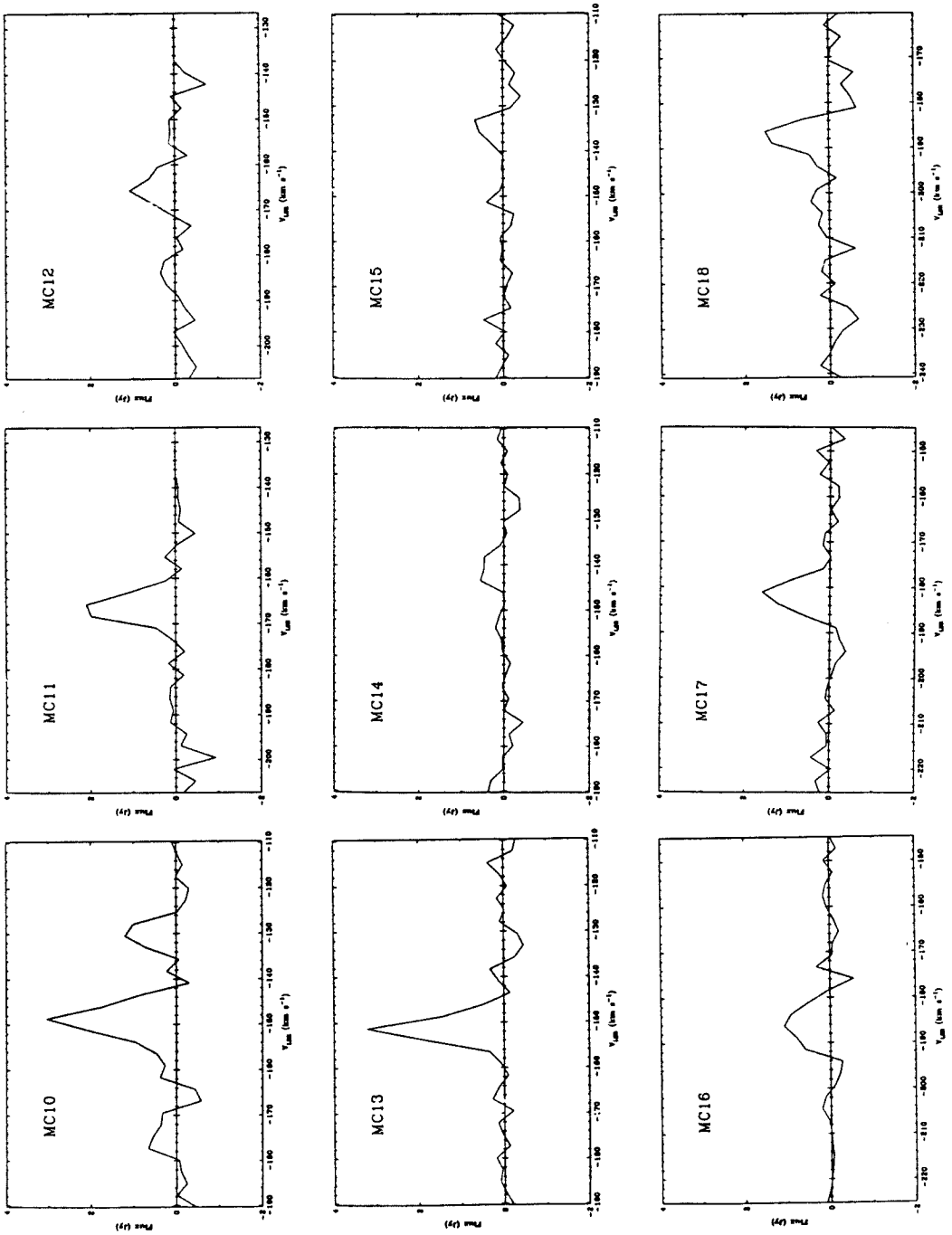

Figure 3 (continued)

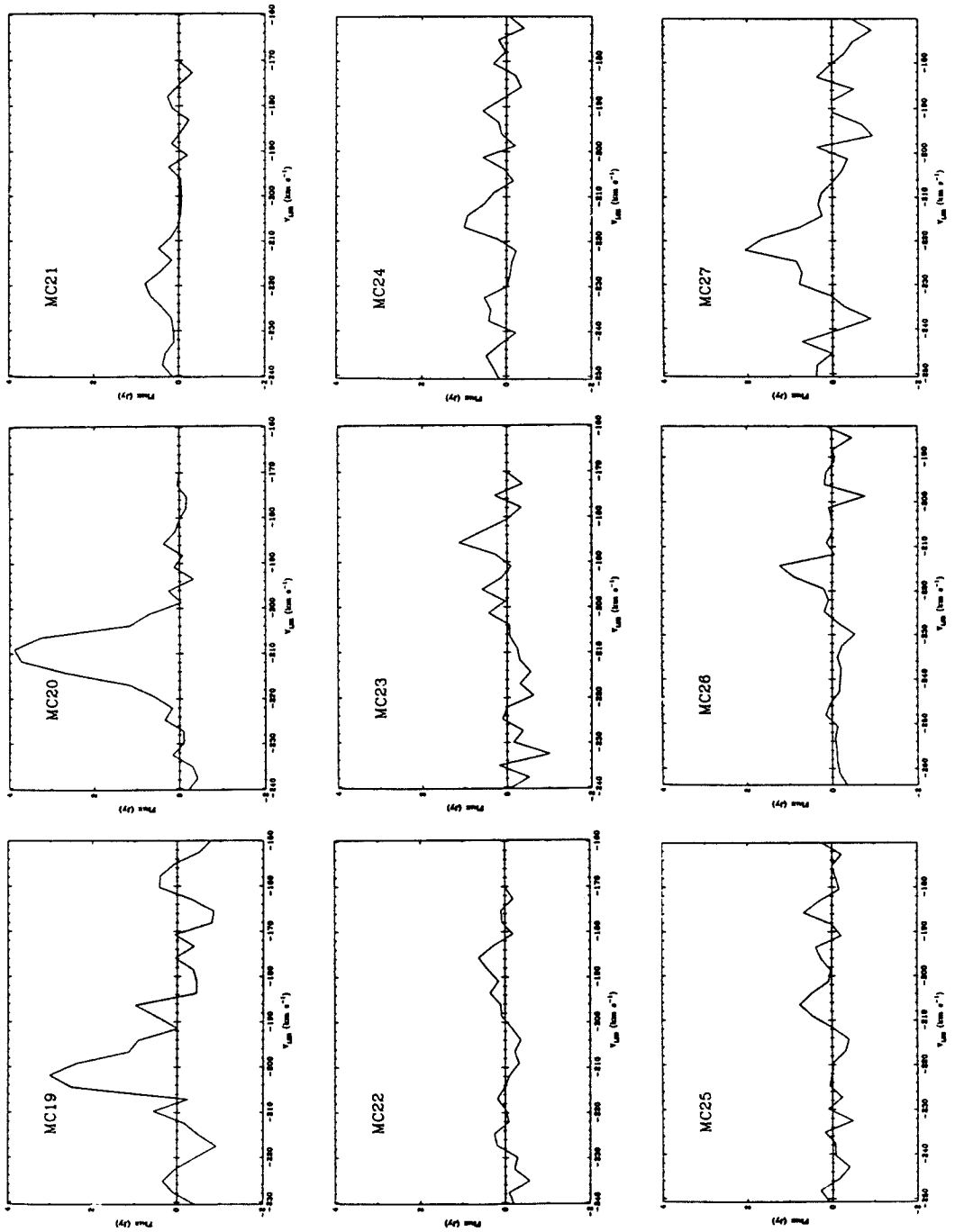

Figure 3 (continued)

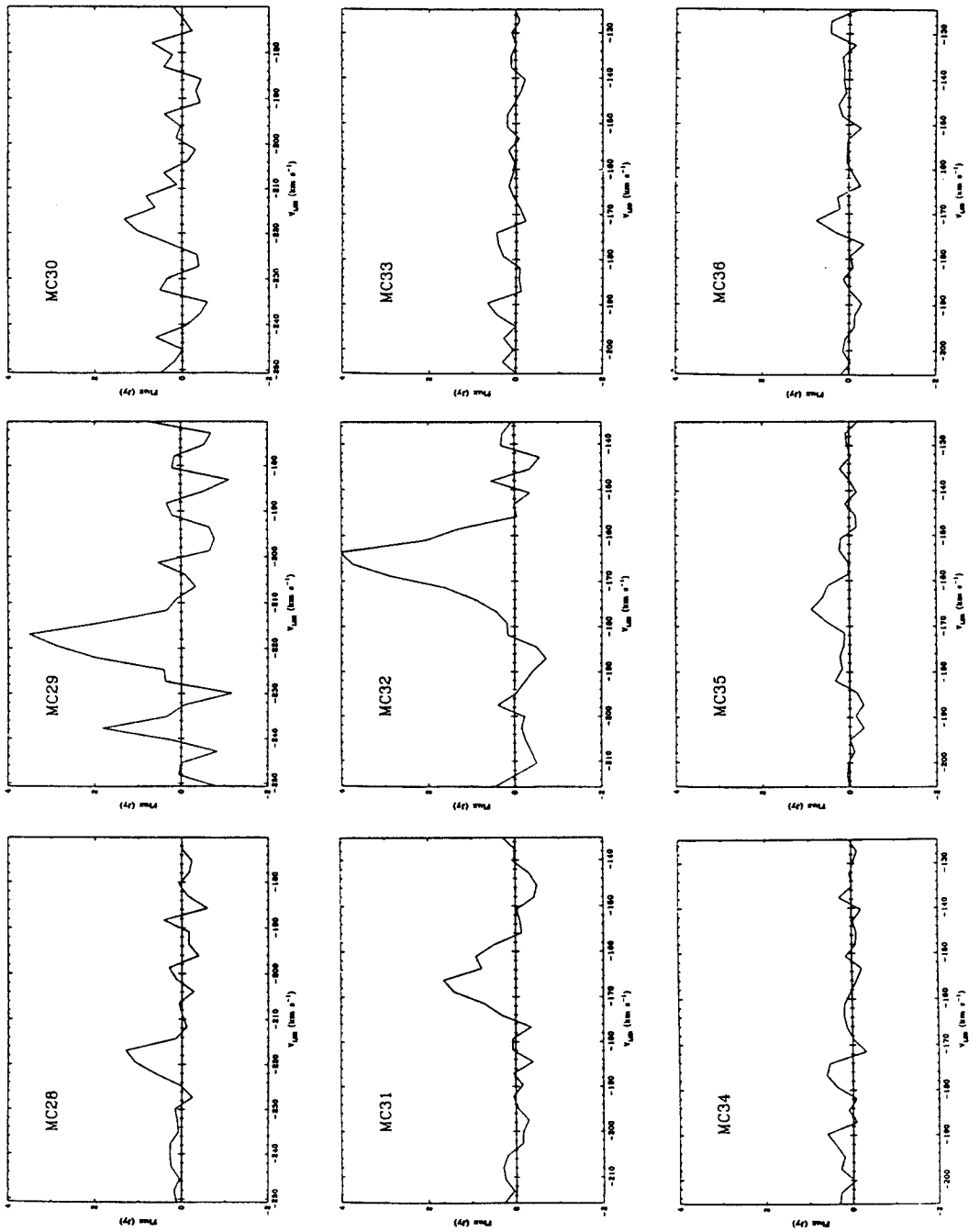

Figure 3 (continued)

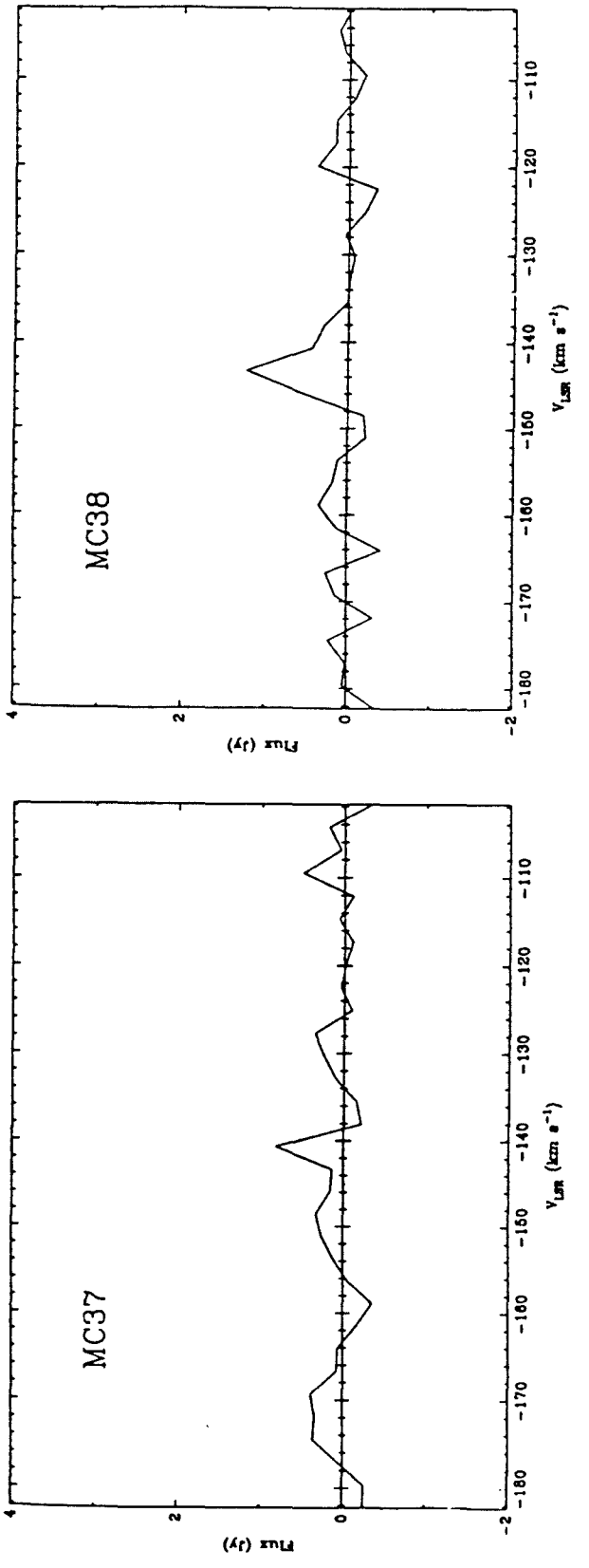

Figure 4

Relationships Among Mass, Diameter, and Velocity Width

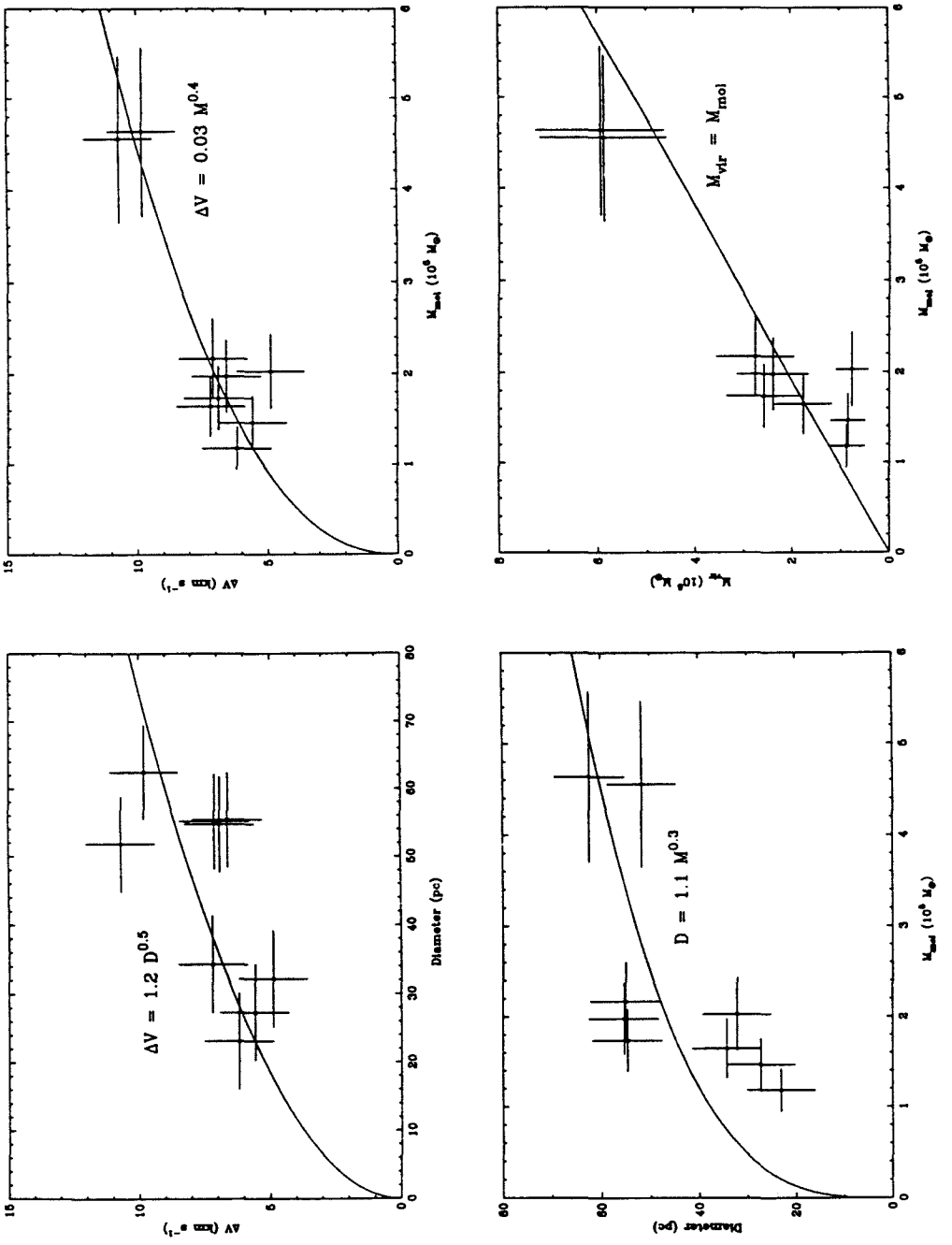

Figure 5

Mass Distribution of M33 and Galactic Clouds

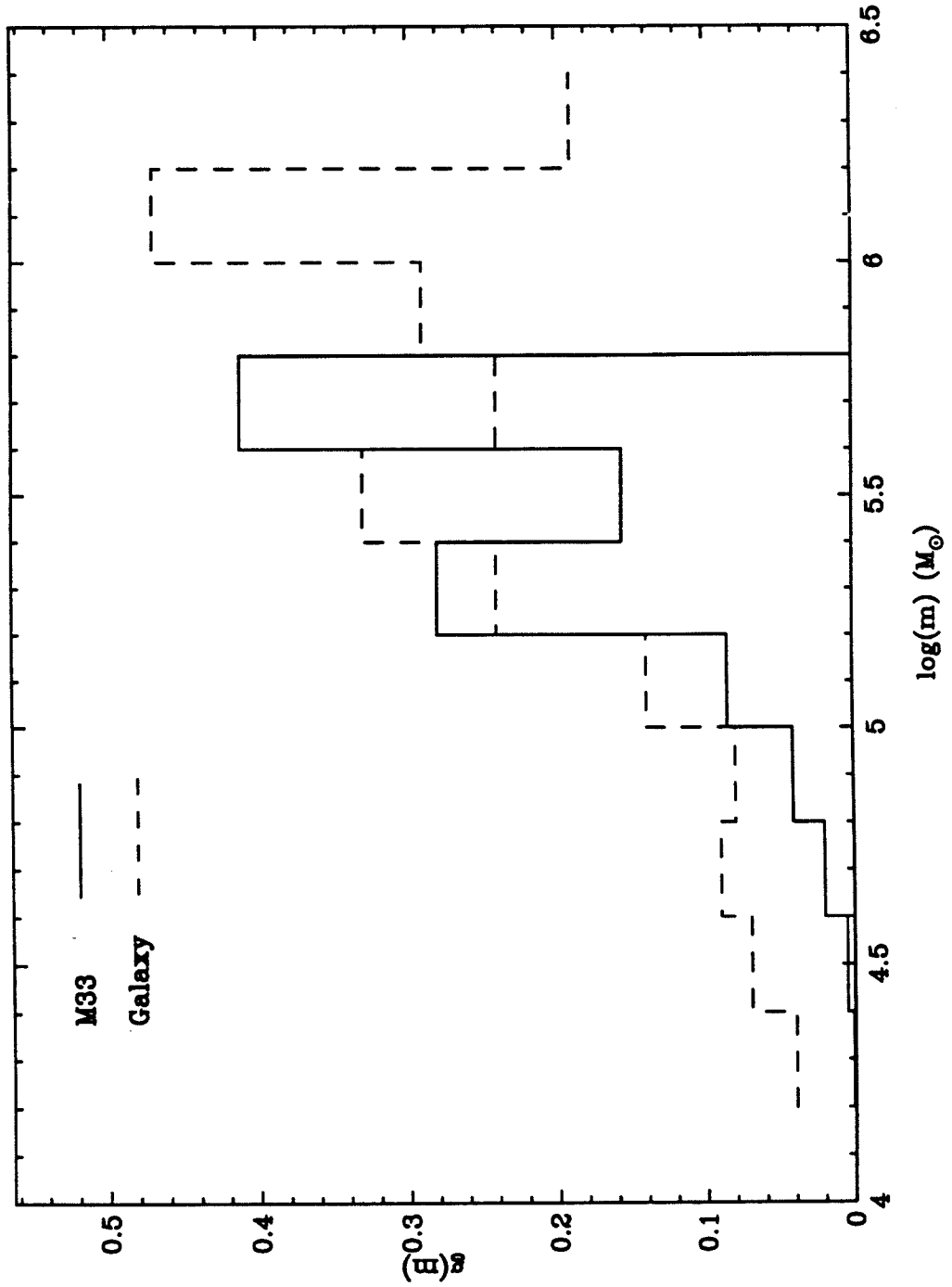

CHAPTER 5

The Interstellar Medium and Spiral Structure in M33

I. Introduction

The interaction between the interstellar medium and galactic spiral structure remains one of the more interesting observational and theoretical problems in the study of galactic structure. In particular, observations of the various components involved in high-mass star formation may allow us to distinguish between competing spiral arm models. The presence of a spiral density wave may be indicated by streaming motions in the gas across the arms. In contrast, stochastic, self-propagating arms should not show any systematic motions of the gas across the arms. High-resolution observations of the velocity structure of the molecular gas across the spiral arms of the grand-design galaxy M51 have provided strong observational support for the presence of a density wave (Vogel, Kulkarni, and Scoville 1988). In addition, the high-mass star formation lies downstream of the molecular gas ridge, which indicates a significant time lag between the gas entering the arm and the onset of OB star formation. Since spiral arm properties vary considerably from one galaxy to another, detailed observations of galaxies with a range of morphological types are critical for a complete understanding of the spiral phenomenon.

In this chapter, the high-resolution CO data of Chapter 4 and the HI data of Deul and van der Hulst (1987) are combined with new optical Hα data to study the distribution of molecular, atomic, and ionized gas near the molecular clouds in M33. Many of the clouds lie near the southern spiral arm, which has been

postulated to be generated by a spiral density wave (Humphreys and Sandage 1980), and the spatial distributions of these three components of the interstellar medium are used to study the evolution of the interstellar medium in the presence of this underlying spiral structure. In particular, the cycle between the molecular and atomic gas phases in the spiral arms can be clearly defined, whether pre-existing molecular clouds are simply collected in the arms or whether the molecular clouds form in the arms from compression of diffuse atomic gas. The effects of high-mass star formation on the clouds are also addressed, specifically whether the high-mass stars can generate enough photo-dissociating radiation to produce the observed atomic gas peaks.

The optical data reduction is discussed in Section II and the high-mass star formation rates near the molecular clouds are discussed in Section III. The spatial distribution of the atomic and molecular gas and the implied streaming motions in the southern spiral arm are discussed in Section IV. These results are combined with the Hα data to study the cycle between molecular, atomic, ionized gas. The hypothesis that high-mass stars in molecular clouds produce atomic gas peaks via photo-dissociation of molecular hydrogen is tested in Section V and the chapter is summarized in Section VI.

II. Hα Observations and Data Reduction

CCD frames using 100 Å wide filters centered on Hα and adjacent continuum were obtained during photometric conditions at the Palomar 60″ telescope on 16 October 1988 using reimaging optics. The chip scale was rebinned to 1.3″ per pixel and the exposure times were 1200 s for both the continuum and the Hα frames. The frames were erase subtracted and flat fielded using dome flats. The continuum image was scaled to the same flux level as the Hα image using several bright, isolated, unsaturated stars and then subtracted from the Hα image to

produce a continuum-subtracted image. Since the seeing was slightly different for the two frames, bright stars did not subtract out smoothly and for cosmetic purposes the pixels around these stars were smoothed if the star did not lie near extended emission. The transformation to right ascension and declination was calculated from the Cepheids in this field (Freedman, Wilson, and Madore 1990). The reimaging optics introduce a distortion into the rectilinear coordinate frame; however, since a linear fit to the secondary standards is accurate to 1 pixel (1.3″) and most molecular clouds lie within the region covered by the standards, no attempt was made to correct for this distortion. Region 6 and Field 4A lie just outside the region covered by the secondary standards and the uncertainties in the absolute position of the Hα images are slightly larger there.

The planetary nebulae NGC 7027, IC 5217, and IC 2003 were used as absolute flux standards (Shaw and Kaler 1982; Barker 1978) and were observed over a range of airmasses from 1 to 2.2. The filter centered on the Hα line was sufficiently wide to include emission from the [NII] line at 6583 A. The transmission of the filter for the [NII] line at the blueshifted velocity of M33 is 98% of the transmission at Hα. The fluxes of the nebulae in the adjacent continuum filter were $\sim$ 3% of the flux in the on-line filter. The counts in both filters were divided by the exposure times and the continuum counts subtracted from the line counts. The net counts were then corrected upward to counts above the atmosphere using an extinction at Hα of 0.096 mag/airmass from the Palomar extinction tables. The emission from the nebulae (Hα + 0.98 N[II]) was then used to calculate the conversion factor between counts s^{-1} and erg cm^{-2} s^{-1} above the atmosphere. The calculated conversion factors for the repeated planetary nebulae observations agree to within $\pm$5%.

III. High-Mass Star Formation in the Molecular Clouds

Of the sample of 28 molecular clouds more massive than 0.5×10^5 $M_\odot$ (Table 2, Chapter 4), eleven have no associated Hα emission (MC6-9, MC11-12, MC21, MC24, MC26-27, and MC32). Many of the HII regions associated with clouds are considerably less luminous than the Orion nebula (Schraml and Mezger 1969) and some are probably ionized by a single B star. The number of clouds with and without Hα emission is consistent with all clouds having OB star formation, but with stars on the far side of clouds being obscured by dust. Alternatively, not all clouds may be currently forming high-mass stars. Given the high extinction of these dense clouds, it is impossible with these data to distinguish between these two possibilities.

The Hα luminosity can be related to the high mass ($M\geq 10$ $M_\odot$) star formation rate, using the formula

$$SFR(\geq 10M_\odot) = \frac{L_{39}}{702}\ M_\odot\ yr^{-1} \qquad (1)$$

where L_{39} is the Hα luminosity in units of 10^{39} erg s^{-1} (Kennicutt 1983). Assuming a standard initial mass function, the total mass of stars with masses greater than 10 $M_\odot$ is $2600L_{39}$ $M_\odot$ and the number of O5 stars contained in the nebula is $15L_{39}$ (Kennicutt 1988). A combined foreground and internal reddening of A_V=0.9 mag (Chapter 3) corresponding to $A_{H\alpha}$=0.75 mag is used to convert the HII region fluxes to true luminosities. The counts are also scaled down by a factor of 0.75 to correct for the [NII] emission (Kennicutt 1983). The average background level (sky plus diffuse emission) was measured in four areas of the image that did not show significant Hα emission and this level was subtracted from the total counts to obtain the Hα luminosity for individual HII regions in the clouds.

The total star formation rates, the amount of mass in high-mass stars, and

the number of O5 stars are given for each cloud in Table 1, as are the time scales for gas depletion due to high-mass star formation. Previous HII region identifications are also indicated (Boulesteix *et al.* 1974; Courtes *et al.* 1987). Some of the HII regions require a large cluster of high-mass stars to ionize the observed region, while others may be ionized by a single OB star. Five of the HII regions are sufficiently luminous to contain several O5 stars. Two luminous regions are each surrounded by four molecular clouds (MC1-4 and MC16-19), and are sufficiently complicated that HII regions associated with the individual clouds cannot be identified.

Assuming that only high-mass stars form in the clouds, the time scale for gas depletion in an individual cloud ranges from 4×10^8 to 2×10^{10} yrs. We do not include the nearby atomic gas peaks (Section IV) in calculating the gas depletion time scales and also do not include mass returned to the interstellar medium by evolving stars. The time scale estimates are upper limits, since high internal extinction causes an underestimate of the star formation rate. In addition, if the clouds are also forming lower mass stars, the lifetimes should be decreased by up to a factor of seven (Kennicutt 1983).

IV. The Molecular, Atomic and Ionized Gas Distributions: Evidence For Streaming Motions?

Comparison of the CO and HI maps reveals that most of the large molecular clouds lie in regions with HI column densities greater than 4×10^{20} cm^{-2}, the mean column density for the inner 7′ of the galaxy. Of 19 clouds with masses greater than 0.8×10^5 $M_\odot$, 13 lie in regions with an above average HI column density. Notable exceptions to this trend are MC7, MC27, and MC28, which are in regions with mean densities of $\sim 3 \times 10^{20}$ cm^{-2}, and MC11, which lies in a hole in the local HI distribution with mean density 2×10^{20} cm^{-2}.

The CO and HI maps are overlaid on grey-scale plots of the Hα emission in Figure 1. The spatial distributions of the Hα, CO, and HI emission show that these three interstellar medium phases are always closely associated. All but two small Hα emission regions lie near a molecular cloud. In addition, *each* atomic hydrogen peak is associated with a molecular cloud, with a mean offset between the peaks of 15″ (60 pc). The sense of the offset (azimuthally and radially) between the CO and the HI peaks is not constant over the face of the galaxy, and is also not generally constant even within a given region.

Two small Hα emission regions do not lie near a cloud, one south of MC10, the other south of MC27-28. The full-width half-maximum diameters of these regions are 2.4 and 2.6 pixels, respectively, similar to the diameters of stellar images ($\sim$ 2.2 pixels). Thus these two regions may be planetary nebula, Wolf-Rayet stars, or other emission-line stars (Neese, Armandroff, and Massey 1989).

Systematic displacements between the CO and HI peaks would be expected in the presence of a spiral density wave if the molecular gas were forming from the atomic gas entering the density wave or if the atomic gas was the result of photo-dissociation of molecular hydrogen by the ultraviolet flux from young stars. This high-mass star formation need not be triggered by the density wave, but rather could be an ongoing process with the density wave simply inducing streaming motions leading to a uniform offset between the molecular and atomic gas. The massive southern spiral arm in M33 has been postulated to be due to a spiral density wave (Humphreys and Sandage 1980) and a small offset is seen in these data between the atomic and molecular gas. Seven molecular clouds lie on or near this arm (MC7, MC11, MC13, and MC16-19). For six of these clouds the HI emission peak lies downstream (i.e., towards the outer edge of the arm) of the molecular gas. The direction of this offset, downstream from the molecular

clouds, suggests that it is the atomic gas that is formed from the molecular gas in the spiral arm.

The close association between the three phases of the interstellar medium, combined with the observed offset between the molecular and atomic gas, suggests that the atomic gas has recently been produced via photo-dissociation of molecular hydrogen by high-mass stars. We would thus expect to find the HI emission lying between the molecular and atomic gas peaks. An opposing scenario, in which atomic gas condenses in the arms to form molecular clouds that then forms stars, would produce CO peaks lying between the Hα and HI peaks. This scenario is ruled out if one accepts the systematic HI-CO offset as evidence of streaming motions. However it is of interest to examine the spatial distribution of all three phases to see if we can find additional evidence for the density wave scenario.

Five of the seven clouds in the southern arm have Hα emission. For MC16 and MC17 the three emission peaks are coincident and thus consistent with either scenario. The cloud MC18 has the CO peak lying between the other two gas peaks, while MC19 has a strong Hα peak offset from the line between the CO and HI peaks and a weak Hα peak lying directly between the two gas peaks. MC13 shows no alignment between the three emission peaks. Thus the Hα emission does not provide any additional evidence for the spiral density wave theory.

Assuming that gas passes through the spiral pattern from the inside of the arm to the outside, the offsets of the HI and CO peaks suggest that the dominant mechanism operating to shift gas from one phase of the interstellar medium to another in the southern spiral arm is photo-dissociation and ionization of molecular gas by radiation from high-mass stars. In particular, the molecular

clouds are not condensing directly out of clouds of atomic hydrogen as the gas enters the spiral arms. This situation is similar to that in the grand-design spiral galaxy M51 (Vogel, Kulkarni, and Scoville 1988). A comparison of the velocities of the atomic and molecular gas in the vicinity of the spiral arm might provide more conclusive evidence regarding the density wave hypothesis.

V. Is the Atomic Gas Near Molecular Clouds Produced by Photo-dissociation?

The amount of atomic hydrogen produced through photo-dissociation of molecular hydrogen by high-mass stars can be calculated if the mean density of the clouds and the numbers and masses of the stars are known. The number of high mass stars can be obtained from the Hα flux (Section III) and the average cloud density can be calculated from their masses and radii. Photo-dissociation of molecular hydrogen is a line-absorption process and thus is more complicated than the classical Stromgren sphere analysis for ionization of atomic hydrogen. Most analyses (cf. Hollenbach, Werner, and Salpeter 1971; van Dishoeck 1987) focus on the problem of diffuse clouds embedded in the interstellar radiation field, with the aim of estimating the column density required to form molecular hydrogen in the center of the cloud. The problem of interest here is how much atomic hydrogen can be produced by a group of hot stars embedded in a dense molecular cloud.

The effect of hot stars on nearby molecular gas has recently been studied in some detail by van der Werf (1989). In his treatment, the total hydrogen density is assumed constant and the fraction of molecular gas at a distance r from the star is

$$f(r) \equiv \frac{2n_{H_2}(r)}{n} = \left[\frac{9.73 \times 10^5 \chi}{n}\beta_l(\tau_l)\beta_c(\tau_c) + 1\right]^{-1} \qquad (2)$$

where n_{H_2} and n are the volume density of molecular hydrogen and hydrogen

nuclei (HI + $2H_2$) in cm^{-3}, respectively, χ is the energy density of the star at 1000 Å in units of the local Galactic interstellar radiation field (2×10^{-8} photons cm^{-2} s^{-1} Hz^{-1} (Habing 1968)) evaluated at the edge of the Stromgren sphere, $\beta_l(\tau_l)$ is the attenuation in the line, and $\beta_c(\tau_c)$ is the continuum attenuation. A grain temperature of 30 K was assumed. For molecular hydrogen column densities between 10^{17} and 10^{20} cm^{-2}, the line attenuation is independent of the velocity width of the cloud,

$$\beta_l(\tau_l) = \frac{7 \times 10^5}{\sqrt{N_{H_2}}} \tag{3}$$

where N_{H_2} is the molecular hydrogen column density in cm^{-2}. The continuum attenuation is

$$\beta_c(\tau_c) = e^{-3 \times 10^{-21} N} \tag{4}$$

where $N = nr$ is the total hydrogen column density.

The mass of atomic hydrogen in the region in which both atomic and molecular hydrogen exist is given by

$$M_{HI} = 4\pi m_H \int_{R_s}^{R} n_{HI}(r) r^2 dr \tag{5}$$

where R_s is the radius of the Stromgren sphere. Now $n_{HI} = n - 2n_{H_2} = n(1-f)$, so the integral in Equation (5) is given by

$$\int_{R_s}^{R} n_{HI}(r) r^2 dr = n \int_{R_s}^{R} (1 - f(r)) r^2 dr \tag{6}$$

To take out the dependence of Equation (2) on N_{H_2}, we define $\overline{f}$ such that

$$N_{H_2}(R) = \int_0^R n_{H_2}(r) dr = n \int_0^R f(r) dr/2 \equiv \overline{f} n R/2 \tag{7}$$

giving

$$\overline{f} = \frac{1}{R} \int_0^R f(r) dr \tag{8}$$

Substituting for β_l, β_c, and N_{H_2} in Equation (2) and integrating the result we obtain an expression relating $\overline{f}$ and R,

$$\overline{f}(R) = \frac{1}{R}\int_0^R \left[\frac{9.64\times10^{11}\chi}{n^{1.5}\sqrt{\overline{f}(r)}}\frac{e^{-3\times10^{-21}nr}}{\sqrt{r}} + 1\right]^{-1} dr \qquad (9)$$

where r is measured from the edge of the Stromgren sphere.

Rather than expressing Equation (9) as a partial differential Equation and producing an exact solution to the function $f(r)$, we chose instead to evaluate the integrals for $\overline{f}$ and M_{HI} in thin shells across which $f(r)$ was assumed to vary, but $\overline{f}$ would remain approximately constant. For given values of n and χ, $\overline{f}$ was incremented in steps of 0.001 and the radius R_i that satisfied Equation (9) was found for each $\overline{f}_i$, using $(\overline{f_{i+1}} + \overline{f_i})/2$ instead of $\overline{f}(r)$ in the right-hand side of Equation (9). The contribution of this shell to the atomic hydrogen mass was calculated by integrating Equation (6) between R_i and R_{i+1}, again using $(\overline{f_{i+1}} + \overline{f_i})/2$ instead of $\overline{f}(r)$ in Equation (6). This process was continued until $f(r)$ was greater than 0.95.

In order to calculate the atomic hydrogen mass produced by a given HII region, the Stromgren radius and the ultraviolet radiation energy density produced by the stars in the HII region must be known. Adopting the modified Miller-Scalo initial mass function (Kennicutt 1983; Chapter 3) and using the scaling between Hα luminosity and the total mass in stars more massive than 10 $M_\odot$ given by Kennicutt (1988), we obtain the relation between Hα luminosity and numbers of stars per mass bin given in Table 2. The excitation parameters u and the stellar flux scaling A, where the ultraviolet flux χ at a distance R from the star is $\chi = AR^{-2}$, are given for individual stars in Table 2 and are averages obtained from the more detailed table given by van der Werf (1989). The mass ranges corresponding to each range of spectral type were estimated from Humphreys and McElroy (1984). For an individual star, the Stromgren radius is given by

$R_s = un^{-2/3}$, where u is proportional to the cube root of the number of Lyman continuum photons and absorption of photons by dust is ignored. For a group of stars, the Stromgren radius is $R_s = n^{-2/3}\sqrt[3]{\sum_i u_i^3}$ and the ultraviolet flux at the Stromgren radius is $\chi = \sum_i A_i R_s^{-2}$.

The function $f(r)$ is plotted for a range of hydrogen densities and Hα luminosities in Figure 2, while the photo-dissociated HI mass is plotted as a function of these parameters in Figure 3. The mean hydrogen nuclei density in individual clouds was calculated from the molecular mass using the expression (obtained from the observed relations between mass, velocity width, diameter, and density in Chapter 4) $n = 300/\sqrt{M_{mol}/10^5\ M_\odot}$ cm^{-3}, where M_{mol} is the molecular mass in M$_\odot$. The extinction-corrected Hα fluxes of the individual clouds listed in Table 3 were used to calculate the amount of atomic hydrogen produced by the HII regions. These values were compared with the amount of HI observed in the peaks close to the molecular clouds, subtracting off the mean HI column density in the map (4.25×10^{20} cm^{-2}). These calculations show that the photo-dissociation model can only produce the observed HI excesses if hydrogen nuclei densities within the clouds are a factor of 1-7 smaller than the calculated mean densities. Densities $n_H \sim 40 - 160$ cm^{-3} are required to bring the model results into agreement with the observations.

The model calculations suggest that mean hydrogen densities calculated from cloud masses and radii may not representative of the gas density in large volumes of the cloud. For example, if a molecular cloud consisted of many small, dense clumps with more diffuse gas occupying a much larger volume, the typical hydrogen density seen by the dissociating photons would be significantly smaller. If 10% of the volume of a cloud was made up of clumps with densities eight times the overall mean density, the density in the remaining 90% of the cloud

would be only one quarter of the mean density. Thus if the M33 molecular clouds are sufficiently clumpy, the photo-dissociating radiation from the high mass stars is sufficient to produce the atomic gas peaks seen near the molecular clouds. There exists much evidence in our own Galaxy that molecular clouds are clumped on many spatial scales, so this scenario for molecular clouds in M33 is not unreasonable.

If the calculated mean hydrogen densities *are* representative of most of the volume of the cloud, the photo-dissociating radiation from massive stars is not sufficient to produce the atomic gas seen near the molecular clouds. With only 5-25% of the observed atomic excess explained by photo-dissociation, the rest of the atomic gas may be in atomic mantles shielding the molecular clouds from the general (normal) interstellar radiation field. The expected HI column density from these mantles can be estimated by assuming that each cloud is surrounded by a transition zone corresponding to one magnitude of visual extinction, which corresponds to a hydrogen nuclei column density of 2×10^{21} (Bohlin, Savage, and Drake 1978). Across this transition zone the composition will gradually change from purely atomic at the outer edge to mostly molecular at the inner edge, so we assume that half the total column density is in the form of atomic hydrogen. Then the expected HI surface density is given by

$$N_{HI} = \int_{R_l}^{R_u} N_c(R) 4\pi R^2 2 \times 10^{21} dR \qquad (10)$$

where $N_c(R)$ is the surface density of molecular clouds of radius R, R_u and R_l are the upper and lower radius cutoffs to the molecular cloud distribution, respectively, and the 10^{21} cm^{-2} HI shielding layer lies on both sides of the cloud.

We can constrain $N_c(R)$ using single dish CO measurements of the total surface density of molecular gas, N_{H_2}, since

$$N_{H_2} = \int_{R_l}^{R_u} N_c(R)(4\pi/3) R^3 n_{H_2}(R) dR \qquad (11)$$

Comparing Equations (10) and (11) reveals that for $n_{H_2}(R) = 200(20\,pc/R_{pc})$ (Chapter 4) the expected HI surface density is independent of (i) R_u, (ii) R_l, and (iii) the assumed form of $N_c(R)$. The average single dish flux within the half power beam width in the fields observed with the interferometer is 51 Jy km s^{-1} (Chapter 4, Table 4). Correcting for the single dish beam response by scaling the flux up by a factor of 1.4 (Chapter 2) and correcting for the inclination, we obtain a mean H_2 column density perpendicular to the plane of the galaxy of 4.6×10^{20} H_2 cm^{-2}. Thus the expected average HI column density is 5×10^{20} cm^{-2}, in good agreement with the mean HI column density in the central $4'$ radius of M33. Thus we suggest that the mean HI column density in the inner kiloparsec of M33 is due to atomic mantles surrounding molecular clouds, but that these mantles do not explain the atomic gas peaks found near the molecular clouds.

Another possibility is that the HI clumps are not due to photo-dissociation but rather are large agglomerations of atomic gas that are forming molecular clouds. However, this scenario requires the gas near the southern spiral arm be streaming out of the arm rather than into it. While this scenario may explain the large clump of atomic gas associated with MC35, it is unlikely to be the dominant mechanism for clouds near the southern spiral arm. A final possibility is that the atomic gas clouds are separate structures not physically related to the molecular clouds. However, this cannot explain why the atomic and molecular clouds are *always* found in such close physical proximity.

Thus we suggest that the atomic gas in the inner kiloparsec of M33 can be explained by two dominant phases, both associated with molecular clouds: atomic gas mantles and dissociation-product atomic gas. The atomic gas mantles surround all molecular clouds and form a transition zone in which the molecular gas

is building up sufficient column density to be self-shielding. High-mass stars that have recently formed in molecular clouds photo-dissociate molecular hydrogen to produce large atomic gas clouds that may recombine to form molecular gas once the high-mass stars die or drift out of the cloud. One striking result of this model is that the observed atomic gas distribution can be entirely accounted for by these two atomic components both associated with molecular clouds, which leaves no place for a large mass contribution from a diffuse HI component in the inner kiloparsec of M33. Observed correlations between HII regions and regions with high atomic gas densities (Viallefond and Goss 1986) are then explained by both components being intimately related to the molecular clouds.

VI. Conclusions

The data from Chapter 4 has been combined with previously published HI maps and new Hα data to study the effects of spiral structure on the interstellar medium and nature of the cycle between the atomic and molecular gas. The main results are listed below.

(1) Roughly two-thirds of the molecular clouds are currently undergoing high-mass star formation as indicated by Hα emission. Some of the clouds are forming stars sufficiently vigorously that they contain several of the most massive O5 stars. The inferred high-mass star formation rates range from 5×10^{-6} to 5×10^{-4} $M_\odot$ yr^{-1}, with a total mass of stars more massive than 10 $M_\odot$ from 10-1200 $M_\odot$. The remaining clouds may either not be forming high-mass stars at this time or the stars may be heavily obscured. Upper limits on the time scales for gas depletion in the individual clouds are 4×10^8 to 2×10^{10} yrs, assuming the clouds are only forming high-mass ($M > 10$ $M_\odot$) stars.

(2) Comparison of the CO, HI, and Hα emission peaks reveals that these three phases of the interstellar medium are always found in close proximity. There

is a systematic offset between the molecular and atomic gas peaks in the vicinity of the massive southern spiral arm that we interpret as being due to streaming motions as the material enters a spiral density wave. The streaming motions indicated by the relative offset of the HI and the CO peaks are inconsistent with the picture in which the HI condenses in the arms to form the molecular clouds.

(3) The proximity of the Hα, CO, and HI emission peaks, combined with the offset between the HI and CO peaks near the southern spiral arm, suggests that the atomic gas is formed via photo-dissociation of the molecular gas by recent high-mass star formation. The amount of atomic gas that can be formed by high-mass stars in the cloud is calculated from the Hα emission and a simple model for the photo-dissociation of molecular hydrogen. If we assume that the mean density in most of the cloud volume is reduced by roughly a factor of four from the overall cloud density, then the photo-dissociating radiation from the high mass stars is sufficient to produce the atomic gas peaks near the molecular clouds.

(4) An analysis of the amount of atomic hydrogen in atomic mantles shielding the molecular clouds from the normal interstellar radiation field reveals that the mean atomic hydrogen column density observed in the inner 8′ of M33 may be entirely due to these atomic mantles. Thus in this region of M33, the observed HI column density may be explained by two components, dissociation-product atomic hydrogen and atomic mantles around molecular clouds, both of which are closely associated with molecular clouds. In particular, there remains little room to include a diffuse HI component (independent of the dense molecular clouds) in this region of the galaxy.

TABLE 1

High-Mass Star Formation Rates

Field ID	SFR ($M_\odot$ yr^{-1})	$M_{stars>10M_\odot}$ ($M_\odot$)	Number of O5 Stars	Gas Depletion Time (yr)	Previous HII Region ID[a]
MC1-4[b]	4.7×10^{-4}	1200	5	1.4×10^{9}	93,99
MC16-19[b]	3.6×10^{-4}	910	4	1.6×10^{9}	87
MC10	5.6×10^{-5}	140	...	3.9×10^{9}	16
MC13	2.5×10^{-4}	630	3	8.0×10^{8}	4
MC20	1.4×10^{-4}	340	1	3.3×10^{9}	79,Z171
MC28	4.8×10^{-6}	10	...	1.7×10^{10}	...
MC29	1.4×10^{-5}	40	...	2.1×10^{10}	75
MC30	2.2×10^{-5}	50	...	4.5×10^{9}	76
MC31	1.0×10^{-5}	30	...	1.6×10^{10}	Z138
MC35	1.7×10^{-4}	440	2	4.0×10^{8}	37
MC38	1.7×10^{-5}	40	...	3.5×10^{9}	...

[a] HII region identifications from Boulesteix *et al.* (1974) and Courtes *et al.* (1987).

[b] These regions are sufficiently confused that the Hα emission due to individual clouds cannot be separated.

TABLE 2

Stellar Parameters for O and Early B Stars

Spectral Type	Mass ($M_\odot$)	u (pc cm^{-2})	A (NLTE)	Number of Stars
O4-5.5	70	100	10000	$10L_{39}$
O6-7.5	40	50	3300	$18L_{39}$
O8-9.5	25	32	1400	$28L_{39}$
B0-1	15	10	300	$71L_{39}$
B2-3	9	2	50	$166L_{39}$

TABLE 3

Amount of Photo-Dissociated Atomic Hydrogen

Field ID	L_{39}	n_H(obs.) (cm^{-3})	M_{HI}(model) ($M_\odot$)	n_H(fit) (cm^{-3})	M_{HI}(fit) ($M_\odot$)	M_{HI}(obs.) ($M_\odot$)
MC1-4[a]	0.33	250	7600	120	23000	21000
MC16-19[a]	0.25	270	6500	50	80000	72000
MC10	0.039	200	2900	160	4300	4300
MC13	0.18	220	7000	50	66000	72000
MC20	0.094	140	10000	110	15000	15000
MC28	0.0034	340	800	150	3900	3500
MC29	0.011	180	2000	110	5100	4800[b]
MC30	0.014	300	800	110	5100	4800[b]
MC31	0.0083	240	1200	40	30000	26000
MC35	0.12	360	2500	50	51000	55000
MC38	0.011	390	500	150	2900	2900

[a] These regions are sufficiently confused that the Hα emission due to individual clouds cannot be separated.

[b] These two clouds share a single atomic gas peak and so the HI mass was divided equally between them to obtain the best fit model density.

Figure Captions

Fig. 1 – Integrated intensity maps of each of the regions observed in CO (solid contours) are combined with the high-resolution HI Westerbork map (dashed contours; Deul and van der Hulst 1987) and overlaid on grey-scale plots of the Hα emission. The HI contours start at 5×10^{20} cm^{-2} and increase in units of 10^{20} cm^{-2}. The CO contours are scaled logarithmically and the first CO contour level is 2.0 Jy beam^{-1} km s^{-1} unless noted otherwise. (a) Region 1. The first CO contour level is 5.0 Jy beam^{-1} km s^{-1}. (b) Region 2. (c) Region 3. (d) Region 4. (e) Region 5. The first CO contour level is 1.0 Jy beam^{-1} km s^{-1}. (f) Region 6.

Fig. 2 – The molecular gas fraction is plotted as a function of radius for a range of densities and Hα luminosities, where $R = 0$ is the edge of the Stromgren sphere. The solid line corresponds to a density of 400 cm^{-3}, the dashed line to 200 cm^{-3}, the dot-dashed line to 100 cm^{-3}, and the dotted line to 50 cm^{-3}. (a) Hα luminosity of 5×10^{36} erg s^{-1} ($L_{39} = 0.005$). (b) $L_{39} = 0.01$. (c) $L_{39} = 0.05$. (d) $L_{39} = 0.1$. (e) $L_{39} = 0.33$.

Fig. 3 – The total mass of atomic hydrogen produced via photo-dissociation is plotted as a function of density for several Hα luminosities. The solid line is for an Hα luminosity $L_{39} = 0.33$, the dashed line for $L_{39} = 0.1$, the dot-dashed line for $L_{39} = 0.05$, the dotted line for $L_{39} = 0.01$, and the three dot-dashed line for $L_{39} = 0.005$. The highest luminosity corresponds to an HII region that is luminous enough to contain several O5 stars, while the lowest corresponds to a single B0 (10 $M_\odot$) star.

Figure 1a

CO, HI, and Hα Distributions Near Molecular Clouds

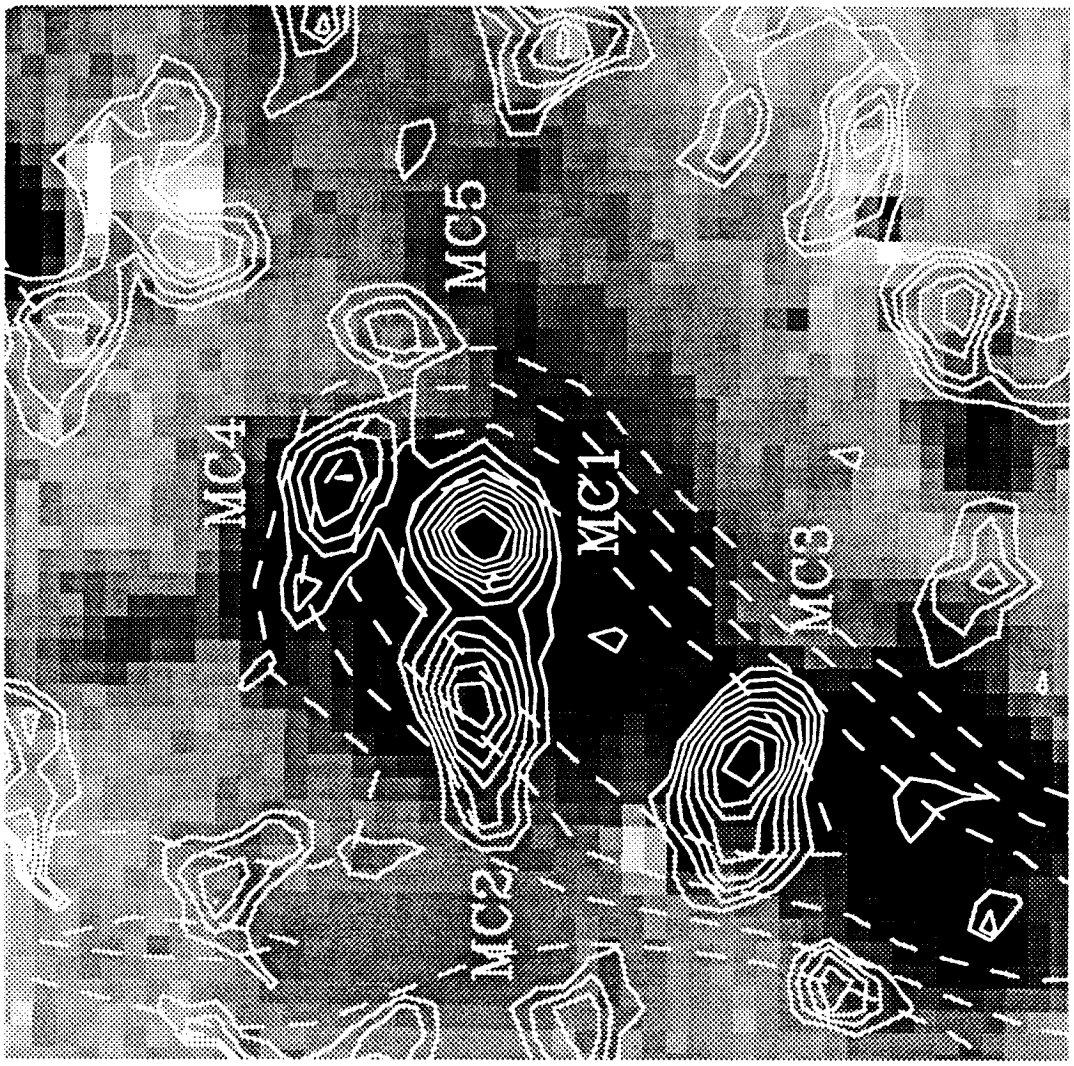

Figure 1b

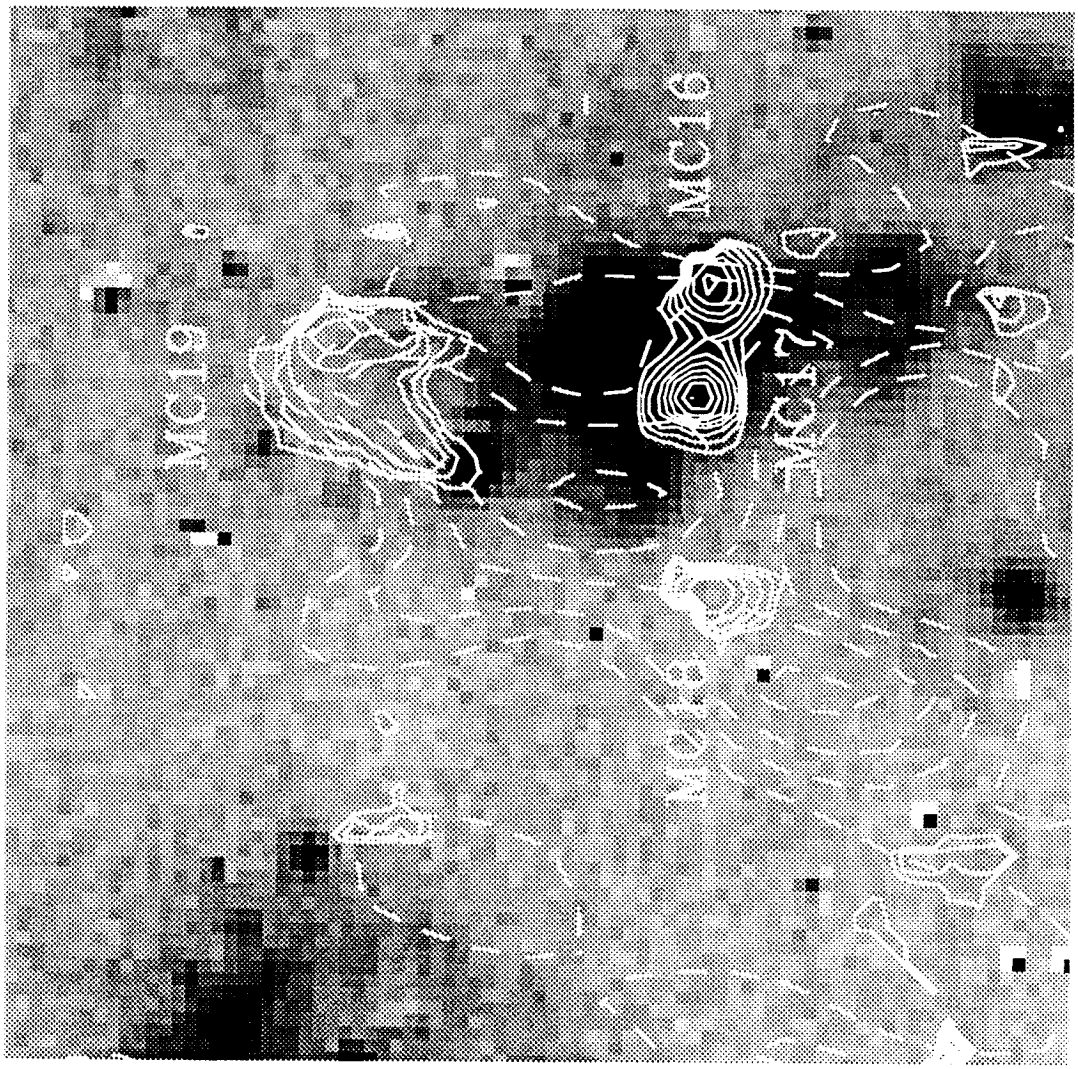

Figure 1c

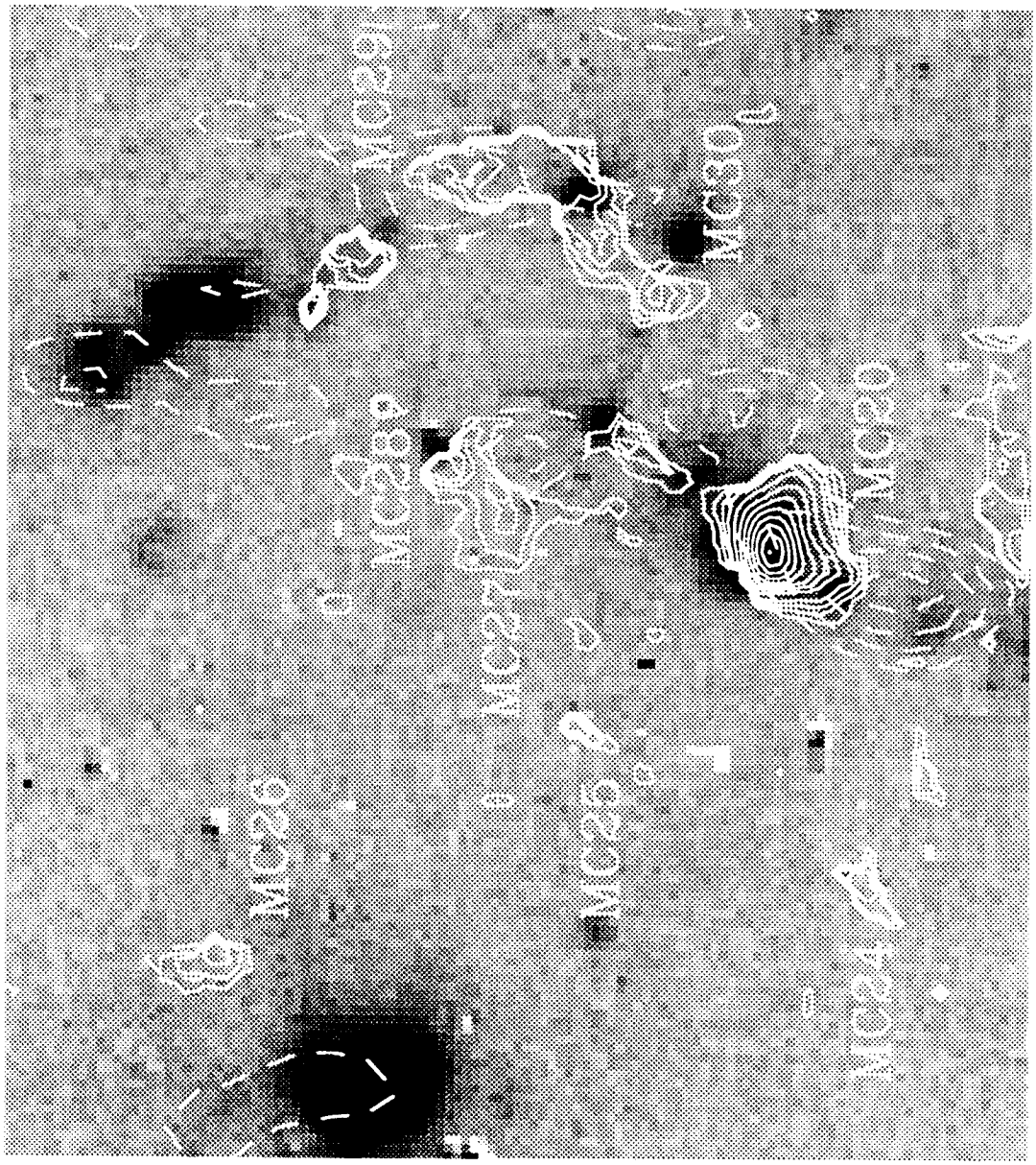

Figure 1d

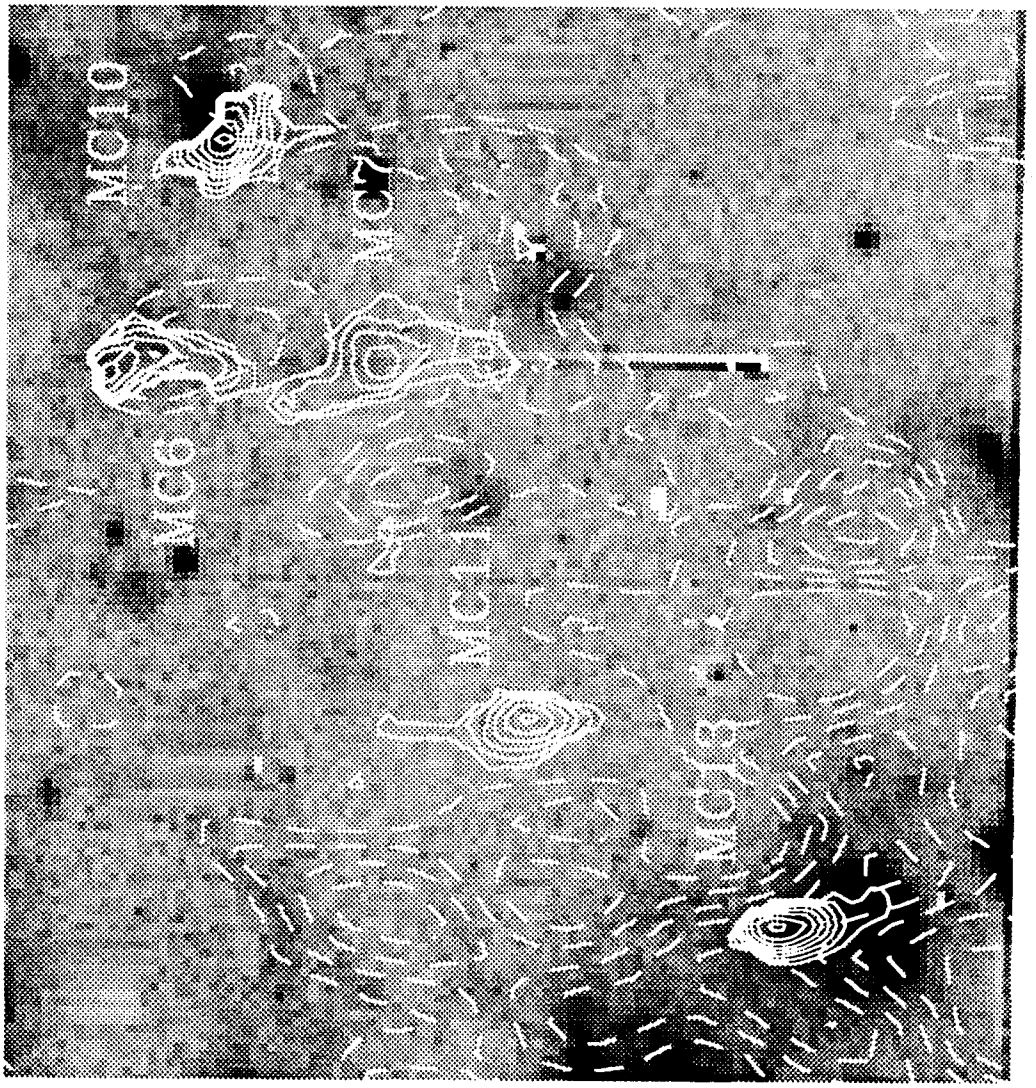

Figure 1e

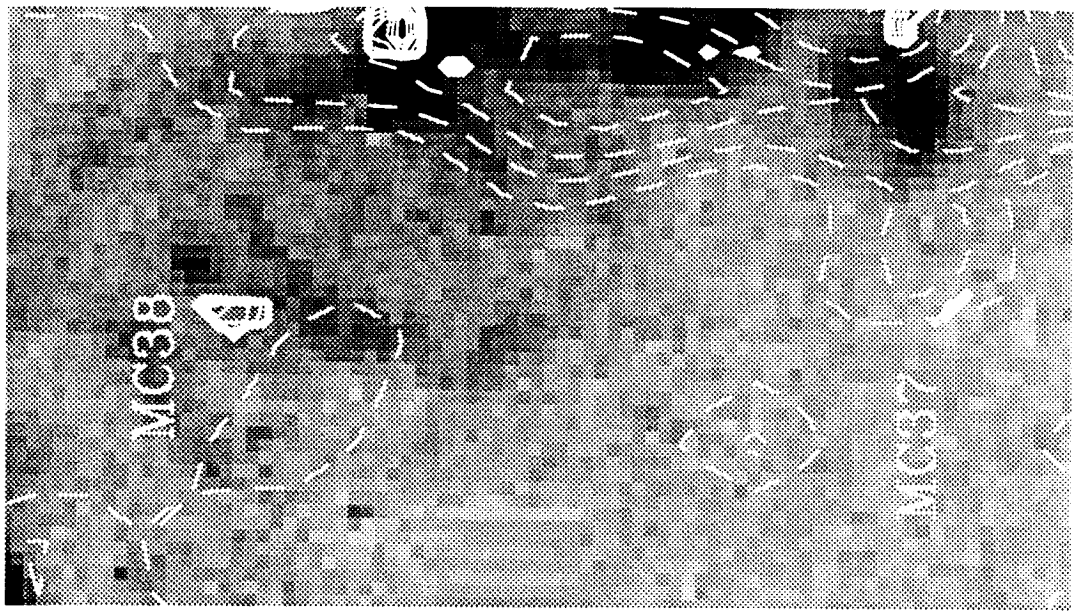

Figure 1f

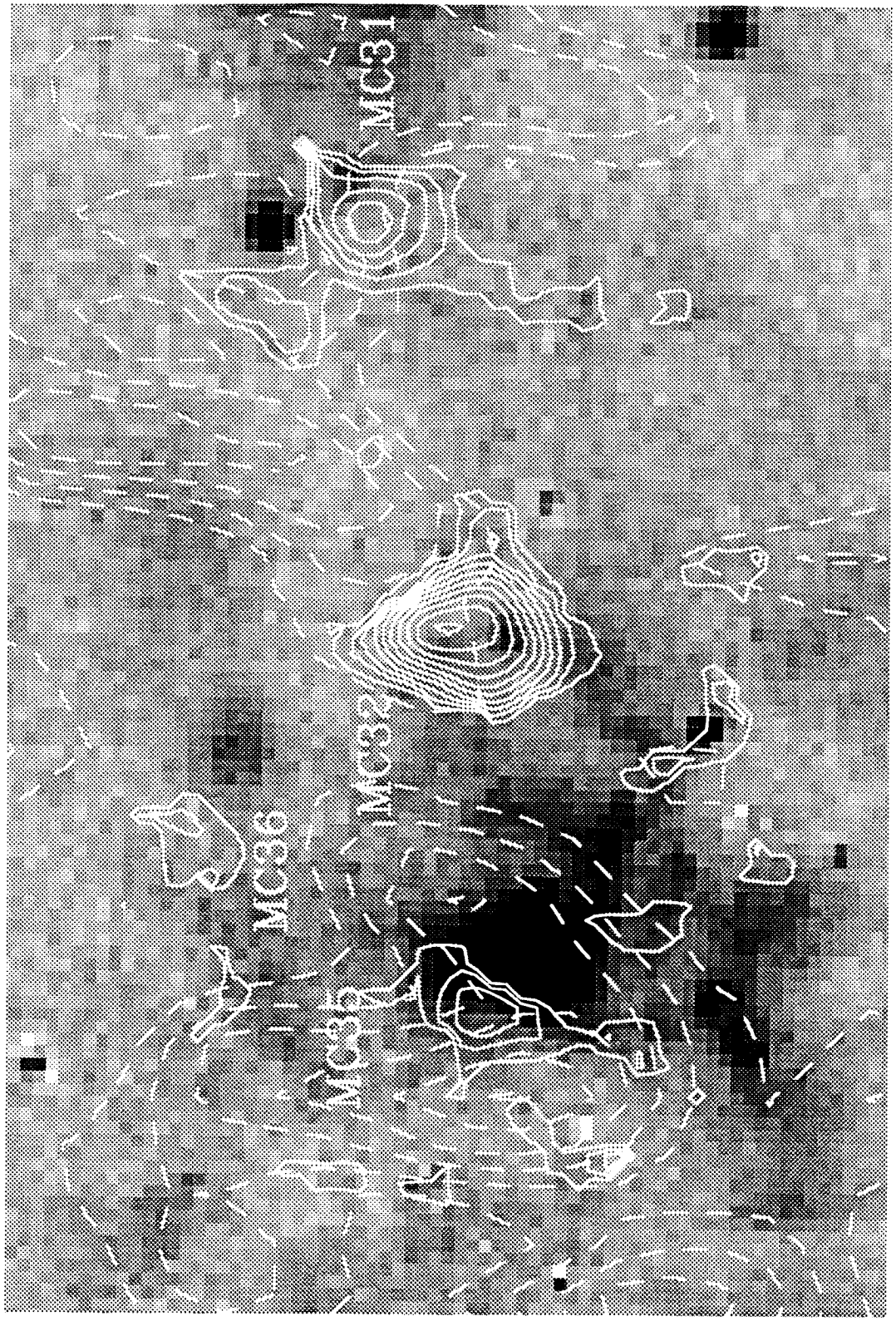

Figure 2a-d

Molecular Gas Fraction as a Function of Radius

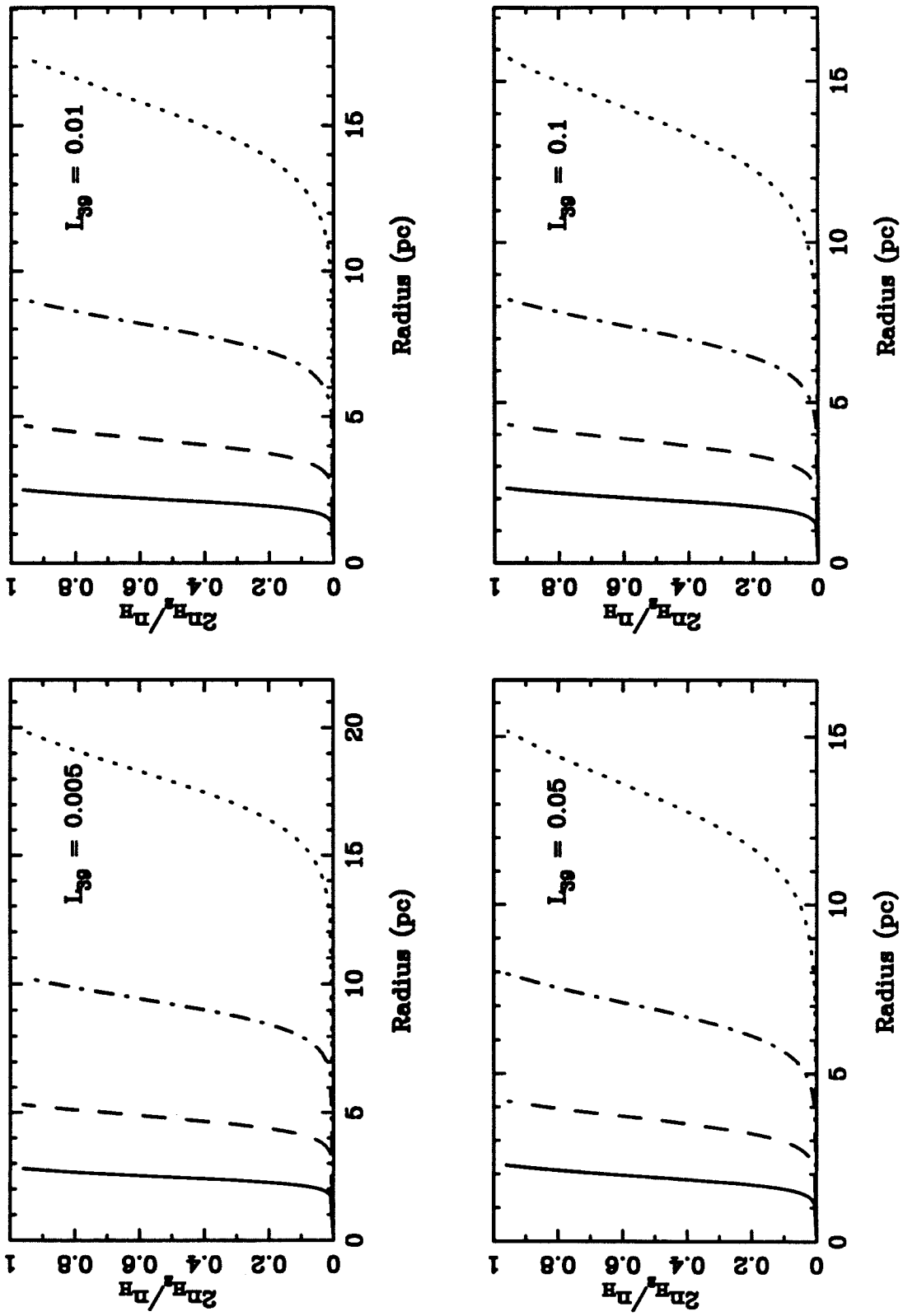

Figure 2e

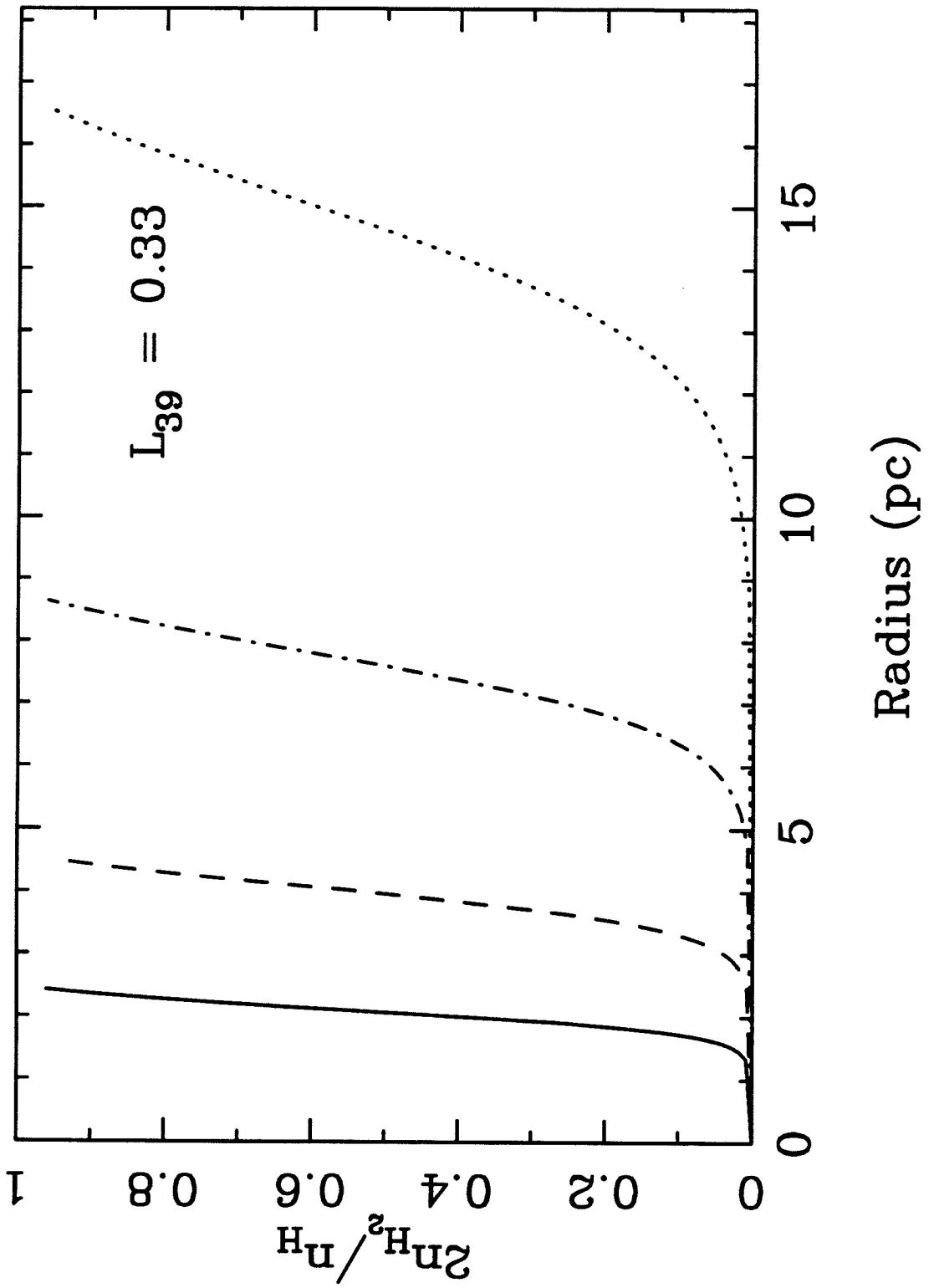

Figure 3

Total HI Mass as a Function of Density and HII Luminosity

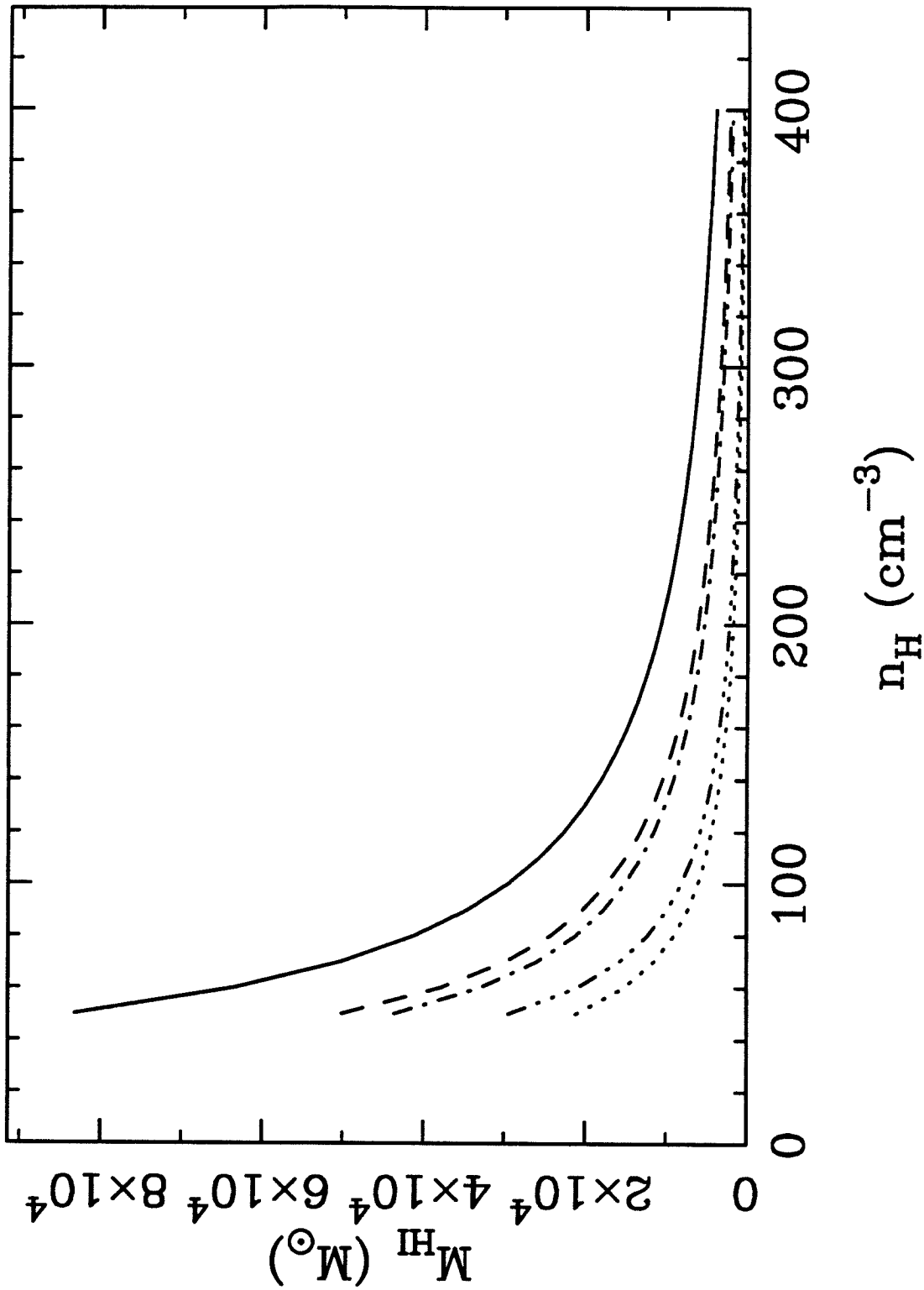

CHAPTER 6

High-Mass Star Formation in M33

I. Introduction

Detailed information on the star formation properties of different regions of a single galaxy can be used to shed light on the star formation process in more distant galaxies. By comparing arm and interarm regions we can determine whether spiral arms have a high star formation efficiency or whether the arms have a high star formation rate due to a higher surface density of molecular gas. Whether forming an association destroys the parent cloud may be constrained by comparing the spatial distribution of associations with the molecular and atomic gas distributions. Finally, observational methods used to measure the high-mass star formation rate in distant galaxies, such as Hα and far-infrared luminosities, may be compared directly with the rate obtained from number counts of blue stars. This comparison is important since neither the Hα nor the far-infrared luminosity is as physically direct as the simple star count method.

Recent studies either have limited spatial resolution in the CO observations or ignore the molecular component altogether. The ratio of the Hα or far-infrared luminosity to the molecular gas mass is often used to trace the high-mass star formation efficiency. A recent study of 200 spiral galaxies finds no evidence for a dependence of these ratios on the morphological type of the galaxy (Young *et al.* 1990). No radial variation in these ratios were found in NGC 6946 (Tacconi and Young 1986), although the ratios are higher in the spiral arms (Tacconi and Young 1990). Such studies can only look for variations in star formation properties on kiloparsec scales. Recent work on M31 and M33 using IRAS and

HI data has been reviewed in Chapter 1. Neither study included the molecular gas distribution.

All the observations are now available for a complete study of high-mass star formation in M33. The data presented in previous chapters are combined in this chapter to obtain high-mass star formation rates and efficiencies and to look for variations in these quantities at different positions in the inner disk of M33. Star formation rates and efficiencies are calculated using calibrated Hα data in Section II. The properties of the far-infrared emission in the inner disk obtained from high-resolution IRAS maps are discussed in Section III. The star formation rates obtained from far-infrared and Hα luminosities are compared with those obtained from optical photometry in Section IV. The relationship between OB associations and molecular clouds is discussed in Section V and the paper is summarized in Section VI.

II. Star Formation Rates and Efficiencies in M33

The high-mass star formation rate can be obtained from the Hα luminosity (Kennicutt 1983). However, differential or internal reddening of the HII regions may result in an underestimate of the star formation rate. Also, the observed emission must be corrected for the contribution of [NII] emission if the filter is not sufficiently narrow. Finally, extrapolating from high-mass to total star formation rates is quite uncertain because of a strong dependence on the assumed initial mass function. The details of the reduction and calibration of the Hα data are given in Chapter 5.

The high-mass star formation rate is

$$SFR(\geq 10\,M_{\odot}) = L_{39}/702 \qquad (1)$$

where L_{39} is the H_{α} luminosity in units of 10^{39} erg s^{-1} and the star formation rate is in solar masses per year (Kennicutt 1983). Adopting the modified Miller-

Scalo initial mass function (Kennicutt 1983; Chapter 3), the total star formation rate is

$$SFR(\geq 0.1\,M_{\odot}) = L_{39}/112 \qquad (2)$$

The total reddening-corrected Hα luminosity for the $\sim$ 5 kpc^2 of M33 covered by the single dish CO map (Chapter 2) is 4.8×10^{39} erg s^{-1}, which corresponds to a high-mass star formation rate of 0.007 M$_{\odot}$ yr^{-1} and a total star formation rate of 0.04 M$_{\odot}$ yr^{-1}. The total amount of molecular gas is 3.4×10^7 M$_{\odot}$, which gives a gas depletion time (the mass of molecular gas divided by the total star formation rate) of 9×10^8 yr.

The single dish CO map is overlaid on the continuum-subtracted Hα image in Figure 1. The molecular hydrogen masses, Hα luminosities, star formation rates, and gas depletion time scales are given in Table 1 for each of the six molecular gas complexes identified in Chapter 2. The depletion times vary by a factor of six and thus some regions of the galaxy are turning gas into stars much more efficiently than other regions. The southern spiral arm contains three of the molecular complexes (2-4). These three complexes contain one-third of the molecular gas and one-quarter of the Hα luminosity of this region of the galaxy. Thus on average the star formation efficiency of the southern spiral arm is similar to the star formation efficiency of the inner disk and *the large amounts of star formation occurring in this arm are simply due to the presence of large amounts of molecular gas.*

Because of the flocculent spiral structure of M33, it is difficult to precisely delineate arm and interarm regions. Instead of defining arm boundaries, the CO map was divided into areas with and without CO emission $>$ 1.5 K km s^{-1} and the star formation properties of these two areas were analyzed. The high-mass star formation rate for regions with strong CO emission is 0.005 M$_{\odot}$ yr^{-1}, while

regions without much CO emission cover roughly the same area on the galaxy and have a high-mass star formation rate of 0.002 $M_\odot$ yr^{-1}. However, the relative gas depletion time scales for the two regions agree to within 15% if the molecular gas mass in the weak-lined regions is calculated assuming an average emission of 1 K km s^{-1} (2σ). (The gas depletion time scale for the low-emission regions is thus an upper limit to the true gas depletion time.) Thus in M33 the star formation efficiency in the interarm regions is the same as the star formation efficiency in regions on the arms and in the nucleus.

III. Dust in the Inner Disk of M33

The intrinsic resolution of the IRAS observations ranges from 1′ to 7′ (Deul 1989). Higher resolution can be obtained using deconvolution techniques. A total of six independent scans of M33 were obtained during the mission, of which four were oriented in the same direction. The four scans were median filtered in groups of three and the resulting maps deconvolved using a Richardson-Lucy technique (Richardson 1972, Lucy 1974; details of the IRAS application are given in Aumann, Fowler, and Melnyk 1990). The four median-filtered maps at 60 and 100 μ agreed very well. We chose to use maps produced after only 10 iterations of the deconvolution process, since for more iterations it was hard to see how the deconvolution algorithm arrived at the final structure from the original raw maps. The final maps and the resulting 60/100 μm color map are shown in Figure 2 for the inner 8′ x 8′ of M33. The final resolution is 1.4 x 0.9′ at 60 μm and 2.2 x 1.4′ at 100 μm.

The far-infrared properties of M33 in the region covered by the single dish CO map are used to measure the properties of the dust and the gas-to-dust ratio. The flux from NGC 595, which is visible in the northwest corner of Figure 2, is excluded since it was not mapped in CO. For the region of M33 covered by the

CO map, the 100 μm flux is 173 Jy and the 60 μm flux is 66 Jy. The total far-infrared luminosity from 42.5 to 122.5 μm is given by

$$L_{IR} = 6 \times 10^5 D^2 (2.58 f_{60} + f_{100}) \quad (3)$$

(Lonsdale *et al.* 1985; Thronson and Telesco 1986), where L_{IR} is in $L_\odot$, D is the distance to the galaxy in Mpc, and f_{60} and f_{100} are the 60 and 100 μm fluxes in Jy. The far-infrared luminosity of the central region of M33 is 1.3×10^8 $L_\odot$. Comparing this with the molecular hydrogen mass yields a value for the ratio of far-infrared luminosity to molecular hydrogen mass of 3.8 $L_\odot$ $M_\odot^{-1}$, slightly higher than the mean value (2.8 $L_\odot$ $M_\odot^{-1}$) obtained for giant molecular clouds in the Galactic disk (Scoville and Good 1989).

Adopting an emissivity law $Q \propto \nu^n$ with $n = 1$, the mean dust temperature obtained from the 60/100 μm color (Lonsdale *et al.* 1985) in this region of M33 is 33 K, with a peak value of 46 K and a minimum value of less than 25 K. The total mass of dust can be calculated from the 100 μm flux and the dust temperature, T_d, and is given by

$$M_d = 5 D^2 f_{100} (exp(144/T_d) - 1) \quad (4)$$

(Thronson and Telesco 1986), where M_d is in $M_\odot$. The mass of dust in this region of M33 is 4.2×10^4 $M_\odot$, which corresponds to a molecular gas-to-dust ratio of ~ 900 and a total gas-to-dust ratio of ~ 1300.

Gas-to-dust ratios were calculated for Galactic molecular clouds using their published far-infrared properties (Scoville and Good 1989). Dust masses were calculated from the temperatures, distances, and 100 μm fluxes using Equation (4) and compared to the published virial masses. The average gas-to-dust ratio is 1200 for seven molecular clouds that do not contain HII regions and 700 for the clouds with HII regions. If seven clouds with gas-to-dust ratios larger than

1500 are dropped from the sample, the mean gas-to-dust ratios are 600 and 400, respectively. Thus the gas-to-dust ratio in M33 is similar to the mean value for Galactic molecular clouds.

The Galactic gas-to-dust ratio obtained from extinction measurements is 100-150 (Hildebrand 1983). The disagreement between this value and the ratio calculated from IRAS data may be due either to an incorrect opacity law or to a significant contribution by cold dust to which the IRAS data is not sensitive. Varying the emissivity law changes both the dust temperature calculated from the 60/100 μm ratio and the value of Q at 100 μm. However, these two effects cancel each other out when n is changed by ± 1. Thus the most likely explanation for the discrepancy is the presence of considerable amounts of cold dust. Since dust in molecular clouds with HII regions is warmer than dust in clouds without much massive star formation, the gas-to-dust ratio for clouds with HII regions should be closer to the true value of $\sim$ 150 than the ratio for clouds without HII regions. In addition, the gas-to-dust ratio in M33 should be considerably higher than the true value since it is an average over both warm and cool regions. Thus the gas-to-dust ratios obtained from IRAS observations of the inner disk of M33 and of molecular clouds in the Galaxy are consistent with significant amounts of dust in M33 being contained in a cold component beyond the sensitivity range of the IRAS satellite.

The far-infrared emission can be used to estimate star formation rates (Thronson and Telesco 1986), but there are considerable uncertainties in this calculation. One potential problem is that a large contribution to the far-infrared emission may be made by cool dust not directly associated with recent star formation (Walterbos and Schwering 1987). Another uncertainty is the choice of the initial mass function. Thronson and Telesco adopt a Salpeter initial mass

function, which has a constant slope over the entire range of mass. To be consistent with the star formation rates calculated from Hα luminosities in Section II, we adopt the modified Miller-Scalo initial mass function, which gives a high-mass star formation rate of

$$SFR_{IR}(\geq 10\,M_{\odot}) = 9.2 \times 10^{-11} L_{IR} \tag{5}$$

and a total star formation rate of

$$SFR_{IR}(\geq 0.1\,M_{\odot}) = 6.3 \times 10^{-10} L_{IR} \tag{6}$$

where Equations (5) and (6) are in solar units. Thus the far-infrared emission in the inner disk of M33 corresponds to an OB star formation rate of 0.012 $M_{\odot}$ yr^{-1} and a total star formation rate of 0.08 $M_{\odot}$ yr^{-1}.

The far-infrared star formation rates are roughly twice as large as those calculated using the Hα fluxes. The relatively good agreement between the two star formation rates shows that M33 is different from M31 in the relative proportions of far-infrared emission due to cool and warm dust. If the amount of cool dust in M33 were similar to the amount in M31, the star formation rate obtained from the Hα emission would have been ten times lower than the rate estimated from the far-infrared emission. Instead, at least half of the far-infrared emission in the inner disk of M33 is directly related to recent star formation with the remainder presumably due to a cool cirrus component. This result is in good agreement with previous calculations for the entire disk of M33 (Deul 1989; Rice *et al.* 1990).

The far-infrared emission has been measured for each of the six molecular complexes by integrating the far-infrared flux over the area of the complex. The individual 100 μm fluxes are more uncertain than the 60 μm fluxes since the 100 μm map has a lower resolution than the CO map. The mean dust temperatures

and far-infrared luminosity are given for the six complexes in Table 2. Also given are the infrared luminosity to molecular gas mass ratio and the ratio of the Hα to infrared luminosity. In general, regions with lower dust temperatures have lower Hα to far-infrared luminosity ratios than regions with high dust temperatures. Thus regions with a low efficiency of high-mass star formation have lower mean dust temperatures. Star formation rates calculated for the individual complexes from both the far-infrared and the Hα luminosity generally agree to within a factor of two.

IV. High-Mass Star Formation Rates From BV Photometry

Measuring high-mass star formation rates using Hα or far-infrared luminosity requires models for the luminosity output of a star and assumptions about the shape of the initial mass function. For nearby galaxies a more direct method is possible, namely using optical photometry to determine the number of high-mass stars directly via star counts. The main difficulty with this method is that evolution along the main sequence occurs with increasing luminosity at constant color and thus the evolutionary tracks for stars of different masses overlap (Chapter 3). This results in uncertainties in the masses of individual stars on the main sequence of at least 50%. Despite the uncertainties, this method of estimating star formation rates is a more physically direct method and so it is interesting to compare global star formation rates measured in this way with those obtained from Hα or far-infrared luminosity.

The high-mass star formation rate is given by

$$SFR = \sum_i \frac{n_i m_i}{t_i} \qquad (7)$$

where n_i is the number of stars of mass m_i with main sequence lifetime t_i. Stars were assigned a mass by comparing their position in the color-magnitude diagram

with evolutionary tracks from Maeder and Meynet (1988) as described in Chapter 3. Corrections for incompleteness in the photometry and in the main sequence coverage (Chapter 3) increase the raw star formation rates by a factor of $\sim$1.5. The star formation rate is fairly insensitive to the blue B-V cutoff used to define the edge of the main sequence for $0 \leq B - V \leq 0.4$ mag.

The star formation rate is quite sensitive to the mean reddening, varying by a factor of two when the reddening is changed by ± 0.1 mag. Adopting a mean reddening of 0.3 mag (Chapter 3), the star formation rate in the region of M33 covered by the single dish CO map is 0.015 $M_\odot$ yr^{-1} for stars more massive than 20 $M_\odot$. Assuming a modified Miller-Scalo initial mass function, this corresponds to a star formation rate for stars more massive than 10 $M_\odot$ of 0.026 $M_\odot$ yr^{-1}. This is a factor of $\sim$ 3 higher than the star formation rate obtained from Hα emission for stars more massive than 10 $M_\odot$ and a factor of $\sim$ 2 higher than the rate obtained from the far-infrared luminosity. Given the factor of two uncertainties in the photometric masses, the agreement between the different methods is acceptable.

Although it is difficult to assign accurate masses to individual stars using photometry alone, it *is* possible to assign a minimum mass to stars on the main sequence. This is because a star of a given mass reaches a maximum V magnitude at the end of its main sequence evolution and then evolves very rapidly out of the main sequence band to redder colors. Thus we can place a reliable *lower* limit on the high-mass star formation rate using optical photometry (Chapter 3). The lower limit to the high-mass star formation rate for stars above 10 $M_\odot$ is 0.0042 ± 0.0018 $M_\odot$ yr^{-1}, where the uncertainty is due to an uncertainty in the mean reddening of ± 0.1 mag. The only correction is for incompleteness in the photometry, which increases the star formation rate by 10%. This lower limit

is consistent with star formation rates obtained from the Hα and far-infrared luminosities.

Thus the high-mass star formation rate derived from number counts of individual blue stars is in reasonable agreement with rates obtained using either the Hα or the far-infrared luminosities. Although the star count method is physically a more direct indicator of high-mass star formation, uncertainties in masses obtained from photometry alone limit the resulting accuracy in the star formation rate to no better than 50%. A more accurate comparison of the star formation rates will be possible only when spectra are obtained for a significant fraction of the blue stars in this sample.

V. OB Associations and Molecular Clouds

The masses of the OB associations given in Chapter 3 are compared with the masses of the molecular clouds given in Chapter 4 to determine the star formation efficiency required to form an OB association from a single molecular cloud. The masses of the OB associations in stars more massive than 20 $M_\odot$ range from 300 to 5000 $M_\odot$ with a mean mass of 600 $M_\odot$. Because of incompleteness in the photometry and in the coverage of the main sequence at the faint end, the total mass in stars above 20 $M_\odot$ is $\sim$ 1.6 times the observed masses. An initial mass function must be adopted in order to estimate the mass in low-mass stars. This procedure is uncertain since the cluster may be forming stars along the entire initial mass function or may be forming only high-mass stars. Assuming the cluster forms stars of all masses gives the maximum possible mass for the cluster and thus gives an upper limit to the required star formation efficiency.

Adopting the modified Miller-Scalo initial mass function (Kennicutt 1983), the amount of mass in stars more massive than 10 $M_\odot$ is 1.75 times the mass in stars more massive than 20 $M_\odot$. The total mass of the association is then

seven times the mass in stars more massive than 10 $M_\odot$. Thus the inferred total masses of the associations range from 6×10^3 to 10^5 $M_\odot$ with a mean of 1.2×10^4 $M_\odot$. The masses of molecular clouds in M33 range from 5×10^4 to 5×10^5 $M_\odot$ with a mean of 10^5 $M_\odot$. Comparing the masses of typical OB associations and molecular clouds implies a star formation efficiency of 12%. A large star formation efficiency of 20% is required to form the largest OB association from the largest molecular cloud.

Stars are born in a molecular cloud with some random velocity relative to the mean motion of the cloud due to the internal motions of the gas from which the star formed. It is interesting to compare the observed association diameters with the distance an individual star can travel during the lifetime of the association. In other words, is the association old enough for the stars to have diffused out to their present positions if they were all born within one molecular cloud? The radii of the associations range from 10 to 120 pc with a mean radius of 40 pc, while their ages range from 3.6×10^6 to 1.4×10^7 yr with a mean of 8×10^6 yr. The three-dimensional velocity dispersions of the clouds are 4-7 km s^{-1} (Wilson and Scoville 1990a) and a star moving at 5 km s^{-1} travels a distance of 50 pc in 10^7 yr. Thus the sizes of typical associations are consistent with the stars having diffused outward from a single cloud core region.

One possible exception to this simple picture is the largest association, which has an age of 4×10^6 yr and a radius of 120 pc. Assuming that stars are born with a random velocity of 7 km s^{-1} and form throughout a cloud with a radius of 40 pc, the radius of this association should only be 70 pc. The association is near the nucleus of the galaxy and thus has been spread out by differential galactic rotation, but this can only explain half the observed discrepancy. Another possibility is that this association is actually two associations that happen to lie

very close together. The brightest stars lie in two clumps on opposite edges of the association and the prominent Hα emission (see Figure 4) is confined to the northeast edge of the association. If the association is two separate associations, this would also resolve the problem of the large star formation efficiency required to form this association from a single molecular cloud.

The spatial distributions of OB associations and molecular clouds are compared in Figure 3. The positions of Wolf-Rayet stars are also included in this plot (Massey and Conti 1983; Massey *et al.* 1987). Half of the clouds more massive than 10^5 $M_\odot$ are found near an OB association. Four of these clouds lie along the northeast edge of the large OB association near the center of the galaxy. Three-quarters of all clouds lie near a group of at least three OB stars. These statistics are similar to what is found for the physical association of HII regions and molecular clouds (Chapter 5).

Out of the 24 Wolf-Rayet stars in this region, seven lie more than 75 pc away from the nearest OB association. Assuming that Wolf-Rayet stars have masses of at least 40 $M_\odot$ and hence ages of $< 5 \times 10^6$ yr, these stars would need velocities > 15 km s^{-1} in order for them to have formed in an association. This is unlikely and thus these Wolf-Rayet stars were probably formed in smaller groups of stars. Thus very massive stars do not form exclusively in large OB associations.

The positions of the OB associations are overlaid on a continuum-subtracted Hα CCD image in Figure 4. Roughly half of the associations show nearby Hα emission. One explanation for why so many associations do not contain HII regions is that the associations have drifted away from their parent molecular clouds and thus do not lie near any high-density gas. Another possibility is that the association has destroyed the original molecular cloud. In this case one might expect to see a hole in both the molecular and atomic gas distributions near the

association. Our ability to test these two cases is limited by the incomplete coverage of the inner disk with high-resolution CO observations.

OB associations are evenly distributed between regions of the galaxy with strong and weak CO emission. Thus no evidence is found for a correlation of the OB associations with peaks or holes in the molecular gas. This is in contrast to a recent study that found that OB associations tend to lie in small holes in the atomic gas distribution (Deul and den Hartog 1990). Unfortunately, the resolution of the CO map (200 pc) is insufficient to resolve structures as fine as the small HI holes ($\sim 40 - 100$ pc).

To compare the spatial distribution of the molecular gas and the blue stars at the same resolution, the blue star counts were binned to the resolution of the single dish CO map. A point-by-point comparison of the CO flux and blue star counts shows no correlation. However, the mean distance of a blue star peak from the nearest molecular peak is 45″, while the expected mean separation for a random distribution is 63±6″. Thus the peaks in the blue star counts and the molecular gas are correlated at the 3σ level, in the sense that they tend to be found closer together than would be expected for a random distribution. The separation vectors are randomly oriented and show no evidence for a strong global pattern. This result is similar to what is found for a comparison of the CO and HI peaks in Chapter 2.

VI. Conclusions

We have used optical, far-infrared, and millimeter-line data to study the properties of high-mass star formation in the nearby galaxy M33. The main results are summarized below.

(1) The Hα emission in this region of the galaxy corresponds to high-mass and total star formation rates of 0.007 and 0.04 $M_\odot$ yr^{-1}, respectively. The

star formation rates calculated from the 60 and 100 μm IRAS emission agree reasonably well with the rates calculated from Hα emission. Roughly half of the far-infrared luminosity is probably due to a significant cool dust component, in agreement with previous studies.

(2) The Hα and CO data have been used to measure the star formation efficiency for the inner disk of M33. The implied gas depletion time is 9×10^8 yr. The high-mass star formation efficiency in the molecular complexes and in the southern spiral arm is the same on average as the star formation efficiency in regions with very little CO emission. Thus the spiral arms in M33 are regions with high star formation rates, but *not* unusually high star formation efficiencies.

(3) The high-mass star formation rate has been estimated using number counts of individual high-mass stars. This rate is uncertain by a factor of at least 50% due to the degeneracy of stellar magnitudes and colors along the main sequence. A lower limit to the high-mass star formation rate obtained from these data is 0.0042 $M_\odot$ yr^{-1}, consistent with the rate obtained from Hα emission.

(4) A comparison of the masses of OB associations and molecular clouds reveals that a star formation efficiency of $\sim$ 10% is required to form an OB association from a single molecular cloud. Two-thirds of the molecular clouds more massive than 10^5 $M_\odot$ show evidence for recent high-mass star formation.

TABLE 1

Hα Luminosity of Molecular Complexes in M33

Complex	M_{H_2} ($M_\odot$)	$L_{H\alpha}$ (erg s^{-1})	$SFR(\geq 10M_\odot)$ ($M_\odot$ yr^{-1})	$SFR(\geq 0.1M_\odot)$ ($M_\odot$ yr^{-1})	Gas Depletion Time (yr)
1	3.9×10^{6}	5.4×10^{38}	7.6×10^{-4}	4.8×10^{-3}	8×10^{8}
2	3.3×10^{6}	3.8×10^{38}	5.4×10^{-4}	3.4×10^{-3}	1×10^{9}
3	7.4×10^{6}	3.8×10^{38}	5.5×10^{-4}	3.4×10^{-3}	2×10^{9}
4	2.2×10^{6}	5.2×10^{38}	7.4×10^{-4}	4.6×10^{-3}	5×10^{8}
5	3.8×10^{6}	1.6×10^{38}	2.3×10^{-4}	1.4×10^{-3}	3×10^{9}
6	4.9×10^{6}	4.1×10^{38}	5.8×10^{-4}	3.6×10^{-3}	1×10^{9}

TABLE 2

Far-Infrared Properties of Molecular Complexes in M33

Complex	L_{IR} ($L_\odot$)	$\overline{T_D}$ (K)	$L_{H\alpha}/L_{IR}$ (erg s^{-1} $L_\odot^{-1}$)	L_{IR}/M_{H_2} ($L_\odot$ $M_\odot^{-1}$)
1	1.6×10^{7}	33	3.3×10^{31}	4.1
2	6.3×10^{6}	35	6.0×10^{31}	1.9
3	1.0×10^{7}	33	3.7×10^{31}	1.4
4	4.6×10^{6}	36	1.1×10^{32}	2.1
5	7.2×10^{6}	30	2.9×10^{31}	1.9
6	1.4×10^{7}	30	2.2×10^{31}	2.9

Figure Captions

Fig. 1 – The single dish CO map of M33 is overlaid on a continuum-subtracted Hα image. The first contour is 1.1 K km s^{-1} and the contours increase by 0.4 K km s^{-1}. The center of the map is at $\alpha_{1950} = 01^h\ 31^m\ 03.0^s$, $\delta_{1950} = 30^o\ 23'\ 54''$. The coordinates are labeled in arcminute offsets from the center.

Fig. 2 – The deconvolved IRAS maps are plotted for the inner 8′ of M33, the same area of the galaxy shown in Figure 1. (a) 60 μm IRAS map. The contour levels start at 0.17 Jy per square arcminute and increase by 0.17 Jy per square arcminute to 1.7 Jy per square arcminute and then increase by 0.34 Jy per square arcminute. The 1σ noise level in the map is 0.08 Jy per square arcminute. (b) 100 μm IRAS map. The contour levels start at 0.34 Jy per square arcminute and increase by 0.34 Jy per square arcminute. The 1σ noise level in the map is 0.23 Jy per square arcminute. (e) 60/100 μm map. The contour levels are 26 K, 30 K, 33 K, 36 K, 40 K, 45 K, and 51 K, where an emissivity index $n = 1$ has been assumed.

Fig. 3 – The spatial distributions of OB associations and Wolf-Rayet stars are compared with that of molecular clouds. The regions mapped at high resolution for molecular clouds are indicated by the large, overlapping circles. The molecular clouds are indicated by open circles, the Wolf-Rayet stars by open stars, and the boundaries of the OB associations by the irregularly shaped contours. The center of the map is the same as in Figure 1 and the coordinates are labeled in arcminute offsets from the center.

Fig. 4 – The boundaries of the OB associations are overlaid on a continuum-subtracted Hα image. The area of the Hα image not surveyed for OB associations is outlined by the heavy dark line.

Figure 1

Single Dish CO Map Overlaid on Hα Emission

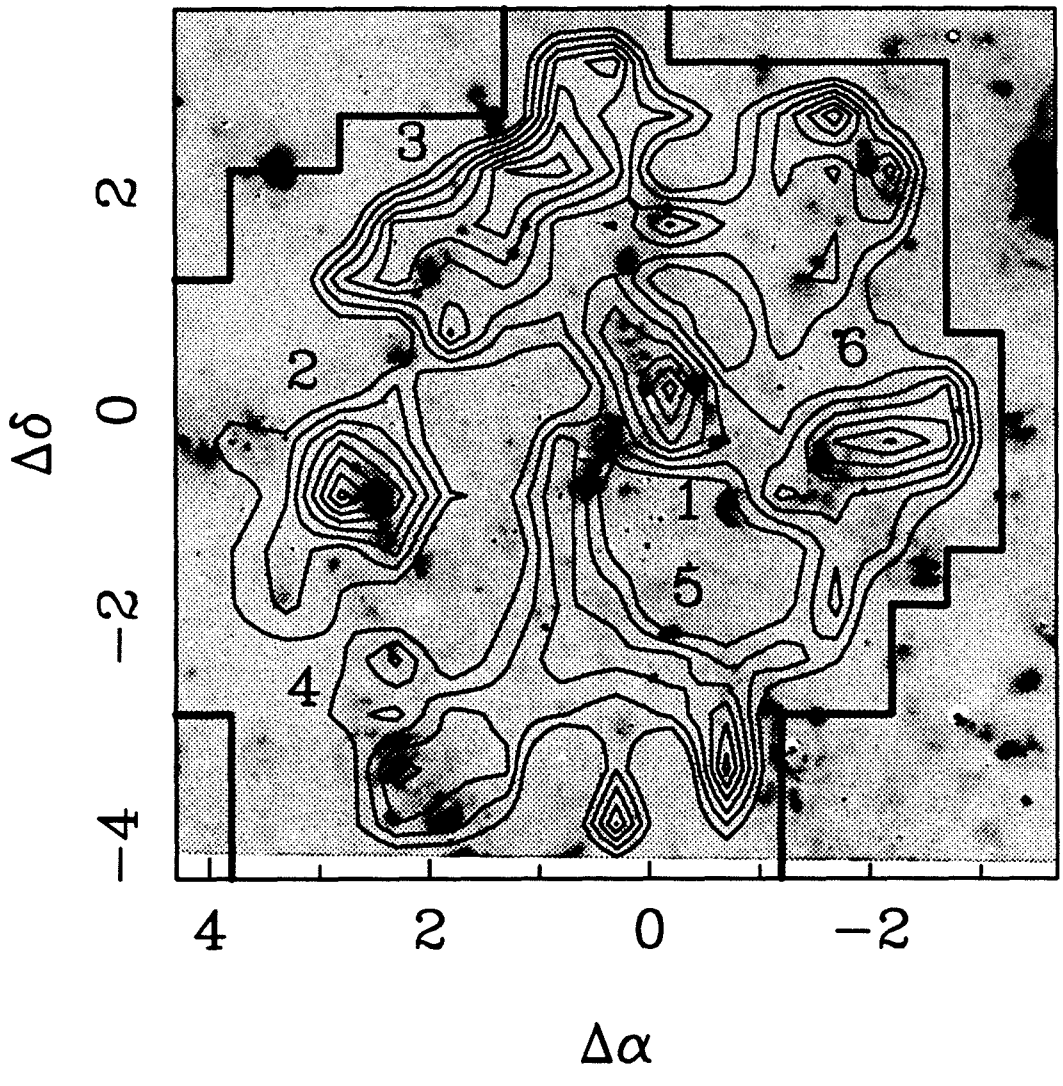

Figure 2a-b

Deconvolved IRAS Maps

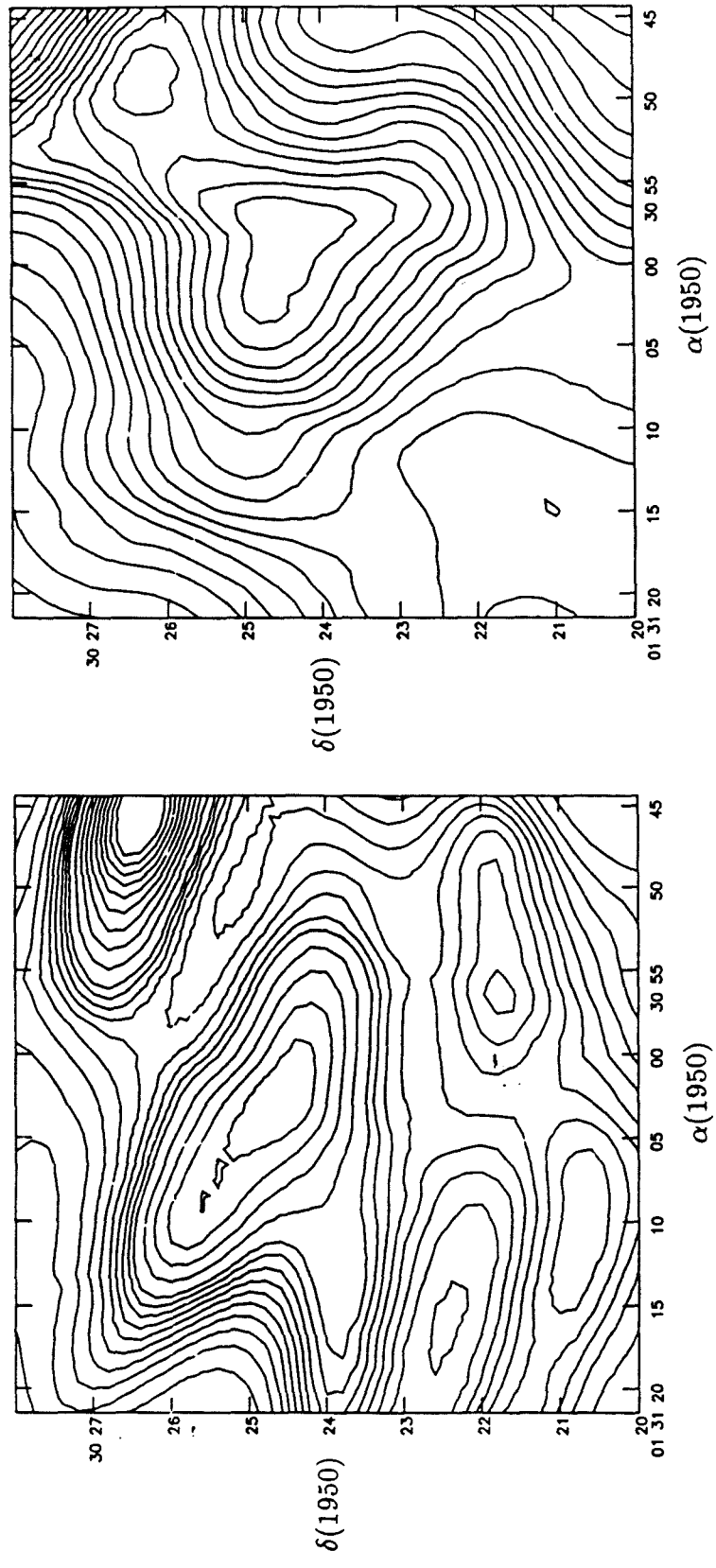

Figure 2c

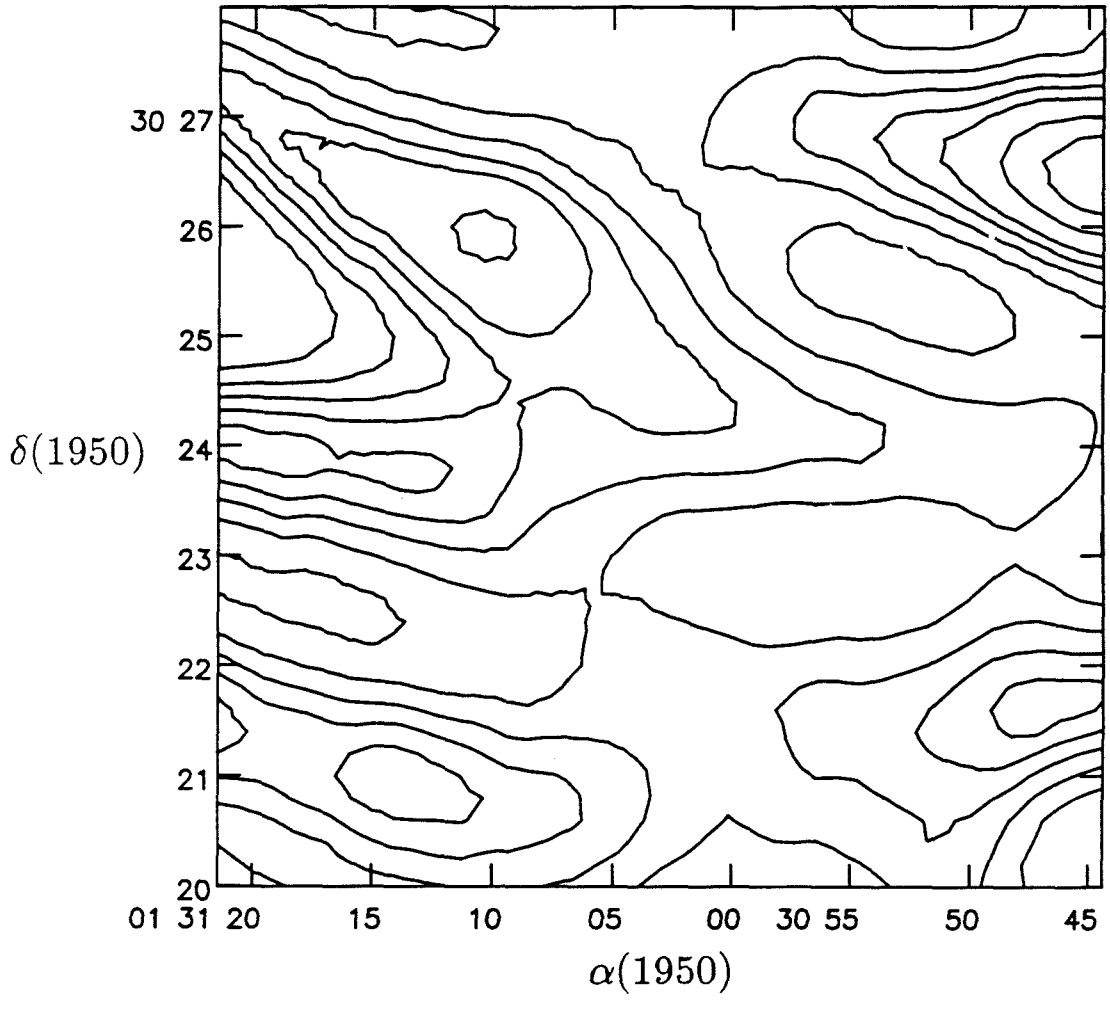
30 27
26
25
δ(1950) 24
23
22
21
20
01 31 20
15
10
05
00
30 55
50
45
α(1950)

Figure 3

Spatial Distributions of Associations, Wolf-Rayet Stars,

and Molecular Clouds

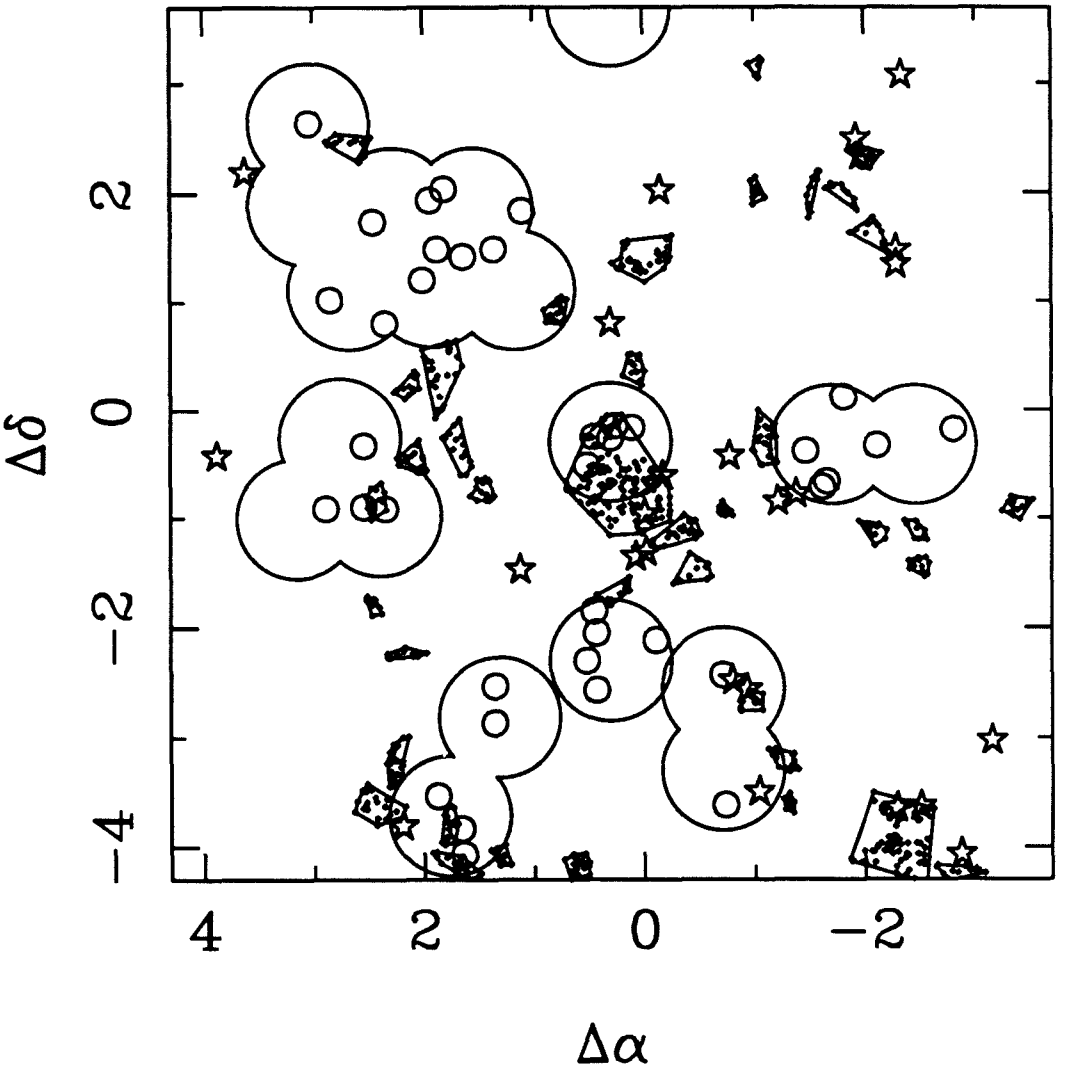

Figure 4

OB Associations and Hα Emission

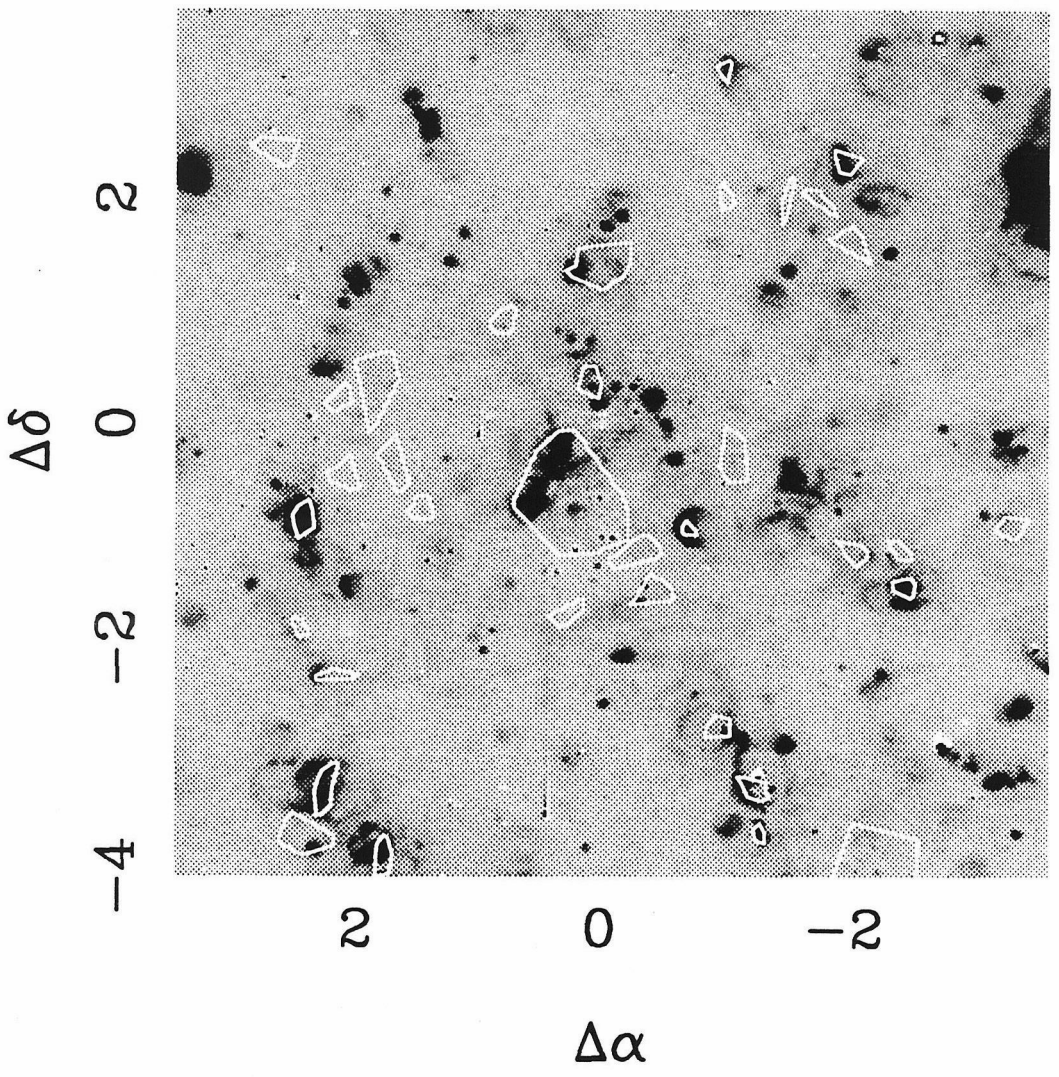

CHAPTER 7

Conclusions and Future Prospects

The new millimeter-wave and optical data presented in this thesis have been used to study high-mass star formation and its relationship with the interstellar medium in the inner 4′ radius of the nearby spiral galaxy M33. The total mass of molecular hydrogen in this region is 3.4×10^7 $M_\odot$, roughly twice the mass in atomic hydrogen. Within a radius of 800 pc, no evidence is seen for an exponential decrease in the azimuthally averaged molecular hydrogen column density. The rotation curve obtained from the molecular gas agrees well with previous observations, yielding a disk mass of 5×10^8 $M_\odot$ within a radius of 800 pc and a molecular gas-mass-to-total-mass ratio of 4%. The expected atomic hydrogen column density associated with the mantles of molecular clouds can account for the observed mean atomic hydrogen column density in the inner disk of M33. Thus only a small fraction of the observed HI can be in a diffuse component not directly associated with molecular clouds.

The properties of individual molecular clouds in M33 have been compared with those of Galactic giant molecular clouds. The velocity widths, diameters, peak brightness temperatures, and masses of the 38 clouds mapped in this study are very similar to those of Galactic clouds. The velocity widths and diameters of the M33 clouds are related by $V_{FWHM} = (1.2^{+1.3}_{-0.6})D_{pc}^{0.5\pm0.2}$, which agrees within the errors with the velocity-diameter relation for Galactic clouds. Masses calculated using the virial theorem and the integrated CO line fluxes agree to within 10% for this sample, implying that in this region of M33 the value of the conversion factor from CO flux to H_2 column density, α, is similar to that of our

own Galaxy. This is the first direct confirmation that the Galactic value of α is appropriate in an external galaxy.

The mass distribution of clouds in M33 is consistent with the Galactic distribution ($N(M) \propto M^{-1.6}$) for $M = 0.8 - 4 \times 10^5$ $M_\odot$ but shows a total lack of clouds with masses greater than 4×10^5 $M_\odot$. A simple model is proposed to explain the high-mass cutoff as arising from the competing processes of cloud growth through accretion and cloud destruction due to star formation. Comparison of the flux detected with the interferometer with single dish data indicates that roughly 50% of the molecular gas resides in structures less massive than 0.8×10^5 $M_\odot$, in contrast to the Galaxy where only 15% of the H_2 mass is in these small structures.

Accurate photometry of individual high-mass stars is important for studying their properties and for estimating star formation rates. New UBV CCD photometry has been used to re-identify the OB associations using a "friends of friends" grouping algorithm, in which the major remaining source of subjectivity is the search radius chosen. We identify 41 associations in this region of M33, each containing at least ten blue stars. These associations have mean radii of 40 pc, masses of 60 $M_\odot$, and ages of 8×10^6 yr. Thus a star formation efficiency of $\sim$10% is required to form individual associations from a single molecular cloud. The number of supergiants of different spectral types has been calculated for fourteen associations each containing at least twenty bright stars. No evidence is found for a gradient in the ratio of blue-to-red stars in the inner two kiloparsecs of M33, despite a decrease of a factor of two in the metallicity over this radius range.

A comparison of the properties of blue stars in different environments suggests that variations in either the mean age of the populations or the upper

mass cutoff to the initial mass function may occur in M33. The blue luminosity function for stars in the field is deficient at bright magnitudes relative to the luminosity function for stars in associations. This may indicate a difference in the number of very high mass stars between the two groups, which would imply that either field stars are older on average than stars in associations or very massive stars are only formed in associations. In addition, associations in the northern arm do not contain any stars more massive than ~ 20 $M_{\odot}$ while the southern arm contains several stars with masses of 60 $M_{\odot}$. This difference may be due to a sudden cessation of star formation or to a lower upper mass cutoff to the initial mass function in the northern arm.

Two independent lines of evidence suggest that the southern spiral arm is generated by a spiral density wave. First, the offset between the peaks in the molecular and atomic gas is consistent with streaming motions as the material enters a spiral density wave. Second, the OB associations in the southern spiral arm show a weak age gradient perpendicular to the arm, consistent with the presence of a spiral density wave. However, the northern arm has an age gradient running along the arm, as would be expected for a stochastic star formation arm.

The cycle between the molecular, atomic, and ionized gas phases of the interstellar medium has been studied by combining new Hα data with the interferometric CO data and previously published high-resolution HI maps. The relative offset of the HI and CO peaks in the southern spiral arm is not consistent with the HI condensing in the arms to form molecular clouds, since the HI appears most strongly on the downstream side of the molecular gas. A comparison of the spatial distributions of the Hα, CO, and HI emission peaks indicates that the atomic gas is probably formed via photo-dissociation of molecular gas by recent high-mass star formation. Roughly two-thirds of the molecular clouds with

$M > 0.5 \times 10^5$ $M_\odot$ contain recent massive star formation as traced by the Hα emission. High-mass star formation rates for the individual clouds range from 0.5-50$\times 10^{-5}$ $M_\odot$ yr^{-1}. The photo-dissociating flux produced by these stars is sufficient to produce the atomic gas near the molecular clouds if the molecular clouds are sufficiently clumpy.

The high-mass star formation rate and efficiency in the inner disk of M33 are measured by combining optical, far-infrared, and millimeter data. The high-mass star formation rate calculated from the Hα emission over an area of 5 kpc^2 is 0.007 $M_\odot$ yr^{-1}, which corresponds to a total star formation rate of 0.04 $M_\odot$ yr^{-1}. The star formation rate obtained from the far-infrared emission is within a factor of two of the rate obtained from the Hα emission. A lower limit to the high-mass star formation rate obtained from number counts of the blue, high-mass stars is consistent with the results obtained from the Hα and far-infrared emission.

The single dish CO map reveals six large scale features with sizes of 200-400 pc that in several cases are associated with spiral arms. The masses of these molecular complexes (3-10$\times 10^6$ $M_\odot$) are insufficient to gravitationally or tidally bind them given their measured sizes, velocity dispersions, and distances from the center of M33. The high-mass star formation efficiency varies by a factor of six from one molecular complex to another. However, the southern spiral arm and the molecular complexes have similar star formation efficiencies to regions of the galaxy containing little molecular gas. Thus the large amount of star formation occurring in the spiral arms of M33 is simply due to the presence of large amounts of molecular gas and not to an increased efficiency of star formation in the arms.

In summary, we have arrived at the following physical picture of high-mass star formation and the interstellar medium in M33. Star formation rates and

efficiencies vary from one region of the galaxy to another, but are reasonably uniform on average, i.e., no systematic difference is found between arm and interarm regions. However, differences are found in the properties of the highest mass stars in associations and in the field, as well as between the two spiral arms, which may indicate variations in the initial mass function or in the mean age of the stars. On a smaller scale, the areas of most recent high-mass star formation (HII regions) are always associated with molecular clouds. These stars photo-dissociate part of the cloud to produce atomic hydrogen peaks that are observed to lie near all molecular clouds. The observed mean atomic hydrogen column density is explained by the atomic mantles that shield individual molecular clouds from the general interstellar radiation field. Finally, the gradient in OB association ages and the offset between the atomic and molecular gas peaks across the southern spiral arm are evidence that this arm is generated by a spiral density wave.

Some interesting problems remain unresolved by this study and are prime areas for future research. For example, the exact nature of the relationship between the OB associations and molecular clouds is not clear because of incomplete high-resolution CO mapping of the inner disk. In addition, the lack of HII emission in many large OB associations cannot be easily explained. Interferometric CO observations in some OB associations and HII regions that have not yet been mapped in CO should help to define these relationships. It is also important to learn whether the close association between HII regions and molecular clouds extends to all of the HII regions in the inner disk.

The differences in the luminosity functions of association and field stars provide a tantalizing clue that variations in the high-mass end of the initial mass function may exist. Such variations would have important implications

for starburst galaxies, which have been postulated to have only high-mass star formation in order to extend their gas depletion times. Confirmation of the lack of high-mass stars in the northern arm associations and in the field can only be obtained spectroscopically and thus spectroscopy of the brightest stars in these regions should be a high priority.

The large metallicity gradient in M33 has not been fully exploited to test stellar evolution and molecular line formation theories due to the limit range of radius observed in this thesis. The properties of OB associations at much larger radii and lower metallicities will be very useful for constraining the effects of lower metallicity on stellar evolution. The properties of individual molecular clouds in a lower metallicity environment are crucial for resolving the controversy in the CO to H_2 conversion factor α. Such information would have a large impact on understanding star formation in dwarf galaxies, whose very weak CO lines may be due to either a deficiency of molecular gas or a larger value of α.

Finally, a comparison of the star-forming component of M33 with that of other nearby galaxies will provide important information on how star formation varies with galaxian environment. The Local Group contains an Sb-type spiral galaxy, M31, and two dwarf irregular galaxies, IC1613 and NGC 6822. Studies of these galaxies can reveal whether the properties of molecular clouds and OB associations vary from one galaxy to another. How the star formation rates and efficiencies vary between different galaxies can also be determined and any organized structure such as density waves or self-propagating star formation identified. Coordinated millimeter and optical observations of these galaxies would be an important first step towards understanding the effect of environment on the massive star formation process.

References

Aumann, H. H., Fowler, J. W., and Melnyk, M. 1990, *A. J.*, in press.

Bania, T. M. 1977, *Ap. J.* **216**, 381.

Barker, T. 1978, *Ap. J.* **219**, 914.

Blair, W. P. and Kirshner, R. P. 1985, *Ap. J.* **289**, 582.

Blaauw, A. 1964, *A. R. A. A.* **2**, 213.

Blitz, L. 1985, *Ap. J.* **296**, 481.

Bohlin, R. C., Savage, B. D., and Drake, J. F. 1978, *Ap. J.* **224**, 132.

Bosma, A. 1978, Ph.D. Thesis, University of Groningen.

Bloemen, J. B. G. M., *et al.* 1986, *Astr. Ap.* **154**, 25.

Boulanger, F., Vogel, S. N., Viallefond, F., and Ball, R. 1988, in *Molecular Clouds in the Milky Way and External Galaxies*, eds. R. Dickman, R. Snell, and J. Young, (New York: Springer-Verlag), 401.

Boulesteix, J., Courtes, G., Laval, A., Monnet, G., and Petit, H. 1974, *Astr. Ap.* **37**, 33.

Boulesteix, J., Colin, J., Athanassoula, E., and Monnet, G. 1979, in *Photometry, Kinematics, and Dynamics of Galaxies*, ed. D. S. Evans, (Austin: University of Texas Press), 271.

Boulesteix, J., Dubout-Crillon, R., and Monnet, G. 1981, *Astr. Ap.* **104**, 15.

Bronfman, L., Cohen, R. S., Alvarez, H., May, J., and Thaddeus, P. 1988, *Ap. J.* **324**, 248.

Casoli, F. and Combes, F. 1988, *Astr. Ap.* **198**, 43.

Casoli, F., Combes, F., and Stark, A. A. 1987, *Astr. Ap.* **173**, 43.

Christian, C. A. and Schommer, R. A. 1987, *A. J.* **93**, 557.

Christian, C. A., Adams, M., Barnes, J. V., Butcher, H., Hayes, D. S., Mould, J. R., and Siegel, M. 1985, *P. A. S. P.* **97**, 363.

Clemens, D. P. 1985, *Ap. J.* **295**, 422.

Cohen, R. S., Dame, T. M., Garay, G., Montani, J., Rubio, M., and Thaddeus, P. 1988, *Ap. J. Lett.* **331**, 95.

Courtes, G., Petit, H., Dodonov, S., and Petit, M. 1987, *Astr. Ap.* **174**, 28.

de Loore, C. 1988, *Astr. Ap.* **203**, 71.

Deul, E. R. 1989, *Astr. Ap.*, **218**, 78.

Deul, E. R. and van der Hulst, J. M. 1987, *Astr. Ap. Suppl.* **67**, 509.

Deul, E. R. and den Hartog, R. H. 1990 *Astr. Ap.*, submitted.

Dickman, R. L., Snell, R. L., and Schloerb, F. P. 1987, *Ap. J.* **309**, 326.

Fitzgerald, M. P. 1970, *Astr. Ap.* **4**, 234.

Flower, P. J. 1977, *Astr. Ap.* **54**, 31.

Freedman, W. L. 1985a, *Ap. J.* **299**, 74.

Freedman, W. L. 1985b, *A. J.* **90**, 2499.

Freedman, W. L. 1985c, in *Cepheids: Theory and Observations*, ed. B. F. Madore (New York: Cambridge University Press), 225.

Freedman, W. L. 1988, *A. J.* **96**, 1248.

Freedman, W. L., Wilson, C. D., and Madore, B. F. 1990, in preparation.

Gallagher, J. S., Goad, J. W., and Mould, J. 1982, *Ap. J.* **263**, 101.

Garmany, C. D., Conti, P. S., and Chiosi, C. 1982, *Ap. J.* **263**, 777.

Habing, H. 1968, *Bull. Astron. Inst. Neth.* **19**, 421.

Hildebrand, R. 1983, *Quart. J. R. A. S.* **24**, 267.

Hodge P. 1986, in *Luminous Stars and Associations in Galaxies* (I. A. U. Symp. 116), eds. C. W. H. de Loore, A. J. Willis, and P. Laskarides (D. Reidel: Boston), 369.

Hollenbach, D. J., Werner, M. W., and Salpeter, E. E. 1971, *Ap. J.* **163**, 165.

Hubble, E. 1926, *Ap. J.* **63**, 236.

Humphreys, R. M. 1979, in *Large-Scale Characteristics of the Galaxy*, ed. W. B. Burton, [D. Reidel: Boston], 93.

Humphreys, R. M. and Sandage, A. R. 1980, *Ap. J. Suppl.* **44**, 319.

Humphreys, R. M. and McElroy, D. B. 1984, *Ap. J.* **284**, 565.

Jog, C. J. and Ostriker, J. P. 1988, *Ap. J.* **328**, 404.

Kennicutt, R. C. 1983, *Ap. J.* **272**, 54.

Kennicutt, R. C. 1988, *Ap. J.* **334**, 144.

Kunchev, P. Z. and Ivanov, G. R. 1984, *Ap. Sp. Sci.* **106**, 371.

Kwan, J. 1979, *Ap. J.* **229**, 567.

Kwitter, K. B. and Aller, L. H. 1981, *M. N. R. A. S.* **195**, 939.

Lada, C. J., Margulis, M., Sofue, Y., Nakai, N., and Handa, T. 1988, *Ap. J.* **328**, 143.

Landolt, A. 1983, *A. J.* **88**, 439.

Lonsdale, C. J., Helou, G., Good, J. C. and Rice, W. 1985, *Cataloged Galaxies and Quasars Observed in the IRAS Survey*, (Pasadena: Jet Propulsion Laboratory).

Lucy, L. B. 1974, *A. J.* **79**, 745.

Madore, B. F., McAlary, C. W., McLaren, R. A., Welch, D. L., Neugebauer, G., and Matthews, K. 1985, *Ap. J.* **294**, 560.

Maeder, A. 1980, *Astr. Ap.* **92**, 101.

Maeder, A. and Meynet, G. 1988, *Astr. Ap. Suppl.* **76**, 411.

Maloney, P. and Black, J. H. 1988, *Ap. J.* **325**, 389.

Massey, P. 1985, *P. A. S. P.*, **97**, 5.

Massey, P. and Conti, P. S. 1983, *Ap. J.* **273**, 576.

Massey, P., Conti, P. S., and Armandroff, T. E. 1987, *A. J.* **94**, 1538.

Massey, P., Conti, P. S., Moffat, A. F. J., and Shara, M. M. 1987, *P. A. S. P.* **99**, 816.

Massey, P., Garmany, C. D., Silkey, M., and Degioia-Eastwood, K. 1989, *A. J.* **97**, 107.

Massey, P., Parker, J. W., and Garmany, C. D. 1989, *A. J.* **98**, 1305.

MacLaren, I., Richardson, K. M., and Wolfendale, A. W. 1988, *Ap J.* **333**, 821.

McCall, M. L., Rybski, P. M., and Shields, G. A. 1985, *Ap. J. Suppl.* **57**, 1.

McKee, C. F. 1989, *Ap. J.* **345**, 782.

Meylan, G. and Maeder, A. 1982, *Astr. Ap.* **108**, 148.

Mezger, P. G. and Smith, L. F. 1977, in *Star Formation, I. A. U. Symp.* **75**, eds. T. de Jong and A. Maeder, (Dordrecht: Reidel), 133.

Myers, P. M. and Goodman, A. A. 1988, *Ap. J.* **329**, 392.

Neese, C., Armandroff, T. E., and Massey, P. 1989, *B. A. A. S.* **21**, 774.

Newton, K. 1980, *M. N. R. A. S.* **190**, 689.

Oort, J. H. 1977 *Ann. Rev. Astr. Ap.* **15**, 295.

Pagel, B. E. P. 1985, in *Production and Distribution of C, N, O Elements* (ESO workshop), eds. I. J. Danziger, F. Matteucci, and K. Kjär, 155.

Pagel, B. E. P., Edmunds, M. G., Blackwell, D. E., Chun, M. S., and Smith, G. 1979, *M. N. R. A. S.* **189**, 95.

Ratnatunga, K. U. and Bahcall, J. N. 1985, *Ap. J. Suppl.* **59**, 63.

Rice, W., Lonsdale, C. J., Soifer, B. T., Neugebauer, G., Koplan, E. L., Lloyd, L. A., de Jong, T., and Habing, H. J. 1988, *Ap. J. Suppl.* **68**, 91.

Rice, W., Boulanger, F., Viallefond, F., Soifer, B. T., and Freedman, W. L. 1990, *Ap. J.*, submitted.

Richardson, W. H. 1972, *J. Opt. Soc. Am.* **62**, 55.

Roberts, W. W., Roberts, M. S., and Shu, F. H. 1975, *Ap. J.* **196**, 381.

Rogstad, D. H. and Shostak, G. S. 1972, *Ap. J.* **176**, 315.

Rubin, V. and Ford, F. 1985, *Carnegie Institute of Washington Annual Report*, 66.

Sanders, D. B., Scoville, N. Z., and Solomon, P. M. 1985, *Ap. J.* **289**, 373.

Sandage, A. 1983, *A. J.*, **88**, 1108.

Sandage, A. and Carlson, G. 1983, *Ap. J. Lett.*, **267**, 25.

Sandage, A. R. and Humphreys, R. M. 1980, *Ap. J. Lett.* **236**, 1.

Schraml, J. and Mezger, P. G. 1969, *Ap. J.* **156**, 269.

Scoville, N. Z. 1972, *Ap. J. Letters* **175**, L127.

Scoville, N. Z. and Good, J. C. 1989, *Ap. J.* **339**, 149.

Scoville, N. Z. and Sanders, D. B. 1987, in *Interstellar Processes*, eds. D. J. Hollenbach and H. A. Thronson, (Dordrecht: D. Reidel), 21.

Scoville, N. Z., Yun, M. S., Clemens, D. P., Sanders, D. B., and Waller, W. H. 1987, *Ap. J. Suppl.* **63**, 821.

Shaw, R. A. and Kaler, J. B. 1982, *Ap. J.* **261**, 510.

Solomon, P. M., Barrett, J., Sanders, D. B., and de Zafra, R. 1983, *Ap. J. Letters* **266**, L106.

Solomon, P. M., Rivolo, A. R., Barrett, J., and Yahil, A. 1987, *Ap. J.* **319**, 730.

Stetson, P. 1987, *P. A. S. P.* **99**, 191.

Stark, A. A. and Brand, J. 1989, *Ap. J.* **339**, 763.

Strong, A. W., *et al.* 1988, *Astr. Ap.* **207**, 1.

Tacconi, L. and Young, J. S. 1986, *Ap. J.* **308**, 600.

Tacconi, L. and Young, J. S. 1990, *Ap. J.*, in press.

Thronson, H. A. and Telesco, C. M. 1986, *Ap. J.* **311**, 98.

van der Werf, P. 1989, Ph.D. Thesis, University of Leiden.

van Dishoeck, E. F. 1987, in *Astrochemistry*, eds. M. S. Vardya and S. P. Taraf-
dar, [Reidel: Boston], 51.

Viallefond, F., Goss, W. M., van der Hulst, J. M., and Crane, P. C. 1986, *Astr. Ap. Suppl.* **64**, 237.

Viallefond, F. and Goss, W. M. 1986, *Astr. Ap.* **154**, 357.

Vilchez, J. M., Pagel, B. E. J., Diaz, A. I., Terlevich, E., and Edmunds, M. G. 1988, *M. N. R. A. S.* **235**, 633.

Vogel, S. N., Boulanger, F., and Ball, R. 1987, *Ap. J. Lett.* **321**, 145.

Vogel, S. N., Kulkarni, S. R., and Scoville, N. Z. 1988, *Nature* **334**, 402.

Walker, M. F. 1964, *A. J.* **69**, 744.

Walterbos, R. A. M. 1986, Ph.D. Thesis, University of Leiden.

Walterbos, R. A. M. and Kennicutt, R. C. 1988, *Astr. Ap.* **198**, 61.

Walterbos, R. A. M. and Schwering, P. B. W. 1987, *Astr. Ap.* **180** 27.

Whitworth, A. 1979, *M. N. R. A. S.* **186**, 59.

Wilson, C. D. and Scoville, N. 1989a, *Ap. J.* **347**, 743.

Wilson, C. D. and Scoville, N. Z. 1989b, *Ap. Space Sci.* **156**, 269.

Wilson, C. D., Freedman, W. L., and Madore, B. F. 1990, *A. J.* **99**, 149.

Wilson, C. D., Scoville, N. Z., Freedman, W. L., Madore, B. F., and Sanders, D. B. 1988, *Ap. J.* **333**, 611.

Young, J. S. 1987, in *Star Formation in Galaxies*, ed. C. J. Lonsdale Persson, (NASA Conference Publication 2466), 197.

Young, J. S. and Scoville, N. 1982, *Ap. J. Lett.* **260**, 11.

Young, J. S. *et al.* 1990, in preparation.

APPENDIX

TABLE 2 (Chapter 3)

UBV Photometry of Blue Stars in M33

Number	α(1950)	δ(1950)	X	Y	V	B-V	U-B	σ_V	σ_B	σ_U
1	1 30 56.9	30 28 49	-1100	210	19.71	-0.22	...	0.04	0.03	...
2	1 30 52.9	30 28 46	-1092	-12	18.92	0.26	0.40	0.02	0.03	0.06
3	1 30 54.1	30 28 46	-1091	54	19.11	-0.06	...	0.03	0.03	...
4	1 30 53.1	30 28 45	-1090	-2	19.93	-0.13	...	0.05	0.03	...
5	1 30 57.6	30 28 47	-1090	247	19.79	-0.05	...	0.07	0.06	...
6	1 30 53.2	30 28 45	-1088	4	19.06	0.16	-0.16	0.03	0.03	0.06
7	1 30 56.0	30 28 45	-1086	161	19.99	-0.15	...	0.05	0.03	...
8	1 30 56.0	30 28 45	-1083	161	19.94	-0.01	...	0.07	0.06	...
9	1 30 52.7	30 28 43	-1082	-20	20.99	-0.31	-0.86	0.08	0.04	0.06
10	1 30 53.2	30 28 43	-1081	6	19.95	-0.13	...	0.05	0.03	...
11	1 30 54.0	30 28 43	-1080	50	20.86	0.10	-0.88	0.07	0.06	0.07
12	1 30 53.8	30 28 43	-1078	39	18.86	0.03	-0.36	0.02	0.03	0.06
13	1 30 55.7	30 28 43	-1075	141	19.64	0.24	...	0.04	0.04	...
14	1 31 02.2	30 28 45	-1074	497	19.82	0.10	...	0.06	0.05	...
15	1 31 13.6	30 28 48	-1074	1124	15.24	0.30	-0.47	0.05	0.05	0.03
16	1 31 14.4	30 28 48	-1072	1167	20.26	0.03	-0.77	0.07	0.05	0.03
17	1 31 12.9	30 28 47	-1068	1081	19.66	-0.14	-0.84	0.06	0.05	0.03
18	1 30 48.5	30 28 38	-1064	-255	19.15	0.19	0.34	0.03	0.03	0.06
19	1 30 53.2	30 28 38	-1057	3	18.01	0.16	0.01	0.02	0.03	0.06
20	1 30 53.5	30 28 37	-1053	21	18.90	0.16	-0.04	0.03	0.03	0.07
21	1 31 05.0	30 28 38	-1045	651	20.54	0.11	...	0.08	0.06	...
22	1 30 50.1	30 28 34	-1044	-164	20.25	-0.05	...	0.05	0.03	...
23	1 30 56.0	30 28 35	-1041	156	20.49	0.31	...	0.12	0.11	...
24	1 31 08.4	30 28 38	-1037	838	20.34	0.06	-1.01	0.08	0.06	0.03
25	1 31 02.7	30 28 33	-1024	522	18.74	0.03	...	0.05	0.05	...
26	1 31 01.7	30 28 32	-1024	467	19.97	0.09	-0.77	0.07	0.06	0.03
27	1 31 10.1	30 28 35	-1022	929	20.24	0.30	-0.24	0.07	0.06	0.04
28	1 31 06.4	30 28 33	-1019	728	20.76	0.30	...	0.09	0.07	...
29	1 31 11.7	30 28 34	-1018	1018	20.94	-0.24	...	0.11	0.07	...
30	1 30 46.5	30 28 26	-1018	-363	20.53	0.30	0.37	0.05	0.05	0.08
31	1 30 55.3	30 28 29	-1018	118	20.31	0.37	-0.43	0.05	0.06	0.08
32	1 30 55.3	30 28 29	-1016	120	20.34	0.16	...	0.08	0.06	...
33	1 30 53.3	30 28 28	-1015	8	18.69	0.22	...	0.03	0.03	...
34	1 31 12.5	30 28 33	-1013	1062	19.75	0.14	...	0.08	0.09	...
35	1 30 58.3	30 28 29	-1012	280	18.38	0.00	-0.58	0.05	0.05	0.03
36	1 30 55.7	30 28 28	-1011	142	20.05	0.10	...	0.05	0.05	...
37	1 31 03.0	30 28 29	-1008	541	18.88	0.06	...	0.05	0.05	...
38	1 31 11.7	30 28 32	-1007	1017	19.42	-0.04	-1.14	0.07	0.06	0.04
39	1 31 12.7	30 28 31	-1003	1069	20.37	0.09	-0.86	0.08	0.06	0.04
40	1 31 11.7	30 28 31	-1002	1013	19.14	0.13	-0.94	0.06	0.06	0.04
41	1 31 08.3	30 28 29	-1000	831	19.61	0.13	-0.97	0.06	0.06	0.03
42	1 31 03.2	30 28 27	-998	548	18.93	0.01	...	0.05	0.05	...
43	1 30 58.1	30 28 24	-994	273	18.55	0.06	-0.73	0.05	0.05	0.03
44	1 30 53.6	30 28 23	-993	23	20.58	0.57	-0.72	0.05	0.06	0.07
45	1 31 08.1	30 28 27	-991	818	19.42	0.06	-0.64	0.06	0.05	0.03
46	1 30 52.8	30 28 22	-991	-21	20.21	0.25	-0.11	0.05	0.04	0.07
47	1 31 15.0	30 28 28	-986	1197	19.10	0.19	-0.04	0.05	0.05	0.03
48	1 31 00.3	30 28 23	-985	394	18.73	0.28	-0.38	0.05	0.05	0.03

TABLE 2 (cont.)

Number	α(1950)	δ(1950)	X	Y	V	B-V	U-B	σ_V	σ_B	σ_U
49	1 30 52.5	30 28 20	-984	-34	19.88	0.34	...	0.05	0.04	...
50	1 30 57.3	30 28 21	-982	227	20.76	-0.13	...	0.06	0.05	...
51	1 31 03.3	30 28 22	-978	556	19.95	0.16	-1.38	0.07	0.06	0.05
52	1 30 56.1	30 28 19	-976	163	19.67	-0.11	...	0.04	0.03	...
53	1 30 56.1	30 28 19	-973	164	19.58	0.04	-0.85	0.06	0.05	0.03
54	1 31 02.6	30 28 21	-972	518	19.71	0.04	...	0.05	0.06	...
55	1 31 03.0	30 28 20	-970	538	19.16	0.27	...	0.05	0.06	...
56	1 31 00.3	30 28 19	-967	393	20.01	-0.26	...	0.11	0.06	...
57	1 30 49.5	30 28 14	-960	-202	18.47	0.36	0.48	0.02	0.03	0.06
58	1 31 13.4	30 28 21	-959	1107	20.05	0.05	...	0.06	0.05	...
59	1 30 57.6	30 28 16	-958	244	19.87	0.03	-0.88	0.07	0.06	0.03
60	1 31 11.6	30 28 19	-954	1010	20.17	-0.13	-0.55	0.11	0.06	0.04
61	1 30 54.7	30 28 14	-953	85	19.59	0.13	-0.12	0.03	0.03	0.06
62	1 30 57.0	30 28 14	-952	211	19.29	-0.07	...	0.03	0.03	...
63	1 30 53.6	30 28 13	-951	24	18.85	0.28	0.11	0.02	0.03	0.06
64	1 30 55.6	30 28 12	-947	135	19.84	-0.01	0.30	0.05	0.03	0.07
65	1 31 05.6	30 28 15	-944	682	20.25	0.22	-0.33	0.08	0.06	0.04
66	1 31 07.1	30 28 13	-934	760	17.73	0.27	-0.03	0.02	0.01	0.02
67	1 31 11.9	30 28 14	-930	1025	19.54	0.06	-0.88	0.06	0.05	0.03
68	1 31 17.2	30 28 15	-927	1312	19.25	0.27	-0.15	0.05	0.05	0.04
69	1 31 05.6	30 28 11	-925	679	19.88	0.14	...	0.07	0.06	...
70	1 31 10.6	30 28 12	-924	956	18.80	0.18	-0.46	0.05	0.05	0.03
71	1 31 05.6	30 28 10	-924	679	19.92	0.03	-0.54	0.06	0.05	0.04
72	1 31 06.7	30 28 9	-918	738	20.77	0.22	...	0.11	0.08	...
73	1 31 05.8	30 28 8	-915	691	18.43	0.04	-0.90	0.01	0.01	0.04
74	1 31 06.3	30 28 8	-915	717	19.46	0.74	-0.81	0.06	0.24	0.04
75	1 31 14.1	30 28 10	-910	1145	20.30	0.41	-1.01	0.06	0.06	0.04
76	1 30 47.3	30 28 1	-909	-320	19.67	0.11	...	0.03	0.04	...
77	1 30 56.5	30 28 4	-908	181	20.15	-0.14	...	0.05	0.03	...
78	1 31 02.5	30 28 5	-908	509	18.92	0.06	-0.13	0.05	0.05	0.15
79	1 31 01.4	30 28 4	-905	448	18.82	0.16	-0.25	0.05	0.05	0.03
80	1 31 16.4	30 28 9	-904	1271	18.33	0.23	-0.37	0.05	0.05	0.03
81	1 30 57.5	30 28 2	-902	237	18.07	0.11	-0.59	0.04	0.05	0.02
82	1 30 56.1	30 28 2	-900	160	17.19	0.09	...	0.02	0.02	...
83	1 30 56.1	30 28 1	-898	161	17.09	0.21	-0.44	0.04	0.05	0.02
84	1 31 14.2	30 28 6	-894	1149	20.43	-0.05	-1.04	0.07	0.06	0.03
85	1 31 13.3	30 28 6	-894	1098	20.16	0.04	-0.32	0.06	0.05	0.04
86	1 31 15.1	30 28 6	-894	1198	20.61	-0.12	-0.94	0.09	0.06	0.04
87	1 31 00.6	30 28 1	-893	403	20.58	0.07	...	0.10	0.07	...
88	1 30 55.4	30 27 59	-892	123	20.37	0.28	...	0.05	0.05	...
89	1 31 16.6	30 28 6	-891	1281	18.32	0.17	...	0.05	0.05	...
90	1 31 08.6	30 28 3	-890	845	18.09	0.01	-1.00	0.05	0.05	0.03
91	1 30 55.5	30 27 59	-889	124	20.25	0.36	...	0.07	0.07	...
92	1 31 04.1	30 28 1	-888	598	20.04	0.16	...	0.07	0.06	...
93	1 30 55.0	30 27 57	-883	100	20.71	-0.15	...	0.07	0.05	...
94	1 30 50.5	30 27 56	-883	-146	20.17	-0.13	-0.81	0.05	0.03	0.06
95	1 30 56.3	30 27 57	-882	167	17.58	0.07	...	0.02	0.03	...
96	1 31 01.8	30 27 59	-881	469	19.14	0.07	0.26	0.11	0.06	0.11
97	1 31 05.8	30 27 60	-880	691	20.63	0.38	...	0.26	0.08	...
98	1 30 56.3	30 27 57	-879	168	17.44	0.15	-0.58	0.04	0.05	0.02
99	1 30 56.1	30 27 55	-874	158	18.21	0.39	0.31	0.02	0.03	0.06
100	1 31 15.2	30 28 1	-872	1201	18.45	0.18	-0.35	0.07	0.06	0.04

TABLE 2 (cont.)

Number	α(1950)	δ(1950)	X	Y	V	B-V	U-B	σ_V	σ_B	σ_U
101	1 31 02.7	30 27 57	-870	521	18.53	0.28	-0.62	0.05	0.05	0.03
102	1 31 16.1	30 28 1	-869	1255	20.90	0.05	-1.02	0.10	0.07	0.04
103	1 31 15.1	30 28 0	-868	1199	19.71	0.11	-0.76	0.15	0.10	0.07
104	1 31 06.5	30 27 57	-868	727	18.57	0.15	-1.00	0.05	0.05	0.03
105	1 31 02.6	30 27 54	-861	516	18.32	0.07	...	0.05	0.05	...
106	1 31 06.6	30 27 54	-855	735	20.20	-0.21	...	0.08	0.06	...
107	1 31 02.5	30 27 52	-849	506	18.54	0.04	-0.69	0.05	0.05	0.03
108	1 30 56.6	30 27 49	-847	183	19.64	0.14	...	0.04	0.06	...
109	1 30 45.8	30 27 46	-847	-405	19.65	-0.19	-0.82	0.03	0.03	0.06
110	1 30 56.6	30 27 49	-845	184	19.46	0.24	-0.07	0.06	0.06	0.03
111	1 30 57.4	30 27 46	-834	227	19.11	0.21	...	0.06	0.06	...
112	1 30 55.2	30 27 46	-833	109	19.51	0.38	0.51	0.03	0.03	0.07
113	1 30 49.7	30 27 44	-833	-191	20.25	0.05	-0.41	0.05	0.04	0.07
114	1 30 59.8	30 27 45	-826	359	19.57	0.14	-0.71	0.06	0.06	0.05
115	1 30 50.2	30 27 42	-824	-167	20.03	0.00	-0.67	0.04	0.03	0.06
116	1 30 49.8	30 27 42	-824	-187	18.50	-0.09	-0.79	0.02	0.03	0.06
117	1 30 47.2	30 27 41	-823	-329	19.25	0.06	-0.59	0.03	0.03	0.06
118	1 30 56.3	30 27 42	-816	168	20.77	-0.16	-0.57	0.07	0.04	0.10
119	1 30 51.6	30 27 40	-816	-88	20.61	0.35	...	0.05	0.05	...
120	1 30 57.0	30 27 42	-816	206	20.37	-0.20	...	0.05	0.03	...
121	1 31 09.7	30 27 46	-816	904	19.99	-0.17	-0.98	0.06	0.05	0.03
122	1 30 57.0	30 27 41	-813	207	20.54	-0.24	-1.06	0.10	0.06	0.03
123	1 31 11.1	30 27 45	-810	979	20.44	0.25	-0.62	0.09	0.07	0.05
124	1 30 59.1	30 27 40	-803	323	20.15	-0.04	-0.69	0.07	0.06	0.03
125	1 31 05.5	30 27 42	-803	669	19.52	0.13	-0.87	0.05	0.05	0.03
126	1 30 51.4	30 27 37	-801	-99	19.55	-0.14	-0.32	0.05	0.03	0.07
127	1 31 12.7	30 27 43	-800	1063	19.37	0.16	-0.41	0.06	0.06	0.04
128	1 30 52.1	30 27 37	-800	-63	20.22	-0.08	0.09	0.05	0.03	0.07
129	1 30 51.2	30 27 36	-797	-110	18.74	0.05	-0.96	0.03	0.06	0.06
130	1 30 52.6	30 27 36	-796	-34	19.88	-0.01	-0.66	0.04	0.03	0.06
131	1 30 47.5	30 27 34	-794	-312	20.13	0.14	-0.57	0.05	0.04	0.06
132	1 30 47.8	30 27 34	-794	-298	20.58	0.00	-0.46	0.05	0.04	0.07
133	1 30 53.8	30 27 36	-794	28	20.12	0.14	0.10	0.05	0.04	0.07
134	1 30 51.1	30 27 34	-792	-120	16.55	0.15	-0.35	0.02	0.02	0.06
135	1 31 16.7	30 27 42	-790	1285	20.73	0.04	...	0.10	0.06	...
136	1 30 57.1	30 27 35	-787	210	20.72	-0.16	...	0.10	0.06	...
137	1 31 12.9	30 27 39	-781	1076	20.60	-0.23	...	0.21	0.07	...
138	1 30 50.7	30 27 32	-781	-139	19.64	0.23	-0.82	0.04	0.14	0.08
139	1 31 13.4	30 27 38	-779	1103	19.89	-0.10	...	0.06	0.06	...
140	1 30 46.3	30 27 29	-776	-378	20.86	-0.17	-0.63	0.06	0.04	0.06
141	1 31 11.1	30 27 37	-775	977	18.85	0.15	...	0.05	0.07	...
142	1 30 53.5	30 27 31	-774	15	17.81	-0.06	...	0.02	0.03	...
143	1 31 01.9	30 27 34	-773	473	19.60	-0.15	-0.70	0.07	0.05	0.03
144	1 30 53.6	30 27 31	-773	21	19.26	0.02	-0.81	0.05	0.05	0.07
145	1 31 10.0	30 27 35	-768	916	19.52	0.34	-0.98	0.06	0.05	0.03
146	1 31 01.3	30 27 32	-766	441	17.10	0.27	-0.08	0.04	0.05	0.02
147	1 30 50.7	30 27 28	-765	-139	20.52	-0.06	...	0.06	0.05	...
148	1 31 12.7	30 27 35	-765	1066	16.98	0.19	-0.55	0.05	0.05	0.03
149	1 30 52.1	30 27 28	-763	-62	20.94	0.07	-0.55	0.08	0.06	0.07
150	1 30 51.6	30 27 27	-760	-93	20.48	0.34	...	0.05	0.05	...

TABLE 2 (cont.)

Number	α(1950)	δ(1950)	X	Y	V	B-V	U-B	σ_V	σ_B	σ_U
151	1 30 53.2	30 27 27	-759	-5	20.11	-0.36	...	0.06	0.05	...
152	1 30 52.4	30 27 27	-758	-48	18.92	0.09	0.06	0.03	0.03	0.07
153	1 30 48.9	30 27 25	-756	-238	19.37	0.05	-0.59	0.03	0.03	0.06
154	1 30 53.2	30 27 26	-754	-1	18.38	-0.05	-0.60	0.02	0.03	0.06
155	1 31 12.1	30 27 31	-750	1029	20.78	0.29	...	0.08	0.07	...
156	1 30 51.1	30 27 25	-750	-119	19.65	-0.04	...	0.03	0.03	...
157	1 30 53.7	30 27 25	-750	22	20.38	0.02	...	0.11	0.06	...
158	1 30 56.7	30 27 26	-748	188	19.08	-0.32	...	0.04	0.03	...
159	1 30 54.8	30 27 25	-747	87	18.10	0.12	-0.50	0.02	0.03	0.06
160	1 31 10.3	30 27 30	-745	930	18.58	0.15	-0.90	0.05	0.05	0.03
161	1 30 56.6	30 27 25	-742	183	19.72	-0.03	...	0.05	0.07	...
162	1 30 52.2	30 27 23	-741	-61	20.25	-0.20	0.15	0.23	0.16	0.15
163	1 30 56.6	30 27 24	-740	184	19.86	-0.46	-0.76	0.22	0.06	0.04
164	1 30 57.2	30 27 23	-733	214	19.88	-0.16	...	0.04	0.03	...
165	1 30 57.2	30 27 22	-732	215	19.70	0.13	-1.09	0.06	0.11	0.03
166	1 31 10.2	30 27 26	-730	927	20.40	-0.13	-0.75	0.07	0.06	0.04
167	1 30 56.8	30 27 22	-729	191	19.82	-0.08	...	0.04	0.03	...
168	1 31 15.0	30 27 27	-728	1189	19.11	0.36	-0.25	0.05	0.05	0.04
169	1 30 56.3	30 27 21	-727	163	19.75	-0.20	...	0.04	0.03	...
170	1 30 56.0	30 27 20	-724	149	19.95	-0.21	...	0.04	0.03	...
171	1 30 50.6	30 27 16	-715	-144	19.97	-0.06	-0.44	0.04	0.03	0.06
172	1 30 58.1	30 27 19	-715	262	19.32	0.06	-0.39	0.05	0.05	0.03
173	1 31 01.9	30 27 19	-711	469	20.26	0.33	-0.15	0.08	0.06	0.05
174	1 30 56.9	30 27 17	-708	197	20.05	-0.03	...	0.05	0.04	...
175	1 31 13.8	30 27 22	-708	1125	20.04	0.18	-0.92	0.06	0.06	0.04
176	1 31 11.6	30 27 21	-706	1000	18.89	0.16	-0.18	0.05	0.05	0.03
177	1 30 49.2	30 27 14	-706	-223	18.31	-0.13	-0.78	0.02	0.03	0.06
178	1 30 56.9	30 27 16	-705	198	19.92	0.02	...	0.07	0.06	...
179	1 31 10.1	30 27 20	-705	920	20.10	0.36	-0.75	0.07	0.06	0.04
180	1 30 47.0	30 27 13	-704	-344	20.05	-0.13	-0.85	0.04	0.03	0.06
181	1 30 51.5	30 27 14	-703	-98	20.57	-0.18	-0.77	0.06	0.04	0.06
182	1 30 56.8	30 27 15	-702	190	18.57	-0.10	...	0.02	0.03	...
183	1 30 46.6	30 27 11	-699	-365	19.33	-0.12	...	0.03	0.03	...
184	1 30 56.8	30 27 14	-699	191	18.49	-0.01	-0.83	0.05	0.05	0.03
185	1 31 09.3	30 27 18	-698	876	20.56	0.32	...	0.08	0.07	...
186	1 31 01.6	30 27 15	-696	454	20.18	-0.10	...	0.08	0.06	...
187	1 30 50.8	30 27 12	-696	-139	19.55	0.21	-0.13	0.03	0.03	0.06
188	1 30 52.6	30 27 12	-694	-40	20.12	-0.07	-0.65	0.05	0.03	0.06
189	1 30 46.5	30 27 10	-693	-369	20.14	-0.25	-0.91	0.05	0.04	0.06
190	1 30 48.7	30 27 10	-689	-252	20.90	0.09	...	0.07	0.06	...
191	1 30 52.5	30 27 10	-685	-44	19.06	0.03	-0.07	0.03	0.03	0.06
192	1 31 12.8	30 27 16	-683	1065	18.58	0.20	-0.30	0.05	0.05	0.03
193	1 30 45.9	30 27 7	-682	-403	19.87	0.21	-0.87	0.04	0.17	0.07
194	1 30 46.1	30 27 6	-677	-394	19.47	0.06	-0.61	0.04	0.03	0.06
195	1 30 51.8	30 27 8	-676	-81	19.42	-0.05	-0.42	0.03	0.06	0.06
196	1 30 55.8	30 27 8	-674	136	20.72	0.35	0.29	0.10	0.06	0.08
197	1 30 55.6	30 27 6	-665	126	20.88	0.27	1.03	0.10	0.06	0.15
198	1 31 02.0	30 27 8	-665	477	20.01	-0.08	-0.78	0.15	0.06	0.03
199	1 30 57.5	30 27 6	-664	229	20.90	-0.28	...	0.09	0.04	...
200	1 30 53.4	30 27 3	-657	5	20.53	0.09	...	0.06	0.05	...

TABLE 2 (cont.)

Number	α(1950)	δ(1950)	X	Y	V	B-V	U-B	σ_V	σ_B	σ_U
201	1 30 58.6	30 27 5	-656	290	19.06	0.11	-0.13	0.05	0.05	0.03
202	1 31 09.3	30 27 8	-656	873	19.93	-0.01	-1.00	0.09	0.05	0.03
203	1 30 59.8	30 27 5	-655	355	20.69	-0.04	...	0.12	0.10	...
204	1 31 12.2	30 27 9	-655	1032	19.28	-0.05	...	0.17	0.12	...
205	1 30 56.5	30 27 3	-652	176	20.07	0.26	0.23	0.05	0.05	0.07
206	1 30 56.4	30 27 3	-652	168	19.99	-0.07	0.48	0.07	0.04	0.08
207	1 30 51.6	30 27 2	-652	-93	19.92	-0.02	-0.83	0.05	0.05	0.06
208	1 31 09.7	30 27 7	-649	895	20.17	0.02	-0.75	0.07	0.06	0.04
209	1 31 00.8	30 27 2	-641	407	19.83	0.10	...	0.07	0.06	...
210	1 30 46.1	30 26 57	-640	-394	20.17	-0.09	...	0.05	0.03	...
211	1 30 51.3	30 26 59	-639	-109	19.49	-0.15	-0.79	0.03	0.03	0.06
212	1 30 57.0	30 26 60	-637	204	20.57	-0.14	...	0.07	0.04	...
213	1 30 54.9	30 26 59	-636	88	20.22	0.26	...	0.05	0.04	...
214	1 30 53.4	30 26 58	-636	4	19.99	-0.09	-0.11	0.07	0.06	0.12
215	1 30 53.5	30 26 58	-633	8	18.42	0.02	-0.42	0.04	0.03	0.06
216	1 30 48.6	30 26 56	-632	-260	20.58	-0.16	-0.91	0.05	0.09	0.06
217	1 30 57.9	30 26 59	-632	249	20.50	0.06	-1.08	0.09	0.07	0.03
218	1 31 09.8	30 27 2	-630	904	20.92	-0.27	-0.72	0.10	0.06	0.04
219	1 31 03.3	30 27 0	-630	546	19.43	0.20	-0.32	0.05	0.05	0.06
220	1 31 03.1	30 26 59	-626	533	18.60	0.30	0.24	0.05	0.05	0.04
221	1 30 53.6	30 26 56	-625	16	19.74	0.33	...	0.04	0.03	...
222	1 31 16.8	30 27 2	-621	1283	19.55	0.13	0.40	0.06	0.05	0.29
223	1 31 08.5	30 26 58	-612	831	20.19	-0.21	...	0.07	0.06	...
224	1 31 10.3	30 26 57	-606	929	20.26	0.09	-0.24	0.08	0.06	0.05
225	1 31 08.1	30 26 55	-602	810	18.55	-0.01	-1.00	0.05	0.05	0.04
226	1 31 16.0	30 26 57	-600	1238	20.01	0.01	-0.98	0.06	0.05	0.03
227	1 30 53.0	30 26 49	-596	-16	18.75	0.06	-0.38	0.03	0.03	0.06
228	1 30 57.2	30 26 50	-593	212	19.65	0.04	...	0.04	0.03	...
229	1 30 56.9	30 26 50	-593	195	20.16	0.11	-0.11	0.05	0.04	0.07
230	1 31 11.1	30 26 54	-593	972	19.21	0.18	-0.31	0.05	0.05	0.03
231	1 31 00.2	30 26 51	-593	378	19.98	-0.05	-0.90	0.08	0.06	0.03
232	1 30 57.2	30 26 49	-590	213	19.58	0.01	...	0.06	0.05	...
233	1 31 08.2	30 26 52	-588	811	19.55	-0.17	-1.38	0.06	0.05	0.04
234	1 30 50.6	30 26 45	-581	-151	19.47	0.32	0.32	0.04	0.03	0.06
235	1 31 08.8	30 26 50	-580	845	18.05	0.52	-0.53	0.05	0.05	0.03
236	1 30 53.6	30 26 45	-579	13	20.99	0.20	...	0.09	0.06	...
237	1 31 11.6	30 26 50	-576	999	20.76	-0.09	...	0.07	0.05	...
238	1 31 08.1	30 26 49	-575	805	18.84	-0.04	...	0.05	0.04	...
239	1 30 57.2	30 26 45	-575	213	20.17	0.12	...	0.05	0.04	...
240	1 31 08.1	30 26 49	-574	807	18.62	0.03	-1.10	0.05	0.05	0.04
241	1 30 54.6	30 26 44	-574	68	20.49	0.02	...	0.05	0.04	...
242	1 31 12.0	30 26 49	-570	1018	20.66	0.05	-0.47	0.09	0.07	0.05
243	1 31 08.0	30 26 48	-570	801	19.78	-0.05	...	0.05	0.04	...
244	1 30 48.2	30 26 39	-561	-282	20.25	0.39	0.58	0.05	0.04	0.08
245	1 31 00.3	30 26 43	-561	380	19.99	0.03	...	0.04	0.03	...
246	1 31 11.1	30 26 46	-560	973	19.87	0.24	...	0.03	0.03	...
247	1 30 58.2	30 26 42	-559	268	20.55	0.21	...	0.04	0.05	...
248	1 31 11.2	30 26 46	-558	975	19.92	0.30	0.24	0.06	0.06	0.04
249	1 31 12.3	30 26 46	-557	1034	20.38	0.17	...	0.04	0.04	...
250	1 30 53.7	30 26 39	-552	16	20.15	0.10	...	0.05	0.04	...

TABLE 2 (cont.)

Number	α(1950)	δ(1950)	X	Y	V	B-V	U-B	σ_V	σ_B	σ_U
251	1 30 52.7	30 26 38	-551	-38	18.45	-0.04	-0.61	0.03	0.03	0.06
252	1 31 06.7	30 26 42	-550	732	20.52	0.17	...	0.06	0.08	...
253	1 30 56.3	30 26 39	-549	160	20.70	-0.16	-0.88	0.15	0.04	0.06
254	1 31 06.7	30 26 42	-548	732	20.49	0.24	...	0.08	0.06	...
255	1 31 14.5	30 26 44	-547	1159	20.82	0.19	-0.82	0.11	0.09	0.05
256	1 30 49.5	30 26 36	-547	-212	19.70	-0.16	...	0.04	0.03	...
257	1 30 56.3	30 26 38	-546	161	20.42	-0.15	...	0.08	0.08	...
258	1 30 52.6	30 26 37	-546	-42	20.39	-0.17	-0.72	0.10	0.06	0.07
259	1 30 59.6	30 26 39	-544	342	20.29	-0.26	...	0.19	0.03	...
260	1 30 46.1	30 26 34	-542	-399	20.38	0.28	...	0.05	0.04	...
261	1 31 13.1	30 26 43	-541	1079	20.63	-0.36	...	0.16	0.05	...
262	1 30 48.3	30 26 34	-541	-280	20.12	0.23	0.26	0.05	0.03	0.07
263	1 31 13.1	30 26 42	-540	1080	20.14	0.04	-0.93	0.07	0.05	0.04
264	1 30 59.5	30 26 38	-540	333	20.46	0.16	...	0.07	0.03	...
265	1 30 57.9	30 26 37	-538	248	20.95	0.10	...	0.04	0.06	...
266	1 31 09.5	30 26 40	-537	883	20.69	0.30	...	0.05	0.04	...
267	1 30 52.7	30 26 35	-536	-38	20.51	-0.11	...	0.06	0.05	...
268	1 31 14.3	30 26 42	-536	1147	20.93	0.07	...	0.05	0.04	...
269	1 31 13.7	30 26 41	-534	1113	20.89	0.30	...	0.07	0.09	...
270	1 30 50.2	30 26 33	-534	-171	20.56	-0.02	-0.81	0.06	0.04	0.06
271	1 30 56.7	30 26 35	-534	181	19.89	0.19	...	0.04	0.03	...
272	1 30 57.9	30 26 36	-533	248	20.64	0.02	...	0.04	0.05	...
273	1 30 54.7	30 26 35	-532	71	19.49	0.11	...	0.04	0.03	...
274	1 30 51.6	30 26 33	-532	-97	20.35	-0.21	...	0.05	0.04	...
275	1 30 56.7	30 26 35	-532	183	20.04	0.04	...	0.05	0.06	...
276	1 31 13.4	30 26 40	-530	1094	20.09	-0.10	...	0.06	0.04	...
277	1 31 15.0	30 26 40	-529	1182	20.99	-0.05	...	0.04	0.04	...
278	1 31 13.9	30 26 40	-528	1123	19.47	0.11	...	0.04	0.04	...
279	1 31 13.4	30 26 40	-528	1096	19.84	0.10	...	0.06	0.06	...
280	1 30 52.4	30 26 33	-528	-53	20.17	0.02	-0.69	0.05	0.04	0.07
281	1 31 13.9	30 26 39	-527	1125	19.38	0.04	-0.65	0.06	0.05	0.03
282	1 31 14.5	30 26 40	-527	1158	19.68	0.02	...	0.03	0.03	...
283	1 31 14.6	30 26 39	-526	1161	19.74	-0.07	...	0.06	0.05	...
284	1 30 57.7	30 26 34	-526	239	20.23	0.04	...	0.03	0.04	...
285	1 31 10.9	30 26 38	-524	958	19.71	0.02	...	0.03	0.03	...
286	1 31 14.9	30 26 39	-524	1176	19.60	-0.07	...	0.03	0.03	...
287	1 30 51.9	30 26 32	-524	-80	19.85	-0.11	-0.46	0.04	0.03	0.06
288	1 31 10.9	30 26 38	-523	959	19.68	0.09	-1.16	0.10	0.08	0.03
289	1 31 14.9	30 26 39	-522	1178	19.07	0.23	...	0.06	0.05	...
290	1 30 54.5	30 26 32	-521	61	20.59	0.22	-1.16	0.07	0.06	0.07
291	1 31 08.1	30 26 36	-518	807	20.58	-0.09	-0.89	0.04	0.04	0.03
292	1 31 08.1	30 26 35	-517	808	20.73	-0.24	...	0.08	0.06	...
293	1 30 52.0	30 26 30	-516	-73	19.90	-0.27	-0.99	0.05	0.03	0.06
294	1 30 50.5	30 26 28	-511	-160	19.59	0.10	-0.52	0.03	0.03	0.02
295	1 30 49.1	30 26 28	-510	-233	20.62	0.10	...	0.05	0.04	...
296	1 31 13.3	30 26 35	-510	1089	19.34	0.36	-0.01	0.05	0.05	0.04
297	1 30 44.6	30 26 26	-510	-482	19.81	-0.24	...	0.03	0.03	...
298	1 30 54.0	30 26 29	-509	36	20.69	0.09	-0.62	0.13	0.05	0.03
299	1 31 17.6	30 26 36	-508	1328	20.38	0.11	...	0.11	0.06	...
300	1 30 58.0	30 26 29	-506	255	20.99	0.02	-0.65	0.05	0.04	0.03

TABLE 2 (cont.)

Number	α(1950)	δ(1950)	X	Y	V	B-V	U-B	σ_V	σ_B	σ_U
301	1 30 45.4	30 26 25	-506	-435	19.73	-0.21	-0.93	0.03	0.05	0.08
302	1 30 52.4	30 26 27	-505	-52	19.24	-0.22	-0.79	0.04	0.03	0.06
303	1 30 49.3	30 26 26	-505	-224	20.93	0.04	...	0.06	0.05	...
304	1 31 07.6	30 26 31	-501	780	18.81	-0.03	-0.89	0.03	0.03	0.23
305	1 30 52.5	30 26 26	-501	-49	20.60	-0.08	...	0.06	0.07	...
306	1 30 52.5	30 26 26	-500	-50	20.18	-0.04	...	0.07	0.06	...
307	1 31 15.4	30 26 33	-499	1206	20.14	0.13	0.34	0.03	0.04	0.05
308	1 30 52.4	30 26 26	-498	-55	20.93	-0.19	...	0.08	0.07	...
309	1 31 09.2	30 26 31	-498	864	20.62	0.22	0.57	0.08	0.06	0.07
310	1 31 15.5	30 26 33	-498	1209	20.04	0.30	...	0.07	0.06	...
311	1 31 13.3	30 26 32	-497	1092	20.83	0.36	...	0.09	0.09	...
312	1 31 13.4	30 26 32	-495	1096	20.20	0.23	...	0.92	0.80	...
313	1 30 52.1	30 26 25	-495	-72	20.38	-0.40	-0.84	0.05	0.04	0.07
314	1 31 12.7	30 26 31	-494	1057	20.82	-0.32	...	0.17	0.05	...
315	1 31 14.9	30 26 32	-493	1178	19.78	-0.02	...	0.03	0.03	...
316	1 30 58.2	30 26 26	-492	262	20.72	0.37	...	0.05	0.04	...
317	1 31 15.0	30 26 31	-491	1180	19.63	0.07	...	0.06	0.05	...
318	1 31 00.0	30 26 26	-490	362	19.01	0.02	-0.89	0.06	0.05	0.03
319	1 31 17.4	30 26 32	-490	1313	18.18	-0.08	...	0.05	0.05	...
320	1 30 54.3	30 26 24	-486	48	19.81	-0.08	-0.76	0.05	0.05	0.04
321	1 30 54.2	30 26 23	-486	46	19.58	0.17	...	0.04	0.06	...
322	1 30 54.2	30 26 23	-486	43	20.72	0.13	...	0.13	0.12	...
323	1 30 56.3	30 26 24	-485	159	19.26	0.09	...	0.04	0.01	...
324	1 31 13.5	30 26 29	-484	1102	18.58	-0.04	...	0.07	0.04	...
325	1 31 13.6	30 26 29	-483	1104	18.55	0.00	-1.08	0.05	0.05	0.03
326	1 30 56.3	30 26 23	-483	160	19.06	0.18	-0.19	0.20	0.16	0.09
327	1 31 07.3	30 26 27	-482	763	19.73	0.09	...	0.03	0.03	...
328	1 31 07.4	30 26 26	-481	764	19.83	0.05	...	0.08	0.06	...
329	1 30 50.9	30 26 21	-480	-134	19.25	-0.07	-0.84	0.07	0.07	0.03
330	1 31 09.7	30 26 27	-479	890	19.97	-0.43	...	0.08	0.05	...
331	1 30 57.4	30 26 23	-479	219	19.39	-0.26	-0.55	0.15	0.03	0.06
332	1 30 57.4	30 26 22	-477	219	20.24	0.19	...	0.07	0.11	...
333	1 31 17.6	30 26 29	-476	1322	20.37	-0.18	...	0.12	0.08	...
334	1 31 07.4	30 26 25	-476	766	20.44	0.26	-1.38	0.13	0.09	0.04
335	1 30 57.4	30 26 22	-476	221	19.13	0.07	-0.71	0.19	0.17	0.07
336	1 30 51.1	30 26 20	-475	-126	20.67	-0.05	-0.75	0.05	0.04	0.04
337	1 30 58.9	30 26 22	-475	301	19.82	0.08	-0.86	0.04	0.03	0.02
338	1 30 54.4	30 26 20	-471	57	19.82	-0.13	-0.99	0.04	0.02	0.03
339	1 30 51.3	30 26 19	-470	-113	20.69	0.49	-1.31	0.05	0.06	0.07
340	1 30 52.3	30 26 19	-470	-58	19.11	0.20	0.05	0.01	0.00	0.15
341	1 30 56.9	30 26 20	-469	191	20.87	0.22	-0.65	0.05	0.07	0.03
342	1 30 45.4	30 26 17	-469	-438	20.53	-0.06	-0.93	0.05	0.06	0.05
343	1 31 09.0	30 26 24	-469	855	20.10	-0.09	-0.82	0.08	0.06	0.03
344	1 30 57.5	30 26 20	-468	227	20.67	0.17	-0.49	0.04	0.04	0.03
345	1 30 52.2	30 26 19	-468	-66	18.79	-0.05	-0.77	0.02	0.04	0.09
346	1 31 09.1	30 26 24	-468	857	20.23	-0.17	-1.20	0.07	0.05	0.03
347	1 30 44.8	30 26 16	-467	-470	18.13	-0.17	...	0.03	0.04	...
348	1 30 54.3	30 26 19	-467	47	20.72	0.06	-0.57	0.05	0.05	0.05
349	1 31 07.1	30 26 23	-466	752	18.45	0.28	-0.63	0.09	0.04	0.26
350	1 30 55.5	30 26 19	-465	116	20.86	-0.13	...	0.06	0.06	...

TABLE 2 (cont.)

Number	α(1950)	δ(1950)	X	Y	V	B-V	U-B	σ_V	σ_B	σ_U
351	1 31 14.3	30 26 25	-464	1143	20.88	-0.12	-0.52	0.08	0.05	0.18
352	1 30 59.0	30 26 20	-463	304	21.00	0.31	...	0.07	0.06	...
353	1 31 17.3	30 26 25	-462	1307	15.86	0.27	...	0.05	0.05	...
354	1 30 44.8	30 26 15	-461	-469	17.05	0.06	-0.87	0.02	0.02	0.04
355	1 30 57.1	30 26 18	-460	200	20.72	0.13	-0.86	0.05	0.05	0.03
356	1 30 50.7	30 26 16	-460	-149	18.75	0.13	-0.76	0.02	0.07	0.02
357	1 30 53.7	30 26 17	-459	16	19.32	-0.09	-1.01	0.04	0.03	0.06
358	1 31 13.4	30 26 23	-458	1094	20.79	0.18	0.76	0.23	0.05	0.19
359	1 30 60.0	30 26 19	-458	360	20.84	-0.02	0.14	0.08	0.06	0.15
360	1 31 16.8	30 26 24	-458	1279	19.31	0.11	-0.93	0.06	0.06	0.06
361	1 30 51.9	30 26 16	-457	-81	20.09	0.39	...	0.16	0.10	...
362	1 31 11.6	30 26 22	-457	994	19.81	0.14	-0.75	0.07	0.08	0.03
363	1 30 53.2	30 26 16	-456	-9	19.94	0.18	-0.83	0.04	0.05	0.03
364	1 30 51.2	30 26 15	-455	-122	18.19	-0.10	-0.87	0.00	0.02	0.02
365	1 31 11.6	30 26 22	-455	995	19.84	-0.10	...	0.06	0.05	...
366	1 30 53.6	30 26 16	-453	10	20.46	-0.37	-0.98	0.10	0.04	0.03
367	1 30 49.5	30 26 14	-453	-215	19.65	-0.07	-0.75	0.03	0.05	0.03
368	1 30 58.1	30 26 17	-451	255	20.90	0.13	-0.25	0.05	0.05	0.03
369	1 30 56.8	30 26 16	-451	184	20.89	0.32	...	0.06	0.05	...
370	1 30 52.1	30 26 14	-450	-70	19.06	0.22	-0.14	0.04	0.02	0.02
371	1 30 57.8	30 26 16	-448	239	19.76	0.28	-0.83	0.03	0.06	0.02
372	1 30 54.6	30 26 15	-448	64	20.83	0.33	-0.33	0.07	0.06	0.08
373	1 31 10.0	30 26 20	-448	907	19.34	0.38	0.02	0.08	0.07	0.03
374	1 30 53.8	30 26 14	-448	21	20.06	0.07	-0.10	0.04	0.05	0.04
375	1 30 53.8	30 26 14	-447	21	20.05	0.10	...	0.01	0.03	...
376	1 30 53.9	30 26 14	-447	29	20.76	-0.16	...	0.02	0.03	...
377	1 30 53.9	30 26 14	-447	28	20.75	-0.17	-0.87	0.06	0.05	0.03
378	1 31 02.3	30 26 17	-447	485	19.85	-0.14	...	0.16	0.03	...
379	1 31 10.0	30 26 19	-447	908	19.52	0.16	...	0.06	0.05	...
380	1 30 51.0	30 26 13	-445	-132	20.36	-0.14	-0.72	0.05	0.04	0.03
381	1 30 53.2	30 26 13	-445	-15	20.12	0.01	-0.70	0.04	0.04	0.09
382	1 30 47.4	30 26 12	-444	-329	19.08	-0.12	-0.92	0.05	0.04	0.01
383	1 30 57.0	30 26 14	-442	194	20.67	-0.05	...	0.06	0.04	...
384	1 30 56.0	30 26 13	-441	141	20.87	-0.15	-1.14	0.06	0.04	0.03
385	1 31 01.3	30 26 15	-439	432	20.78	0.04	...	0.08	0.08	...
386	1 31 01.4	30 26 14	-437	434	20.87	0.29	...	0.07	0.12	...
387	1 30 53.0	30 26 12	-437	-24	20.48	0.19	...	0.04	0.05	...
388	1 30 56.7	30 26 12	-435	180	20.49	0.18	...	0.20	0.02	...
389	1 31 09.3	30 26 16	-434	870	20.68	0.27	...	0.09	0.07	...
390	1 30 44.9	30 26 8	-434	-467	19.22	0.27	-0.63	0.04	0.03	0.05
391	1 30 56.7	30 26 12	-433	181	20.68	0.01	-0.98	0.06	0.07	0.03
392	1 31 05.5	30 26 14	-432	663	20.46	-0.16	...	0.10	0.03	...
393	1 31 16.8	30 26 18	-431	1281	19.17	-0.15	...	0.05	0.05	...
394	1 31 06.5	30 26 14	-430	716	20.72	0.30	-0.31	0.05	0.04	0.05
395	1 31 00.9	30 26 12	-430	408	20.37	-0.78	-1.05	0.40	0.06	0.02
396	1 31 00.9	30 26 12	-429	407	19.75	-0.16	-0.98	0.24	0.06	0.02
397	1 30 48.2	30 26 8	-429	-286	19.92	0.19	0.11	0.03	0.03	0.03
398	1 30 45.9	30 26 7	-428	-412	20.01	0.12	-0.69	0.04	0.03	0.03
399	1 30 54.7	30 26 10	-428	70	19.32	0.06	-0.45	0.00	0.01	0.07
400	1 30 56.9	30 26 10	-426	193	20.73	-0.24	...	0.06	0.04	...

TABLE 2 (cont.)

Number	α(1950)	δ(1950)	X	Y	V	B-V	U-B	σ_V	σ_B	σ_U
401	1 30 56.9	30 26 10	-424	192	20.84	0.06	-0.83	0.07	0.08	0.19
402	1 31 07.3	30 26 13	-424	758	20.92	0.23	...	0.04	0.04	...
403	1 30 56.5	30 26 9	-423	166	19.76	0.17	-0.17	0.04	0.03	0.06
404	1 30 52.7	30 26 8	-423	-39	20.85	0.28	...	0.08	0.06	...
405	1 30 57.0	30 26 9	-422	194	20.83	0.35	-0.71	0.07	0.12	0.26
406	1 30 56.5	30 26 9	-421	167	19.75	0.05	-0.10	0.11	0.25	0.09
407	1 31 12.5	30 26 13	-418	1046	20.42	0.26	-0.04	0.08	0.06	0.05
408	1 31 16.4	30 26 14	-417	1257	20.12	0.28	...	0.13	0.06	...
409	1 31 01.0	30 26 9	-416	415	18.84	0.06	-0.94	0.22	0.04	0.12
410	1 31 17.7	30 26 15	-416	1327	20.18	0.22	-0.22	0.07	0.06	0.04
411	1 31 05.7	30 26 11	-416	672	20.57	0.36	...	0.15	0.11	...
412	1 31 09.8	30 26 12	-414	897	20.95	-0.68	...	0.29	0.06	...
413	1 30 44.8	30 26 3	-413	-474	20.99	0.20	...	0.13	0.14	...
414	1 31 05.7	30 26 10	-413	672	19.90	0.38	...	0.06	0.06	...
415	1 31 09.8	30 26 11	-413	897	20.33	0.14	...	0.07	0.06	...
416	1 31 05.7	30 26 10	-412	671	20.85	0.21	...	0.27	0.15	...
417	1 30 52.7	30 26 6	-412	-38	20.21	0.14	...	0.06	0.05	...
418	1 30 53.9	30 26 5	-409	24	19.84	0.11	-0.12	0.06	0.05	0.04
419	1 30 54.6	30 26 5	-408	66	18.89	-0.12	...	0.05	0.02	...
420	1 31 01.0	30 26 7	-408	411	20.31	-0.14	-0.90	0.13	0.04	0.03
421	1 30 53.8	30 26 4	-405	21	20.21	0.21	...	0.08	0.08	...
422	1 30 57.0	30 26 5	-405	195	20.88	0.26	...	0.05	0.05	...
423	1 30 52.2	30 26 4	-405	-69	20.39	0.21	-0.88	0.07	0.12	0.05
424	1 30 52.2	30 26 4	-404	-69	20.00	0.39	...	0.49	0.28	...
425	1 30 52.7	30 26 4	-404	-41	19.21	-0.07	-0.31	0.04	0.04	0.05
426	1 30 46.2	30 26 2	-404	-398	20.34	0.00	-1.07	0.04	0.08	0.04
427	1 31 00.9	30 26 6	-403	407	20.26	0.26	-1.06	0.07	0.05	0.03
428	1 31 01.1	30 26 6	-402	421	20.77	-0.19	-1.33	0.08	0.03	0.03
429	1 31 05.9	30 26 7	-402	683	20.29	0.35	...	0.09	0.25	...
430	1 31 05.9	30 26 7	-401	683	20.36	0.12	-0.29	0.04	0.03	0.03
431	1 31 06.0	30 26 7	-400	685	20.76	-0.20	...	0.10	0.06	...
432	1 30 45.4	30 26 0	-400	-439	20.58	0.34	...	0.04	0.05	...
433	1 31 05.8	30 26 7	-399	676	19.90	0.16	...	0.29	0.12	...
434	1 31 05.8	30 26 7	-399	675	19.90	0.16	0.38	0.29	0.12	0.27
435	1 31 08.8	30 26 7	-398	839	20.70	0.20	...	0.08	0.10	...
436	1 31 01.9	30 26 5	-398	464	20.84	0.17	...	0.34	0.47	...
437	1 31 08.7	30 26 7	-398	836	20.70	0.08	...	0.07	0.09	...
438	1 31 05.8	30 26 6	-398	676	19.72	0.30	...	0.06	0.06	...
439	1 30 52.6	30 26 2	-398	-45	19.57	0.36	-0.63	0.04	0.04	0.05
440	1 31 08.8	30 26 7	-396	839	19.42	0.32	...	0.06	0.05	...
441	1 31 00.7	30 26 4	-395	399	16.61	0.23	-0.94	0.06	0.03	0.02
442	1 31 00.7	30 26 4	-394	400	16.67	0.20	...	0.08	0.05	...
443	1 31 08.0	30 26 6	-393	794	20.19	0.82	-1.22	0.12	0.12	0.03
444	1 30 54.5	30 26 1	-390	60	20.50	-0.13	-0.63	0.05	0.04	0.06
445	1 30 57.8	30 26 2	-389	238	20.75	0.38	...	0.05	0.06	...
446	1 30 58.0	30 26 2	-389	248	20.23	0.09	-0.75	0.04	0.03	0.03
447	1 31 08.7	30 26 5	-388	835	20.20	0.24	-0.71	0.06	0.04	0.03
448	1 30 57.5	30 26 1	-387	220	20.91	0.22	...	0.09	0.04	...
449	1 30 57.7	30 26 1	-386	235	20.81	0.85	-1.28	0.06	0.05	0.05
450	1 30 58.2	30 26 1	-383	262	21.00	0.06	-0.49	0.04	0.04	0.04

TABLE 2 (cont.)

Number	α(1950)	δ(1950)	X	Y	V	B-V	U-B	σ_V	σ_B	σ_U
451	1 30 44.8	30 25 56	-383	-471	20.82	0.18	...	0.05	0.05	...
452	1 30 57.9	30 26 0	-382	244	20.63	0.22	-0.14	0.06	0.06	0.05
453	1 31 05.1	30 26 2	-382	640	20.83	0.03	-1.07	0.04	0.04	0.03
454	1 30 52.0	30 25 58	-381	-81	20.71	-0.06	...	0.05	0.05	...
455	1 31 12.2	30 26 4	-380	1026	20.05	-0.07	-0.83	0.08	0.07	0.03
456	1 30 53.5	30 25 58	-379	0	20.54	0.11	...	0.04	0.05	...
457	1 30 44.6	30 25 55	-378	-483	19.93	0.25	-0.03	0.03	0.03	0.09
458	1 30 57.7	30 25 59	-377	232	20.69	0.27	...	0.04	0.04	...
459	1 30 54.7	30 25 58	-377	66	20.20	-0.10	...	0.04	0.04	...
460	1 31 10.6	30 26 3	-376	940	20.37	0.04	0.11	0.26	0.08	0.04
461	1 31 12.7	30 26 3	-375	1055	20.09	-0.23	-0.83	0.18	0.05	0.03
462	1 31 10.4	30 26 2	-373	926	17.34	0.06	-0.61	0.08	0.06	0.03
463	1 31 01.5	30 25 59	-371	439	20.77	-0.13	-1.37	0.07	0.04	0.03
464	1 30 57.1	30 25 57	-370	199	20.92	0.13	0.15	0.06	0.06	0.06
465	1 30 58.4	30 25 57	-369	270	20.85	0.17	-0.57	0.04	0.03	0.04
466	1 31 01.3	30 25 58	-369	431	19.57	0.05	-1.30	0.06	0.05	0.03
467	1 30 51.8	30 25 55	-368	-88	19.95	0.07	-0.53	0.04	0.03	0.03
468	1 31 11.1	30 26 1	-366	965	19.73	0.25	...	0.08	0.09	...
469	1 31 01.2	30 25 57	-366	425	20.89	0.07	...	0.12	0.06	...
470	1 30 52.1	30 25 54	-363	-72	20.45	-0.12	...	0.04	0.04	...
471	1 30 51.7	30 25 53	-361	-95	18.80	0.16	-0.37	0.02	0.02	0.03
472	1 31 08.3	30 25 59	-361	815	20.58	0.03	-0.77	0.06	0.04	0.03
473	1 30 45.6	30 25 51	-360	-430	20.32	-0.11	-0.83	0.04	0.03	0.03
474	1 30 45.2	30 25 51	-360	-454	20.44	0.00	-0.80	0.04	0.03	0.03
475	1 31 04.8	30 25 57	-360	619	20.38	-0.02	-0.69	0.05	0.04	0.03
476	1 31 04.2	30 25 57	-359	588	20.85	0.32	-0.03	0.05	0.04	0.05
477	1 31 10.2	30 25 59	-359	916	20.63	0.50	-1.22	0.08	0.29	0.03
478	1 31 14.0	30 25 60	-358	1127	20.59	0.06	...	0.04	0.07	...
479	1 31 06.8	30 25 57	-355	728	20.90	0.11	-0.41	0.04	0.04	0.06
480	1 30 52.6	30 25 52	-352	-45	20.52	-0.08	...	0.06	0.05	...
481	1 30 48.7	30 25 50	-352	-261	20.78	-0.13	-1.06	0.05	0.04	0.03
482	1 31 05.3	30 25 55	-350	647	20.88	0.02	-0.48	0.04	0.04	0.04
483	1 30 47.2	30 25 49	-350	-345	20.75	0.10	-0.70	0.05	0.05	0.03
484	1 31 01.9	30 25 54	-349	462	19.88	0.22	-0.85	0.05	0.03	0.02
485	1 30 51.6	30 25 50	-348	-103	20.84	-0.10	-1.05	0.06	0.06	0.04
486	1 30 56.8	30 25 51	-345	182	20.75	0.14	-0.19	0.05	0.05	0.04
487	1 30 54.5	30 25 50	-345	54	20.96	0.07	-0.62	0.06	0.05	0.04
488	1 30 52.9	30 25 50	-345	-30	19.91	0.17	-0.09	0.04	0.04	0.04
489	1 31 13.3	30 25 56	-344	1086	19.16	0.08	-0.35	0.03	0.03	0.03
490	1 30 52.2	30 25 49	-343	-67	20.24	0.30	0.09	0.04	0.04	0.05
491	1 30 56.8	30 25 51	-343	183	20.21	0.37	0.20	0.05	0.06	0.04
492	1 31 06.7	30 25 54	-343	727	19.61	0.08	-0.68	0.03	0.03	0.04
493	1 31 02.6	30 25 52	-341	502	20.09	0.21	0.42	0.03	0.03	0.03
494	1 31 12.7	30 25 55	-339	1051	17.65	0.13	-0.05	0.04	0.04	0.03
495	1 30 57.2	30 25 49	-337	204	19.53	-0.08	-0.86	0.03	0.03	0.03
496	1 30 45.5	30 25 46	-337	-434	20.99	-0.35	...	0.06	0.04	...
497	1 30 53.7	30 25 48	-336	14	20.20	-0.12	-0.76	0.04	0.03	0.03
498	1 30 46.2	30 25 45	-335	-396	20.50	-0.05	-0.80	0.04	0.04	0.03
499	1 30 57.4	30 25 49	-334	217	20.43	0.03	-0.89	0.04	0.03	0.04
500	1 31 05.1	30 25 51	-334	634	20.42	0.07	-0.76	0.03	0.04	0.03

TABLE 2 (cont.)

Number	α(1950)	δ(1950)	X	Y	V	B-V	U-B	σ_V	σ_B	σ_U
501	1 31 06.0	30 25 51	-333	688	20.93	0.08	...	0.01	0.06	...
502	1 31 01.9	30 25 50	-333	461	19.38	0.15	-0.38	0.04	0.03	0.02
503	1 31 06.0	30 25 51	-333	688	20.93	0.08	-0.76	0.01	0.06	0.29
504	1 31 05.7	30 25 51	-333	671	20.74	-0.04	0.02	0.12	0.06	0.06
505	1 31 09.3	30 25 52	-331	868	20.62	-0.08	-1.04	0.07	0.06	0.06
506	1 31 06.1	30 25 51	-330	690	20.20	0.30	...	0.21	0.04	...
507	1 31 08.0	30 25 51	-329	795	20.77	0.87	-0.68	0.08	0.07	0.06
508	1 31 00.4	30 25 48	-329	379	19.53	0.29	-0.76	0.06	0.03	0.03
509	1 31 09.5	30 25 51	-328	874	19.60	0.08	-1.18	0.06	0.05	0.03
510	1 30 46.3	30 25 44	-327	-394	19.97	-0.07	-0.72	0.04	0.03	0.03
511	1 31 04.1	30 25 49	-327	581	20.23	0.26	-0.05	0.03	0.03	0.03
512	1 30 53.4	30 25 46	-327	-2	20.38	0.26	...	0.05	0.05	...
513	1 30 51.5	30 25 45	-325	-110	20.64	-0.24	-0.93	0.06	0.05	0.04
514	1 30 47.1	30 25 43	-322	-350	20.61	0.18	0.10	0.17	0.05	0.05
515	1 31 03.9	30 25 48	-322	568	20.14	0.19	...	0.03	0.03	...
516	1 31 10.5	30 25 50	-322	932	20.42	-0.14	-0.60	0.05	0.07	0.07
517	1 30 51.5	30 25 44	-322	-106	20.82	-0.16	-0.63	0.07	0.06	0.05
518	1 31 15.3	30 25 51	-321	1196	20.97	0.07	...	0.05	0.05	...
519	1 31 00.6	30 25 46	-320	390	20.90	0.00	...	0.06	0.04	...
520	1 31 05.1	30 25 47	-318	634	20.28	0.20	-0.72	0.05	0.03	0.03
521	1 31 06.3	30 25 48	-317	704	20.78	0.09	...	0.02	0.01	...
522	1 31 06.3	30 25 48	-317	703	20.78	0.09	-0.50	0.02	0.01	0.05
523	1 31 02.2	30 25 46	-314	479	20.96	0.34	...	0.05	0.04	...
524	1 31 12.6	30 25 49	-313	1048	19.90	0.19	-0.71	0.03	0.03	0.03
525	1 30 45.4	30 25 39	-311	-445	18.14	-0.11	-0.94	0.02	0.02	0.03
526	1 30 56.6	30 25 43	-310	172	20.75	-0.04	...	0.05	0.04	...
527	1 31 02.4	30 25 44	-309	489	20.06	-0.08	-0.94	0.03	0.03	0.03
528	1 30 56.6	30 25 42	-308	173	20.43	0.24	-0.61	0.03	0.05	0.04
529	1 31 03.7	30 25 45	-308	559	20.83	0.15	...	0.05	0.04	...
530	1 31 03.6	30 25 45	-308	555	20.42	0.15	...	0.04	0.03	...
531	1 30 52.3	30 25 41	-308	-65	20.88	0.27	...	0.07	0.06	...
532	1 31 02.2	30 25 44	-308	480	20.80	-0.04	-0.89	0.05	0.03	0.03
533	1 30 47.5	30 25 39	-306	-328	19.74	0.06	-0.77	0.03	0.03	0.03
534	1 31 06.6	30 25 45	-306	720	20.55	0.08	-0.05	0.03	0.03	0.05
535	1 30 51.3	30 25 39	-303	-118	18.39	-0.02	-0.54	0.04	0.02	0.03
536	1 30 49.1	30 25 39	-303	-239	19.97	0.22	0.03	0.03	0.03	0.03
537	1 30 49.4	30 25 39	-302	-225	20.29	0.09	-0.36	0.04	0.04	0.03
538	1 31 00.6	30 25 42	-302	388	20.59	0.40	...	0.07	0.05	...
539	1 31 02.4	30 25 42	-297	486	18.34	0.14	-1.02	0.03	0.03	0.02
540	1 30 51.3	30 25 38	-295	-121	18.34	-0.05	-0.71	0.02	0.02	0.03
541	1 31 01.8	30 25 41	-294	452	19.50	-0.04	-0.88	0.05	0.03	0.03
542	1 31 01.0	30 25 40	-293	409	20.19	0.40	...	0.05	0.03	...
543	1 31 11.5	30 25 43	-292	983	19.52	0.12	-0.07	0.03	0.03	0.03
544	1 31 13.3	30 25 44	-291	1084	20.37	-0.03	-0.67	0.03	0.03	0.05
545	1 31 06.5	30 25 41	-289	712	20.34	0.14	...	0.04	0.03	...
546	1 31 15.3	30 25 44	-289	1193	20.34	0.22	...	0.03	0.04	...
547	1 31 01.8	30 25 39	-288	452	20.15	0.01	-0.70	0.03	0.03	0.05
548	1 31 00.7	30 25 39	-287	393	20.09	0.04	...	0.15	0.09	...
549	1 30 59.6	30 25 38	-286	335	20.05	0.09	-0.80	0.04	0.03	0.03
550	1 30 55.6	30 25 37	-286	114	20.35	0.32	0.41	0.05	0.04	0.05

TABLE 2 (cont.)

Number	α(1950)	δ(1950)	X	Y	V	B-V	U-B	σ_V	σ_B	σ_U
551	1 31 01.0	30 25 38	-285	409	19.67	0.05	0.28	0.07	0.03	0.04
552	1 31 07.3	30 25 40	-283	754	20.41	0.02	...	0.05	0.05	...
553	1 31 00.6	30 25 38	-283	389	18.55	0.16	...	0.10	0.07	...
554	1 30 48.6	30 25 34	-283	-269	20.08	0.24	0.04	0.05	0.06	0.04
555	1 31 00.9	30 25 38	-282	402	19.23	0.03	-1.07	0.05	0.03	0.02
556	1 31 00.6	30 25 37	-280	390	18.46	0.05	...	0.10	0.06	...
557	1 30 54.1	30 25 35	-280	35	21.00	0.38	...	0.08	0.09	...
558	1 31 05.6	30 25 39	-280	665	20.32	0.39	-0.72	0.04	0.04	0.03
559	1 31 10.4	30 25 40	-279	924	20.72	0.01	...	0.05	0.05	...
560	1 31 07.3	30 25 39	-278	756	20.43	0.27	...	0.05	0.05	...
561	1 31 00.5	30 25 37	-278	382	17.96	0.25	-0.34	0.06	0.04	0.03
562	1 31 08.4	30 25 39	-277	814	20.31	0.06	...	0.04	0.04	...
563	1 31 02.5	30 25 36	-273	493	18.95	0.16	...	0.03	0.04	...
564	1 31 10.4	30 25 38	-273	923	20.06	-0.08	...	0.03	0.05	...
565	1 31 02.1	30 25 36	-272	473	19.34	0.20	...	0.03	0.04	...
566	1 31 06.8	30 25 37	-269	730	20.27	0.11	-0.77	0.04	0.04	0.05
567	1 31 00.6	30 25 35	-269	388	20.75	-0.01	...	0.06	0.04	...
568	1 31 00.5	30 25 34	-269	384	20.53	-0.02	...	0.06	0.04	...
569	1 31 01.0	30 25 34	-268	408	20.25	0.17	...	0.05	0.05	...
570	1 31 02.2	30 25 35	-268	476	19.33	0.32	...	0.03	0.04	...
571	1 31 00.9	30 25 34	-267	405	20.75	0.04	...	0.06	0.06	...
572	1 31 06.0	30 25 36	-267	684	20.67	0.06	...	0.02	0.02	...
573	1 31 02.1	30 25 34	-267	470	17.56	0.31	-0.87	0.03	0.03	0.02
574	1 31 06.0	30 25 36	-267	684	20.66	0.06	-0.66	0.04	0.04	0.03
575	1 31 00.5	30 25 33	-265	381	20.24	0.57	-1.41	0.06	0.07	0.04
576	1 30 52.4	30 25 31	-265	-62	18.89	-0.35	-0.86	0.04	0.02	0.03
577	1 30 46.2	30 25 29	-264	-398	19.73	-0.20	-1.03	0.03	0.02	0.03
578	1 31 01.9	30 25 34	-264	460	20.46	0.00	-0.65	0.04	0.04	0.08
579	1 31 10.2	30 25 36	-263	916	19.62	-0.03	-0.86	0.03	0.03	0.03
580	1 31 01.8	30 25 33	-261	452	20.97	0.28	...	0.06	0.04	...
581	1 31 02.9	30 25 33	-261	514	20.58	0.30	...	0.04	0.04	...
582	1 30 49.0	30 25 29	-260	-247	20.28	-0.35	...	0.04	0.03	...
583	1 30 54.0	30 25 30	-260	27	18.87	-0.21	-0.69	0.02	0.02	0.04
584	1 31 01.3	30 25 32	-260	426	20.86	0.06	-0.71	0.04	0.04	0.04
585	1 31 01.9	30 25 32	-259	458	20.20	0.11	-0.82	0.03	0.04	0.05
586	1 31 09.8	30 25 35	-258	891	20.24	0.01	-0.70	0.03	0.03	0.03
587	1 30 51.0	30 25 29	-258	-136	20.26	0.40	...	0.04	0.05	...
588	1 31 05.2	30 25 33	-258	638	20.19	0.11	-0.80	0.03	0.04	0.03
589	1 30 60.0	30 25 32	-258	355	20.01	0.20	-0.16	0.04	0.03	0.03
590	1 31 02.5	30 25 32	-258	491	20.12	0.03	-0.87	0.04	0.04	0.06
591	1 31 10.7	30 25 35	-257	941	20.11	0.04	...	0.05	0.04	...
592	1 30 53.0	30 25 29	-256	-29	20.33	-0.19	-1.02	0.14	0.11	0.07
593	1 30 52.9	30 25 29	-256	-33	20.94	-0.59	-0.74	0.24	0.13	0.12
594	1 31 02.4	30 25 32	-255	488	20.28	0.14	-1.04	0.04	0.05	0.07
595	1 31 10.7	30 25 34	-255	944	19.19	0.02	-1.15	0.03	0.04	0.03
596	1 30 53.9	30 25 29	-253	21	20.79	-0.13	-0.66	0.06	0.05	0.07
597	1 31 10.9	30 25 34	-253	951	20.12	0.06	...	0.03	0.03	...
598	1 31 15.4	30 25 35	-252	1197	20.81	0.30	...	0.04	0.04	...
599	1 31 00.7	30 25 30	-251	394	20.57	0.35	...	0.05	0.04	...
600	1 31 01.7	30 25 30	-251	447	20.83	0.17	-1.00	0.05	0.06	0.03

TABLE 2 (cont.)

Number	α(1950)	δ(1950)	X	Y	V	B-V	U-B	σ_V	σ_B	σ_U
601	1 31 01.8	30 25 30	-250	456	20.54	0.23	...	0.03	0.04	...
602	1 31 11.3	30 25 33	-248	972	20.89	-0.08	...	0.05	0.04	...
603	1 31 02.6	30 25 30	-247	500	20.07	0.15	-1.04	0.03	0.03	0.03
604	1 30 59.9	30 25 29	-247	347	20.72	0.12	...	0.06	0.04	...
605	1 31 02.0	30 25 30	-247	462	20.93	-0.02	...	0.06	0.05	...
606	1 31 01.9	30 25 29	-246	456	20.13	0.14	...	0.03	0.03	...
607	1 31 06.3	30 25 31	-245	697	20.29	-0.03	...	0.05	0.05	...
608	1 31 06.2	30 25 31	-245	696	20.29	-0.03	-0.56	0.05	0.05	0.27
609	1 30 53.6	30 25 26	-244	3	20.07	-0.31	-0.66	0.06	0.03	0.03
610	1 31 06.9	30 25 30	-243	732	20.52	0.11	-0.40	0.04	0.04	0.04
611	1 31 01.5	30 25 28	-243	435	20.95	0.22	-0.14	0.06	0.06	0.09
612	1 31 11.3	30 25 31	-242	974	20.60	-0.01	-1.16	0.03	0.04	0.03
613	1 31 12.3	30 25 32	-242	1027	20.42	0.45	-1.32	0.05	0.21	0.03
614	1 30 59.9	30 25 27	-240	350	17.82	0.34	-0.07	0.03	0.03	0.02
615	1 31 01.7	30 25 28	-240	447	20.89	-0.10	-0.43	0.07	0.04	0.05
616	1 30 59.7	30 25 27	-239	340	19.67	0.36	...	0.03	0.03	...
617	1 31 07.0	30 25 29	-235	740	20.76	-0.20	-0.65	0.08	0.04	0.03
618	1 30 53.6	30 25 24	-235	2	20.09	-0.26	...	0.04	0.04	...
619	1 30 52.2	30 25 24	-234	-71	20.08	0.17	-1.03	0.08	0.08	0.06
620	1 31 10.6	30 25 29	-233	936	20.12	0.26	...	0.03	0.04	...
621	1 30 52.1	30 25 23	-232	-79	19.84	-0.07	-1.03	0.04	0.04	0.03
622	1 31 06.1	30 25 27	-232	689	20.77	-0.07	...	0.06	0.03	...
623	1 31 06.1	30 25 27	-232	688	20.77	-0.07	-0.81	0.06	0.03	0.36
624	1 30 55.1	30 25 24	-231	86	18.75	0.04	-0.86	0.02	0.02	0.03
625	1 30 52.2	30 25 23	-230	-73	19.85	-0.23	-0.73	0.07	0.05	0.05
626	1 30 52.0	30 25 22	-229	-84	20.49	0.00	-1.08	0.06	0.05	0.07
627	1 31 06.1	30 25 27	-228	688	20.42	-0.03	...	0.02	0.01	...
628	1 31 06.1	30 25 26	-228	687	20.42	-0.03	-0.79	0.02	0.01	0.09
629	1 30 58.1	30 25 24	-227	252	19.58	0.23	-0.11	0.03	0.03	0.02
630	1 31 06.2	30 25 25	-223	696	19.65	0.12	...	0.06	0.02	...
631	1 31 06.2	30 25 25	-223	695	19.65	0.12	-0.12	0.06	0.02	0.14
632	1 31 08.2	30 25 26	-222	806	18.04	0.14	-0.11	0.03	0.03	0.05
633	1 30 57.8	30 25 22	-222	236	20.76	-0.05	-0.07	0.14	0.03	0.07
634	1 30 53.4	30 25 21	-220	-5	20.27	-0.12	-0.91	0.04	0.04	0.03
635	1 31 12.2	30 25 26	-219	1022	18.38	0.35	0.75	0.05	0.03	0.03
636	1 31 05.8	30 25 24	-219	674	19.91	0.13	...	0.03	0.08	...
637	1 31 01.5	30 25 23	-219	437	20.31	0.10	-0.88	0.04	0.03	0.03
638	1 31 05.8	30 25 24	-219	674	19.89	0.10	-0.73	0.03	0.04	0.02
639	1 31 02.0	30 25 23	-218	466	18.77	0.31	-0.11	0.03	0.03	0.02
640	1 31 06.2	30 25 24	-217	694	20.92	0.18	...	0.08	0.04	...
641	1 31 06.2	30 25 24	-217	693	20.92	0.18	-0.51	0.08	0.04	0.13
642	1 30 59.6	30 25 22	-217	331	20.92	0.16	-0.67	0.05	0.03	0.04
643	1 31 12.4	30 25 26	-216	1035	19.00	-0.04	-0.78	0.03	0.04	0.03
644	1 30 59.7	30 25 21	-214	340	19.96	-0.03	-0.79	0.04	0.03	0.02
645	1 30 51.0	30 25 18	-213	-140	19.52	-0.13	-0.96	0.03	0.02	0.03
646	1 31 09.0	30 25 23	-210	846	20.44	0.01	-0.56	0.03	0.04	0.03
647	1 30 58.2	30 25 19	-209	256	20.51	0.14	-0.31	0.06	0.03	0.03
648	1 31 06.8	30 25 22	-208	726	19.73	0.38	0.60	0.03	0.04	0.04
649	1 31 14.4	30 25 24	-207	1143	20.74	-0.04	-0.40	0.06	0.09	0.06
650	1 31 10.9	30 25 23	-205	949	20.72	0.24	-0.82	0.04	0.04	0.09

TABLE 2 (cont.)

Number	α(1950)	δ(1950)	X	Y	V	B-V	U-B	σ_V	σ_B	σ_U
651	1 31 05.7	30 25 20	-202	666	18.24	0.25	-0.03	0.03	0.04	0.02
652	1 31 15.0	30 25 23	-202	1175	20.95	0.18	...	0.07	0.05	...
653	1 31 11.8	30 25 20	-193	1000	20.91	0.11	...	0.04	0.04	...
654	1 30 49.6	30 25 13	-193	-215	20.64	-0.10	-0.91	0.05	0.04	0.03
655	1 30 45.0	30 25 11	-190	-469	19.81	-0.10	-0.88	0.03	0.02	0.03
656	1 31 13.5	30 25 19	-185	1091	20.96	0.03	0.08	0.06	0.04	0.07
657	1 31 14.9	30 25 19	-185	1172	20.15	0.23	...	0.03	0.04	...
658	1 31 11.9	30 25 18	-184	1003	20.94	0.09	...	0.04	0.04	...
659	1 30 59.9	30 25 14	-184	349	19.63	0.10	-1.05	0.04	0.03	0.02
660	1 30 51.8	30 25 11	-184	-98	20.68	0.31	-0.92	0.05	0.05	0.04
661	1 31 11.4	30 25 17	-182	980	20.45	0.23	...	0.05	0.04	...
662	1 31 00.7	30 25 14	-182	393	20.15	0.18	0.55	0.03	0.03	0.04
663	1 31 12.0	30 25 17	-181	1011	20.80	0.17	0.42	0.04	0.06	0.11
664	1 31 05.0	30 25 15	-180	627	18.53	-0.05	-0.98	0.03	0.04	0.02
665	1 30 50.4	30 25 10	-179	-172	19.65	0.47	-0.82	0.03	0.03	0.03
666	1 31 08.5	30 25 15	-178	817	20.46	0.32	...	0.04	0.04	...
667	1 31 11.4	30 25 16	-178	976	20.27	0.40	...	0.05	0.05	...
668	1 31 08.9	30 25 15	-176	841	20.37	0.05	-0.63	0.04	0.04	0.03
669	1 31 09.7	30 25 15	-175	886	20.77	0.43	-1.10	0.04	0.11	0.04
670	1 31 04.8	30 25 13	-174	614	20.20	-0.02	-0.88	0.04	0.04	0.03
671	1 31 05.0	30 25 13	-174	624	19.10	0.17	-1.01	0.03	0.05	0.02
672	1 30 51.8	30 25 9	-174	-94	20.79	0.24	-0.90	0.07	0.05	0.03
673	1 31 06.1	30 25 14	-174	689	19.43	0.30	...	0.02	0.00	...
674	1 31 06.1	30 25 14	-174	688	19.43	0.30	-0.34	0.02	0.00	0.11
675	1 31 05.2	30 25 13	-173	637	20.98	0.09	-1.01	0.05	0.05	0.04
676	1 31 12.0	30 25 15	-170	1007	19.39	0.22	-0.18	0.03	0.04	0.03
677	1 31 05.1	30 25 12	-167	633	20.99	0.32	...	0.05	0.06	...
678	1 31 11.4	30 25 14	-166	974	19.20	0.22	-0.56	0.03	0.04	0.03
679	1 30 54.0	30 25 8	-166	27	20.99	0.29	...	0.07	0.06	...
680	1 31 14.4	30 25 14	-164	1139	20.28	0.33	...	0.03	0.04	...
681	1 31 15.7	30 25 14	-163	1214	18.97	0.16	...	0.08	0.10	...
682	1 31 07.5	30 25 11	-162	762	20.37	-0.01	-0.67	0.05	0.04	0.05
683	1 31 13.1	30 25 13	-162	1069	20.90	0.03	...	0.04	0.04	...
684	1 31 05.1	30 25 10	-160	633	20.18	-0.06	-1.10	0.04	0.03	0.03
685	1 30 54.6	30 25 7	-160	58	19.58	-0.04	-0.17	0.03	0.02	0.03
686	1 31 05.4	30 25 10	-160	647	20.85	0.12	-0.74	0.06	0.03	0.05
687	1 31 07.4	30 25 10	-158	759	20.72	0.10	...	0.06	0.05	...
688	1 31 04.2	30 25 9	-157	584	20.62	0.18	-0.56	0.04	0.03	0.03
689	1 31 09.5	30 25 10	-155	873	20.77	0.08	-0.20	0.05	0.04	0.07
690	1 30 53.0	30 25 5	-154	-30	20.16	0.17	-0.27	0.04	0.04	0.03
691	1 30 45.9	30 25 2	-151	-418	19.99	-0.13	-0.88	0.03	0.02	0.03
692	1 30 47.3	30 25 2	-150	-344	19.25	0.03	-0.36	0.02	0.02	0.03
693	1 31 05.0	30 25 8	-149	624	19.08	-0.02	-0.62	0.03	0.03	0.02
694	1 31 08.3	30 25 9	-149	809	20.22	0.18	0.46	0.06	0.04	0.06
695	1 31 05.8	30 25 7	-147	669	18.93	-0.07	...	0.21	0.01	...
696	1 31 05.8	30 25 7	-147	669	18.93	-0.07	-0.97	0.21	0.01	0.07
697	1 30 54.2	30 25 4	-146	37	20.77	0.20	-0.04	0.05	0.05	0.05
698	1 31 05.1	30 25 6	-143	633	19.69	-0.10	-1.11	0.05	0.03	0.03
699	1 30 48.7	30 25 1	-142	-268	20.09	0.14	-0.12	0.03	0.03	0.03
700	1 31 05.2	30 25 6	-141	638	19.76	-0.01	-1.03	0.04	0.03	0.03

TABLE 2 (cont.)

Number	α(1950)	δ(1950)	X	Y	V	B-V	U-B	σ_V	σ_B	σ_U
701	1 30 52.8	30 25 2	-141	-40	20.46	-0.30	-0.77	0.09	0.04	0.04
702	1 31 05.5	30 25 5	-137	653	18.75	0.06	-0.85	0.03	0.03	0.02
703	1 30 52.1	30 24 60	-134	-80	20.67	-0.08	-0.82	0.06	0.05	0.04
704	1 31 05.3	30 25 4	-133	641	18.49	0.45	-0.88	0.04	0.03	0.02
705	1 30 59.1	30 25 1	-129	304	19.55	0.38	0.22	0.06	0.03	0.03
706	1 31 11.2	30 25 5	-129	965	20.33	0.25	...	0.07	0.05	...
707	1 31 05.4	30 25 3	-127	647	19.94	0.12	...	0.06	0.04	...
708	1 30 55.7	30 24 59	-126	114	20.84	0.39	1.36	0.05	0.05	0.13
709	1 31 10.9	30 25 4	-126	950	20.57	0.32	-0.82	0.07	0.16	0.04
710	1 31 05.5	30 25 2	-126	651	20.33	0.03	-1.55	0.08	0.04	0.03
711	1 31 07.6	30 25 3	-125	768	20.09	0.13	-0.80	0.07	0.05	0.03
712	1 31 09.1	30 25 3	-125	848	19.71	0.51	-0.80	0.08	0.13	0.03
713	1 31 02.4	30 25 1	-125	482	20.67	-0.11	-1.34	0.18	0.09	0.03
714	1 31 12.0	30 25 4	-124	1009	19.95	0.49	-0.56	0.05	0.05	0.04
715	1 31 04.9	30 25 2	-124	622	20.85	0.19	...	0.06	0.06	...
716	1 30 52.3	30 24 57	-123	-69	19.83	-0.08	-0.46	0.04	0.03	0.05
717	1 31 11.5	30 25 3	-122	979	20.73	0.38	...	0.08	0.05	...
718	1 31 11.7	30 25 3	-122	992	20.01	-0.17	...	0.08	0.08	...
719	1 31 05.2	30 25 1	-122	637	20.75	0.35	...	0.05	0.13	...
720	1 31 15.2	30 25 4	-122	1185	19.60	0.23	...	0.04	0.04	...
721	1 30 52.8	30 24 57	-121	-41	20.79	-0.46	-0.13	0.06	0.05	0.06
722	1 31 05.0	30 25 1	-121	623	20.58	0.38	...	0.06	0.06	...
723	1 30 52.5	30 24 57	-120	-57	20.19	0.06	-0.78	0.04	0.05	0.03
724	1 30 53.6	30 24 57	-120	0	19.95	-0.10	-0.91	0.04	0.03	0.03
725	1 31 11.7	30 25 3	-120	991	19.45	0.36	...	0.06	0.09	...
726	1 31 02.5	30 24 60	-119	491	20.95	-0.12	...	0.11	0.05	...
727	1 31 05.7	30 25 1	-119	662	20.75	-0.08	-0.99	0.08	0.04	0.03
728	1 31 07.1	30 25 1	-119	742	20.82	-0.02	-1.34	0.04	0.04	0.03
729	1 30 54.4	30 24 57	-118	47	19.77	-0.31	-1.16	0.04	0.02	0.03
730	1 31 10.3	30 25 2	-118	917	20.58	0.08	-1.36	0.17	0.08	0.03
731	1 31 02.5	30 24 59	-118	488	20.76	0.02	...	0.09	0.05	...
732	1 31 07.3	30 25 1	-117	752	20.99	0.11	-1.89	0.11	0.12	0.06
733	1 31 10.6	30 25 2	-116	933	18.45	0.65	-0.58	0.08	0.12	0.03
734	1 31 10.3	30 25 2	-116	917	20.98	-0.16	...	0.25	0.09	...
735	1 31 05.0	30 24 60	-116	626	20.75	0.33	...	0.06	0.06	...
736	1 31 11.9	30 25 2	-116	1003	20.73	0.04	...	0.06	0.06	...
737	1 31 10.6	30 25 1	-114	932	20.19	-0.52	...	0.37	0.20	...
738	1 31 02.6	30 24 59	-114	492	18.97	0.35	-1.21	0.06	0.03	0.02
739	1 31 07.4	30 24 60	-113	755	19.90	0.07	...	0.06	0.04	...
740	1 31 02.1	30 24 58	-112	464	20.14	0.30	...	0.07	0.07	...
741	1 31 02.2	30 24 58	-112	472	20.22	0.33	-0.89	0.07	0.05	0.03
742	1 31 02.0	30 24 57	-110	463	20.40	0.03	-1.91	0.10	0.08	0.04
743	1 31 01.9	30 24 57	-109	455	20.54	0.02	-1.19	0.08	0.04	0.03
744	1 31 07.8	30 24 58	-106	778	20.13	0.20	-0.25	0.08	0.09	0.13
745	1 31 02.1	30 24 56	-105	467	20.42	0.17	...	0.07	0.05	...
746	1 31 02.6	30 24 56	-105	494	19.74	0.50	-1.67	0.06	0.12	0.02
747	1 30 52.5	30 24 53	-104	-58	20.78	-0.10	-0.88	0.11	0.09	0.04
748	1 30 58.1	30 24 54	-102	247	19.72	1.01	-0.91	0.04	0.11	0.03
749	1 30 59.9	30 24 54	-99	345	20.69	0.07	-1.00	0.06	0.05	0.03
750	1 31 11.4	30 24 58	-98	974	20.82	-0.50	-0.74	0.08	0.07	0.03

TABLE 2 (cont.)

Number	α(1950)	δ(1950)	X	Y	V	B-V	U-B	σ_V	σ_B	σ_U
751	1 30 55.9	30 24 52	-97	127	19.61	0.04	-0.81	0.03	0.02	0.06
752	1 31 08.9	30 24 56	-96	836	20.53	-0.35	-0.67	0.07	0.07	0.03
753	1 31 07.2	30 24 56	-95	743	20.30	-0.12	-0.75	0.03	0.04	0.03
754	1 30 51.9	30 24 50	-93	-95	20.94	-0.39	-0.75	0.06	0.04	0.03
755	1 30 50.4	30 24 48	-85	-177	20.60	0.15	-1.00	0.05	0.08	0.03
756	1 31 07.2	30 24 53	-83	745	20.67	0.81	-1.78	0.05	0.15	0.07
757	1 30 52.1	30 24 48	-82	-84	19.43	0.05	-0.52	0.03	0.02	0.03
758	1 30 53.5	30 24 48	-81	-4	20.77	0.17	-0.59	0.06	0.06	0.04
759	1 31 08.6	30 24 53	-81	820	19.79	-0.02	-0.90	0.09	0.07	0.03
760	1 31 12.5	30 24 53	-77	1035	19.62	0.04	-0.65	0.19	0.10	0.03
761	1 31 08.4	30 24 51	-76	808	20.88	0.14	...	0.08	0.09	...
762	1 31 05.7	30 24 51	-76	662	20.98	0.20	0.31	0.05	0.04	0.10
763	1 31 02.5	30 24 50	-76	487	20.63	-0.42	...	0.07	0.04	...
764	1 31 02.7	30 24 49	-74	497	20.80	0.14	-1.89	0.08	0.05	0.03
765	1 31 04.7	30 24 49	-72	607	20.12	-0.02	-0.20	0.35	0.03	0.03
766	1 31 09.5	30 24 51	-72	869	20.83	-0.34	-0.77	0.17	0.06	0.04
767	1 31 05.4	30 24 49	-70	645	19.14	0.20	-0.99	0.06	0.04	0.02
768	1 31 03.9	30 24 49	-70	565	20.61	0.15	...	0.13	0.06	...
769	1 30 57.8	30 24 46	-69	232	20.62	0.79	-1.43	0.05	0.14	0.06
770	1 31 09.8	30 24 50	-68	889	20.79	-0.56	...	0.16	0.09	...
771	1 31 10.1	30 24 49	-65	906	19.79	0.49	-1.72	0.07	0.09	0.03
772	1 30 52.0	30 24 44	-64	-85	19.83	-0.09	-0.87	0.04	0.03	0.03
773	1 30 55.6	30 24 43	-59	108	19.58	-0.14	-1.07	0.03	0.02	0.03
774	1 30 55.7	30 24 43	-57	117	20.31	0.04	...	0.04	0.04	...
775	1 31 05.1	30 24 45	-54	628	20.81	0.31	-1.52	0.06	0.23	0.03
776	1 31 09.7	30 24 47	-54	883	20.98	-0.18	...	0.08	0.09	...
777	1 31 03.6	30 24 45	-54	547	20.70	-0.33	-1.36	0.28	0.06	0.03
778	1 31 03.8	30 24 44	-52	558	20.47	0.51	-1.66	0.22	0.22	0.03
779	1 31 15.4	30 24 48	-51	1191	20.98	-0.01	...	0.07	0.05	...
780	1 31 12.0	30 24 47	-50	1009	20.02	-0.38	-1.04	0.22	0.09	0.03
781	1 31 02.1	30 24 43	-49	463	19.90	-0.08	...	0.16	0.10	...
782	1 31 10.9	30 24 46	-49	947	21.00	0.00	-0.13	0.14	0.09	0.08
783	1 31 09.8	30 24 45	-48	886	20.61	-0.16	...	0.42	0.09	...
784	1 31 01.7	30 24 43	-47	445	19.75	-0.42	...	0.19	0.19	...
785	1 31 02.2	30 24 43	-47	470	17.61	0.12	-1.31	0.37	0.13	0.02
786	1 31 02.2	30 24 43	-47	469	17.49	0.59	-1.76	0.29	0.15	0.02
787	1 31 00.8	30 24 42	-46	391	20.98	0.00	-0.90	0.08	0.06	0.08
788	1 31 09.8	30 24 45	-45	885	19.91	-0.44	...	0.17	0.09	...
789	1 31 11.9	30 24 45	-44	1001	20.96	0.03	...	0.42	0.09	...
790	1 31 06.6	30 24 43	-42	712	20.37	0.14	...	0.04	0.04	...
791	1 31 01.8	30 24 41	-41	448	20.07	-0.35	...	0.13	0.08	...
792	1 30 51.0	30 24 37	-39	-143	20.31	0.38	...	0.05	0.05	...
793	1 31 01.8	30 24 41	-39	448	20.56	-0.55	...	0.18	0.10	...
794	1 31 09.4	30 24 42	-35	865	19.50	-0.05	-0.86	0.22	0.09	0.06
795	1 31 02.9	30 24 40	-34	506	20.40	0.79	-0.90	0.07	0.08	0.07
796	1 31 09.4	30 24 42	-34	864	19.87	0.24	...	0.29	0.14	...
797	1 31 03.1	30 24 40	-32	517	20.89	-0.53	-1.19	0.16	0.04	0.03
798	1 31 10.8	30 24 42	-32	942	18.99	-0.86	-0.21	0.28	0.07	0.03
799	1 31 10.8	30 24 42	-31	941	18.67	-0.54	-0.35	0.20	0.07	0.03
800	1 31 12.1	30 24 42	-31	1009	20.09	-0.01	...	0.31	0.09	...

TABLE 2 (cont.)

Number	α(1950)	δ(1950)	X	Y	V	B-V	U-B	σ_V	σ_B	σ_U
801	1 31 12.1	30 24 42	-29	1009	20.80	-0.22	...	0.46	0.11	...
802	1 31 02.1	30 24 38	-29	464	19.82	-0.38	...	0.28	0.06	...
803	1 31 11.4	30 24 41	-29	973	21.00	0.08	-1.04	0.11	0.08	0.13
804	1 31 02.1	30 24 38	-29	462	19.10	0.10	...	0.17	0.05	...
805	1 31 11.9	30 24 41	-27	998	20.89	-0.43	...	0.14	0.09	...
806	1 31 09.0	30 24 40	-27	844	19.66	0.62	-1.41	0.05	0.23	0.03
807	1 31 02.0	30 24 37	-23	457	20.69	0.17	-1.08	0.08	0.06	0.05
808	1 31 10.7	30 24 40	-22	933	20.41	0.33	...	0.08	0.07	...
809	1 31 04.8	30 24 37	-21	610	20.05	0.18	-1.40	0.28	0.22	0.02
810	1 31 10.5	30 24 39	-20	924	20.90	0.39	...	0.11	0.10	...
811	1 31 02.2	30 24 35	-15	470	20.79	0.55	-1.13	0.11	0.13	0.05
812	1 31 09.2	30 24 37	-12	854	20.72	0.18	...	0.06	0.12	...
813	1 31 01.6	30 24 34	-12	436	20.35	-0.02	...	0.07	0.07	...
814	1 31 01.5	30 24 34	-10	433	20.20	-0.34	...	0.09	0.07	...
815	1 30 56.1	30 24 32	-9	135	20.68	-0.03	...	0.05	0.05	...
816	1 31 12.7	30 24 37	-9	1044	20.92	-0.14	-1.54	0.25	0.14	0.03
817	1 30 55.9	30 24 32	-9	123	20.87	0.22	0.10	0.07	0.06	0.08
818	1 31 01.9	30 24 33	-8	451	20.27	0.22	...	0.09	0.11	...
819	1 30 57.6	30 24 32	-7	218	20.34	0.26	-0.88	0.06	0.04	0.03
820	1 31 01.9	30 24 33	-6	450	20.58	0.14	...	0.11	0.15	...
821	1 31 02.1	30 24 33	-5	462	20.79	-0.01	-1.36	0.09	0.05	0.05
822	1 31 10.5	30 24 35	-4	921	20.79	-0.20	...	0.32	0.08	...
823	1 31 10.6	30 24 35	-2	928	20.75	0.12	...	0.53	0.48	...
824	1 30 55.3	30 24 29	2	93	20.10	0.31	...	0.04	0.04	...
825	1 31 02.4	30 24 31	2	482	19.92	0.06	...	0.15	0.09	...
826	1 31 02.4	30 24 31	3	481	19.86	0.14	...	0.21	0.09	...
827	1 31 11.2	30 24 34	4	964	21.00	-0.30	...	0.64	0.34	...
828	1 31 09.5	30 24 32	7	868	20.83	0.31	...	0.13	0.44	...
829	1 30 50.0	30 24 26	9	-201	20.75	0.02	-0.92	0.08	0.04	0.03
830	1 31 15.5	30 24 34	10	1198	19.80	0.03	...	0.02	0.03	...
831	1 31 09.8	30 24 32	10	887	19.29	0.20	-0.88	0.08	0.05	0.03
832	1 30 59.6	30 24 28	11	329	20.69	0.02	...	0.06	0.07	...
833	1 31 07.1	30 24 30	11	738	17.90	0.02	-0.81	0.06	0.04	0.03
834	1 31 11.1	30 24 32	12	957	20.97	-0.08	...	0.60	0.44	...
835	1 31 10.3	30 24 31	12	910	20.80	-0.11	...	0.46	0.11	...
836	1 31 01.7	30 24 28	13	441	20.19	-0.31	...	0.10	0.04	...
837	1 31 04.1	30 24 29	13	570	20.41	-0.07	...	0.08	0.07	...
838	1 30 50.5	30 24 25	13	-173	20.18	-0.02	-1.04	0.04	0.03	0.03
839	1 31 01.7	30 24 28	15	441	20.31	-0.02	...	0.09	0.06	...
840	1 31 11.3	30 24 31	16	964	20.79	0.14	-1.11	0.09	0.11	0.05
841	1 31 06.4	30 24 29	17	699	20.89	0.17	...	0.19	0.24	...
842	1 31 11.2	30 24 30	17	963	20.02	0.25	...	0.04	0.03	...
843	1 31 05.3	30 24 28	19	636	20.73	0.29	-1.45	0.07	0.08	0.03
844	1 31 03.9	30 24 27	21	559	20.15	0.17	-1.32	0.06	0.04	0.03
845	1 30 56.3	30 24 25	21	144	18.53	-0.16	-0.99	0.02	0.02	0.03
846	1 31 10.3	30 24 29	21	912	19.95	0.11	...	0.03	0.03	...
847	1 31 10.3	30 24 29	21	913	20.68	-0.38	-1.23	0.33	0.08	0.03
848	1 30 57.3	30 24 25	22	201	20.78	-0.11	...	0.14	0.05	...
849	1 31 01.6	30 24 26	25	438	19.73	-0.02	...	0.06	0.07	...
850	1 30 56.4	30 24 24	26	150	19.93	-0.08	...	0.04	0.04	...

TABLE 2 (cont.)

Number	α(1950)	δ(1950)	X	Y	V	B-V	U-B	σ_V	σ_B	σ_U
851	1 31 00.6	30 24 25	26	379	20.22	0.04	-0.71	0.08	0.05	0.05
852	1 30 57.0	30 24 23	28	185	20.35	0.03	-0.78	0.04	0.04	0.03
853	1 30 56.2	30 24 23	30	142	20.32	0.03	...	0.09	0.05	...
854	1 31 10.5	30 24 27	30	924	19.01	-0.05	-0.83	0.09	0.07	0.03
855	1 30 52.3	30 24 21	30	-74	20.83	0.33	-0.16	0.06	0.05	0.06
856	1 30 59.5	30 24 23	31	318	19.70	1.17	-2.55	0.06	0.13	0.04
857	1 31 10.5	30 24 27	32	924	19.65	-0.69	...	0.18	0.07	...
858	1 31 14.4	30 24 28	32	1135	20.86	0.26	...	0.23	0.34	...
859	1 31 05.9	30 24 25	33	673	20.32	0.23	...	0.20	0.32	...
860	1 31 14.3	30 24 27	34	1130	20.00	0.01	-0.60	0.14	0.15	0.04
861	1 31 06.4	30 24 24	36	699	20.33	-0.03	-1.05	0.12	0.36	0.16
862	1 31 06.4	30 24 24	37	700	20.33	-0.03	...	0.12	0.36	...
863	1 31 08.9	30 24 25	37	837	18.74	0.37	0.33	0.06	0.04	0.03
864	1 31 13.3	30 24 26	37	1076	18.46	0.14	-0.81	0.01	0.01	0.14
865	1 31 11.5	30 24 25	39	974	20.99	-0.13	...	0.67	0.42	...
866	1 31 10.3	30 24 25	39	913	20.81	0.09	...	0.33	0.07	...
867	1 31 11.5	30 24 25	40	975	20.63	-0.02	-0.86	0.05	0.04	0.03
868	1 30 49.6	30 24 18	40	-222	20.74	0.18	...	0.05	0.05	...
869	1 31 11.7	30 24 24	43	987	20.08	0.26	...	0.59	0.32	...
870	1 31 11.0	30 24 24	44	952	20.66	0.26	...	0.04	0.04	...
871	1 31 11.3	30 24 24	44	965	20.18	0.19	...	0.06	0.06	...
872	1 30 55.4	30 24 19	46	93	18.94	0.24	-0.03	0.03	0.02	0.03
873	1 30 54.5	30 24 18	46	44	20.83	0.60	-0.74	0.06	0.08	0.05
874	1 31 06.6	30 24 22	47	711	20.48	0.14	0.30	0.07	0.04	0.07
875	1 31 12.0	30 24 23	48	1001	20.13	0.01	-0.83	0.04	0.03	0.03
876	1 31 12.0	30 24 23	48	1002	20.42	-0.15	...	0.49	0.20	...
877	1 31 08.6	30 24 22	50	816	20.35	0.26	-0.23	0.05	0.03	0.04
878	1 31 08.6	30 24 22	50	815	20.35	0.29	...	0.04	0.03	...
879	1 30 55.6	30 24 18	50	109	20.77	-0.03	-0.66	0.06	0.06	0.04
880	1 30 59.8	30 24 19	51	335	20.31	0.40	...	0.21	0.09	...
881	1 31 11.3	30 24 22	52	965	19.89	0.09	-0.83	0.03	0.03	0.03
882	1 31 09.5	30 24 22	52	865	20.45	0.25	0.20	0.03	0.05	0.07
883	1 31 09.0	30 24 21	52	837	20.39	0.04	-0.15	0.06	0.03	0.04
884	1 31 12.1	30 24 22	54	1008	18.52	0.10	-0.71	0.03	0.03	0.03
885	1 30 59.9	30 24 18	54	344	20.30	-0.22	...	0.08	0.05	...
886	1 31 01.9	30 24 19	54	452	20.72	-0.17	...	0.09	0.13	...
887	1 30 52.6	30 24 15	56	-57	19.33	-0.08	-0.91	0.01	0.03	0.13
888	1 30 54.5	30 24 16	56	44	19.35	0.30	-0.03	0.03	0.02	0.04
889	1 30 54.5	30 24 16	57	45	19.52	0.17	...	0.27	0.06	...
890	1 31 06.4	30 24 19	58	699	20.59	0.18	0.19	0.05	0.04	0.05
891	1 31 03.3	30 24 18	58	526	20.30	-0.02	...	0.05	0.04	...
892	1 31 03.2	30 24 18	59	520	18.66	-0.12	-0.74	0.02	0.03	0.04
893	1 31 11.5	30 24 21	60	975	20.82	-0.03	-0.25	0.04	0.04	0.05
894	1 31 06.4	30 24 19	60	698	20.61	0.25	...	0.09	0.06	...
895	1 31 10.2	30 24 20	62	904	19.14	0.18	-0.10	0.04	0.03	0.04
896	1 31 03.2	30 24 17	62	521	18.61	-0.12	-0.84	0.02	0.03	0.03
897	1 30 48.5	30 24 13	62	-283	19.91	0.27	-0.75	0.05	0.14	0.20
898	1 30 44.6	30 24 11	62	-494	20.72	-0.06	-0.88	0.04	0.03	0.04
899	1 30 55.2	30 24 14	65	84	20.45	-0.13	-0.25	0.10	0.05	0.03
900	1 31 08.7	30 24 18	66	825	20.18	0.04	-0.85	0.03	0.03	0.04

TABLE 2 (cont.)

Number	α(1950)	δ(1950)	X	Y	V	B-V	U-B	σ_V	σ_B	σ_U
901	1 31 10.8	30 24 18	69	937	20.71	0.04	-0.78	0.03	0.04	0.04
902	1 31 11.7	30 24 18	69	985	20.76	0.13	...	0.03	0.03	...
903	1 31 08.9	30 24 17	70	832	20.21	-0.32	...	0.07	0.04	...
904	1 30 59.1	30 24 13	73	295	19.34	-0.62	-0.58	0.10	0.02	0.05
905	1 31 14.2	30 24 18	74	1125	18.40	0.06	-0.94	0.03	0.03	0.03
906	1 31 13.1	30 24 18	74	1064	20.67	0.53	-0.69	0.05	0.06	0.05
907	1 30 45.9	30 24 9	75	-424	19.41	0.04	-0.88	0.03	0.03	0.09
908	1 30 57.9	30 24 12	76	231	19.58	-0.07	-0.78	0.03	0.02	0.03
909	1 30 53.5	30 24 11	76	-8	19.72	0.10	-0.49	0.03	0.04	0.15
910	1 30 56.8	30 24 12	77	171	20.75	0.57	-0.69	0.05	0.14	0.07
911	1 30 46.4	30 24 8	77	-399	19.84	-0.21	...	0.02	0.02	...
912	1 31 13.9	30 24 17	79	1105	20.98	0.17	...	0.03	0.04	...
913	1 31 10.0	30 24 15	81	894	20.98	0.07	-1.25	0.04	0.03	0.04
914	1 30 59.2	30 24 11	81	302	20.52	-0.06	...	0.04	0.04	...
915	1 31 00.7	30 24 12	83	386	19.07	-0.16	-0.62	0.03	0.02	0.03
916	1 30 58.0	30 24 10	84	237	20.08	0.22	0.21	0.03	0.02	0.04
917	1 30 46.1	30 24 7	85	-412	20.33	0.13	...	0.09	0.16	...
918	1 30 52.1	30 24 8	86	-87	20.51	0.09	0.17	0.05	0.01	0.18
919	1 31 10.1	30 24 14	87	897	20.93	0.00	...	0.08	0.04	...
920	1 31 00.7	30 24 10	90	386	20.53	-0.52	...	0.07	0.04	...
921	1 31 14.5	30 24 14	90	1140	19.70	0.01	-0.93	0.02	0.03	0.03
922	1 31 10.1	30 24 12	93	900	20.64	0.05	...	0.04	0.05	...
923	1 31 10.3	30 24 12	93	910	19.55	0.23	-0.69	0.02	0.09	0.03
924	1 31 10.9	30 24 12	94	942	20.61	0.11	-0.57	0.03	0.03	0.04
925	1 31 02.5	30 24 9	95	484	18.70	-0.02	-0.85	0.01	0.02	0.03
926	1 31 08.7	30 24 11	98	824	19.59	0.20	-0.50	0.02	0.03	0.03
927	1 31 03.1	30 24 9	98	517	20.45	0.02	-1.20	0.07	0.06	0.05
928	1 31 01.3	30 24 8	98	417	19.02	0.50	-0.86	0.05	0.07	0.04
929	1 31 00.3	30 24 8	99	364	20.81	0.35	...	0.07	0.07	...
930	1 30 56.7	30 24 6	100	166	20.33	0.39	...	0.07	0.04	...
931	1 31 13.4	30 24 11	101	1076	20.11	0.33	0.68	0.03	0.03	0.06
932	1 30 58.8	30 24 7	101	279	20.10	0.18	-0.18	0.19	0.04	0.12
933	1 30 47.5	30 24 3	102	-338	20.38	-0.14	-0.92	0.03	0.02	0.04
934	1 30 59.4	30 24 7	102	311	20.16	0.16	-0.46	0.06	0.03	0.04
935	1 31 06.5	30 24 9	102	701	20.54	0.07	-0.96	0.02	0.31	0.06
936	1 30 58.8	30 24 6	104	282	20.61	0.36	...	0.07	0.08	...
937	1 30 59.8	30 24 6	105	334	20.89	0.60	-1.68	0.13	0.08	0.05
938	1 30 45.5	30 24 1	107	-446	19.58	-0.07	-0.75	0.02	0.02	0.04
939	1 31 03.3	30 24 7	107	527	20.62	-0.48	-1.39	0.08	0.06	0.04
940	1 31 03.2	30 24 7	107	523	20.37	0.09	-1.03	0.06	0.08	0.07
941	1 31 02.8	30 24 7	107	497	20.23	0.14	...	0.04	0.03	...
942	1 31 06.8	30 24 8	108	716	19.91	-0.14	-0.53	0.02	0.04	0.03
943	1 31 00.5	30 24 5	109	370	20.46	0.27	...	0.08	0.06	...
944	1 30 46.0	30 24 1	109	-423	19.38	0.02	-1.12	0.03	0.05	0.03
945	1 30 56.1	30 24 4	110	131	20.72	0.18	...	0.09	0.08	...
946	1 30 45.4	30 24 0	111	-454	19.93	-0.10	...	0.08	0.17	...
947	1 30 45.4	30 24 0	111	-454	19.99	-0.03	-0.76	0.03	0.03	0.05
948	1 31 01.2	30 24 5	112	411	20.83	0.37	...	0.12	0.09	...
949	1 30 46.3	30 24 0	112	-403	20.23	-0.20	-0.94	0.01	0.02	0.12
950	1 31 00.4	30 24 4	113	367	19.14	-0.08	-0.61	0.03	0.02	0.04

TABLE 2 (cont.)

Number	α(1950)	δ(1950)	X	Y	V	B-V	U-B	σ_V	σ_B	σ_U
951	1 31 10.4	30 24 8	113	913	19.06	0.17	-0.57	0.02	0.03	0.03
952	1 31 09.4	30 24 7	113	858	19.88	0.02	-0.92	0.03	0.04	0.03
953	1 31 04.2	30 24 5	114	578	20.91	0.09	-0.27	0.07	0.04	0.05
954	1 30 58.4	30 24 4	114	256	20.72	0.16	...	0.09	0.06	...
955	1 30 56.2	30 24 3	114	136	19.76	0.26	-0.02	0.03	0.04	0.05
956	1 30 56.5	30 24 3	115	153	20.64	0.00	...	0.16	0.07	...
957	1 30 51.5	30 24 1	116	-122	19.74	-0.01	-0.54	0.11	0.01	0.15
958	1 31 13.2	30 24 8	116	1065	20.83	0.23	-0.61	0.03	0.05	0.05
959	1 31 06.9	30 24 5	118	725	20.97	0.27	-0.78	0.08	0.04	0.05
960	1 30 59.6	30 24 3	118	324	19.09	0.28	0.14	0.03	0.02	0.04
961	1 31 02.9	30 24 4	119	501	19.51	0.17	-1.17	0.05	0.04	0.03
962	1 30 56.8	30 24 2	119	171	20.83	-0.11	...	0.07	0.05	...
963	1 30 56.4	30 24 1	120	148	20.56	-0.49	...	0.07	0.06	...
964	1 30 45.8	30 23 57	123	-435	19.03	-0.01	-0.84	0.04	0.05	0.11
965	1 31 08.5	30 24 5	123	810	19.96	0.24	...	0.03	0.09	...
966	1 31 03.0	30 24 3	124	509	20.57	0.18	...	0.09	0.07	...
967	1 31 01.9	30 24 2	124	446	20.16	0.16	0.48	0.04	0.03	0.06
968	1 30 45.3	30 23 56	126	-459	19.12	-0.03	-0.72	0.01	0.03	0.14
969	1 31 03.2	30 24 2	127	521	20.54	0.08	...	0.07	0.06	...
970	1 31 13.3	30 24 5	128	1070	20.61	-0.16	-0.71	0.07	0.06	0.03
971	1 31 08.8	30 24 4	128	825	19.42	0.05	...	0.07	0.04	...
972	1 31 09.6	30 24 4	128	869	20.71	0.07	-0.62	0.03	0.04	0.04
973	1 31 00.4	30 24 1	129	365	19.81	0.43	-0.93	0.04	0.05	0.03
974	1 31 11.9	30 24 4	131	996	19.96	0.32	-0.02	0.03	0.04	0.04
975	1 30 46.2	30 23 56	131	-412	19.04	0.05	-0.86	0.00	0.01	0.14
976	1 31 08.5	30 24 3	132	808	20.66	0.30	...	0.04	0.06	...
977	1 30 57.9	30 23 59	132	230	18.10	0.19	-0.60	0.01	0.01	0.03
978	1 31 03.0	30 24 1	132	508	20.30	0.24	...	0.07	0.08	...
979	1 30 59.5	30 23 59	134	319	20.86	0.25	-0.31	0.06	0.05	0.08
980	1 31 15.0	30 24 4	134	1163	20.04	0.17	-0.21	0.03	0.03	0.04
981	1 31 01.8	30 23 60	135	442	19.88	0.35	-0.59	0.03	0.02	0.03
982	1 31 00.7	30 23 59	135	383	20.23	0.20	-1.29	0.05	0.04	0.03
983	1 31 08.5	30 24 1	137	812	20.80	0.10	...	0.04	0.04	...
984	1 31 12.5	30 24 2	139	1031	20.66	0.00	-0.54	0.03	0.04	0.04
985	1 30 53.6	30 23 56	139	-3	20.89	0.29	...	0.05	0.04	...
986	1 30 55.2	30 23 57	139	81	20.48	-0.06	...	0.06	0.08	...
987	1 30 56.4	30 23 57	139	146	20.76	-0.06	...	0.13	0.06	...
988	1 30 56.7	30 23 57	140	164	20.19	0.34	...	0.08	0.10	...
989	1 30 57.5	30 23 57	140	205	18.51	0.10	-0.57	0.01	0.01	0.03
990	1 31 08.4	30 24 1	140	804	20.61	-0.03	-0.99	0.04	0.03	0.05
991	1 30 56.0	30 23 57	140	128	19.85	0.26	-0.57	0.20	0.08	0.04
992	1 30 56.0	30 23 57	140	127	19.96	-0.18	...	0.16	0.42	...
993	1 30 53.3	30 23 56	141	-20	20.70	-0.22	-0.98	0.23	0.18	0.09
994	1 31 03.0	30 23 59	141	511	16.85	-0.02	-0.93	0.01	0.01	0.03
995	1 30 54.1	30 23 56	141	24	20.26	0.13	-0.04	0.03	0.03	0.07
996	1 31 14.1	30 24 2	141	1115	20.88	0.22	-0.47	0.03	0.10	0.06
997	1 31 11.9	30 24 1	141	998	20.54	0.25	...	0.08	0.13	...
998	1 31 12.0	30 24 1	143	999	19.95	0.26	-0.71	0.05	0.09	0.06
999	1 30 57.3	30 23 56	144	197	20.42	-0.03	...	0.08	0.07	...
1000	1 31 11.7	30 24 1	144	987	19.10	-0.03	-0.55	0.03	0.03	0.03

TABLE 2 (cont.)

Number	α(1950)	δ(1950)	X	Y	V	B-V	U-B	σ_V	σ_B	σ_U
1001	1 30 57.3	30 23 56	144	196	20.65	-0.17	...	0.08	0.03	...
1002	1 30 51.0	30 23 54	144	-147	20.62	0.12	-0.76	0.00	0.04	0.15
1003	1 31 00.5	30 23 57	145	373	20.76	0.30	-1.37	0.07	0.06	0.04
1004	1 30 58.8	30 23 56	146	280	20.84	1.70	-0.56	0.07	0.20	0.12
1005	1 31 13.8	30 24 1	147	1100	19.88	0.19	-1.25	0.03	0.11	0.03
1006	1 31 04.0	30 23 57	148	563	20.25	0.00	-0.65	0.03	0.03	0.05
1007	1 31 09.8	30 23 59	149	878	19.93	0.26	...	0.03	0.04	...
1008	1 31 15.0	30 24 1	149	1164	18.77	0.60	-1.73	0.03	0.26	0.03
1009	1 31 03.0	30 23 57	150	507	18.53	-0.05	-1.32	0.04	0.02	0.04
1010	1 31 01.7	30 23 56	150	438	20.95	0.07	-0.45	0.07	0.06	0.05
1011	1 31 07.5	30 23 58	150	754	18.31	0.20	-0.13	0.03	0.03	0.03
1012	1 30 56.8	30 23 54	150	171	20.50	0.27	-0.65	0.07	0.05	0.05
1013	1 30 54.6	30 23 54	150	49	20.39	-0.14	-1.02	0.39	0.05	0.15
1014	1 30 57.5	30 23 55	151	209	19.75	-0.01	-0.82	0.03	0.02	0.03
1015	1 31 03.8	30 23 57	151	550	20.07	0.10	-0.94	0.06	0.02	0.03
1016	1 31 03.9	30 23 56	151	557	19.80	0.31	-0.76	0.08	0.02	0.04
1017	1 31 15.3	30 24 0	151	1182	19.70	0.03	-0.96	0.03	0.03	0.03
1018	1 31 03.2	30 23 56	152	517	19.59	-0.03	...	0.09	0.04	...
1019	1 30 54.0	30 23 53	152	18	20.86	0.29	...	0.06	0.08	...
1020	1 31 15.0	30 23 60	153	1165	20.10	0.11	...	0.09	0.07	...
1021	1 31 09.3	30 23 58	153	851	20.73	0.04	-1.25	0.04	0.04	0.03
1022	1 30 54.1	30 23 53	154	18	20.48	0.45	-1.08	0.05	0.05	0.05
1023	1 30 56.5	30 23 53	155	155	19.28	0.15	-1.02	0.03	0.02	0.04
1024	1 30 54.2	30 23 52	156	27	20.21	-0.24	-0.81	0.04	0.04	0.05
1025	1 30 56.4	30 23 53	157	150	19.77	0.12	-0.01	0.05	0.05	0.06
1026	1 30 54.2	30 23 52	157	27	20.11	-0.09	...	0.13	0.07	...
1027	1 30 58.8	30 23 53	157	278	21.00	0.34	-1.62	0.09	0.17	0.05
1028	1 31 01.4	30 23 54	159	420	19.90	-0.30	-0.70	0.05	0.02	0.03
1029	1 31 10.1	30 23 57	160	896	19.43	0.19	0.25	0.03	0.04	0.04
1030	1 31 01.2	30 23 54	160	407	18.82	0.20	0.24	0.01	0.01	0.03
1031	1 30 53.4	30 23 51	160	-15	20.45	-0.08	-0.61	0.01	0.06	0.28
1032	1 31 10.0	30 23 56	160	889	20.95	0.37	...	0.05	0.06	...
1033	1 31 01.6	30 23 54	160	430	20.99	0.21	...	0.09	0.09	...
1034	1 30 58.3	30 23 52	162	249	19.59	-0.06	-0.88	0.03	0.02	0.03
1035	1 30 50.3	30 23 50	162	-188	20.81	-0.02	-0.50	0.06	0.15	0.21
1036	1 31 09.5	30 23 56	163	864	20.12	0.01	-1.23	0.03	0.06	0.03
1037	1 30 54.1	30 23 51	163	20	20.21	0.04	...	0.09	0.11	...
1038	1 31 11.6	30 23 56	164	977	20.80	-0.35	-1.32	0.06	0.05	0.05
1039	1 30 57.7	30 23 51	165	215	20.23	0.31	0.01	0.04	0.05	0.06
1040	1 31 11.6	30 23 56	166	981	20.53	0.23	...	0.05	0.08	...
1041	1 31 11.1	30 23 55	166	950	20.88	-0.08	-0.65	0.04	0.04	0.04
1042	1 31 11.7	30 23 55	167	982	20.11	0.31	-1.51	0.05	0.06	0.05
1043	1 31 14.5	30 23 56	167	1138	20.90	0.33	...	0.03	0.04	...
1044	1 31 03.5	30 23 53	167	535	18.85	0.01	-1.14	0.04	0.03	0.04
1045	1 31 11.7	30 23 55	168	983	20.72	-0.30	...	0.08	0.06	...
1046	1 31 02.4	30 23 52	168	478	20.13	0.24	0.63	0.03	0.03	0.07
1047	1 30 54.3	30 23 49	168	31	20.75	0.16	...	0.08	0.08	...
1048	1 30 54.1	30 23 49	169	22	18.95	0.00	-0.90	0.02	0.00	0.14
1049	1 31 03.7	30 23 52	169	544	20.75	-0.09	...	0.07	0.06	...
1050	1 30 56.3	30 23 50	170	140	20.59	-0.05	...	0.19	0.04	...

TABLE 2 (cont.)

Number	α(1950)	δ(1950)	X	Y	V	B-V	U-B	σ_V	σ_B	σ_U
1051	1 31 10.6	30 23 54	170	921	20.38	-0.10	-0.81	0.04	0.05	0.03
1052	1 30 57.0	30 23 49	172	181	20.45	0.12	...	0.14	0.12	...
1053	1 31 03.3	30 23 51	172	525	17.28	0.11	-0.84	0.02	0.02	0.03
1054	1 31 07.7	30 23 53	172	765	19.85	0.05	-0.99	0.03	0.03	0.03
1055	1 31 07.9	30 23 53	172	778	18.80	0.24	...	0.04	0.06	...
1056	1 31 09.2	30 23 53	174	848	20.28	0.39	-1.43	0.04	0.21	0.03
1057	1 30 54.3	30 23 48	175	29	19.25	-0.14	-0.94	0.03	0.03	0.03
1058	1 31 01.6	30 23 50	176	432	19.65	0.05	0.20	0.03	0.02	0.04
1059	1 30 57.0	30 23 48	176	177	20.89	0.09	-0.66	0.07	0.05	0.05
1060	1 31 08.6	30 23 52	176	815	20.61	0.37	...	0.03	0.04	...
1061	1 31 04.5	30 23 50	178	591	19.63	-0.09	-0.89	0.02	0.01	0.03
1062	1 31 11.1	30 23 52	179	952	20.71	-0.14	-0.21	0.04	0.04	0.05
1063	1 31 06.6	30 23 50	181	705	20.88	0.25	...	0.17	0.13	...
1064	1 30 56.3	30 23 46	185	143	20.64	-0.05	...	0.06	0.04	...
1065	1 31 09.6	30 23 50	186	870	20.65	0.22	-1.38	0.04	0.10	0.06
1066	1 31 04.0	30 23 48	186	565	20.81	-0.03	...	0.07	0.05	...
1067	1 30 56.3	30 23 46	187	143	20.96	0.12	-0.92	0.16	0.11	0.05
1068	1 31 10.6	30 23 50	187	922	20.62	0.04	-1.17	0.04	0.05	0.03
1069	1 31 15.4	30 23 52	187	1187	20.96	0.14	0.82	0.04	0.04	0.11
1070	1 30 58.3	30 23 46	189	249	20.08	0.14	-0.86	0.05	0.02	0.03
1071	1 31 03.1	30 23 47	189	511	16.11	0.37	-0.08	0.00	0.00	0.03
1072	1 30 53.8	30 23 44	191	5	16.80	0.06	-0.78	0.02	0.02	0.04
1073	1 31 09.1	30 23 48	192	841	20.85	0.13	-1.20	0.05	0.06	0.04
1074	1 30 57.7	30 23 45	193	218	20.70	0.09	-0.63	0.05	0.04	0.04
1075	1 31 00.2	30 23 45	193	354	20.39	-0.05	-0.61	0.05	0.03	0.05
1076	1 31 11.2	30 23 48	197	959	20.92	0.08	...	0.05	0.06	...
1077	1 31 02.7	30 23 45	198	492	19.06	-0.08	-0.84	0.02	0.01	0.03
1078	1 31 05.6	30 23 46	198	651	20.77	0.06	0.31	0.05	0.04	0.07
1079	1 31 03.4	30 23 45	199	527	20.92	-0.21	-0.67	0.07	0.04	0.04
1080	1 31 13.9	30 23 48	200	1105	20.98	0.10	-0.82	0.04	0.04	0.05
1081	1 31 10.8	30 23 47	201	935	20.84	0.53	-1.70	0.05	0.16	0.06
1082	1 30 56.0	30 23 42	201	124	20.12	0.28	...	0.05	0.06	...
1083	1 31 01.6	30 23 44	202	431	20.26	-0.01	-0.81	0.04	0.03	0.06
1084	1 31 09.2	30 23 46	203	848	18.65	0.02	-0.62	0.03	0.03	0.03
1085	1 31 11.4	30 23 47	204	966	20.94	-0.32	-1.13	0.22	0.06	0.06
1086	1 31 13.2	30 23 47	205	1065	20.57	0.17	2.74	0.04	0.05	0.48
1087	1 30 56.7	30 23 41	205	162	20.37	0.18	...	0.29	0.29	...
1088	1 31 10.9	30 23 46	206	940	20.76	0.03	...	0.05	0.06	...
1089	1 30 56.6	30 23 41	206	157	19.87	0.12	-0.41	0.04	0.04	0.05
1090	1 31 05.1	30 23 44	207	622	20.13	0.01	...	0.06	0.04	...
1091	1 31 11.6	30 23 46	208	978	19.80	-0.20	-0.73	0.03	0.05	0.04
1092	1 31 05.1	30 23 44	208	621	19.78	0.36	0.33	0.04	0.04	0.13
1093	1 31 02.0	30 23 42	208	449	20.38	-0.17	-0.60	0.05	0.03	0.03
1094	1 30 58.2	30 23 41	209	242	19.25	-0.01	...	0.04	0.03	...
1095	1 31 02.6	30 23 43	209	487	19.33	-0.20	-0.88	0.02	0.01	0.03
1096	1 31 07.3	30 23 44	209	742	20.83	0.30	0.14	0.15	0.14	0.17
1097	1 31 12.0	30 23 45	209	998	19.65	-0.02	-1.24	0.07	0.06	0.03
1098	1 31 07.7	30 23 44	210	762	20.77	0.07	-0.60	0.05	0.04	0.04
1099	1 31 10.9	30 23 45	210	939	20.90	-0.19	-1.14	0.07	0.05	0.07
1100	1 31 15.0	30 23 46	212	1164	20.95	0.45	-1.67	0.03	0.22	0.03

TABLE 2 (cont.)

Number	α(1950)	δ(1950)	X	Y	V	B-V	U-B	σ_V	σ_B	σ_U
1101	1 31 08.9	30 23 43	213	830	20.79	0.11	...	0.03	0.05	...
1102	1 31 11.6	30 23 44	215	975	20.29	0.07	-1.12	0.07	0.07	0.04
1103	1 30 57.6	30 23 39	215	212	20.75	0.36	...	0.07	0.05	...
1104	1 30 53.8	30 23 38	215	5	18.67	0.11	-0.80	0.02	0.02	0.04
1105	1 31 03.7	30 23 41	216	545	20.35	-0.24	-1.75	0.06	0.04	0.06
1106	1 31 06.8	30 23 42	216	712	19.66	0.10	-0.99	0.24	0.02	0.05
1107	1 31 01.2	30 23 40	218	406	18.42	0.07	-0.05	0.01	0.03	0.03
1108	1 31 01.8	30 23 40	218	443	20.34	-0.23	-1.03	0.04	0.02	0.03
1109	1 30 53.7	30 23 37	218	-3	20.06	0.12	-1.08	0.03	0.03	0.05
1110	1 31 03.9	30 23 41	219	553	19.01	0.40	...	0.02	0.04	...
1111	1 31 03.3	30 23 40	219	523	20.95	-0.27	-0.93	0.09	0.05	0.06
1112	1 31 03.7	30 23 40	220	545	20.57	-0.19	...	0.08	0.06	...
1113	1 30 57.6	30 23 38	221	213	20.17	0.26	0.09	0.04	0.03	0.05
1114	1 31 01.3	30 23 39	222	412	19.09	0.34	0.13	0.03	0.02	0.03
1115	1 30 53.6	30 23 37	222	-11	19.80	0.13	...	0.03	0.03	...
1116	1 31 03.1	30 23 40	222	513	19.21	-0.18	-0.64	0.02	0.02	0.03
1117	1 30 48.6	30 23 35	223	-280	19.58	-0.13	-0.93	0.02	0.02	0.04
1118	1 31 02.2	30 23 39	223	464	20.59	-0.32	-0.72	0.08	0.06	0.05
1119	1 31 02.5	30 23 39	224	479	20.71	-0.25	-0.89	0.08	0.06	0.04
1120	1 31 08.9	30 23 41	225	827	20.89	0.16	-0.80	0.03	0.04	0.04
1121	1 31 11.9	30 23 42	225	994	20.41	-0.25	-1.22	0.15	0.06	0.03
1122	1 30 52.5	30 23 35	226	-68	20.84	0.81	-0.71	0.05	0.07	0.08
1123	1 31 15.3	30 23 42	226	1177	20.87	0.16	...	0.03	0.03	...
1124	1 31 01.8	30 23 38	227	441	18.89	-0.18	-0.97	0.01	0.01	0.03
1125	1 31 02.3	30 23 38	227	470	19.68	-0.15	-0.75	0.03	0.02	0.03
1126	1 30 58.6	30 23 37	228	267	20.85	-0.05	-0.42	0.05	0.03	0.04
1127	1 31 03.0	30 23 38	228	508	20.77	0.31	-0.47	0.07	0.09	0.07
1128	1 31 11.0	30 23 40	229	943	20.21	0.36	...	0.04	0.07	...
1129	1 31 03.8	30 23 38	232	553	20.88	-0.64	-0.65	0.09	0.03	0.05
1130	1 31 03.4	30 23 37	234	526	20.92	-0.41	...	0.12	0.12	...
1131	1 31 03.3	30 23 37	234	521	20.85	-0.30	...	0.09	0.08	...
1132	1 31 03.4	30 23 37	234	529	20.89	-0.12	...	0.11	0.16	...
1133	1 31 12.4	30 23 40	235	1019	20.81	-0.17	-0.79	0.05	0.04	0.04
1134	1 31 14.0	30 23 40	235	1105	20.99	0.18	...	0.04	0.06	...
1135	1 30 59.7	30 23 35	236	328	19.38	-0.01	-0.87	0.02	0.01	0.03
1136	1 30 52.3	30 23 33	236	-81	20.14	0.07	-0.79	0.03	0.02	0.04
1137	1 31 03.8	30 23 36	237	549	20.66	0.05	...	0.08	0.05	...
1138	1 31 04.0	30 23 36	237	560	20.67	-0.17	...	0.07	0.05	...
1139	1 31 10.7	30 23 38	238	930	18.84	0.09	-1.26	0.05	0.06	0.03
1140	1 31 12.7	30 23 39	238	1034	19.96	0.06	-1.41	0.12	0.07	0.03
1141	1 31 09.8	30 23 38	239	880	20.62	0.36	...	0.04	0.06	...
1142	1 30 45.6	30 23 30	239	-447	18.13	-0.08	-0.88	0.01	0.01	0.04
1143	1 31 08.3	30 23 37	240	799	20.23	0.41	-0.76	0.03	0.03	0.03
1144	1 31 02.6	30 23 35	240	485	20.67	-0.22	-0.55	0.08	0.05	0.05
1145	1 31 10.8	30 23 38	241	932	20.49	-0.11	...	0.08	0.11	...
1146	1 30 53.6	30 23 32	241	-6	18.48	0.42	-1.40	0.03	0.09	0.05
1147	1 31 11.1	30 23 37	242	947	20.94	0.07	...	0.18	0.24	...
1148	1 31 00.7	30 23 34	243	382	19.79	-0.19	-0.44	0.03	0.01	0.03
1149	1 31 01.0	30 23 34	243	396	19.69	-0.03	-1.00	0.05	0.03	0.03
1150	1 31 11.1	30 23 37	243	950	20.03	-0.30	...	0.06	0.06	...

TABLE 2 (cont.)

Number	α(1950)	δ(1950)	X	Y	V	B-V	U-B	σ_V	σ_B	σ_U
1151	1 31 01.4	30 23 34	244	417	18.82	-0.18	-0.89	0.05	0.02	0.04
1152	1 30 52.3	30 23 31	244	-77	20.27	-0.21	-0.86	0.07	0.02	0.04
1153	1 31 11.1	30 23 37	244	947	20.50	0.14	...	0.11	0.15	...
1154	1 31 02.3	30 23 34	245	470	18.33	0.12	...	0.04	0.02	...
1155	1 31 01.1	30 23 34	245	402	18.20	0.08	-0.34	0.02	0.01	0.03
1156	1 31 02.2	30 23 34	245	462	19.20	-0.23	-0.98	0.03	0.03	0.03
1157	1 31 09.1	30 23 36	245	838	20.82	-0.05	-1.04	0.03	0.04	0.03
1158	1 31 01.9	30 23 34	245	446	18.54	0.07	...	0.06	0.03	...
1159	1 31 09.3	30 23 36	246	851	20.82	0.22	-1.21	0.04	0.06	0.03
1160	1 31 05.6	30 23 35	246	648	20.71	-0.22	...	0.08	0.04	...
1161	1 31 12.2	30 23 37	246	1009	20.03	0.22	-1.20	0.03	0.04	0.03
1162	1 31 10.9	30 23 36	247	940	19.61	0.64	-2.30	0.04	0.13	0.03
1163	1 31 06.9	30 23 35	247	721	20.89	0.26	...	0.19	0.12	...
1164	1 31 01.6	30 23 33	248	428	17.01	0.36	-0.90	0.05	0.05	0.03
1165	1 30 53.5	30 23 30	248	-15	18.09	0.17	...	0.04	0.02	...
1166	1 31 02.0	30 23 33	248	451	18.16	0.31	-1.09	0.05	0.03	0.04
1167	1 30 52.7	30 23 30	249	-59	20.65	0.25	-0.16	0.04	0.03	0.06
1168	1 31 04.1	30 23 34	249	567	20.16	-0.08	-1.11	0.04	0.02	0.05
1169	1 31 00.9	30 23 32	250	391	20.02	-0.02	-0.91	0.04	0.03	0.03
1170	1 31 01.6	30 23 32	251	427	18.29	0.04	...	0.06	0.08	...
1171	1 31 01.1	30 23 32	252	403	19.73	-0.01	-0.71	0.05	0.03	0.06
1172	1 31 03.1	30 23 33	252	509	20.89	0.12	...	0.07	0.05	...
1173	1 31 08.3	30 23 34	252	794	20.49	0.19	-0.90	0.03	0.03	0.04
1174	1 31 02.9	30 23 32	252	500	20.87	-0.27	-1.02	0.07	0.04	0.04
1175	1 31 05.7	30 23 33	252	652	20.77	-0.15	-0.68	0.07	0.03	0.04
1176	1 30 52.4	30 23 29	253	-77	20.57	-0.11	-0.95	0.04	0.03	0.04
1177	1 31 01.9	30 23 32	254	446	18.52	0.00	...	0.04	0.05	...
1178	1 31 08.6	30 23 33	255	813	20.73	0.23	-1.23	0.03	0.04	0.04
1179	1 31 08.1	30 23 33	256	787	20.24	0.12	...	0.03	0.03	...
1180	1 30 52.0	30 23 28	256	-99	19.78	0.07	-0.73	0.02	0.02	0.04
1181	1 31 02.5	30 23 31	256	476	17.70	0.00	-0.55	0.01	0.01	0.03
1182	1 31 02.8	30 23 31	256	495	20.71	0.14	-1.07	0.07	0.06	0.11
1183	1 30 47.0	30 23 26	257	-373	20.20	-0.18	-1.13	0.13	0.08	0.05
1184	1 31 03.9	30 23 32	257	553	17.37	0.06	-0.32	0.02	0.01	0.03
1185	1 31 04.9	30 23 32	258	607	20.95	-0.07	-0.52	0.06	0.04	0.05
1186	1 30 54.1	30 23 28	258	21	20.32	-0.20	...	0.04	0.03	...
1187	1 31 01.0	30 23 30	258	396	20.16	0.25	-1.03	0.05	0.07	0.04
1188	1 30 46.9	30 23 26	258	-376	20.70	-0.03	-1.03	0.20	0.14	0.09
1189	1 31 02.0	30 23 31	259	450	20.39	-0.03	...	0.15	0.06	...
1190	1 31 01.4	30 23 30	259	420	20.15	-0.09	...	0.09	0.05	...
1191	1 31 00.6	30 23 30	259	374	19.31	-0.20	-0.55	0.02	0.01	0.03
1192	1 31 08.1	30 23 32	259	784	20.28	0.22	...	0.03	0.03	...
1193	1 31 02.9	30 23 31	260	498	19.53	-0.05	-0.93	0.03	0.02	0.04
1194	1 31 10.0	30 23 33	260	888	20.79	0.14	0.70	0.05	0.06	0.11
1195	1 31 12.8	30 23 33	261	1042	20.00	0.66	-0.59	0.03	0.08	0.05
1196	1 31 03.3	30 23 30	262	524	19.34	-0.21	-0.82	0.04	0.04	0.05
1197	1 31 08.4	30 23 32	263	799	20.31	-0.01	-0.84	0.03	0.03	0.03
1198	1 30 59.9	30 23 29	264	335	20.77	-0.06	-0.79	0.05	0.03	0.04
1199	1 31 03.4	30 23 30	264	528	18.72	-0.11	-0.70	0.02	0.02	0.03
1200	1 31 08.6	30 23 31	265	813	20.61	0.49	-0.73	0.03	0.07	0.06

TABLE 2 (cont.)

Number	α(1950)	δ(1950)	X	Y	V	B-V	U-B	σ_V	σ_B	σ_U
1201	1 30 54.0	30 23 26	266	15	19.86	-0.23	-0.97	0.03	0.02	0.04
1202	1 31 03.2	30 23 29	266	518	20.28	0.04	...	0.15	0.06	...
1203	1 31 06.0	30 23 30	267	670	20.92	0.02	0.39	0.08	0.13	1.05
1204	1 31 03.0	30 23 29	267	507	19.76	-0.04	-0.74	0.05	0.02	0.03
1205	1 30 46.2	30 23 24	267	-414	19.24	-0.20	-0.91	0.02	0.02	0.04
1206	1 31 12.1	30 23 32	267	1001	20.44	0.04	-0.41	0.03	0.04	0.20
1207	1 31 04.3	30 23 29	267	574	18.03	-0.10	-0.89	0.01	0.01	0.03
1208	1 31 02.6	30 23 28	269	481	18.76	-0.12	-1.08	0.04	0.01	0.03
1209	1 31 01.9	30 23 28	269	447	18.68	0.12	...	0.03	0.02	...
1210	1 31 04.0	30 23 29	269	559	20.87	0.02	...	0.10	0.09	...
1211	1 31 12.7	30 23 31	270	1034	17.49	0.18	-0.59	0.03	0.03	0.03
1212	1 30 46.0	30 23 23	271	-425	20.72	-0.31	-0.92	0.10	0.03	0.05
1213	1 30 54.2	30 23 25	271	22	20.35	-0.31	-1.32	0.06	0.03	0.05
1214	1 31 01.2	30 23 27	271	407	18.29	-0.01	-0.88	0.01	0.01	0.03
1215	1 31 01.4	30 23 27	272	419	19.44	-0.08	-0.98	0.04	0.03	0.03
1216	1 30 46.2	30 23 22	272	-417	20.25	-0.19	-0.96	0.05	0.03	0.05
1217	1 30 45.3	30 23 22	273	-466	20.51	-0.20	-0.92	0.04	0.02	0.04
1218	1 31 04.9	30 23 28	273	607	20.09	0.17	-0.63	0.06	0.07	0.09
1219	1 30 53.8	30 23 25	273	4	19.68	-0.08	-1.52	0.09	0.07	0.04
1220	1 31 05.5	30 23 28	274	643	20.36	0.19	-0.47	0.04	0.04	0.07
1221	1 31 08.7	30 23 29	275	815	19.63	0.07	-0.19	0.03	0.03	0.03
1222	1 31 02.5	30 23 27	276	476	18.15	-0.12	-0.87	0.02	0.01	0.03
1223	1 31 04.8	30 23 28	276	606	19.94	-0.21	-0.94	0.05	0.04	0.05
1224	1 31 03.3	30 23 27	276	521	19.67	-0.25	-1.05	0.06	0.03	0.03
1225	1 31 04.5	30 23 27	276	587	20.76	-0.20	-0.99	0.07	0.22	0.05
1226	1 31 01.6	30 23 26	276	428	20.02	-0.04	-1.02	0.03	0.04	0.04
1227	1 31 02.1	30 23 26	276	457	18.02	0.10	-0.88	0.01	0.01	0.03
1228	1 31 01.5	30 23 26	276	422	20.66	-0.16	-1.12	0.06	0.07	0.06
1229	1 31 07.0	30 23 28	277	723	19.67	0.01	-0.90	0.04	0.00	0.06
1230	1 30 55.0	30 23 24	279	69	20.50	0.06	...	0.04	0.04	...
1231	1 30 49.2	30 23 22	279	-248	20.30	0.05	-0.91	0.03	0.04	0.04
1232	1 30 46.3	30 23 21	280	-409	17.90	-0.04	-0.86	0.02	0.02	0.04
1233	1 30 53.8	30 23 23	280	-1	18.86	-0.15	-0.95	0.02	0.02	0.04
1234	1 30 45.5	30 23 20	281	-454	20.60	-0.25	-0.84	0.09	0.03	0.05
1235	1 30 53.9	30 23 23	281	9	19.97	-0.15	-1.20	0.04	0.03	0.05
1236	1 30 46.1	30 23 20	282	-420	20.33	0.00	...	0.05	0.05	...
1237	1 31 01.7	30 23 25	282	433	20.16	-0.46	-0.95	0.10	0.03	0.03
1238	1 31 13.1	30 23 29	283	1057	19.04	-0.04	-1.18	0.02	0.03	0.03
1239	1 31 01.9	30 23 24	285	445	19.05	-0.11	-0.98	0.01	0.01	0.03
1240	1 31 08.5	30 23 27	285	803	20.42	0.29	...	0.04	0.08	...
1241	1 31 12.9	30 23 28	285	1046	18.11	0.13	...	0.02	0.04	...
1242	1 30 54.2	30 23 22	285	21	19.50	-0.22	-1.03	0.02	0.02	0.04
1243	1 31 13.8	30 23 28	285	1095	19.21	0.38	...	0.02	0.03	...
1244	1 31 00.5	30 23 24	286	369	20.52	0.09	-0.84	0.06	0.04	0.07
1245	1 30 46.2	30 23 19	287	-416	19.52	-0.20	-0.87	0.04	0.02	0.05
1246	1 30 55.1	30 23 22	288	71	17.92	0.09	-0.54	0.01	0.02	0.01
1247	1 31 03.5	30 23 24	288	530	20.68	0.29	...	0.08	0.05	...
1248	1 31 13.9	30 23 27	289	1099	19.83	0.39	...	0.02	0.03	...
1249	1 31 01.0	30 23 23	289	394	19.89	-0.07	-1.05	0.03	0.03	0.03
1250	1 31 02.5	30 23 24	289	475	20.09	-0.23	-0.88	0.04	0.03	0.03

TABLE 2 (cont.)

Number	α(1950)	δ(1950)	X	Y	V	B-V	U-B	σ_V	σ_B	σ_U
1251	1 31 01.3	30 23 23	289	409	20.89	0.49	-1.68	0.07	0.13	0.06
1252	1 30 52.3	30 23 20	289	-79	20.52	-0.16	-0.75	0.04	0.02	0.04
1253	1 31 08.2	30 23 25	290	791	18.50	0.14	-0.56	0.02	0.03	0.03
1254	1 30 48.0	30 23 19	290	-315	20.56	0.23	0.20	0.04	0.03	0.06
1255	1 30 59.1	30 23 22	291	292	19.93	0.22	-0.12	0.06	0.04	0.04
1256	1 31 03.7	30 23 24	291	542	20.81	-0.09	-0.89	0.06	0.10	0.06
1257	1 30 45.7	30 23 18	291	-442	20.04	-0.17	...	0.03	0.02	...
1258	1 30 59.1	30 23 22	291	291	20.77	-0.62	...	0.11	0.04	...
1259	1 31 12.5	30 23 26	291	1027	20.73	-0.08	...	0.03	0.04	...
1260	1 30 49.1	30 23 19	292	-256	20.58	-0.04	-0.67	0.04	0.03	0.04
1261	1 31 01.0	30 23 22	293	393	20.30	-0.15	...	0.05	0.04	...
1262	1 31 10.0	30 23 25	294	890	20.75	0.11	-1.09	0.05	0.04	0.03
1263	1 31 07.9	30 23 24	294	774	19.60	0.03	-1.49	0.03	0.04	0.03
1264	1 31 07.0	30 23 24	294	724	20.74	0.00	...	0.05	0.03	...
1265	1 30 58.3	30 23 21	295	248	20.35	0.25	...	0.08	0.09	...
1266	1 31 08.9	30 23 24	296	830	19.82	0.35	...	0.03	0.04	...
1267	1 31 08.5	30 23 24	296	806	19.29	0.77	-1.42	0.03	0.09	0.03
1268	1 31 01.0	30 23 21	296	396	20.08	-0.18	...	0.07	0.04	...
1269	1 30 46.1	30 23 17	297	-422	20.64	-0.28	...	0.06	0.03	...
1270	1 30 55.8	30 23 19	298	110	20.70	0.29	...	0.05	0.04	...
1271	1 30 58.3	30 23 20	298	248	19.50	0.10	-1.50	0.04	0.04	0.04
1272	1 31 08.0	30 23 23	298	777	20.52	0.17	...	0.07	0.05	...
1273	1 30 45.9	30 23 16	299	-432	20.43	-0.22	...	0.05	0.04	...
1274	1 31 14.0	30 23 25	301	1108	20.22	0.25	-0.43	0.03	0.03	0.04
1275	1 30 55.9	30 23 19	301	115	20.42	0.05	-0.52	0.04	0.03	0.07
1276	1 30 46.6	30 23 16	302	-394	19.00	-0.07	-0.91	0.02	0.02	0.04
1277	1 31 08.3	30 23 22	302	792	19.58	0.17	...	0.03	0.05	...
1278	1 31 08.3	30 23 22	303	793	19.46	0.29	-1.47	0.09	0.05	0.04
1279	1 30 55.4	30 23 18	303	88	20.17	0.11	-0.87	0.03	0.02	0.05
1280	1 31 13.3	30 23 24	304	1068	20.48	0.02	-1.74	0.03	0.05	0.03
1281	1 31 04.3	30 23 21	304	574	18.51	0.14	...	0.04	0.02	...
1282	1 31 02.1	30 23 20	304	458	19.90	-0.01	-0.75	0.04	0.03	0.07
1283	1 31 08.1	30 23 22	304	784	20.95	-0.02	...	0.05	0.05	...
1284	1 31 03.7	30 23 20	304	541	19.32	-0.04	-0.62	0.03	0.04	0.03
1285	1 31 08.2	30 23 22	305	791	20.82	0.06	...	0.08	0.06	...
1286	1 31 08.6	30 23 22	305	813	19.56	0.21	...	0.03	0.03	...
1287	1 31 06.9	30 23 21	305	716	20.00	0.03	...	0.08	0.03	...
1288	1 31 03.2	30 23 20	305	518	19.15	-0.03	-0.41	0.03	0.02	0.04
1289	1 31 06.9	30 23 21	305	715	19.95	0.06	-1.03	0.03	0.03	0.03
1290	1 31 00.5	30 23 19	305	369	20.12	-0.10	...	0.03	0.03	...
1291	1 31 03.1	30 23 20	306	512	21.00	0.13	...	0.09	0.07	...
1292	1 31 03.9	30 23 20	306	555	19.71	0.01	-0.75	0.04	0.02	0.04
1293	1 31 09.6	30 23 22	306	864	20.48	0.06	-0.92	0.03	0.05	0.03
1294	1 30 46.2	30 23 14	307	-413	17.84	-0.16	-0.67	0.04	0.02	0.04
1295	1 31 01.0	30 23 19	307	394	20.98	-0.09	...	0.06	0.06	...
1296	1 31 01.9	30 23 19	307	443	18.90	0.19	...	0.02	0.02	...
1297	1 30 55.5	30 23 17	307	94	19.85	0.16	...	0.04	0.14	...
1298	1 30 58.4	30 23 18	308	255	20.48	0.12	...	0.08	0.07	...
1299	1 30 55.1	30 23 17	308	72	20.12	-0.14	-0.73	0.10	0.04	0.30
1300	1 31 06.8	30 23 20	309	710	20.74	0.17	...	0.04	0.06	...

TABLE 2 (cont.)

Number	α(1950)	δ(1950)	X	Y	V	B-V	U-B	σ_V	σ_B	σ_U
1301	1 31 06.8	30 23 20	309	711	20.89	0.16	...	0.10	0.06	...
1302	1 30 58.2	30 23 17	310	239	18.91	-0.06	-0.97	0.03	0.02	0.03
1303	1 31 02.0	30 23 18	311	451	18.53	0.24	0.35	0.01	0.01	0.05
1304	1 31 02.5	30 23 18	311	474	19.02	0.07	-0.94	0.03	0.02	0.03
1305	1 30 55.8	30 23 16	311	108	20.52	0.40	...	0.04	0.07	...
1306	1 31 12.6	30 23 21	312	1030	20.81	0.37	...	0.03	0.03	...
1307	1 30 46.1	30 23 13	313	-421	17.24	0.04	-0.56	0.02	0.01	0.04
1308	1 31 06.8	30 23 19	314	712	20.61	-0.09	...	0.01	0.58	...
1309	1 31 03.1	30 23 18	315	508	20.02	-0.09	...	0.03	0.02	...
1310	1 30 58.4	30 23 16	316	254	19.99	-0.34	...	0.07	0.05	...
1311	1 31 02.6	30 23 17	316	484	20.09	0.06	-0.97	0.06	0.03	0.04
1312	1 31 11.9	30 23 20	317	991	20.49	0.14	-0.14	0.03	0.03	0.06
1313	1 30 58.0	30 23 16	317	228	18.56	0.08	-0.86	0.01	0.01	0.03
1314	1 31 13.1	30 23 20	317	1057	20.04	0.03	...	0.03	0.06	...
1315	1 31 00.9	30 23 16	317	388	20.25	-0.03	-0.73	0.05	0.03	0.04
1316	1 30 48.5	30 23 12	318	-288	20.49	-0.11	-0.57	0.04	0.02	0.04
1317	1 30 49.7	30 23 13	319	-223	20.10	-0.16	-0.71	0.04	0.02	0.05
1318	1 31 00.5	30 23 16	319	368	18.43	-0.12	-0.53	0.01	0.01	0.04
1319	1 30 58.4	30 23 15	319	250	19.58	0.05	-1.19	0.05	0.03	0.06
1320	1 30 53.7	30 23 14	319	-5	20.06	0.09	-0.82	0.04	0.02	0.04
1321	1 30 45.8	30 23 11	320	-438	19.35	0.14	-0.32	0.02	0.02	0.04
1322	1 30 58.4	30 23 15	321	254	19.60	0.04	-1.21	0.05	0.04	0.06
1323	1 31 06.9	30 23 18	321	715	18.57	0.51	-1.05	0.19	0.37	0.00
1324	1 31 13.1	30 23 19	321	1059	18.70	0.29	...	0.03	0.04	...
1325	1 31 09.0	30 23 18	322	834	20.85	0.25	...	0.04	0.08	...
1326	1 31 08.0	30 23 18	322	779	20.21	0.64	-1.63	0.03	0.05	0.05
1327	1 31 01.1	30 23 15	322	402	19.60	0.06	-0.92	0.03	0.06	0.03
1328	1 31 13.0	30 23 19	324	1051	20.39	0.34	...	0.04	0.05	...
1329	1 30 58.4	30 23 14	325	251	20.85	-0.16	...	0.11	0.07	...
1330	1 31 02.1	30 23 15	326	452	18.72	0.16	0.06	0.01	0.01	0.03
1331	1 31 03.7	30 23 15	326	545	20.79	-0.09	-0.87	0.06	0.04	0.04
1332	1 31 02.5	30 23 15	327	476	20.56	0.07	-1.19	0.05	0.05	0.03
1333	1 30 57.9	30 23 13	327	224	20.67	0.12	-0.80	0.06	0.04	0.06
1334	1 30 58.2	30 23 13	327	240	19.67	-0.02	-1.23	0.04	0.03	0.04
1335	1 30 59.9	30 23 14	328	336	19.41	0.27	-0.94	0.03	0.04	0.05
1336	1 30 50.7	30 23 11	329	-172	20.99	-0.19	-0.91	0.11	0.09	0.05
1337	1 31 13.2	30 23 18	329	1064	19.56	-0.04	...	0.03	0.05	...
1338	1 31 03.4	30 23 14	329	525	19.57	0.07	...	0.04	0.02	...
1339	1 31 00.5	30 23 13	330	369	19.18	0.06	-0.60	0.02	0.02	0.03
1340	1 30 50.2	30 23 10	330	-198	20.27	-0.14	-0.71	0.05	0.02	0.04
1341	1 31 13.2	30 23 17	330	1061	19.20	0.01	-1.67	0.03	0.04	0.04
1342	1 30 60.0	30 23 13	332	339	19.19	0.32	-0.66	0.03	0.03	0.05
1343	1 31 12.5	30 23 17	332	1021	20.59	0.09	-1.41	0.03	0.03	0.03
1344	1 30 52.6	30 23 10	333	-67	20.39	0.11	...	0.06	0.03	...
1345	1 31 03.6	30 23 13	334	537	20.69	-0.27	-0.98	0.09	0.05	0.06
1346	1 31 04.8	30 23 14	334	602	20.97	0.04	-1.46	0.07	0.08	0.07
1347	1 30 54.0	30 23 10	334	10	20.44	-0.17	-0.86	0.04	0.02	0.04
1348	1 31 05.8	30 23 14	335	656	20.74	0.35	-0.62	0.05	0.04	0.04
1349	1 31 01.5	30 23 12	335	421	16.91	-0.06	-0.92	0.02	0.02	0.04
1350	1 31 04.9	30 23 13	336	607	18.71	-0.08	-0.99	0.01	0.01	0.03

TABLE 2 (cont.)

Number	α(1950)	δ(1950)	X	Y	V	B-V	U-B	σ_V	σ_B	σ_U
1351	1 31 00.9	30 23 12	336	386	19.56	0.20	-0.98	0.06	0.04	0.04
1352	1 30 50.6	30 23 8	338	-177	20.14	0.12	-0.82	0.05	0.06	0.05
1353	1 31 01.5	30 23 12	339	422	17.53	-0.10	-0.76	0.04	0.03	0.07
1354	1 31 01.1	30 23 11	339	399	16.06	-0.07	-0.67	0.04	0.01	0.03
1355	1 31 13.1	30 23 15	339	1058	20.81	0.01	...	0.03	0.04	...
1356	1 30 49.2	30 23 8	339	-250	20.18	-0.05	-0.72	0.03	0.02	0.05
1357	1 30 51.7	30 23 8	340	-113	19.95	-0.21	-0.75	0.03	0.02	0.04
1358	1 30 46.2	30 23 6	340	-418	20.42	0.04	-1.14	0.03	0.08	0.04
1359	1 30 59.5	30 23 11	341	309	20.46	0.17	-0.94	0.05	0.04	0.04
1360	1 31 03.1	30 23 11	342	507	20.28	0.03	-0.70	0.03	0.03	0.03
1361	1 31 00.5	30 23 10	343	367	19.31	0.14	0.07	0.02	0.02	0.04
1362	1 31 06.8	30 23 12	343	709	19.35	0.71	-0.52	0.08	0.06	0.09
1363	1 30 53.5	30 23 8	344	-17	20.44	0.03	-0.56	0.05	0.03	0.05
1364	1 31 05.2	30 23 11	344	622	18.16	0.23	-0.34	0.01	0.01	0.03
1365	1 30 59.7	30 23 10	344	322	20.96	0.28	...	0.08	0.08	...
1366	1 31 08.2	30 23 12	345	786	20.64	0.02	-0.97	0.03	0.04	0.04
1367	1 31 02.8	30 23 11	345	492	19.66	-0.07	-0.75	0.02	0.02	0.03
1368	1 30 59.6	30 23 10	345	317	19.08	0.26	-0.25	0.02	0.01	0.03
1369	1 31 01.9	30 23 10	345	445	20.88	-0.22	-0.81	0.08	0.11	0.06
1370	1 30 51.8	30 23 7	346	-109	19.63	-0.20	-0.87	0.04	0.02	0.04
1371	1 30 52.3	30 23 7	346	-85	20.86	0.22	-0.91	0.05	0.05	0.05
1372	1 30 52.1	30 23 7	346	-95	20.16	-0.03	-1.05	0.03	0.03	0.04
1373	1 30 45.3	30 23 5	346	-463	20.93	-0.17	-0.81	0.05	0.03	0.04
1374	1 30 50.1	30 23 6	347	-201	19.93	0.02	-0.93	0.04	0.03	0.04
1375	1 31 09.3	30 23 12	347	848	19.05	0.22	-0.14	0.02	0.03	0.03
1376	1 31 08.0	30 23 11	348	775	19.93	0.07	-1.18	0.03	0.04	0.03
1377	1 31 11.2	30 23 12	349	953	18.60	0.28	-0.55	0.02	0.03	0.03
1378	1 31 01.9	30 23 9	349	442	20.60	0.17	...	0.06	0.12	...
1379	1 31 09.1	30 23 11	350	835	20.86	0.08	...	0.03	0.03	...
1380	1 31 07.8	30 23 11	350	764	20.14	0.39	-0.32	0.03	0.07	0.05
1381	1 31 13.0	30 23 12	351	1050	20.58	-0.01	-1.22	0.03	0.03	0.04
1382	1 30 49.8	30 23 5	351	-219	18.89	0.32	-0.23	0.02	0.02	0.05
1383	1 30 51.4	30 23 5	352	-132	19.98	-0.23	-0.83	0.06	0.03	0.04
1384	1 30 53.0	30 23 5	354	-43	20.68	0.14	-0.32	0.05	0.04	0.06
1385	1 30 52.2	30 23 5	354	-87	20.25	0.00	-0.94	0.04	0.04	0.04
1386	1 30 60.0	30 23 7	355	336	20.51	0.19	...	0.06	0.13	...
1387	1 31 13.1	30 23 11	356	1054	20.60	0.33	...	0.04	0.03	...
1388	1 30 52.2	30 23 4	357	-91	20.28	0.00	...	0.06	0.04	...
1389	1 31 08.9	30 23 10	358	827	21.00	0.12	-0.73	0.03	0.03	0.05
1390	1 30 46.5	30 23 2	359	-403	19.22	-0.14	-0.83	0.02	0.02	0.04
1391	1 31 03.0	30 23 7	359	503	20.33	-0.22	-0.90	0.04	0.03	0.03
1392	1 31 00.1	30 23 6	360	345	20.43	0.30	...	0.06	0.07	...
1393	1 30 58.1	30 23 5	361	236	20.31	-0.16	-0.87	0.05	0.02	0.03
1394	1 30 59.6	30 23 6	361	318	18.30	0.13	-0.42	0.02	0.01	0.03
1395	1 30 49.8	30 23 3	361	-219	18.33	0.38	-1.08	0.02	0.05	0.04
1396	1 30 59.9	30 23 6	362	334	19.73	0.04	...	0.03	0.06	...
1397	1 31 09.9	30 23 9	362	880	20.18	-0.01	-0.75	0.03	0.03	0.03
1398	1 30 50.9	30 23 2	364	-159	20.92	-0.25	-1.09	0.08	0.05	0.06
1399	1 31 01.8	30 23 6	364	439	18.27	-0.08	-0.89	0.01	0.01	0.03
1400	1 30 51.9	30 23 3	364	-106	19.60	0.14	-0.55	0.02	0.02	0.04

TABLE 2 (cont.)

Number	α(1950)	δ(1950)	X	Y	V	B-V	U-B	σ_V	σ_B	σ_U
1401	1 31 05.9	30 23 7	365	660	20.76	0.42	-0.62	0.03	0.13	0.05
1402	1 31 08.5	30 23 8	365	805	20.80	0.01	-0.56	0.03	0.03	0.04
1403	1 30 57.5	30 23 4	365	201	20.18	0.06	-0.59	0.03	0.08	0.04
1404	1 30 60.0	30 23 5	366	336	19.71	0.12	-1.12	0.04	0.05	0.05
1405	1 31 01.6	30 23 5	367	424	20.70	0.13	...	0.06	0.08	...
1406	1 30 45.8	30 22 60	367	-440	19.67	-0.11	-0.92	0.02	0.02	0.04
1407	1 30 59.5	30 23 4	368	311	20.84	0.24	...	0.14	0.07	...
1408	1 30 54.6	30 23 2	369	43	19.34	0.12	0.10	0.02	0.02	0.04
1409	1 30 52.0	30 23 2	369	-97	20.06	-0.14	-0.39	0.15	0.04	0.07
1410	1 31 04.2	30 23 5	369	568	20.22	0.20	...	0.04	0.04	...
1411	1 30 49.9	30 23 1	369	-217	19.98	-0.09	-0.90	0.05	0.02	0.05
1412	1 30 49.3	30 23 0	369	-250	20.71	-0.13	-0.79	0.05	0.03	0.05
1413	1 31 09.8	30 23 7	370	873	20.75	0.28	-0.78	0.03	0.06	0.06
1414	1 31 12.6	30 23 8	371	1028	20.09	0.37	-0.89	0.03	0.03	0.03
1415	1 30 50.2	30 23 0	371	-196	20.00	-0.21	-0.83	0.04	0.12	0.04
1416	1 30 59.7	30 23 3	372	322	20.51	-0.23	-1.03	0.05	0.02	0.04
1417	1 31 00.5	30 23 4	372	366	20.07	-0.33	...	0.04	0.06	...
1418	1 30 59.2	30 23 3	372	295	19.05	-0.04	-0.87	0.02	0.01	0.03
1419	1 30 57.3	30 23 2	372	191	19.59	-0.04	-0.81	0.12	0.07	0.04
1420	1 31 00.3	30 23 3	372	357	18.30	0.04	-0.47	0.01	0.01	0.03
1421	1 30 50.1	30 23 0	372	-205	19.09	-0.07	-0.61	0.02	0.02	0.05
1422	1 31 04.2	30 23 4	373	567	20.18	-0.11	-1.14	0.04	0.03	0.03
1423	1 30 49.7	30 22 60	373	-225	19.83	-0.14	-0.81	0.04	0.02	0.04
1424	1 30 51.0	30 23 0	373	-155	20.49	0.00	-0.94	0.05	0.04	0.05
1425	1 30 51.5	30 23 0	374	-128	18.26	0.19	0.17	0.02	0.02	0.05
1426	1 31 01.7	30 23 3	374	430	20.75	-0.32	...	0.16	0.04	...
1427	1 30 50.9	30 22 60	375	-162	20.77	0.16	...	0.09	0.09	...
1428	1 31 03.6	30 23 4	375	536	18.43	0.01	-0.50	0.01	0.01	0.03
1429	1 30 59.3	30 23 2	376	302	20.24	0.05	-0.88	0.05	0.02	0.04
1430	1 31 07.3	30 23 4	377	735	16.86	0.25	-0.08	0.01	0.01	0.04
1431	1 30 56.3	30 23 1	378	138	20.90	0.31	...	0.16	0.11	...
1432	1 31 07.7	30 23 4	378	758	18.34	0.16	-0.46	0.02	0.03	0.03
1433	1 30 56.6	30 23 1	379	154	20.78	-0.16	-1.00	0.15	0.11	0.10
1434	1 30 53.4	30 22 59	379	-26	19.08	0.21	-0.20	0.02	0.02	0.04
1435	1 31 00.2	30 23 2	380	349	18.23	0.13	-0.20	0.01	0.01	0.03
1436	1 31 03.0	30 23 2	380	504	20.45	-0.19	-0.67	0.04	0.03	0.04
1437	1 31 05.6	30 23 3	380	646	18.58	0.20	-0.76	0.01	0.01	0.03
1438	1 30 53.7	30 22 59	380	-4	20.58	-0.01	-0.67	0.05	0.03	0.05
1439	1 30 50.9	30 22 58	381	-160	20.68	0.10	-0.92	0.07	0.05	0.05
1440	1 31 00.6	30 23 1	382	371	20.90	0.31	-0.80	0.05	0.04	0.07
1441	1 30 53.9	30 22 59	383	4	19.68	0.55	-0.97	0.12	0.11	0.09
1442	1 30 59.4	30 23 1	383	308	20.25	-0.07	-0.98	0.06	0.03	0.03
1443	1 30 49.1	30 22 57	383	-259	20.28	0.03	-0.97	0.04	0.03	0.05
1444	1 31 07.6	30 23 3	383	751	18.24	0.04	-0.99	0.02	0.03	0.03
1445	1 30 45.8	30 22 56	384	-441	20.59	-0.13	-0.67	0.04	0.02	0.06
1446	1 30 53.9	30 22 58	385	1	18.18	0.26	0.02	0.03	0.02	0.05
1447	1 30 48.9	30 22 57	385	-272	18.00	-0.01	-0.73	0.02	0.02	0.04
1448	1 31 04.2	30 23 1	385	568	18.49	0.04	-0.74	0.01	0.01	0.03
1449	1 30 49.0	30 22 56	387	-267	18.26	0.17	-0.22	0.02	0.02	0.05
1450	1 30 53.7	30 22 58	387	-7	18.68	0.29	0.24	0.03	0.02	0.04

TABLE 2 (cont.)

Number	α(1950)	δ(1950)	X	Y	V	B-V	U-B	σ_V	σ_B	σ_U
1451	1 31 01.2	30 22 60	389	405	20.79	-0.13	-0.26	0.05	0.03	0.07
1452	1 31 08.5	30 23 2	389	804	19.37	0.10	-0.57	0.02	0.03	0.03
1453	1 30 51.9	30 22 57	390	-106	19.99	0.24	-0.54	0.02	0.03	0.04
1454	1 30 58.9	30 22 59	390	275	20.79	0.23	...	0.07	0.05	...
1455	1 31 10.3	30 23 2	391	903	19.18	0.25	-0.16	0.03	0.03	0.03
1456	1 31 03.6	30 22 59	393	536	20.41	-0.32	-0.98	0.04	0.02	0.03
1457	1 30 46.1	30 22 54	394	-421	20.90	-0.32	-0.89	0.05	0.02	0.04
1458	1 31 13.0	30 23 2	396	1047	19.68	-0.07	-0.15	0.05	0.03	0.03
1459	1 31 09.1	30 23 0	398	837	20.45	-0.14	...	0.05	0.14	...
1460	1 31 07.4	30 22 59	399	744	20.68	-0.05	-1.01	0.04	0.08	0.15
1461	1 31 11.2	30 23 1	399	952	20.72	0.03	-0.89	0.04	0.03	0.04
1462	1 30 56.1	30 22 55	400	125	20.79	-0.12	-0.59	0.04	0.02	0.06
1463	1 31 00.7	30 22 57	401	378	18.60	-0.17	-0.91	0.01	0.01	0.03
1464	1 31 01.7	30 22 57	403	428	16.70	0.10	-0.73	0.00	0.01	0.03
1465	1 31 09.2	30 22 59	403	839	19.91	0.35	...	0.05	0.14	...
1466	1 31 03.5	30 22 57	403	526	18.15	-0.06	-0.76	0.02	0.01	0.03
1467	1 30 53.0	30 22 54	404	-48	20.95	0.30	...	0.07	0.09	...
1468	1 31 09.2	30 22 59	404	844	18.66	0.21	-0.59	0.03	0.04	0.04
1469	1 31 09.2	30 22 58	407	840	20.67	-0.15	...	0.09	0.08	...
1470	1 31 02.9	30 22 56	407	497	20.76	-0.36	-0.87	0.06	0.03	0.03
1471	1 30 54.4	30 22 53	408	30	19.80	-0.09	-0.73	0.02	0.02	0.04
1472	1 31 08.0	30 22 57	410	774	17.48	0.20	-0.16	0.03	0.03	0.03
1473	1 31 01.1	30 22 55	410	396	18.12	-0.06	-0.85	0.01	0.01	0.03
1474	1 31 03.9	30 22 55	411	549	20.86	0.02	-0.79	0.06	0.05	0.06
1475	1 31 02.1	30 22 55	412	451	18.86	-0.22	-0.87	0.02	0.01	0.03
1476	1 31 09.3	30 22 57	413	848	20.98	0.05	...	0.05	0.05	...
1477	1 31 09.1	30 22 57	413	835	19.65	0.37	...	0.04	0.03	...
1478	1 31 05.3	30 22 55	413	629	20.43	0.26	-0.69	0.03	0.03	0.03
1479	1 30 52.9	30 22 51	414	-52	19.86	0.30	...	0.04	0.04	...
1480	1 30 49.8	30 22 50	414	-223	19.86	-0.12	-1.17	0.03	0.04	0.04
1481	1 30 56.0	30 22 52	414	119	20.51	0.20	0.31	0.02	0.03	0.09
1482	1 31 10.6	30 22 56	415	918	19.80	0.06	0.21	0.03	0.03	0.04
1483	1 30 50.1	30 22 50	416	-207	20.44	-0.27	...	0.05	0.04	...
1484	1 31 12.6	30 22 57	416	1027	17.52	0.22	-0.95	0.03	0.03	0.03
1485	1 31 03.5	30 22 54	416	529	20.16	-0.08	...	0.05	0.03	...
1486	1 31 09.7	30 22 56	417	869	20.15	0.91	-0.77	0.03	0.12	0.04
1487	1 30 59.7	30 22 52	417	319	20.74	0.20	0.22	0.05	0.04	0.09
1488	1 30 52.8	30 22 50	418	-55	20.74	0.27	...	0.08	0.09	...
1489	1 31 02.9	30 22 53	418	495	19.95	0.28	...	0.04	0.03	...
1490	1 31 15.1	30 22 57	418	1163	20.59	0.28	...	0.03	0.06	...
1491	1 31 05.3	30 22 54	420	625	20.88	0.21	...	0.09	0.07	...
1492	1 31 02.0	30 22 53	420	447	20.55	-0.01	-1.09	0.12	0.04	0.04
1493	1 31 09.3	30 22 55	421	844	20.88	0.17	-0.80	0.04	0.05	0.05
1494	1 31 01.9	30 22 52	421	439	20.50	0.16	...	0.08	0.05	...
1495	1 31 05.3	30 22 53	421	625	20.31	0.77	-0.85	0.06	0.07	0.04
1496	1 30 54.9	30 22 50	421	56	20.95	-0.06	-0.97	0.05	0.03	0.03
1497	1 30 44.9	30 22 47	421	-487	20.81	0.35	...	0.05	0.03	...
1498	1 30 50.1	30 22 48	422	-208	18.69	-0.25	-1.03	0.02	0.02	0.04
1499	1 30 50.5	30 22 48	423	-184	18.88	-0.18	-0.98	0.02	0.02	0.04
1500	1 30 56.8	30 22 50	423	161	20.10	0.18	0.33	0.04	0.02	0.06

TABLE 2 (cont.)

Number	α(1950)	δ(1950)	X	Y	V	B-V	U-B	σ_V	σ_B	σ_U
1501	1 30 50.3	30 22 48	424	-194	21.00	-0.54	-1.08	0.08	0.04	0.05
1502	1 30 51.3	30 22 48	424	-138	20.01	-0.09	-0.91	0.03	0.02	0.05
1503	1 30 47.1	30 22 47	424	-367	20.97	-0.22	-0.14	0.06	0.03	0.05
1504	1 30 56.5	30 22 50	425	143	20.93	0.29	...	0.16	0.17	...
1505	1 31 03.5	30 22 52	426	527	20.24	0.05	-0.86	0.05	0.02	0.04
1506	1 31 02.2	30 22 51	426	456	20.81	-0.38	-0.83	0.05	0.04	0.04
1507	1 30 49.6	30 22 47	427	-232	20.99	-0.24	-1.29	0.07	0.06	0.05
1508	1 31 08.7	30 22 53	427	815	18.59	0.20	-0.93	0.03	0.05	0.03
1509	1 31 07.3	30 22 53	427	734	20.56	0.00	-0.79	0.11	0.02	0.09
1510	1 31 05.7	30 22 52	428	649	18.85	0.25	0.04	0.01	0.01	0.04
1511	1 30 56.0	30 22 49	428	120	20.76	0.19	...	0.07	0.13	...
1512	1 30 56.5	30 22 49	428	144	19.92	0.36	-0.08	0.10	0.05	0.12
1513	1 31 07.6	30 22 52	428	751	20.34	0.05	-0.99	0.03	0.03	0.04
1514	1 30 51.4	30 22 47	429	-136	20.85	-0.10	-0.92	0.07	0.04	0.09
1515	1 30 53.0	30 22 47	430	-44	20.73	-0.18	-0.68	0.05	0.03	0.05
1516	1 31 02.0	30 22 50	431	444	19.22	0.10	...	0.06	0.06	...
1517	1 30 46.3	30 22 45	431	-414	19.78	-0.19	-0.92	0.02	0.02	0.04
1518	1 31 08.4	30 22 52	431	795	20.66	0.09	-0.60	0.03	0.03	0.04
1519	1 31 11.3	30 22 53	431	953	20.57	0.19	-0.25	0.03	0.03	0.06
1520	1 30 51.5	30 22 47	432	-131	19.07	-0.04	-0.64	0.02	0.02	0.04
1521	1 30 53.3	30 22 47	432	-30	20.97	0.14	-1.03	0.06	0.04	0.05
1522	1 30 59.3	30 22 49	433	301	19.75	-0.12	-0.88	0.02	0.06	0.03
1523	1 30 46.6	30 22 45	433	-398	20.93	0.33	0.12	0.05	0.04	0.07
1524	1 31 02.0	30 22 49	434	444	19.09	0.30	-1.14	0.08	0.05	0.06
1525	1 31 15.0	30 22 54	434	1160	19.57	0.05	-0.87	0.03	0.03	0.03
1526	1 30 49.9	30 22 45	436	-215	18.90	-0.91	-0.91	0.07	0.04	0.06
1527	1 31 01.8	30 22 49	436	436	17.80	0.00	-0.62	0.01	0.01	0.03
1528	1 30 50.3	30 22 45	437	-196	20.88	-0.45	...	0.07	0.04	...
1529	1 31 04.5	30 22 49	437	582	20.52	-0.06	-0.96	0.05	0.03	0.03
1530	1 30 48.7	30 22 44	439	-280	20.20	0.10	-0.80	0.05	0.04	0.05
1531	1 31 12.2	30 22 51	439	1004	20.77	0.07	-0.73	0.04	0.03	0.04
1532	1 31 04.4	30 22 49	441	578	20.78	0.16	...	0.06	0.05	...
1533	1 31 02.0	30 22 48	441	448	20.39	0.14	...	0.08	0.03	...
1534	1 31 11.5	30 22 51	441	964	20.51	0.31	...	0.03	0.03	...
1535	1 30 58.9	30 22 47	442	276	20.95	-0.10	-0.76	0.07	0.04	0.04
1536	1 30 59.9	30 22 47	442	331	15.78	0.13	-0.84	0.00	0.00	0.03
1537	1 30 50.5	30 22 44	442	-186	19.37	-0.14	-0.99	0.03	0.02	0.04
1538	1 31 03.7	30 22 48	443	539	20.86	0.08	-0.96	0.07	0.04	0.04
1539	1 31 06.1	30 22 48	444	672	18.87	0.22	0.04	0.14	0.06	0.02
1540	1 31 14.7	30 22 51	444	1140	20.80	0.26	-0.17	0.03	0.06	0.06
1541	1 31 15.3	30 22 51	444	1174	20.08	0.01	-0.96	0.03	0.03	0.03
1542	1 30 54.8	30 22 45	445	54	19.84	-0.03	-0.97	0.02	0.02	0.04
1543	1 31 05.1	30 22 48	445	617	20.25	-0.02	-1.05	0.03	0.02	0.03
1544	1 30 54.8	30 22 44	445	54	19.91	-0.10	...	0.10	0.00	...
1545	1 31 01.4	30 22 46	447	411	19.91	0.06	-1.05	0.02	0.02	0.03
1546	1 30 45.2	30 22 41	447	-475	20.54	0.04	-0.92	0.03	0.02	0.04
1547	1 30 46.0	30 22 41	448	-429	20.43	0.01	-0.62	0.23	0.14	0.04
1548	1 30 49.9	30 22 42	448	-216	19.19	-0.29	-1.08	0.03	0.03	0.05
1549	1 30 59.0	30 22 45	449	281	20.67	0.39	...	0.05	0.04	...
1550	1 30 54.2	30 22 43	450	18	20.67	0.03	...	0.04	0.03	...

TABLE 2 (cont.)

Number	α(1950)	δ(1950)	X	Y	V	B-V	U-B	σ_V	σ_B	σ_U
1551	1 31 05.3	30 22 46	451	624	20.75	0.12	-0.98	0.04	0.03	0.04
1552	1 31 05.1	30 22 46	452	614	19.95	-0.10	-1.13	0.02	0.03	0.03
1553	1 30 55.1	30 22 43	453	68	20.01	-0.70	...	0.18	0.03	...
1554	1 30 59.4	30 22 44	453	303	20.82	0.26	0.75	0.05	0.04	0.09
1555	1 30 49.7	30 22 41	454	-228	19.14	-0.16	...	0.04	0.05	...
1556	1 30 49.8	30 22 41	454	-224	19.06	-0.22	...	0.04	0.05	...
1557	1 31 07.0	30 22 46	455	718	20.96	-0.34	...	0.07	0.03	...
1558	1 31 12.3	30 22 48	455	1010	19.72	0.13	-0.64	0.03	0.03	0.03
1559	1 30 57.2	30 22 43	456	181	20.40	0.08	0.08	0.12	0.03	0.15
1560	1 31 11.3	30 22 47	456	952	20.13	0.39	...	0.05	0.04	...
1561	1 30 55.1	30 22 42	458	70	19.94	0.06	0.29	0.03	0.03	0.07
1562	1 31 15.9	30 22 48	459	1204	20.53	-0.04	-0.71	0.04	0.03	0.03
1563	1 31 03.3	30 22 44	459	517	19.90	0.13	-0.77	0.03	0.02	0.03
1564	1 30 49.8	30 22 40	459	-222	19.15	-0.21	-1.12	0.02	0.02	0.05
1565	1 31 15.7	30 22 48	460	1194	20.85	0.17	-0.81	0.04	0.03	0.05
1566	1 30 54.6	30 22 41	461	41	20.57	0.34	0.18	0.04	0.06	0.07
1567	1 31 09.6	30 22 45	462	860	20.96	0.08	...	0.03	0.07	...
1568	1 31 11.2	30 22 46	462	947	19.29	0.22	-1.09	0.03	0.03	0.03
1569	1 31 12.9	30 22 46	464	1040	20.84	0.07	-0.33	0.03	0.03	0.05
1570	1 31 12.7	30 22 46	464	1031	20.38	0.21	-0.39	0.04	0.05	0.04
1571	1 31 12.1	30 22 45	465	999	20.64	0.13	-0.85	0.03	0.03	0.05
1572	1 31 03.9	30 22 42	467	552	19.34	-0.08	-0.93	0.02	0.02	0.04
1573	1 30 56.0	30 22 39	468	115	20.60	0.77	-1.13	0.09	0.16	0.07
1574	1 31 07.0	30 22 43	469	718	20.80	0.00	-0.84	0.05	0.02	0.03
1575	1 30 54.5	30 22 39	469	36	19.21	-0.09	-0.92	0.02	0.02	0.04
1576	1 31 00.9	30 22 40	470	383	20.94	-0.04	-0.33	0.05	0.19	0.30
1577	1 31 09.0	30 22 43	470	829	19.52	0.16	0.01	0.02	0.03	0.03
1578	1 30 58.8	30 22 40	470	268	20.23	-0.25	-0.86	0.03	0.01	0.03
1579	1 30 56.6	30 22 39	471	151	20.34	-0.05	-0.20	0.08	0.02	0.00
1580	1 30 50.3	30 22 37	471	-194	20.99	-0.32	-1.32	0.07	0.04	0.05
1581	1 30 59.7	30 22 40	471	319	20.72	-0.23	-0.73	0.05	0.02	0.03
1582	1 31 01.8	30 22 40	472	432	18.35	0.27	0.23	0.01	0.01	0.03
1583	1 31 03.0	30 22 41	472	498	20.51	0.13	-0.71	0.04	0.03	0.03
1584	1 31 04.6	30 22 41	472	585	20.50	0.04	-0.59	0.05	0.04	0.03
1585	1 31 10.5	30 22 43	472	910	20.93	0.13	-0.85	0.03	0.04	0.05
1586	1 31 05.8	30 22 41	474	654	20.29	0.17	-0.73	0.03	0.02	0.03
1587	1 31 03.2	30 22 40	474	510	19.19	-0.18	-0.98	0.02	0.01	0.03
1588	1 31 14.7	30 22 44	474	1138	20.61	0.35	-0.58	0.03	0.03	0.04
1589	1 30 57.3	30 22 38	474	188	19.43	0.09	-0.04	0.01	0.01	0.03
1590	1 30 57.1	30 22 38	476	178	20.60	0.03	-0.74	0.11	0.00	0.04
1591	1 31 11.1	30 22 42	476	942	19.41	0.96	-0.76	0.02	0.03	0.04
1592	1 30 57.6	30 22 38	476	206	20.78	0.20	0.19	0.04	0.03	0.06
1593	1 31 02.2	30 22 39	476	456	20.78	-0.05	-0.89	0.05	0.03	0.03
1594	1 31 04.6	30 22 40	478	585	20.94	0.05	...	0.08	0.05	...
1595	1 31 09.6	30 22 41	478	862	20.28	0.21	-1.20	0.03	0.05	0.03
1596	1 30 59.0	30 22 38	478	279	20.69	0.11	-0.28	0.05	0.06	0.07
1597	1 31 09.4	30 22 41	479	852	19.54	0.12	-0.71	0.02	0.03	0.03
1598	1 30 45.6	30 22 33	480	-453	20.68	0.23	...	0.04	0.03	...
1599	1 31 05.7	30 22 40	480	650	20.63	-0.27	-0.92	0.04	0.02	0.03
1600	1 31 00.1	30 22 38	480	343	20.05	-0.21	-0.93	0.08	0.07	0.07

TABLE 2 (cont.)

Number	α(1950)	δ(1950)	X	Y	V	B-V	U-B	σ_V	σ_B	σ_U
1601	1 30 57.8	30 22 37	481	216	20.56	0.25	-0.57	0.05	0.04	0.04
1602	1 31 00.1	30 22 38	481	340	19.72	-0.19	-1.15	0.06	0.05	0.05
1603	1 30 56.9	30 22 37	482	165	20.87	0.04	-1.00	0.05	0.03	0.04
1604	1 31 12.9	30 22 42	482	1044	20.72	0.30	...	0.03	0.03	...
1605	1 30 57.1	30 22 36	484	174	20.57	-0.14	-0.79	0.02	0.03	0.02
1606	1 31 15.7	30 22 42	486	1196	20.69	0.17	-0.09	0.03	0.03	0.06
1607	1 30 53.9	30 22 35	486	3	20.92	0.36	0.14	0.06	0.05	0.09
1608	1 31 03.6	30 22 37	487	531	20.78	-0.26	...	0.08	0.05	...
1609	1 31 13.3	30 22 40	488	1062	19.68	0.13	-0.12	0.03	0.03	0.03
1610	1 31 01.1	30 22 36	489	394	19.19	-0.17	-0.96	0.02	0.01	0.03
1611	1 30 52.3	30 22 33	489	-88	19.02	-0.09	-0.57	0.02	0.02	0.04
1612	1 31 00.4	30 22 36	489	356	20.59	0.32	...	0.04	0.04	...
1613	1 30 57.7	30 22 35	490	210	20.22	0.12	0.15	0.02	0.02	0.04
1614	1 31 02.4	30 22 36	491	468	20.72	-0.13	-0.94	0.07	0.08	0.03
1615	1 31 10.3	30 22 38	492	901	20.34	0.05	-1.07	0.03	0.03	0.03
1616	1 31 09.3	30 22 38	493	842	20.86	0.14	...	0.05	0.06	...
1617	1 31 04.5	30 22 36	494	583	20.86	0.04	...	0.06	0.03	...
1618	1 31 09.6	30 22 38	494	859	19.89	0.07	-0.71	0.04	0.06	0.08
1619	1 31 07.1	30 22 37	495	724	18.98	0.17	-0.10	0.03	0.01	0.00
1620	1 30 58.5	30 22 34	496	251	20.93	-0.15	-0.98	0.05	0.03	0.03
1621	1 31 01.8	30 22 35	497	435	20.40	0.44	-0.56	0.04	0.04	0.04
1622	1 30 47.3	30 22 30	498	-360	20.01	-0.10	-0.56	0.02	0.02	0.04
1623	1 31 09.9	30 22 36	500	876	20.76	-0.03	...	0.05	0.05	...
1624	1 31 02.4	30 22 34	500	464	19.65	-0.05	-0.39	0.06	0.05	0.04
1625	1 31 14.2	30 22 38	500	1112	20.91	-0.11	-0.73	0.04	0.03	0.04
1626	1 31 02.4	30 22 34	502	465	19.55	-0.14	...	0.08	0.06	...
1627	1 30 54.7	30 22 31	503	45	20.49	0.22	-0.43	0.05	0.05	0.05
1628	1 31 02.4	30 22 33	504	466	19.83	0.12	...	0.05	0.06	...
1629	1 30 55.2	30 22 31	504	70	18.75	-0.42	...	0.11	0.05	...
1630	1 31 13.5	30 22 36	504	1073	20.99	0.23	...	0.04	0.04	...
1631	1 30 47.4	30 22 28	505	-352	19.05	0.23	0.19	0.02	0.02	0.04
1632	1 30 55.2	30 22 30	506	70	17.78	0.08	...	0.04	0.02	...
1633	1 30 58.3	30 22 31	506	243	19.36	0.37	0.46	0.02	0.01	0.03
1634	1 31 02.2	30 22 32	508	456	20.94	0.29	...	0.07	0.08	...
1635	1 30 53.1	30 22 29	508	-44	18.88	0.06	-0.43	0.02	0.02	0.04
1636	1 31 11.6	30 22 35	510	972	20.77	0.00	-1.09	0.04	0.03	0.06
1637	1 31 04.1	30 22 32	510	561	20.75	0.09	-0.98	0.04	0.05	0.03
1638	1 31 05.9	30 22 33	510	659	20.92	-0.06	-0.62	0.08	0.02	0.15
1639	1 31 06.1	30 22 32	511	667	20.14	0.09	-0.88	0.10	0.10	0.02
1640	1 31 01.2	30 22 31	512	400	20.78	-0.19	...	0.05	0.04	...
1641	1 31 14.7	30 22 35	512	1139	18.53	0.25	-0.75	0.02	0.03	0.03
1642	1 30 45.6	30 22 26	513	-451	19.91	-0.05	-0.92	0.02	0.02	0.04
1643	1 31 10.9	30 22 34	513	930	20.83	0.02	-1.37	0.05	0.05	0.03
1644	1 31 14.6	30 22 35	514	1135	20.83	0.13	...	0.05	0.06	...
1645	1 31 02.6	30 22 30	515	478	19.70	-0.05	-0.89	0.02	0.01	0.03
1646	1 30 47.7	30 22 26	516	-338	20.35	-0.01	-0.20	0.03	0.03	0.05
1647	1 30 45.3	30 22 24	517	-472	19.03	0.29	0.31	0.02	0.02	0.04
1648	1 31 13.9	30 22 33	518	1097	20.70	0.05	...	0.03	0.03	...
1649	1 31 14.7	30 22 34	518	1140	20.11	0.14	-0.87	0.03	0.04	0.06
1650	1 31 10.4	30 22 32	519	903	20.87	0.18	...	0.04	0.05	...

TABLE 2 (cont.)

Number	α(1950)	δ(1950)	X	Y	V	B-V	U-B	σ_V	σ_B	σ_U
1651	1 31 04.4	30 22 30	519	572	20.51	0.17	-0.55	0.05	0.03	0.06
1652	1 31 03.6	30 22 30	520	531	20.57	0.08	-0.01	0.04	0.03	0.05
1653	1 31 08.2	30 22 31	520	784	19.89	0.06	-0.78	0.03	0.03	0.03
1654	1 30 56.1	30 22 26	523	120	20.67	0.06	-0.82	0.04	0.11	0.11
1655	1 30 55.5	30 22 26	523	88	20.48	0.36	0.63	0.03	0.03	0.08
1656	1 31 13.6	30 22 32	524	1080	18.92	0.49	-1.47	0.02	0.21	0.03
1657	1 31 01.6	30 22 28	524	423	19.99	0.01	-0.11	0.03	0.02	0.03
1658	1 30 51.5	30 22 24	528	-133	19.67	0.10	-0.83	0.02	0.02	0.04
1659	1 30 50.9	30 22 23	529	-167	19.15	0.34	-0.69	0.04	0.06	0.05
1660	1 31 03.1	30 22 27	529	505	20.98	0.28	-0.46	0.05	0.05	0.06
1661	1 31 03.4	30 22 27	529	519	20.52	-0.22	-1.00	0.05	0.05	0.03
1662	1 31 03.0	30 22 27	530	497	20.46	0.15	-0.91	0.03	0.04	0.03
1663	1 31 12.5	30 22 29	534	1015	20.26	0.13	-0.81	0.03	0.05	0.03
1664	1 31 13.3	30 22 29	535	1060	19.15	-0.03	-1.42	0.06	0.04	0.03
1665	1 31 10.5	30 22 28	535	906	20.27	0.44	-1.69	0.04	0.31	0.03
1666	1 31 10.8	30 22 28	537	926	20.86	0.79	-1.98	0.05	0.23	0.04
1667	1 30 44.8	30 22 20	537	-497	19.48	0.22	...	0.02	0.02	...
1668	1 31 13.3	30 22 28	539	1061	20.21	-0.04	...	0.06	0.06	...
1669	1 31 07.2	30 22 26	540	729	20.34	0.35	...	0.01	0.07	...
1670	1 31 13.0	30 22 28	540	1045	19.45	0.16	...	0.05	0.06	...
1671	1 31 01.8	30 22 24	542	432	20.39	-0.09	-1.04	0.03	0.02	0.03
1672	1 31 12.9	30 22 27	542	1041	19.11	0.30	-2.29	0.04	0.08	0.03
1673	1 31 06.3	30 22 25	543	676	20.74	-0.32	-1.01	0.16	0.04	0.07
1674	1 31 06.3	30 22 25	543	676	20.61	-0.15	...	0.17	0.06	...
1675	1 31 03.0	30 22 24	543	498	18.44	0.09	-0.20	0.01	0.01	0.03
1676	1 31 13.1	30 22 27	543	1052	18.47	0.05	...	0.03	0.05	...
1677	1 31 13.3	30 22 27	544	1062	20.66	0.04	...	0.09	0.07	...
1678	1 31 06.0	30 22 24	545	661	20.57	0.10	-0.79	0.08	0.08	0.08
1679	1 31 13.0	30 22 26	546	1043	19.73	-0.12	...	0.05	0.06	...
1680	1 31 08.4	30 22 25	547	794	20.66	0.05	-0.80	0.03	0.04	0.03
1681	1 31 12.4	30 22 26	548	1011	19.08	0.48	-1.52	0.05	0.16	0.03
1682	1 31 10.9	30 22 25	548	929	17.03	-0.06	...	0.12	0.07	...
1683	1 30 52.9	30 22 20	548	-55	20.37	0.04	...	0.04	0.03	...
1684	1 31 10.7	30 22 25	548	921	20.78	0.30	...	0.22	0.07	...
1685	1 30 57.3	30 22 21	549	186	20.65	0.35	0.26	0.04	0.03	0.06
1686	1 31 10.2	30 22 25	549	892	20.85	0.28	-1.46	0.04	0.05	0.04
1687	1 30 57.3	30 22 21	549	186	20.68	0.28	...	0.05	0.06	...
1688	1 31 08.6	30 22 24	549	804	19.39	0.16	-0.67	0.03	0.04	0.03
1689	1 30 49.3	30 22 18	550	-254	20.03	-0.01	-0.85	0.02	0.02	0.04
1690	1 31 13.7	30 22 25	553	1081	20.81	0.54	-1.92	0.05	0.13	0.03
1691	1 31 10.1	30 22 24	553	886	20.80	-0.01	-1.37	0.13	0.15	0.04
1692	1 31 13.0	30 22 24	555	1047	20.05	0.21	...	0.07	0.10	...
1693	1 31 00.8	30 22 20	556	376	20.29	-0.09	-0.76	0.03	0.01	0.03
1694	1 30 46.1	30 22 15	557	-429	20.58	0.31	-0.49	0.05	0.03	0.05
1695	1 31 12.7	30 22 23	560	1031	20.35	0.39	...	0.04	0.12	...
1696	1 31 02.2	30 22 20	561	452	19.88	-0.17	-1.04	0.02	0.01	0.03
1697	1 30 45.4	30 22 14	562	-467	20.29	0.10	...	0.04	0.03	...
1698	1 30 46.2	30 22 14	565	-423	20.74	0.40	0.24	0.04	0.04	0.07
1699	1 30 48.7	30 22 14	565	-287	20.82	0.25	-0.69	0.05	0.03	0.04
1700	1 31 06.2	30 22 20	566	670	20.86	-0.04	-1.19	0.05	0.04	0.07

TABLE 2 (cont.)

Number	α(1950)	δ(1950)	X	Y	V	B-V	U-B	σ_V	σ_B	σ_U
1701	1 31 13.2	30 22 22	566	1054	17.63	0.62	-1.64	0.05	0.13	0.03
1702	1 31 06.3	30 22 19	567	680	19.62	0.04	...	0.04	0.07	...
1703	1 31 02.8	30 22 18	570	487	19.51	0.10	-0.01	0.02	0.01	0.03
1704	1 31 02.7	30 22 17	571	481	20.11	0.40	-0.99	0.03	0.03	0.03
1705	1 31 06.3	30 22 18	571	676	19.60	0.25	...	0.15	0.02	...
1706	1 31 03.1	30 22 17	571	503	20.48	-0.04	-1.04	0.04	0.03	0.03
1707	1 31 14.9	30 22 21	573	1150	20.91	0.23	-0.74	0.04	0.04	0.06
1708	1 31 12.7	30 22 20	575	1025	20.54	0.16	-1.61	0.08	0.07	0.03
1709	1 31 11.2	30 22 19	576	946	19.04	0.04	-0.63	0.07	0.06	0.03
1710	1 31 09.7	30 22 18	576	863	20.18	0.19	-1.01	0.04	0.06	0.03
1711	1 31 02.6	30 22 16	576	475	20.24	0.06	-0.59	0.03	0.02	0.03
1712	1 31 06.5	30 22 17	578	690	19.25	0.18	0.12	0.05	0.06	0.02
1713	1 31 10.2	30 22 18	578	889	18.34	0.08	-0.69	0.05	0.06	0.03
1714	1 30 45.4	30 22 10	579	-467	20.96	0.29	...	0.06	0.03	...
1715	1 31 01.7	30 22 15	580	423	19.33	0.01	0.00	0.02	0.01	0.03
1716	1 31 13.1	30 22 18	580	1047	19.96	0.02	-1.86	0.12	0.14	0.03
1717	1 31 00.9	30 22 14	581	380	19.85	-0.15	-1.05	0.03	0.01	0.03
1718	1 31 10.5	30 22 17	582	905	19.93	-0.03	-1.12	0.16	0.06	0.03
1719	1 30 56.5	30 22 13	583	138	20.96	0.15	...	0.17	0.01	...
1720	1 30 55.3	30 22 12	584	75	20.92	0.20	...	0.20	0.18	...
1721	1 31 03.0	30 22 14	585	496	20.20	0.28	-0.04	0.06	0.03	0.04
1722	1 30 55.3	30 22 11	586	77	20.26	0.34	...	0.10	0.13	...
1723	1 31 01.1	30 22 13	588	395	19.27	0.09	0.12	0.01	0.01	0.03
1724	1 30 47.5	30 22 8	590	-353	20.84	0.28	0.14	0.05	0.04	0.06
1725	1 31 10.9	30 22 15	592	929	20.81	0.23	...	0.06	0.05	...
1726	1 31 10.8	30 22 14	595	925	20.01	0.12	-1.95	0.07	0.06	0.06
1727	1 31 06.8	30 22 13	596	705	20.36	0.06	-0.95	0.08	0.05	0.17
1728	1 31 10.9	30 22 14	597	926	20.33	0.36	...	0.12	0.07	...
1729	1 31 05.9	30 22 12	598	653	20.63	0.06	-0.75	0.05	0.05	0.05
1730	1 31 06.0	30 22 12	598	661	20.32	0.15	...	0.03	0.04	...
1731	1 31 10.9	30 22 13	599	929	20.08	0.20	-1.38	0.05	0.05	0.09
1732	1 30 50.6	30 22 7	599	-184	18.92	-0.07	-1.01	0.03	0.02	0.04
1733	1 31 06.0	30 22 11	601	659	20.73	0.02	...	0.05	0.05	...
1734	1 31 00.6	30 22 9	601	363	19.77	-0.25	-1.14	0.03	0.02	0.03
1735	1 30 50.1	30 22 6	602	-212	20.37	0.35	...	0.03	0.03	...
1736	1 31 03.3	30 22 10	602	511	20.93	-0.04	-0.42	0.05	0.03	0.04
1737	1 31 08.5	30 22 11	605	794	19.95	0.22	...	0.03	0.04	...
1738	1 30 59.5	30 22 8	606	303	19.67	-0.18	-0.92	0.02	0.01	0.03
1739	1 31 00.4	30 22 8	607	353	18.88	-0.20	-1.00	0.02	0.01	0.03
1740	1 31 07.3	30 22 10	609	732	20.62	0.12	...	0.10	0.07	...
1741	1 31 12.2	30 22 11	609	998	20.39	0.19	-1.85	0.04	0.15	0.03
1742	1 31 01.9	30 22 8	610	437	20.23	-0.17	-1.01	0.03	0.02	0.03
1743	1 31 00.8	30 22 7	611	374	20.66	-0.44	...	0.12	0.04	...
1744	1 31 02.0	30 22 8	611	443	20.53	-0.02	-1.20	0.05	0.03	0.03
1745	1 30 52.4	30 22 4	613	-85	20.91	0.03	-1.15	0.04	0.03	0.04
1746	1 30 57.8	30 22 6	613	209	19.41	-0.14	-0.99	0.01	0.01	0.03
1747	1 31 12.8	30 22 11	613	1032	19.40	0.33	...	0.10	0.15	...
1748	1 31 02.2	30 22 7	616	452	20.97	0.12	...	0.06	0.06	...
1749	1 31 10.7	30 22 9	617	916	20.70	-0.45	-1.09	0.20	0.06	0.03
1750	1 31 07.5	30 22 8	619	742	20.42	0.92	-1.52	0.20	0.38	0.01

TABLE 2 (cont.)

Number	α(1950)	δ(1950)	X	Y	V	B-V	U-B	σ_V	σ_B	σ_U
1751	1 31 02.2	30 22 6	620	451	20.67	-0.09	-0.78	0.09	0.03	0.05
1752	1 30 56.9	30 22 4	621	160	20.28	0.02	-1.05	0.03	0.02	0.03
1753	1 30 52.4	30 22 2	623	-86	20.60	-0.24	-1.05	0.04	0.02	0.04
1754	1 31 02.1	30 22 5	624	446	20.98	0.14	-1.05	0.06	0.07	0.04
1755	1 31 03.2	30 22 5	625	508	20.00	0.09	0.19	0.02	0.02	0.04
1756	1 30 49.7	30 22 0	625	-231	20.85	0.04	...	0.05	0.03	...
1757	1 30 50.9	30 21 60	629	-169	19.49	-0.05	-1.15	0.02	0.02	0.04
1758	1 31 14.0	30 22 7	631	1096	20.47	0.35	...	0.22	0.22	...
1759	1 31 05.6	30 22 4	632	640	19.43	0.11	-0.73	0.01	0.01	0.03
1760	1 31 07.9	30 22 5	632	765	19.20	0.01	-1.08	0.03	0.03	0.03
1761	1 31 13.8	30 22 6	633	1087	20.67	0.09	...	0.04	0.03	...
1762	1 31 12.1	30 22 5	637	994	20.19	0.15	...	0.37	0.47	...
1763	1 31 12.1	30 22 5	637	993	19.96	0.10	-0.49	0.05	0.03	0.03
1764	1 30 50.8	30 21 57	640	-175	20.54	-0.08	-1.11	0.04	0.04	0.03
1765	1 31 04.7	30 22 1	643	590	20.87	-0.15	-0.78	0.09	0.02	0.03
1766	1 31 01.5	30 21 60	644	411	20.42	0.22	-0.48	0.05	0.04	0.01
1767	1 31 05.1	30 22 1	645	607	19.55	0.06	-1.05	0.02	0.05	0.21
1768	1 31 02.9	30 21 60	647	487	20.57	-0.15	-1.04	0.02	0.07	0.03
1769	1 31 15.5	30 22 3	647	1182	18.21	0.12	-0.23	0.08	0.09	0.11
1770	1 30 50.0	30 21 55	649	-215	20.69	-0.24	-1.02	0.01	0.07	0.04
1771	1 31 11.7	30 22 2	650	970	20.92	0.00	...	0.05	0.04	...
1772	1 30 50.1	30 21 54	652	-210	20.87	-0.18	...	0.07	0.00	...
1773	1 30 50.4	30 21 54	652	-197	20.76	0.26	...	0.07	0.05	...
1774	1 31 00.7	30 21 56	657	369	20.24	0.01	-0.84	0.04	0.01	0.01
1775	1 31 11.7	30 21 59	659	972	20.61	0.34	-1.57	0.08	0.12	0.03
1776	1 31 00.3	30 21 56	659	349	18.52	0.25	0.15	0.03	0.01	0.00
1777	1 30 51.3	30 21 53	660	-144	19.07	-0.13	-1.03	0.01	0.02	0.03
1778	1 31 03.6	30 21 56	661	526	20.36	-0.21	...	0.00	0.07	...
1779	1 31 03.7	30 21 56	662	534	20.94	-0.07	-1.17	0.05	0.04	0.04
1780	1 31 10.8	30 21 58	662	919	20.28	0.03	...	0.04	0.05	...
1781	1 31 11.4	30 21 58	664	952	20.74	0.06	-0.31	0.05	0.03	0.05
1782	1 31 11.2	30 21 58	665	941	20.81	-0.04	...	0.04	0.04	...
1783	1 31 12.4	30 21 58	666	1009	19.35	-0.20	-2.01	0.23	0.06	0.03
1784	1 31 12.4	30 21 58	667	1008	18.64	0.13	-1.55	0.34	0.70	0.17
1785	1 31 12.0	30 21 57	669	987	20.77	0.03	-1.83	0.22	0.08	0.03
1786	1 30 47.6	30 21 50	669	-347	18.98	0.26	-0.39	0.02	0.02	0.05
1787	1 31 12.0	30 21 57	669	985	20.08	0.17	...	0.04	0.04	...
1788	1 30 47.6	30 21 49	669	-347	19.01	0.21	...	0.04	0.03	...
1789	1 30 51.4	30 21 51	669	-141	20.73	0.06	...	0.05	0.03	...
1790	1 31 11.1	30 21 56	671	939	18.97	0.16	-1.42	0.28	0.15	0.03
1791	1 31 11.1	30 21 56	671	938	18.43	0.46	-1.10	0.44	0.63	0.19
1792	1 31 11.3	30 21 56	672	949	20.16	0.28	-0.52	0.33	0.18	0.36
1793	1 31 12.4	30 21 57	672	1009	20.70	0.01	...	0.05	0.04	...
1794	1 31 12.4	30 21 56	674	1009	20.64	-0.21	-2.00	0.11	0.08	0.04
1795	1 30 57.6	30 21 51	675	197	20.99	0.13	...	0.07	0.04	...
1796	1 30 57.6	30 21 51	676	198	20.98	0.08	...	0.06	0.05	...
1797	1 31 12.3	30 21 56	676	1003	19.70	-0.31	...	0.10	0.05	...
1798	1 31 12.3	30 21 56	676	1002	19.26	-0.08	-1.00	0.03	0.03	0.03
1799	1 31 12.4	30 21 56	676	1008	20.42	-0.06	...	0.77	0.72	...
1800	1 31 13.5	30 21 56	677	1066	20.93	0.96	-0.81	0.04	0.05	0.07

TABLE 2 (cont.)

Number	α(1950)	δ(1950)	X	Y	V	B-V	U-B	σ_V	σ_B	σ_U
1801	1 30 53.0	30 21 49	678	-56	20.94	0.28	...	0.05	0.04	...
1802	1 31 13.0	30 21 55	681	1039	20.93	0.01	-1.03	0.15	0.15	0.08
1803	1 31 03.5	30 21 51	682	523	18.61	-0.09	-0.98	0.01	0.01	0.00
1804	1 31 11.3	30 21 54	682	950	19.09	1.11	-1.05	0.05	0.12	0.02
1805	1 30 52.2	30 21 48	683	-95	20.98	0.22	...	0.06	0.04	...
1806	1 30 45.6	30 21 45	684	-461	19.95	0.12	...	0.05	0.06	...
1807	1 30 59.8	30 21 50	685	320	19.68	-0.10	-0.99	0.00	0.04	0.01
1808	1 30 59.6	30 21 49	685	307	20.60	0.13	-0.99	0.05	0.04	0.04
1809	1 30 59.6	30 21 49	686	307	20.76	-0.09	...	0.25	0.07	...
1810	1 30 55.8	30 21 48	686	100	20.71	0.17	-0.80	0.03	0.07	0.02
1811	1 30 46.6	30 21 45	688	-406	20.31	0.05	-0.86	0.03	0.04	0.07
1812	1 30 49.2	30 21 45	688	-262	20.85	-0.11	...	0.02	0.03	...
1813	1 30 58.0	30 21 48	688	219	20.81	0.27	-0.45	0.15	0.10	0.09
1814	1 30 58.6	30 21 48	690	253	20.23	0.12	-0.75	0.03	0.04	0.00
1815	1 30 45.6	30 21 43	692	-460	19.17	-0.07	-1.14	0.03	0.04	0.07
1816	1 31 03.9	30 21 47	699	543	20.84	-0.05	-0.78	0.17	0.16	0.06
1817	1 30 45.6	30 21 42	700	-460	20.02	-0.12	...	0.05	0.04	...
1818	1 30 55.2	30 21 45	700	66	20.83	0.19	-0.54	0.08	0.06	0.06
1819	1 31 11.9	30 21 50	701	981	20.91	0.01	-0.86	0.04	0.03	0.04
1820	1 30 45.9	30 21 41	703	-445	19.94	0.01	-1.17	0.03	0.06	0.05
1821	1 31 13.4	30 21 50	703	1062	19.58	0.11	-1.17	0.06	0.08	0.02
1822	1 30 57.6	30 21 44	705	199	20.79	-0.01	-1.06	0.06	0.04	0.04
1823	1 30 52.3	30 21 42	706	-94	20.57	-0.09	...	0.16	0.11	...
1824	1 30 52.3	30 21 42	706	-94	20.69	-0.29	-0.75	0.05	0.03	0.05
1825	1 31 04.6	30 21 46	708	581	20.77	0.36	-0.26	0.00	0.03	0.29
1826	1 30 51.2	30 21 41	709	-154	20.88	0.09	-1.04	0.05	0.04	0.05
1827	1 30 45.0	30 21 39	710	-492	20.19	-0.04	-0.78	0.03	0.02	0.05
1828	1 30 45.0	30 21 39	710	-492	20.19	-0.03	...	0.01	0.02	...
1829	1 30 59.3	30 21 43	711	289	19.19	0.32	-1.09	0.01	0.13	0.05
1830	1 31 01.5	30 21 44	712	408	19.96	-0.06	-1.09	0.04	0.04	0.04
1831	1 31 03.5	30 21 44	713	522	20.57	-0.16	-0.97	0.04	0.02	0.03
1832	1 30 59.2	30 21 43	714	288	19.56	0.40	...	0.22	0.02	...
1833	1 31 12.0	30 21 46	716	985	20.90	-0.10	-0.74	0.04	0.03	0.04
1834	1 30 51.3	30 21 40	716	-148	20.02	0.05	0.01	0.03	0.02	0.05
1835	1 31 07.1	30 21 44	717	715	19.86	-0.10	-1.09	0.03	0.07	0.05
1836	1 31 13.2	30 21 45	722	1051	20.70	0.21	...	0.09	0.08	...
1837	1 30 57.8	30 21 40	722	210	20.64	-0.15	-0.63	0.04	0.02	0.04
1838	1 31 13.6	30 21 45	722	1073	19.52	0.19	-0.33	0.04	0.04	0.02
1839	1 30 55.0	30 21 39	724	52	20.54	0.18	-0.15	0.04	0.02	0.05
1840	1 31 11.6	30 21 44	727	961	19.36	0.07	-0.60	0.03	0.03	0.02
1841	1 30 52.6	30 21 37	727	-74	20.14	0.02	-0.06	0.03	0.03	0.05
1842	1 31 04.7	30 21 41	728	588	20.67	-0.08	...	0.00	0.07	...
1843	1 31 04.7	30 21 41	728	588	20.67	-0.13	-0.83	0.07	0.03	0.04
1844	1 30 51.9	30 21 37	729	-114	21.00	0.01	-1.29	0.17	0.09	0.08
1845	1 30 57.2	30 21 38	731	176	20.67	-0.08	-0.69	0.09	0.03	0.16
1846	1 31 04.2	30 21 40	733	560	20.35	0.27	...	0.20	0.09	...
1847	1 31 12.9	30 21 42	735	1035	18.72	0.10	-0.94	0.05	0.04	0.02
1848	1 30 52.3	30 21 35	735	-95	19.50	0.18	0.04	0.00	0.03	0.02
1849	1 30 56.6	30 21 36	739	145	20.10	-0.23	-0.80	0.13	0.07	0.10
1850	1 30 57.2	30 21 36	739	173	19.62	-0.12	-0.93	0.09	0.01	0.06

TABLE 2 (cont.)

Number	α(1950)	δ(1950)	X	Y	V	B-V	U-B	σ_V	σ_B	σ_U
1851	1 31 07.4	30 21 39	740	733	20.53	0.06	-0.96	0.05	0.06	0.03
1852	1 30 57.3	30 21 36	740	179	20.49	-0.01	-0.89	0.05	0.03	0.04
1853	1 31 07.4	30 21 39	740	734	20.61	-0.05	...	0.08	0.04	...
1854	1 30 59.5	30 21 36	740	300	19.73	0.12	-0.25	0.03	0.02	0.04
1855	1 30 59.5	30 21 36	740	300	19.72	0.08	...	0.01	0.06	...
1856	1 30 57.3	30 21 36	740	179	20.49	-0.04	...	0.09	0.02	...
1857	1 31 05.7	30 21 38	742	639	20.18	-0.12	-1.06	0.07	0.03	0.05
1858	1 31 14.9	30 21 41	743	1141	20.99	0.20	...	0.06	0.04	...
1859	1 31 14.4	30 21 40	744	1114	20.94	0.09	-0.81	0.10	0.06	0.04
1860	1 30 59.8	30 21 34	750	317	20.15	0.01	...	0.07	0.05	...
1861	1 30 59.8	30 21 34	750	316	20.11	0.03	-0.77	0.04	0.03	0.04
1862	1 31 00.4	30 21 34	751	351	20.37	0.12	-0.67	0.05	0.04	0.04
1863	1 30 56.9	30 21 33	752	160	19.92	-0.29	...	0.06	0.03	...
1864	1 30 58.0	30 21 33	754	220	20.65	-0.09	-0.91	0.05	0.03	0.04
1865	1 31 00.4	30 21 33	754	347	20.81	-0.03	-0.25	0.07	0.04	0.05
1866	1 31 04.3	30 21 34	757	562	20.97	0.11	...	0.07	0.05	...
1867	1 30 57.5	30 21 32	758	191	20.64	0.04	-0.87	0.05	0.04	0.04
1868	1 30 56.8	30 21 31	759	153	16.12	0.28	-0.30	0.00	0.04	0.06
1869	1 30 57.0	30 21 31	761	162	19.63	0.10	...	0.03	0.03	...
1870	1 31 15.9	30 21 36	765	1198	20.86	0.36	...	0.04	0.04	...
1871	1 30 50.5	30 21 27	769	-190	20.60	-0.36	-0.99	0.07	0.03	0.05
1872	1 30 57.6	30 21 29	771	195	20.30	0.09	...	0.05	0.04	...
1873	1 31 04.4	30 21 30	772	566	20.43	0.29	0.20	0.05	0.04	0.05
1874	1 30 56.7	30 21 27	776	145	19.03	0.13	-1.13	0.03	0.04	0.05
1875	1 30 57.6	30 21 27	776	195	19.61	-0.16	-0.81	0.04	0.02	0.04
1876	1 30 56.6	30 21 27	776	144	19.55	-0.41	...	0.09	0.02	...
1877	1 30 58.2	30 21 27	779	230	20.77	-0.19	-1.22	0.07	0.10	0.04
1878	1 30 57.5	30 21 27	780	193	20.00	-0.16	-0.86	0.05	0.04	0.05
1879	1 30 50.5	30 21 24	782	-193	20.34	-0.03	-0.93	0.03	0.03	0.05
1880	1 30 56.1	30 21 25	783	116	19.86	-0.42	-1.62	0.05	0.04	0.06
1881	1 31 12.9	30 21 31	783	1033	20.90	0.09	...	0.06	0.05	...
1882	1 31 14.8	30 21 31	784	1136	20.61	-0.01	-0.88	0.04	0.04	0.03
1883	1 31 11.3	30 21 30	784	947	20.74	-0.08	-1.18	0.05	0.04	0.02
1884	1 31 03.9	30 21 27	785	539	20.16	0.32	0.10	0.03	0.02	0.05
1885	1 31 13.5	30 21 30	787	1067	19.68	0.01	-0.92	0.07	0.05	0.02
1886	1 31 14.3	30 21 30	789	1107	20.94	0.15	...	0.07	0.06	...
1887	1 31 12.5	30 21 29	790	1014	20.78	0.29	-0.35	0.09	0.08	0.05
1888	1 31 14.4	30 21 29	792	1112	20.46	0.02	-1.47	0.06	0.04	0.03
1889	1 30 54.5	30 21 23	792	23	19.24	-0.17	...	0.03	0.03	...
1890	1 31 05.2	30 21 26	793	610	20.65	0.04	-0.98	0.05	0.03	0.04
1891	1 30 47.4	30 21 20	796	-363	20.62	-0.24	-1.15	0.07	0.03	0.05
1892	1 30 55.2	30 21 21	799	64	20.24	0.35	...	0.04	0.06	...
1893	1 30 54.5	30 21 21	799	24	19.98	-0.04	...	0.04	0.04	...
1894	1 31 14.2	30 21 27	799	1103	18.67	-0.11	-1.36	0.05	0.05	0.02
1895	1 30 47.3	30 21 18	802	-367	20.07	-0.02	-0.94	0.05	0.03	0.05
1896	1 31 14.2	30 21 26	803	1106	19.87	-0.01	...	0.08	0.08	...
1897	1 30 56.1	30 21 21	803	111	19.51	0.84	-0.60	0.04	0.04	0.09
1898	1 30 55.5	30 21 20	803	82	20.66	0.15	...	0.06	0.08	...
1899	1 30 55.6	30 21 20	803	85	20.14	-0.13	-0.73	0.06	0.04	0.04
1900	1 30 55.6	30 21 20	804	87	20.56	-0.15	-1.19	0.06	0.05	0.04

TABLE 2 (cont.)

Number	α(1950)	δ(1950)	X	Y	V	B-V	U-B	σ_V	σ_B	σ_U
1901	1 30 52.6	30 21 19	806	-80	19.76	0.09	0.07	0.03	0.02	0.05
1902	1 30 57.6	30 21 20	806	197	18.00	0.35	-0.08	0.02	0.01	0.03
1903	1 30 57.2	30 21 20	809	174	20.12	-0.15	-0.90	0.12	0.02	0.03
1904	1 30 47.6	30 21 16	812	-354	18.39	-0.07	...	0.03	0.03	...
1905	1 31 02.9	30 21 21	812	485	19.01	0.02	-0.89	0.02	0.01	0.03
1906	1 30 58.9	30 21 19	814	265	20.51	-0.42	-0.73	0.18	0.03	0.04
1907	1 30 56.2	30 21 17	817	119	19.67	-0.18	-1.05	0.00	0.02	0.04
1908	1 30 46.5	30 21 13	821	-411	20.95	0.03	...	0.07	0.04	...
1909	1 31 13.3	30 21 22	822	1051	20.26	-0.08	...	0.13	0.05	...
1910	1 31 00.3	30 21 17	822	343	15.00	0.16	...	0.05	0.12	...
1911	1 30 48.3	30 21 13	823	-316	20.46	-0.20	-0.88	0.04	0.03	0.05
1912	1 30 46.2	30 21 13	824	-431	20.46	-0.14	-0.81	0.04	0.03	0.07
1913	1 31 14.2	30 21 21	824	1101	20.37	-0.04	...	0.07	0.04	...
1914	1 30 56.0	30 21 15	825	106	20.59	0.01	...	0.05	0.06	...
1915	1 31 13.8	30 21 21	825	1083	20.49	0.08	-0.51	0.07	0.06	0.04
1916	1 30 49.0	30 21 13	825	-276	20.29	-0.04	-0.01	0.03	0.03	0.06
1917	1 31 06.5	30 21 18	827	680	20.37	-0.02	-0.98	0.18	0.03	0.13
1918	1 30 47.4	30 21 12	827	-367	20.28	-0.06	...	0.04	0.03	...
1919	1 31 02.7	30 21 17	828	476	19.94	-0.10	-0.83	0.05	0.02	0.04
1920	1 30 56.0	30 21 15	828	109	20.97	-0.17	...	0.07	0.08	...
1921	1 31 11.5	30 21 19	828	955	20.97	-0.34	-1.13	0.21	0.07	0.03
1922	1 30 57.6	30 21 14	831	193	20.51	-0.28	-0.82	0.07	0.03	0.04
1923	1 30 55.0	30 21 14	832	52	19.19	0.14	-1.05	0.04	0.21	0.06
1924	1 30 55.4	30 21 13	832	72	18.32	-0.08	-1.00	0.06	0.05	0.02
1925	1 31 12.1	30 21 19	833	986	20.61	0.01	-0.82	0.07	0.05	0.04
1926	1 30 55.6	30 21 13	833	87	19.20	-0.06	-1.00	0.05	0.06	0.00
1927	1 31 01.6	30 21 15	835	411	20.29	-0.06	-0.74	0.05	0.09	0.04
1928	1 30 49.6	30 21 11	836	-243	20.36	-0.29	-1.11	0.03	0.02	0.05
1929	1 30 56.8	30 21 13	836	150	20.92	-0.02	-0.57	0.22	0.13	0.12
1930	1 31 15.3	30 21 19	836	1165	19.91	0.69	-0.60	0.06	0.07	0.04
1931	1 30 55.3	30 21 12	837	67	19.81	-0.17	-0.92	0.06	0.04	0.04
1932	1 30 55.3	30 21 12	838	68	19.82	-0.16	...	0.02	0.03	...
1933	1 31 12.9	30 21 18	838	1033	20.36	-0.13	...	0.09	0.07	...
1934	1 30 46.3	30 21 9	839	-426	20.81	0.04	...	0.06	0.07	...
1935	1 31 02.9	30 21 14	840	483	17.90	0.24	-0.54	0.02	0.04	0.03
1936	1 31 00.7	30 21 13	841	363	20.14	-0.13	-0.75	0.10	0.06	0.06
1937	1 30 45.5	30 21 8	843	-466	19.37	0.38	-1.66	0.03	0.04	0.05
1938	1 31 05.7	30 21 14	845	639	19.07	0.18	0.00	0.02	0.01	0.03
1939	1 31 00.6	30 21 12	845	359	18.54	0.09	-0.13	0.07	0.03	0.09
1940	1 30 58.0	30 21 11	846	217	20.68	0.22	0.19	0.05	0.04	0.06
1941	1 30 46.4	30 21 7	850	-421	18.68	-0.18	-1.05	0.02	0.02	0.05
1942	1 30 57.5	30 21 10	850	190	18.53	0.17	...	0.02	0.01	...
1943	1 30 45.1	30 21 6	850	-490	20.13	-0.03	...	0.03	0.03	...
1944	1 30 46.6	30 21 6	850	-408	20.18	-0.35	...	0.05	0.05	...
1945	1 30 55.3	30 21 9	851	70	16.92	0.14	-0.61	0.04	0.10	0.01
1946	1 31 15.5	30 21 15	853	1171	20.24	0.32	0.68	0.05	0.06	0.05
1947	1 30 52.0	30 21 7	855	-111	17.97	0.12	0.04	0.02	0.02	0.05
1948	1 31 14.8	30 21 14	855	1134	20.55	0.22	...	0.09	0.05	...
1949	1 30 57.1	30 21 8	856	167	20.22	-0.11	-0.86	0.10	0.04	0.04
1950	1 30 53.8	30 21 7	857	-13	20.77	0.25	...	0.07	0.04	...

TABLE 2 (cont.)

Number	α(1950)	δ(1950)	X	Y	V	B-V	U-B	σ_V	σ_B	σ_U
1951	1 30 59.3	30 21 9	857	285	20.05	0.14	-0.51	0.03	0.06	0.04
1952	1 31 11.5	30 21 13	857	956	18.84	0.17	-0.47	0.08	0.07	0.02
1953	1 30 57.4	30 21 8	858	183	20.91	-0.32	-0.81	0.06	0.04	0.04
1954	1 30 57.6	30 21 8	858	194	19.20	-0.07	-0.77	0.02	0.01	0.03
1955	1 31 11.8	30 21 12	859	969	17.99	0.19	-0.26	0.09	0.07	0.02
1956	1 30 51.2	30 21 6	860	-158	20.88	-0.11	-1.16	0.05	0.03	0.05
1957	1 30 56.1	30 21 6	866	113	20.94	0.06	...	0.09	0.06	...
1958	1 30 56.4	30 21 6	866	127	20.29	-0.03	...	0.13	0.14	...
1959	1 30 56.4	30 21 6	867	128	20.38	-0.02	-1.33	0.05	0.04	0.04
1960	1 30 55.4	30 21 5	867	73	19.15	0.41	-0.63	0.09	0.04	0.04
1961	1 30 51.0	30 21 4	868	-169	20.97	0.04	...	0.06	0.04	...
1962	1 31 03.5	30 21 8	868	516	19.56	0.17	0.11	0.03	0.02	0.04
1963	1 31 01.1	30 21 7	869	386	19.60	-0.02	-0.66	0.06	0.04	0.04
1964	1 31 00.9	30 21 6	870	371	20.44	-0.03	-0.61	0.11	0.07	0.05
1965	1 30 55.1	30 21 4	870	55	20.93	0.47	-0.84	0.14	0.09	0.09
1966	1 30 50.4	30 21 3	870	-203	19.87	0.14	-0.11	0.03	0.04	0.05
1967	1 30 56.0	30 21 4	873	106	20.20	-0.10	...	0.08	0.10	...
1968	1 30 55.9	30 21 4	873	102	17.71	-0.02	-1.08	0.03	0.08	0.06
1969	1 30 46.3	30 21 1	873	-423	20.88	-0.46	-1.20	0.06	0.04	0.05
1970	1 31 12.1	30 21 9	874	984	20.59	-0.49	...	0.07	0.09	...
1971	1 31 12.2	30 21 9	875	991	19.84	-0.51	...	0.11	0.07	...
1972	1 30 59.7	30 21 5	875	310	19.90	-0.02	-1.06	0.03	0.02	0.03
1973	1 31 00.6	30 21 5	876	357	20.93	-0.02	-0.15	0.16	0.09	0.06
1974	1 30 55.3	30 21 3	876	68	18.77	-0.04	-0.39	0.04	0.02	0.04
1975	1 31 12.2	30 21 8	877	990	20.24	-0.91	...	0.16	0.07	...
1976	1 31 12.0	30 21 8	877	981	20.97	-0.30	...	0.09	0.07	...
1977	1 30 45.0	30 20 59	878	-495	20.35	0.32	-0.01	0.03	0.03	0.06
1978	1 30 58.4	30 21 4	878	235	20.97	0.28	-0.96	0.07	0.05	0.04
1979	1 31 13.1	30 21 8	878	1043	20.37	0.38	...	0.08	0.07	...
1980	1 31 05.3	30 21 6	879	617	20.22	-0.12	-0.95	0.05	0.02	0.03
1981	1 30 56.2	30 21 3	879	118	19.67	-0.23	...	0.04	0.03	...
1982	1 30 56.8	30 21 3	880	149	20.40	0.05	-0.78	0.05	0.03	0.04
1983	1 30 55.4	30 21 2	881	71	20.06	0.10	-1.02	0.12	0.03	0.05
1984	1 31 12.1	30 21 7	882	986	20.88	0.26	...	0.06	0.08	...
1985	1 31 07.0	30 21 5	884	705	20.91	0.10	-1.00	0.05	0.06	0.03
1986	1 31 14.2	30 21 7	885	1101	19.51	0.44	-1.26	0.05	0.29	0.02
1987	1 30 56.1	30 21 1	887	109	19.26	-0.34	-0.92	0.04	0.08	0.05
1988	1 30 58.8	30 21 1	888	258	20.27	-0.14	...	0.04	0.04	...
1989	1 30 58.9	30 21 1	888	263	20.84	-0.13	...	0.06	0.06	...
1990	1 30 57.1	30 21 0	891	166	19.53	0.00	-0.72	0.04	0.03	0.04
1991	1 30 55.3	30 20 59	893	68	20.95	0.22	...	0.07	0.07	...
1992	1 31 12.2	30 21 4	893	991	19.00	-0.05	-1.33	0.06	0.05	0.02
1993	1 31 12.3	30 21 4	894	996	20.85	0.14	...	0.17	0.10	...
1994	1 31 12.3	30 21 4	895	998	20.78	0.18	...	0.12	0.08	...
1995	1 31 15.7	30 21 5	895	1182	19.96	0.03	-0.56	0.04	0.03	0.03
1996	1 30 57.6	30 20 59	897	191	20.22	-0.30	...	0.09	0.05	...
1997	1 30 50.4	30 20 56	899	-203	20.85	0.05	...	0.05	0.03	...
1998	1 31 10.3	30 21 2	899	886	20.16	0.23	-1.80	0.06	0.09	0.03
1999	1 31 13.6	30 21 3	899	1069	20.89	0.22	-0.57	0.05	0.06	0.05
2000	1 31 10.3	30 21 2	901	885	20.85	-0.05	...	0.09	0.14	...

TABLE 2 (cont.)

Number	α(1950)	δ(1950)	X	Y	V	B-V	U-B	σ_V	σ_B	σ_U
2001	1 30 56.9	30 20 58	902	155	20.83	0.33	...	0.08	0.07	...
2002	1 31 12.3	30 21 2	903	996	20.85	0.18	...	0.10	0.10	...
2003	1 30 55.4	30 20 56	905	74	20.63	0.10	...	0.06	0.05	...
2004	1 31 11.1	30 21 1	905	929	19.98	0.11	-1.59	0.49	0.28	0.02
2005	1 31 14.6	30 21 2	906	1122	20.97	0.38	...	0.05	0.04	...
2006	1 31 12.2	30 21 1	907	990	19.16	-0.14	-1.58	0.06	0.06	0.02
2007	1 31 12.2	30 21 1	907	993	20.01	0.27	...	0.09	0.08	...
2008	1 31 09.5	30 21 0	907	845	20.32	-0.04	-0.41	0.08	0.05	0.03
2009	1 31 09.5	30 21 0	908	846	20.49	-0.20	-0.41	0.10	0.05	0.03
2010	1 30 56.0	30 20 56	909	104	19.92	-0.04	-1.29	0.02	0.04	0.10
2011	1 30 51.6	30 20 54	910	-134	20.73	-0.23	-0.93	0.06	0.03	0.05
2012	1 30 55.2	30 20 55	912	59	19.24	-0.30	...	0.05	0.03	...
2013	1 30 55.2	30 20 55	912	58	19.10	-0.18	-1.02	0.02	0.02	0.03
2014	1 31 12.0	30 20 60	913	981	19.96	0.09	...	0.07	0.05	...
2015	1 31 12.1	30 20 60	913	986	20.34	-0.03	...	0.09	0.06	...
2016	1 31 11.8	30 20 60	913	969	20.20	0.14	...	0.07	0.06	...
2017	1 30 55.7	30 20 54	914	85	17.59	0.14	-1.25	0.04	0.38	0.05
2018	1 30 55.5	30 20 53	918	78	19.01	-0.11	-1.11	0.03	0.01	0.04
2019	1 31 12.4	30 20 59	918	1003	19.16	-0.71	...	0.12	0.05	...
2020	1 31 08.9	30 20 57	919	812	20.92	0.07	-0.24	0.09	0.04	0.05
2021	1 30 50.5	30 20 51	919	-197	18.68	0.04	-0.48	0.02	0.02	0.05
2022	1 31 12.3	30 20 58	920	998	20.09	-0.08	...	0.10	0.08	...
2023	1 31 12.5	30 20 58	922	1005	19.05	0.13	-0.42	0.06	0.05	0.09
2024	1 30 58.8	30 20 53	922	256	19.59	-0.27	-0.92	0.05	0.02	0.03
2025	1 31 11.8	30 20 57	923	969	18.04	0.14	-0.80	0.07	0.05	0.02
2026	1 30 52.3	30 20 51	925	-98	20.61	0.01	-0.80	0.04	0.03	0.05
2027	1 31 04.4	30 20 54	927	561	20.56	-0.01	...	0.05	0.02	...
2028	1 30 58.5	30 20 52	928	239	19.18	-0.07	-1.04	0.02	0.04	0.03
2029	1 31 11.9	30 20 56	928	973	18.23	0.17	-0.86	0.07	0.05	0.02
2030	1 30 50.4	30 20 49	929	-204	18.76	-0.04	-0.88	0.02	0.02	0.05
2031	1 30 57.1	30 20 51	929	166	20.52	0.17	-0.98	0.04	0.03	0.04
2032	1 30 47.8	30 20 48	930	-344	19.41	-0.09	-1.04	0.02	0.02	0.05
2033	1 30 52.4	30 20 49	931	-91	19.38	-0.06	-0.71	0.02	0.02	0.05
2034	1 30 50.8	30 20 48	935	-180	20.45	-0.14	-0.97	0.04	0.03	0.05
2035	1 31 13.0	30 20 55	936	1036	20.87	0.29	...	0.05	0.13	...
2036	1 30 45.7	30 20 46	937	-460	20.84	-0.05	...	0.06	0.03	...
2037	1 31 13.5	30 20 54	937	1062	20.50	0.29	-0.02	0.04	0.05	0.14
2038	1 31 12.3	30 20 54	939	996	19.82	0.16	-1.15	0.04	0.04	0.02
2039	1 30 48.2	30 20 46	939	-323	19.71	-0.12	-0.85	0.03	0.02	0.05
2040	1 31 01.4	30 20 50	939	397	20.89	0.19	-0.63	0.06	0.05	0.05
2041	1 30 54.7	30 20 47	942	34	20.02	0.27	...	0.03	0.03	...
2042	1 30 56.3	30 20 48	942	117	19.34	-0.02	-0.92	0.08	0.04	0.00
2043	1 31 02.8	30 20 50	944	476	19.90	-0.21	-0.94	0.03	0.01	0.03
2044	1 31 12.0	30 20 52	944	981	20.78	0.20	...	0.05	0.03	...
2045	1 31 12.3	30 20 52	944	995	20.59	0.12	...	0.06	0.04	...
2046	1 30 49.0	30 20 45	946	-279	20.48	0.06	-0.88	0.03	0.03	0.05
2047	1 30 57.1	30 20 47	947	165	20.60	0.22	-0.45	0.05	0.03	0.05
2048	1 31 08.2	30 20 51	947	773	20.30	0.16	-0.39	0.05	0.03	0.03
2049	1 30 56.5	30 20 47	947	131	20.37	0.03	-0.88	0.01	0.10	0.11
2050	1 31 12.3	30 20 51	950	993	19.67	0.23	-1.18	0.04	0.03	0.02

TABLE 2 (cont.)

Number	α(1950)	δ(1950)	X	Y	V	B-V	U-B	σ_V	σ_B	σ_U
2051	1 31 14.6	30 20 51	952	1124	20.28	0.25	0.23	0.04	0.03	0.05
2052	1 31 02.3	30 20 47	952	451	20.45	0.07	-0.33	0.04	0.03	0.04
2053	1 30 44.7	30 20 42	952	-515	20.46	0.29	...	0.04	0.05	...
2054	1 31 11.8	30 20 50	953	970	20.52	0.06	-1.36	0.04	0.03	0.03
2055	1 31 08.1	30 20 49	954	764	20.17	0.09	-0.64	0.06	0.03	0.03
2056	1 30 45.8	30 20 42	955	-457	20.03	-0.22	-0.89	0.03	0.03	0.05
2057	1 30 49.2	30 20 42	959	-270	19.92	0.26	-0.53	0.03	0.03	0.05
2058	1 31 12.2	30 20 49	960	988	19.69	0.34	-0.93	0.04	0.06	0.03
2059	1 31 15.7	30 20 50	961	1181	20.25	0.09	-0.53	0.08	0.07	0.04
2060	1 31 12.4	30 20 48	962	1000	18.96	0.49	-1.35	0.06	0.12	0.06
2061	1 30 52.0	30 20 42	963	-116	20.68	-0.29	-1.02	0.05	0.03	0.05
2062	1 31 14.5	30 20 49	963	1113	19.52	0.36	...	0.03	0.04	...
2063	1 30 51.3	30 20 41	965	-155	19.70	-0.07	-0.93	0.03	0.02	0.05
2064	1 31 10.8	30 20 47	967	913	20.75	-0.09	-0.72	0.05	0.03	0.04
2065	1 30 53.3	30 20 41	967	-44	18.79	-0.18	-1.05	0.02	0.02	0.05
2066	1 30 45.6	30 20 38	968	-465	19.29	-0.06	-1.11	0.03	0.03	0.05
2067	1 30 55.5	30 20 41	969	77	20.20	0.19	-0.91	0.04	0.05	0.12
2068	1 31 13.3	30 20 47	970	1049	20.40	0.19	...	0.04	0.03	...
2069	1 30 45.8	30 20 38	971	-456	16.39	0.12	-0.83	0.02	0.02	0.05
2070	1 31 00.1	30 20 42	972	326	20.52	-0.22	-0.98	0.08	0.02	0.04
2071	1 30 52.6	30 20 40	972	-85	19.48	0.34	...	0.06	0.07	...
2072	1 30 47.5	30 20 38	972	-360	19.17	0.15	-0.32	0.02	0.02	0.05
2073	1 31 12.1	30 20 46	973	987	20.67	-0.02	-0.86	0.04	0.03	0.04
2074	1 30 47.7	30 20 38	973	-351	20.48	-0.14	-0.19	0.06	0.03	0.05
2075	1 31 09.9	30 20 45	975	861	20.98	-0.05	-0.68	0.04	0.03	0.04
2076	1 30 52.6	30 20 39	975	-83	20.42	-0.19	...	0.14	0.10	...
2077	1 31 12.4	30 20 45	975	999	20.69	0.31	...	0.04	0.03	...
2078	1 30 51.1	30 20 38	976	-163	20.23	0.04	-1.07	0.03	0.08	0.05
2079	1 30 56.7	30 20 40	976	140	20.41	-0.25	-0.85	0.07	0.04	0.07
2080	1 31 13.3	30 20 45	977	1048	18.51	0.18	-0.44	0.03	0.03	0.02
2081	1 30 57.1	30 20 40	978	164	20.74	-0.11	-0.98	0.05	0.03	0.04
2082	1 30 56.9	30 20 39	979	150	20.02	-0.13	-1.02	0.01	0.07	0.04
2083	1 30 54.8	30 20 39	980	36	19.00	-0.14	-1.01	0.02	0.02	0.05
2084	1 31 13.6	30 20 44	980	1065	20.34	0.46	-1.29	0.04	0.07	0.04
2085	1 30 55.5	30 20 38	981	77	19.98	-0.17	...	0.16	0.09	...
2086	1 30 55.8	30 20 38	982	90	20.77	0.09	...	0.13	0.09	...
2087	1 31 13.1	30 20 44	983	1040	21.00	0.00	...	0.05	0.04	...
2088	1 31 06.5	30 20 41	983	676	20.28	0.12	-0.54	0.22	0.08	0.20
2089	1 30 52.0	30 20 37	983	-118	20.48	-0.06	...	0.07	0.04	...
2090	1 30 55.5	30 20 38	984	77	18.78	0.06	-1.18	0.02	0.02	0.03
2091	1 30 55.5	30 20 38	984	77	18.95	-0.05	...	0.27	0.10	...
2092	1 31 13.5	30 20 43	985	1060	19.27	0.36	0.28	0.03	0.03	0.04
2093	1 30 58.9	30 20 38	987	261	20.79	0.16	-0.91	0.06	0.04	0.04
2094	1 30 50.6	30 20 35	988	-192	20.24	-0.14	...	0.04	0.03	...
2095	1 30 55.6	30 20 37	988	83	20.46	-0.27	...	0.04	0.07	...
2096	1 31 13.4	30 20 43	988	1053	19.91	0.06	-0.03	0.04	0.03	0.04
2097	1 30 55.6	30 20 37	989	82	20.43	-0.19	-1.08	0.05	0.03	0.05
2098	1 30 55.3	30 20 37	989	66	17.23	-0.03	-0.89	0.07	0.06	0.08
2099	1 30 47.3	30 20 34	991	-374	20.32	0.18	-0.83	0.05	0.06	0.05
2100	1 30 50.5	30 20 34	992	-198	19.65	0.38	...	0.03	0.03	...

TABLE 2 (cont.)

Number	α(1950)	δ(1950)	X	Y	V	B-V	U-B	σ_V	σ_B	σ_U
2101	1 30 57.8	30 20 37	992	202	19.90	0.38	-1.33	0.04	0.25	0.03
2102	1 30 48.9	30 20 33	993	-288	20.67	-0.22	-0.89	0.04	0.03	0.05
2103	1 30 50.6	30 20 34	994	-191	19.50	0.30	...	0.03	0.03	...
2104	1 30 51.7	30 20 34	995	-135	20.60	0.31	...	0.06	0.04	...
2105	1 30 46.1	30 20 32	996	-442	18.59	0.09	0.05	0.03	0.02	0.05
2106	1 30 49.6	30 20 33	996	-248	20.67	-0.15	...	0.04	0.03	...
2107	1 30 55.4	30 20 35	996	69	19.58	-0.11	...	0.01	0.12	...
2108	1 30 49.5	30 20 33	996	-255	20.53	-0.22	...	0.04	0.03	...
2109	1 30 55.4	30 20 35	996	69	19.59	-0.03	-1.06	0.03	0.02	0.04
2110	1 30 48.1	30 20 32	998	-330	20.43	-0.11	-1.04	0.03	0.03	0.05
2111	1 30 51.5	30 20 33	999	-147	20.34	0.29	...	0.04	0.06	...
2112	1 31 09.1	30 20 38	1000	818	20.91	0.01	...	0.04	0.03	...
2113	1 30 55.5	30 20 34	1000	74	20.52	-0.31	...	0.05	0.04	...
2114	1 31 14.6	30 20 40	1000	1120	20.41	0.37	...	0.04	0.04	...
2115	1 30 50.0	30 20 32	1000	-228	19.88	-0.14	-0.93	0.04	0.03	0.05
2116	1 31 13.0	30 20 39	1000	1030	19.82	0.20	-0.23	0.04	0.04	0.04
2117	1 30 51.3	30 20 32	1001	-156	19.65	0.49	-0.80	0.03	0.03	0.05
2118	1 30 53.4	30 20 33	1002	-42	20.40	-0.29	-1.02	0.03	0.03	0.05
2119	1 30 58.9	30 20 35	1002	259	20.73	-0.11	-0.97	0.05	0.03	0.04
2120	1 30 51.7	30 20 32	1003	-135	20.99	0.26	...	0.06	0.05	...
2121	1 31 12.5	30 20 39	1003	1004	18.30	0.04	-0.80	0.03	0.03	0.02
2122	1 31 14.8	30 20 39	1004	1129	20.21	0.38	...	0.04	0.04	...
2123	1 30 55.4	30 20 33	1006	71	19.78	-0.30	-1.12	0.07	0.04	0.04
2124	1 30 55.4	30 20 33	1006	70	19.00	-0.16	...	0.03	0.03	...
2125	1 30 49.9	30 20 31	1006	-230	19.98	-0.11	-0.61	0.04	0.03	0.06
2126	1 30 54.8	30 20 32	1007	34	20.45	0.22	...	0.03	0.03	...
2127	1 30 55.7	30 20 32	1007	84	19.36	-0.18	-1.13	0.00	0.01	0.03
2128	1 30 50.9	30 20 31	1007	-178	19.94	0.01	...	0.03	0.03	...
2129	1 30 50.3	30 20 30	1008	-211	18.89	0.22	0.23	0.02	0.02	0.05
2130	1 30 53.8	30 20 31	1009	-16	19.90	0.04	-0.32	0.03	0.02	0.05
2131	1 30 51.6	30 20 31	1009	-140	20.41	-0.03	-1.37	0.05	0.07	0.06
2132	1 31 12.9	30 20 37	1010	1027	20.81	0.19	...	0.06	0.05	...
2133	1 30 48.9	30 20 29	1011	-287	20.74	0.10	-0.70	0.04	0.03	0.05
2134	1 31 13.7	30 20 37	1011	1071	19.16	0.16	0.05	0.03	0.03	0.02
2135	1 31 13.3	30 20 37	1013	1049	20.59	0.38	...	0.04	0.05	...
2136	1 30 44.9	30 20 27	1013	-505	20.66	-0.07	-0.62	0.07	0.03	0.05
2137	1 30 53.5	30 20 30	1014	-37	20.35	-0.05	...	0.04	0.03	...
2138	1 30 55.3	30 20 31	1014	66	18.86	0.03	-0.98	0.06	0.01	0.06
2139	1 30 50.9	30 20 29	1014	-178	19.28	-0.10	-1.01	0.03	0.02	0.07
2140	1 30 54.4	30 20 30	1015	15	19.62	-0.23	-1.13	0.03	0.02	0.05
2141	1 31 09.8	30 20 35	1015	856	20.34	0.08	-1.12	0.04	0.03	0.03
2142	1 30 51.1	30 20 29	1015	-166	20.17	0.13	-0.61	0.05	0.03	0.05
2143	1 31 07.4	30 20 34	1018	725	20.52	0.11	-0.80	0.04	0.03	0.03
2144	1 30 51.3	30 20 28	1018	-153	20.76	0.09	...	0.07	0.04	...
2145	1 31 13.3	30 20 35	1018	1051	19.52	0.13	-0.51	0.03	0.03	0.02
2146	1 30 50.2	30 20 28	1018	-215	20.68	0.26	...	0.05	0.04	...
2147	1 31 07.4	30 20 33	1019	725	20.71	-0.05	-0.99	0.05	0.03	0.04
2148	1 31 11.7	30 20 34	1020	960	20.95	0.08	...	0.04	0.03	...
2149	1 31 09.7	30 20 34	1020	849	20.85	0.29	...	0.05	0.03	...
2150	1 30 50.8	30 20 28	1021	-183	18.61	0.01	-0.53	0.02	0.02	0.05

TABLE 2 (cont.)

Number	α(1950)	δ(1950)	X	Y	V	B-V	U-B	σ_V	σ_B	σ_U
2151	1 31 12.6	30 20 34	1021	1008	20.55	0.01	-0.90	0.04	0.05	0.04
2152	1 31 01.9	30 20 31	1023	424	20.90	0.22	-0.22	0.06	0.04	0.06
2153	1 30 51.3	30 20 27	1024	-153	20.40	-0.14	...	0.14	0.03	...
2154	1 30 50.1	30 20 27	1024	-223	20.19	0.30	...	0.07	0.07	...
2155	1 30 50.1	30 20 26	1026	-219	18.98	0.11	...	0.03	0.03	...
2156	1 31 08.1	30 20 32	1026	762	20.70	0.06	-0.94	0.04	0.03	0.04
2157	1 31 13.5	30 20 33	1027	1057	19.55	0.36	0.42	0.03	0.03	0.04
2158	1 31 06.8	30 20 31	1027	693	20.99	0.02	-0.82	0.05	0.03	0.04
2159	1 31 04.7	30 20 30	1029	576	20.28	-0.04	-1.03	0.03	0.02	0.03
2160	1 31 06.8	30 20 31	1029	693	20.95	-0.03	-0.83	0.06	0.04	0.04
2161	1 31 13.3	30 20 33	1029	1048	19.75	0.00	-0.85	0.04	0.03	0.02
2162	1 30 51.0	30 20 26	1029	-173	19.96	-0.12	-0.87	0.08	0.04	0.05
2163	1 30 52.7	30 20 26	1030	-81	18.95	0.02	-0.73	0.03	0.02	0.05
2164	1 30 52.4	30 20 26	1030	-95	19.62	-0.18	-0.67	0.33	0.03	0.05
2165	1 31 08.6	30 20 31	1030	790	20.44	0.08	-1.08	0.04	0.03	0.03
2166	1 31 12.1	30 20 32	1031	982	19.21	0.14	-0.62	0.04	0.03	0.02
2167	1 31 07.9	30 20 31	1031	755	18.76	0.29	0.21	0.03	0.03	0.02
2168	1 30 51.9	30 20 25	1032	-124	20.74	-0.06	-0.76	0.05	0.04	0.05
2169	1 31 10.0	30 20 31	1032	868	20.81	0.23	...	0.06	0.05	...
2170	1 30 53.5	30 20 26	1032	-35	19.97	-0.26	-1.08	0.04	0.03	0.05
2171	1 30 45.9	30 20 23	1033	-453	19.99	0.46	-1.66	0.03	0.35	0.05
2172	1 31 08.4	30 20 30	1033	778	20.42	0.02	-1.22	0.04	0.03	0.03
2173	1 30 53.9	30 20 25	1035	-14	18.72	0.45	-0.83	0.02	0.02	0.05
2174	1 31 13.8	30 20 31	1036	1077	20.76	0.40	...	0.04	0.03	...
2175	1 31 14.6	30 20 32	1036	1120	19.56	0.13	-0.14	0.03	0.03	0.02
2176	1 30 49.5	30 20 24	1036	-252	20.79	-0.21	-0.79	0.05	0.03	0.05
2177	1 31 10.1	30 20 30	1037	870	19.56	0.10	-1.13	0.03	0.03	0.02
2178	1 30 47.3	30 20 22	1039	-377	19.96	-0.07	...	0.03	0.03	...
2179	1 30 47.4	30 20 22	1040	-371	19.35	-0.06	...	0.03	0.03	...
2180	1 31 12.3	30 20 30	1040	996	18.58	0.12	-1.00	0.03	0.04	0.02
2181	1 30 51.1	30 20 23	1040	-169	18.97	0.04	...	0.04	0.03	...
2182	1 31 10.0	30 20 29	1041	865	20.91	0.07	...	0.05	0.05	...
2183	1 31 11.8	30 20 29	1042	964	20.43	0.02	...	0.05	0.03	...
2184	1 30 52.1	30 20 23	1043	-111	18.47	0.15	-0.16	0.02	0.02	0.05
2185	1 31 08.1	30 20 28	1043	766	20.13	0.09	-0.39	0.04	0.03	0.03
2186	1 31 10.8	30 20 28	1046	913	20.35	0.16	...	0.04	0.03	...
2187	1 30 52.4	30 20 22	1049	-96	18.50	0.11	-0.94	0.03	0.03	0.05
2188	1 30 47.5	30 20 20	1049	-367	20.19	-0.15	-1.10	0.03	0.03	0.05
2189	1 31 12.9	30 20 28	1049	1024	20.54	0.06	-0.69	0.04	0.04	0.04
2190	1 31 12.5	30 20 28	1050	1005	19.80	-0.03	-1.20	0.04	0.03	0.03
2191	1 31 09.9	30 20 26	1052	863	20.40	0.21	-1.46	0.05	0.05	0.04
2192	1 30 52.9	30 20 21	1052	-67	19.25	0.01	-0.39	0.03	0.02	0.05
2193	1 30 54.4	30 20 21	1053	13	20.62	0.32	...	0.17	0.15	...
2194	1 31 12.4	30 20 27	1054	1000	20.22	0.08	-1.26	0.04	0.03	0.05
2195	1 31 09.5	30 20 26	1055	839	20.89	0.09	...	0.04	0.03	...
2196	1 31 09.6	30 20 25	1055	845	20.81	0.10	...	0.04	0.03	...
2197	1 31 09.5	30 20 25	1057	838	20.49	0.34	...	0.04	0.08	...
2198	1 31 13.9	30 20 26	1061	1079	19.95	0.29	-0.99	0.04	0.03	0.03
2199	1 31 06.0	30 20 23	1061	646	20.49	0.25	-0.30	0.04	0.03	0.04
2200	1 31 09.6	30 20 24	1062	843	20.86	0.09	...	0.04	0.04	...

TABLE 2 (cont.)

Number	α(1950)	δ(1950)	X	Y	V	B-V	U-B	σ_V	σ_B	σ_U
2201	1 30 51.1	30 20 18	1062	-165	17.93	0.13	-1.14	0.03	0.03	0.05
2202	1 31 05.5	30 20 23	1062	621	20.13	-0.04	-1.04	0.03	0.02	0.03
2203	1 31 14.1	30 20 25	1062	1092	20.57	0.21	...	0.07	0.05	...
2204	1 31 07.5	30 20 23	1063	729	20.31	0.11	-1.06	0.04	0.03	0.02
2205	1 30 51.1	30 20 18	1063	-170	18.12	-0.05	-0.69	0.03	0.04	0.05
2206	1 30 57.1	30 20 19	1064	159	20.65	0.24	-1.02	0.06	0.19	0.06
2207	1 31 14.3	30 20 25	1064	1103	20.48	0.31	...	0.05	0.04	...
2208	1 31 07.5	30 20 23	1064	729	20.32	-0.14	-0.93	0.04	0.02	0.04
2209	1 31 08.2	30 20 23	1065	768	18.93	0.08	-1.02	0.04	0.03	0.02
2210	1 31 12.9	30 20 24	1065	1024	19.82	-0.01	-0.92	0.04	0.03	0.02
2211	1 30 51.4	30 20 17	1066	-153	19.99	0.04	-0.32	0.04	0.03	0.06
2212	1 31 13.8	30 20 24	1067	1076	20.13	-0.06	-0.88	0.04	0.03	0.03
2213	1 31 15.6	30 20 24	1068	1175	20.03	-0.06	-0.88	0.04	0.04	0.03
2214	1 31 02.7	30 20 20	1069	469	19.40	0.04	-0.90	0.03	0.01	0.03
2215	1 30 49.7	30 20 16	1069	-242	19.13	-0.02	-0.96	0.03	0.02	0.05
2216	1 30 47.5	30 20 15	1069	-364	20.38	-0.26	-1.05	0.03	0.02	0.05
2217	1 31 15.8	30 20 24	1069	1183	19.47	0.05	-0.66	0.03	0.04	0.03
2218	1 31 11.7	30 20 23	1069	958	20.18	0.10	-0.76	0.04	0.03	0.03
2219	1 31 09.9	30 20 22	1070	859	20.69	0.06	-1.46	0.06	0.04	0.04
2220	1 30 50.9	30 20 16	1071	-177	19.93	-0.07	-1.07	0.05	0.03	0.05
2221	1 30 48.0	30 20 15	1072	-336	20.95	0.04	-0.51	0.07	0.03	0.06
2222	1 31 10.9	30 20 22	1073	915	19.45	0.14	-0.49	0.03	0.03	0.03
2223	1 30 54.0	30 20 16	1075	-9	20.18	-0.13	-0.78	0.03	0.03	0.11
2224	1 30 49.2	30 20 14	1076	-273	20.01	-0.19	-1.17	0.03	0.02	0.05
2225	1 30 46.8	30 20 13	1076	-405	20.44	0.34	-0.05	0.03	0.03	0.06
2226	1 30 50.2	30 20 14	1078	-219	19.71	0.27	0.04	0.03	0.03	0.09
2227	1 31 11.8	30 20 21	1079	966	19.69	0.09	-0.55	0.03	0.03	0.02
2228	1 30 50.6	30 20 14	1079	-198	19.51	-0.17	-0.77	0.04	0.02	0.05
2229	1 30 51.2	30 20 14	1079	-162	20.67	0.14	...	0.05	0.05	...
2230	1 30 50.0	30 20 14	1079	-226	18.56	0.02	-0.93	0.02	0.02	0.05
2231	1 30 51.7	30 20 14	1080	-137	19.53	-0.18	-1.05	0.03	0.02	0.05
2232	1 30 51.0	30 20 14	1080	-171	20.97	-0.28	-1.06	0.06	0.04	0.05
2233	1 30 46.5	30 20 12	1082	-420	20.84	0.06	...	0.04	0.03	...
2234	1 31 09.1	30 20 19	1082	816	20.33	0.21	-1.10	0.05	0.03	0.03
2235	1 30 50.9	30 20 13	1083	-181	19.20	-0.13	-1.09	0.02	0.02	0.05
2236	1 30 51.4	30 20 13	1083	-151	18.91	-0.04	-0.74	0.06	0.04	0.05
2237	1 31 11.3	30 20 19	1085	936	20.86	0.20	...	0.05	0.04	...
2238	1 31 04.4	30 20 17	1085	562	20.81	-0.25	-1.03	0.05	0.03	0.04
2239	1 31 15.3	30 20 20	1085	1158	19.83	-0.03	-0.85	0.04	0.04	0.02
2240	1 30 51.8	30 20 13	1086	-131	20.84	-0.25	-0.78	0.16	0.08	0.27
2241	1 30 53.7	30 20 13	1087	-27	20.70	-0.17	-0.98	0.04	0.03	0.05
2242	1 30 51.2	30 20 12	1087	-163	20.87	0.08	...	0.06	0.05	...
2243	1 31 09.9	30 20 18	1088	862	20.89	-0.02	...	0.05	0.04	...
2244	1 30 49.9	30 20 11	1089	-237	18.82	-0.03	-0.74	0.02	0.02	0.05
2245	1 30 51.8	30 20 12	1089	-129	20.71	-0.31	-0.81	0.15	0.07	0.22
2246	1 31 04.2	30 20 16	1090	550	19.82	-0.17	-1.08	0.02	0.01	0.03
2247	1 30 53.5	30 20 12	1090	-35	20.81	-0.25	-0.87	0.05	0.03	0.05
2248	1 31 09.9	30 20 17	1092	862	20.79	0.10	-2.10	0.05	0.04	0.03
2249	1 30 54.0	30 20 12	1093	-9	17.55	-0.03	-0.97	0.02	0.02	0.05
2250	1 30 48.0	30 20 10	1094	-337	20.78	-0.26	-0.97	0.05	0.03	0.05

TABLE 2 (cont.)

Number	α(1950)	δ(1950)	X	Y	V	B-V	U-B	σ_V	σ_B	σ_U
2251	1 30 58.5	30 20 13	1095	238	19.83	0.08	-0.46	0.02	0.02	0.04
2252	1 30 45.3	30 20 8	1096	-489	19.40	0.08	-0.47	0.03	0.04	0.10
2253	1 30 51.4	30 20 10	1096	-150	20.08	-0.23	...	0.04	0.03	...
2254	1 30 47.1	30 20 9	1096	-387	18.39	0.09	...	0.03	0.05	...
2255	1 30 49.1	30 20 9	1097	-276	20.25	0.07	-0.82	0.03	0.03	0.05
2256	1 30 51.5	30 20 10	1097	-145	20.03	-0.16	...	0.04	0.03	...
2257	1 30 47.2	30 20 8	1097	-384	19.93	-0.01	...	0.08	0.05	...
2258	1 30 57.2	30 20 11	1098	167	19.16	-0.03	-0.80	0.02	0.01	0.03
2259	1 30 52.4	30 20 10	1099	-100	20.99	-0.28	...	0.06	0.04	...
2260	1 30 50.9	30 20 9	1099	-177	20.85	-0.19	-0.81	0.05	0.05	0.05
2261	1 30 56.6	30 20 11	1099	135	19.09	0.16	-0.03	0.02	0.02	0.05
2262	1 30 52.0	30 20 9	1100	-117	20.63	-0.02	-0.77	0.07	0.05	0.10
2263	1 30 52.0	30 20 9	1100	-122	18.85	0.12	-0.04	0.02	0.02	0.06
2264	1 30 53.9	30 20 10	1101	-17	20.48	0.02	...	0.04	0.03	...
2265	1 30 47.9	30 20 8	1101	-345	20.53	-0.06	...	0.04	0.03	...
2266	1 31 09.6	30 20 15	1101	845	20.30	0.18	-1.07	0.09	0.04	0.04
2267	1 30 54.2	30 20 10	1101	-2	20.06	-0.26	-1.05	0.04	0.03	0.05
2268	1 31 10.2	30 20 15	1102	875	20.62	0.04	...	0.05	0.03	...
2269	1 30 50.1	30 20 8	1102	-223	18.38	-0.11	-1.08	0.02	0.03	0.05
2270	1 30 50.6	30 20 8	1103	-196	20.84	-0.19	-0.89	0.11	0.08	0.22
2271	1 31 01.4	30 20 12	1103	393	20.64	0.36	-0.02	0.05	0.05	0.06
2272	1 31 11.2	30 20 15	1104	933	18.89	0.06	-0.99	0.03	0.03	0.02
2273	1 31 07.5	30 20 13	1104	728	20.77	-0.10	-0.65	0.06	0.06	0.04
2274	1 30 51.2	30 20 8	1104	-164	19.19	-0.27	-0.87	0.03	0.03	0.05
2275	1 30 44.8	30 20 6	1106	-514	20.30	0.00	...	0.03	0.03	...
2276	1 30 49.9	30 20 7	1106	-236	19.16	-0.04	-0.34	0.02	0.05	0.05
2277	1 30 50.5	30 20 7	1106	-200	18.22	0.02	-0.43	0.02	0.02	0.06
2278	1 31 11.9	30 20 14	1107	970	18.79	-0.03	-0.96	0.03	0.03	0.02
2279	1 30 46.9	30 20 6	1107	-399	20.29	0.01	-0.91	0.03	0.03	0.05
2280	1 31 10.0	30 20 13	1108	866	18.66	0.13	-1.70	0.30	0.20	0.02
2281	1 31 10.9	30 20 13	1109	912	20.71	0.37	-0.86	0.04	0.22	0.06
2282	1 31 13.1	30 20 14	1109	1036	20.88	-0.01	...	0.07	0.14	...
2283	1 31 13.2	30 20 14	1110	1040	18.64	0.06	...	0.04	0.04	...
2284	1 30 53.5	30 20 7	1111	-40	20.41	0.26	-0.49	0.03	0.03	0.05
2285	1 31 03.1	30 20 10	1111	487	19.41	1.24	-1.36	0.02	0.28	0.04
2286	1 31 07.8	30 20 12	1111	747	19.65	0.02	-1.35	0.06	0.05	0.02
2287	1 30 47.6	30 20 5	1111	-358	20.51	-0.13	...	0.25	0.04	...
2288	1 31 03.5	30 20 10	1113	508	20.12	0.38	-0.47	0.04	0.03	0.05
2289	1 30 50.7	30 20 6	1113	-193	19.35	-0.19	-1.04	0.03	0.02	0.05
2290	1 31 11.0	30 20 12	1114	920	20.14	0.28	0.49	0.04	0.06	0.10
2291	1 30 53.9	30 20 7	1114	-17	20.26	0.13	-0.94	0.03	0.03	0.05
2292	1 30 45.8	30 20 4	1114	-457	20.32	-0.15	-0.82	0.03	0.02	0.05
2293	1 30 46.8	30 20 4	1115	-402	20.10	0.09	-1.13	0.03	0.04	0.05
2294	1 30 56.4	30 20 7	1116	118	20.22	0.35	-0.01	0.03	0.03	0.04
2295	1 31 08.1	30 20 10	1117	760	20.44	-0.20	...	0.09	0.05	...
2296	1 30 52.9	30 20 6	1117	-69	20.28	-0.08	-0.98	0.04	0.03	0.05
2297	1 31 08.1	30 20 10	1118	761	20.34	-0.11	-1.35	0.07	0.05	0.03
2298	1 31 13.2	30 20 12	1119	1040	20.48	0.03	-0.89	0.05	0.03	0.04
2299	1 30 49.9	30 20 4	1119	-235	19.60	0.07	0.07	0.03	0.02	0.05
2300	1 31 04.1	30 20 8	1120	541	20.73	-0.60	...	0.11	0.06	...

TABLE 2 (cont.)

Number	α(1950)	δ(1950)	X	Y	V	B-V	U-B	σ_V	σ_B	σ_U
2301	1 30 50.9	30 20 4	1121	-181	19.33	-0.14	-0.93	0.02	0.02	0.05
2302	1 30 56.9	30 20 6	1121	149	20.16	-0.33	-0.57	0.18	0.14	0.10
2303	1 30 46.3	30 20 2	1122	-434	20.48	-0.15	...	0.03	0.03	...
2304	1 30 52.9	30 20 4	1122	-73	20.17	-0.25	...	0.14	0.07	...
2305	1 30 52.4	30 20 4	1122	-99	20.36	-0.10	-0.92	0.03	0.03	0.05
2306	1 31 04.6	30 20 8	1123	569	19.45	-0.25	-1.11	0.02	0.02	0.03
2307	1 31 11.3	30 20 10	1123	937	20.73	0.29	-0.38	0.06	0.08	0.06
2308	1 31 04.2	30 20 8	1124	549	20.32	-0.35	-1.08	0.04	0.06	0.04
2309	1 30 52.9	30 20 4	1124	-71	20.55	-0.19	...	0.19	0.11	...
2310	1 31 10.4	30 20 9	1125	885	20.63	0.15	-0.98	0.05	0.05	0.04
2311	1 30 51.9	30 20 3	1125	-124	18.98	0.01	-0.82	0.03	0.02	0.05
2312	1 31 07.9	30 20 8	1125	748	20.12	-0.03	-1.02	0.05	0.03	0.03
2313	1 30 50.1	30 20 3	1125	-224	20.67	0.05	0.28	0.04	0.03	0.09
2314	1 30 52.5	30 20 3	1126	-92	20.54	0.00	-0.94	0.03	0.03	0.05
2315	1 31 10.5	30 20 9	1127	894	20.77	-0.06	-1.19	0.05	0.04	0.04
2316	1 31 15.3	30 20 10	1127	1152	20.33	-0.01	-0.90	0.04	0.03	0.03
2317	1 30 49.9	30 20 2	1127	-236	20.48	-0.09	-0.72	0.04	0.03	0.05
2318	1 30 49.3	30 20 2	1128	-266	20.19	-0.21	-0.84	0.05	0.05	0.07
2319	1 31 03.0	30 20 6	1128	481	20.24	-0.28	-1.19	0.03	0.02	0.03
2320	1 31 07.5	30 20 7	1129	730	18.65	0.12	-0.65	0.05	0.03	0.02
2321	1 30 56.9	30 20 4	1130	150	20.49	0.40	...	0.05	0.09	...
2322	1 31 04.6	30 20 6	1130	567	19.28	-0.68	...	0.05	0.03	...
2323	1 31 07.5	30 20 7	1131	730	18.66	0.08	-0.82	0.02	0.01	0.03
2324	1 30 48.2	30 20 1	1131	-330	20.46	-0.05	-1.08	0.04	0.03	0.06
2325	1 31 04.5	30 20 6	1132	564	19.51	-1.51	...	0.08	0.10	...
2326	1 30 52.3	30 20 2	1132	-104	20.58	0.29	...	0.04	0.03	...
2327	1 30 49.4	30 20 1	1133	-264	20.03	0.00	-1.01	0.04	0.04	0.07
2328	1 31 09.3	30 20 7	1133	826	20.60	0.29	...	0.22	0.13	...
2329	1 31 10.7	30 20 7	1134	904	20.16	0.53	-1.64	0.07	0.14	0.03
2330	1 30 53.3	30 20 2	1134	-47	19.92	0.04	-1.13	0.03	0.02	0.05
2331	1 30 51.0	30 20 1	1135	-173	19.94	-0.15	-0.75	0.10	0.02	0.05
2332	1 31 04.5	30 20 5	1135	564	18.14	-0.09	-1.16	0.03	0.01	0.03
2333	1 31 05.0	30 20 5	1135	591	19.46	-0.16	-1.11	0.02	0.01	0.03
2334	1 31 15.3	30 20 8	1136	1155	20.78	-0.06	-0.66	0.04	0.04	0.04
2335	1 31 04.5	30 20 5	1136	564	18.31	-0.25	...	0.02	0.01	...
2336	1 31 11.7	30 20 7	1136	958	19.51	0.75	-1.14	0.05	0.09	0.02
2337	1 31 10.4	30 20 7	1136	887	19.65	0.17	-1.03	0.05	0.04	0.02
2338	1 31 07.7	30 20 6	1136	738	20.49	0.00	...	0.08	0.03	...
2339	1 31 10.0	30 20 6	1137	863	20.64	-0.47	-1.22	0.14	0.05	0.02
2340	1 31 08.4	30 20 6	1138	777	19.05	0.25	-0.92	0.06	0.04	0.02
2341	1 31 07.7	30 20 5	1138	739	20.51	-0.05	...	0.04	0.03	...
2342	1 31 09.4	30 20 6	1138	831	20.76	-0.09	...	0.31	0.08	...
2343	1 30 47.6	30 19 59	1138	-362	20.92	-0.41	-0.95	0.05	0.03	0.05
2344	1 30 47.8	30 19 59	1138	-353	18.01	0.06	-0.29	0.02	0.02	0.05
2345	1 31 03.3	30 20 4	1139	496	20.60	-0.18	-1.05	0.05	0.03	0.03
2346	1 30 48.0	30 19 59	1140	-342	20.70	-0.27	...	0.04	0.03	...
2347	1 31 04.3	30 20 4	1140	550	19.64	-0.08	-1.25	0.03	0.03	0.04
2348	1 30 54.6	30 20 1	1140	19	20.62	-0.22	-0.89	0.04	0.03	0.05
2349	1 31 02.9	30 20 3	1141	478	19.32	-0.21	-1.08	0.04	0.01	0.03
2350	1 31 04.4	30 20 4	1141	557	20.15	-0.13	...	0.07	0.05	...

TABLE 2 (cont.)

Number	α(1950)	δ(1950)	X	Y	V	B-V	U-B	σ_V	σ_B	σ_U
2351	1 31 04.0	30 20 3	1141	534	17.15	-0.04	-1.06	0.02	0.02	0.03
2352	1 30 50.5	30 19 59	1142	-201	20.23	-0.14	-0.96	0.03	0.03	0.05
2353	1 30 48.7	30 19 58	1142	-301	20.73	-0.03	...	0.05	0.03	...
2354	1 31 04.0	30 20 3	1143	536	19.23	-0.06	...	0.10	0.10	...
2355	1 30 47.3	30 19 57	1144	-377	20.45	-0.13	-1.02	0.03	0.03	0.05
2356	1 30 45.3	30 19 57	1144	-485	20.89	-0.18	0.09	0.09	0.03	0.09
2357	1 30 48.5	30 19 58	1145	-315	20.59	-0.28	-1.08	0.04	0.03	0.05
2358	1 31 09.4	30 20 4	1145	833	16.75	-0.02	-1.32	0.12	0.08	0.02
2359	1 31 04.6	30 20 3	1145	570	18.63	-0.12	-1.09	0.02	0.01	0.03
2360	1 31 08.4	30 20 4	1146	777	19.57	0.34	...	0.09	0.06	...
2361	1 31 07.6	30 20 3	1147	731	20.73	0.12	-0.91	0.05	0.03	0.04
2362	1 31 04.1	30 20 2	1147	540	19.99	-0.10	...	0.04	0.04	...
2363	1 31 04.5	30 20 2	1148	562	20.36	0.11	...	0.08	0.06	...
2364	1 30 49.1	30 19 57	1149	-279	20.93	-0.26	-0.82	0.05	0.03	0.05
2365	1 30 53.1	30 19 58	1149	-59	19.87	0.38	...	0.03	0.03	...
2366	1 31 07.3	30 20 3	1149	714	18.78	0.17	-0.13	0.04	0.03	0.02
2367	1 30 51.1	30 19 57	1150	-172	20.33	-0.18	-0.82	0.04	0.03	0.06
2368	1 31 09.7	30 20 3	1150	846	19.42	0.09	-1.77	0.14	0.08	0.02
2369	1 31 07.3	30 20 2	1150	715	18.81	0.14	-0.32	0.02	0.01	0.03
2370	1 31 04.0	30 20 1	1150	534	19.73	-0.22	-1.23	0.03	0.02	0.04
2371	1 31 10.7	30 20 3	1150	901	19.44	0.44	-1.35	0.06	0.09	0.02
2372	1 31 09.0	30 20 3	1151	809	20.98	0.06	...	0.08	0.06	...
2373	1 31 10.2	30 20 3	1151	876	21.00	0.21	-0.72	0.07	0.06	0.05
2374	1 31 09.1	30 20 3	1152	817	20.85	0.19	...	0.09	0.10	...
2375	1 30 50.7	30 19 56	1153	-194	20.49	-0.14	-0.98	0.04	0.03	0.05
2376	1 31 07.7	30 20 2	1153	739	20.04	-0.05	...	0.04	0.03	...
2377	1 31 04.2	30 20 1	1154	545	20.74	-0.28	-1.12	0.06	0.04	0.05
2378	1 30 44.7	30 19 54	1155	-520	19.48	-0.08	...	0.02	0.02	...
2379	1 31 04.5	30 19 60	1157	563	19.94	0.02	...	0.05	0.05	...
2380	1 31 05.7	30 20 0	1158	627	20.25	-0.15	...	0.04	0.02	...
2381	1 31 08.9	30 20 1	1158	802	19.28	0.83	-1.12	0.08	0.20	0.03
2382	1 31 15.8	30 20 3	1159	1184	17.32	0.11	-0.71	0.04	0.06	0.02
2383	1 31 03.4	30 19 59	1160	503	20.54	0.08	-0.88	0.04	0.03	0.04
2384	1 31 04.6	30 19 59	1160	567	20.21	-0.03	-1.03	0.06	0.06	0.07
2385	1 31 09.4	30 20 1	1160	832	20.96	-0.09	-2.46	0.07	0.07	0.04
2386	1 30 50.3	30 19 54	1162	-214	20.49	-0.09	-0.72	0.04	0.03	0.06
2387	1 30 49.8	30 19 54	1163	-244	20.07	-0.03	...	0.03	0.05	...
2388	1 31 04.8	30 19 58	1164	578	20.93	-0.38	...	0.07	0.05	...
2389	1 30 48.7	30 19 53	1164	-301	20.86	0.03	-0.72	0.04	0.03	0.05
2390	1 31 09.2	30 19 60	1164	820	20.60	0.01	...	0.09	0.06	...
2391	1 31 11.5	30 20 0	1165	946	20.66	0.62	-1.89	0.06	0.12	0.03
2392	1 30 50.1	30 19 53	1165	-227	20.67	0.03	...	0.04	0.03	...
2393	1 30 47.6	30 19 53	1165	-360	19.81	0.05	-0.98	0.03	0.02	0.05
2394	1 30 55.0	30 19 55	1166	41	20.72	0.20	-0.70	0.16	0.25	0.12
2395	1 31 09.7	30 19 59	1166	846	20.97	0.25	...	0.09	0.10	...
2396	1 30 50.2	30 19 53	1166	-218	20.22	-0.05	-0.54	0.03	0.03	0.05
2397	1 31 06.7	30 19 58	1167	682	20.33	0.26	...	0.04	0.04	...
2398	1 31 09.1	30 19 59	1168	816	20.85	-0.26	...	0.14	0.06	...
2399	1 31 03.3	30 19 57	1169	495	20.84	0.12	-0.99	0.06	0.04	0.04
2400	1 31 06.7	30 19 58	1169	683	20.49	0.10	-1.13	0.06	0.04	0.03

TABLE 2 (cont.)

Number	α(1950)	δ(1950)	X	Y	V	B-V	U-B	σ_V	σ_B	σ_U
2401	1 31 04.5	30 19 57	1169	560	19.80	-0.14	...	0.03	0.02	...
2402	1 31 03.9	30 19 57	1169	532	20.29	-0.20	-1.09	0.04	0.03	0.04
2403	1 30 46.2	30 19 51	1171	-440	20.84	-0.16	-0.35	0.05	0.03	0.05
2404	1 31 08.5	30 19 58	1172	782	18.10	0.23	-0.23	0.08	0.05	0.03
2405	1 30 57.3	30 19 54	1173	167	20.38	0.02	-1.22	0.04	0.05	0.04
2406	1 31 04.6	30 19 56	1175	566	19.36	-0.02	-1.15	0.03	0.02	0.03
2407	1 30 51.3	30 19 51	1176	-159	20.76	-0.05	-1.15	0.09	0.04	0.05
2408	1 30 53.8	30 19 52	1176	-22	20.52	-0.08	-0.96	0.03	0.04	0.05
2409	1 31 06.2	30 19 55	1178	655	19.66	0.24	...	0.04	0.03	...
2410	1 31 13.3	30 19 58	1179	1044	20.50	0.16	...	0.16	0.17	...
2411	1 30 56.2	30 19 52	1179	107	19.15	-0.06	-1.07	0.04	0.07	0.08
2412	1 31 06.2	30 19 55	1180	656	19.70	0.09	-0.88	0.02	0.02	0.03
2413	1 31 04.7	30 19 54	1181	575	19.99	-0.04	...	0.03	0.02	...
2414	1 31 08.7	30 19 55	1181	791	20.80	-0.20	-1.09	0.10	0.05	0.04
2415	1 30 58.2	30 19 52	1181	217	20.49	-0.20	-1.02	0.04	0.02	0.03
2416	1 31 09.1	30 19 55	1185	812	20.70	-0.20	-0.97	0.10	0.05	0.04
2417	1 30 56.0	30 19 50	1186	97	19.77	-0.17	-1.14	0.07	0.04	0.07
2418	1 30 59.2	30 19 51	1189	272	20.12	0.20	0.07	0.03	0.02	0.05
2419	1 30 51.0	30 19 48	1190	-177	20.82	0.01	-1.20	0.07	0.04	0.05
2420	1 31 05.2	30 19 52	1192	602	20.92	-0.04	...	0.06	0.05	...
2421	1 31 07.3	30 19 53	1192	713	20.49	0.20	...	0.08	0.08	...
2422	1 31 07.3	30 19 53	1192	715	18.98	0.18	-0.63	0.04	0.03	0.02
2423	1 31 12.6	30 19 54	1193	1007	20.40	-0.37	-0.93	0.35	0.05	0.04
2424	1 30 49.1	30 19 46	1194	-282	19.42	0.28	-0.28	0.03	0.02	0.05
2425	1 31 07.3	30 19 52	1194	715	18.86	0.11	-0.57	0.02	0.01	0.03
2426	1 31 04.3	30 19 51	1194	549	20.32	-0.11	-1.15	0.03	0.03	0.03
2427	1 31 02.3	30 19 50	1197	441	20.77	0.16	-0.34	0.05	0.04	0.04
2428	1 31 07.2	30 19 51	1197	708	20.71	0.08	...	0.04	0.05	...
2429	1 30 53.7	30 19 46	1201	-28	20.08	0.17	-0.15	0.03	0.03	0.05
2430	1 30 49.2	30 19 45	1202	-273	19.83	-0.03	...	0.03	0.04	...
2431	1 31 07.9	30 19 50	1205	749	20.47	-0.12	-1.02	0.06	0.03	0.02
2432	1 30 49.2	30 19 43	1208	-276	18.81	-0.15	-1.04	0.02	0.02	0.05
2433	1 31 11.1	30 19 50	1209	922	20.18	-0.22	-0.75	0.28	0.06	0.02
2434	1 31 10.3	30 19 49	1210	880	19.91	-0.45	-0.80	0.39	0.06	0.02
2435	1 30 50.9	30 19 43	1211	-185	18.85	-0.02	-0.97	0.03	0.03	0.05
2436	1 30 57.1	30 19 44	1213	158	19.01	-0.16	-1.10	0.03	0.00	0.08
2437	1 30 51.2	30 19 42	1215	-167	20.12	-0.14	-0.66	0.04	0.03	0.06
2438	1 30 49.8	30 19 41	1216	-244	20.29	0.06	-1.10	0.05	0.11	0.05
2439	1 30 50.7	30 19 42	1216	-193	18.93	0.11	...	0.03	0.03	...
2440	1 30 46.2	30 19 40	1218	-443	20.73	-0.15	...	0.04	0.03	...
2441	1 31 09.7	30 19 47	1218	848	19.64	-0.06	-0.78	0.11	0.05	0.02
2442	1 30 51.9	30 19 41	1219	-126	19.64	-0.14	-1.03	0.03	0.02	0.05
2443	1 31 06.9	30 19 46	1220	691	20.86	0.13	...	0.04	0.03	...
2444	1 30 51.2	30 19 41	1221	-169	18.07	0.01	-0.64	0.02	0.02	0.05
2445	1 31 06.7	30 19 45	1223	683	20.60	0.33	0.43	0.04	0.03	0.07
2446	1 31 10.3	30 19 46	1225	878	20.30	0.02	-1.60	0.11	0.26	0.02
2447	1 31 10.3	30 19 45	1227	878	20.98	-0.53	...	0.19	0.29	...
2448	1 31 05.5	30 19 44	1227	617	19.87	0.32	-0.27	0.02	0.03	0.04
2449	1 30 57.3	30 19 41	1227	166	19.70	-0.15	-1.16	0.02	0.01	0.03
2450	1 30 50.5	30 19 39	1228	-208	19.83	-0.02	-1.10	0.03	0.03	0.05

TABLE 2 (cont.)

Number	α(1950)	δ(1950)	X	Y	V	B-V	U-B	σ_V	σ_B	σ_U
2451	1 30 46.9	30 19 37	1229	-401	19.75	0.02	-0.19	0.03	0.04	0.05
2452	1 30 45.1	30 19 36	1231	-500	20.55	-0.04	-0.58	0.03	0.03	0.05
2453	1 31 03.1	30 19 42	1232	487	20.87	-0.27	-0.85	0.06	0.03	0.04
2454	1 31 07.3	30 19 43	1234	713	19.45	0.03	-0.91	0.03	0.03	0.02
2455	1 30 49.3	30 19 37	1235	-274	20.93	-0.26	-1.08	0.11	0.03	0.05
2456	1 31 07.3	30 19 42	1236	713	19.58	-0.11	...	0.02	0.01	...
2457	1 30 50.8	30 19 36	1238	-188	20.89	0.00	...	0.09	0.06	...
2458	1 30 57.9	30 19 38	1239	200	20.56	0.11	-1.08	0.05	0.03	0.04
2459	1 30 52.4	30 19 35	1246	-100	20.59	-0.18	-0.65	0.04	0.03	0.05
2460	1 30 50.5	30 19 35	1246	-206	20.24	-0.03	-1.08	0.04	0.03	0.05
2461	1 30 50.6	30 19 34	1246	-199	20.21	-0.09	...	0.04	0.03	...
2462	1 31 01.9	30 19 38	1248	420	20.69	0.24	-0.32	0.05	0.06	0.05
2463	1 30 50.4	30 19 34	1248	-212	18.77	0.12	-0.17	0.02	0.02	0.05
2464	1 31 04.4	30 19 38	1248	553	21.00	-0.17	...	0.06	0.03	...
2465	1 30 50.5	30 19 33	1253	-206	20.94	0.31	...	0.07	0.06	...
2466	1 30 49.6	30 19 33	1253	-256	20.91	-0.18	-0.67	0.05	0.03	0.05
2467	1 31 03.8	30 19 36	1256	521	20.81	-0.09	-1.04	0.05	0.03	0.04
2468	1 31 10.0	30 19 38	1256	859	20.87	-0.07	-1.15	0.09	0.05	0.03
2469	1 30 47.0	30 19 31	1257	-395	20.42	-0.15	-1.08	0.03	0.03	0.05
2470	1 31 04.1	30 19 36	1257	537	19.74	-0.12	-0.95	0.04	0.01	0.03
2471	1 31 11.2	30 19 38	1258	927	20.22	0.18	-1.47	0.15	0.08	0.02
2472	1 31 10.4	30 19 37	1261	881	20.01	0.42	-0.98	0.09	0.12	0.03
2473	1 31 10.3	30 19 37	1263	880	20.98	-0.08	...	0.19	0.17	...
2474	1 31 06.4	30 19 35	1264	664	19.54	0.36	-1.12	0.04	0.06	0.02
2475	1 31 06.4	30 19 35	1266	664	19.82	0.04	...	0.02	0.03	...
2476	1 31 02.6	30 19 34	1266	454	18.54	0.12	-0.70	0.02	0.01	0.04
2477	1 30 50.4	30 19 30	1266	-210	18.75	0.36	-0.60	0.02	0.02	0.05
2478	1 31 06.0	30 19 34	1267	643	20.06	0.03	-0.48	0.03	0.02	0.04
2479	1 30 56.2	30 19 31	1268	107	20.07	-0.10	-1.05	0.02	0.04	0.04
2480	1 30 49.4	30 19 29	1269	-266	18.29	0.09	-0.25	0.02	0.02	0.05
2481	1 30 57.1	30 19 31	1271	157	19.95	-0.16	-1.00	0.03	0.03	0.05
2482	1 30 55.0	30 19 30	1272	39	20.77	-0.26	...	0.05	0.03	...
2483	1 31 02.4	30 19 32	1272	443	17.03	0.07	-0.79	0.01	0.01	0.03
2484	1 31 11.3	30 19 35	1272	935	20.88	0.02	-1.21	0.21	0.07	0.03
2485	1 31 07.1	30 19 33	1273	702	20.44	-0.13	-0.26	0.04	0.03	0.03
2486	1 30 57.4	30 19 30	1275	170	20.65	-0.29	...	0.05	0.03	...
2487	1 31 07.1	30 19 33	1275	703	20.64	-0.20	...	0.04	0.03	...
2488	1 30 56.3	30 19 29	1276	110	20.61	-0.05	-1.00	0.14	0.13	0.07
2489	1 30 50.1	30 19 27	1278	-230	20.26	-0.29	-0.90	0.10	0.03	0.05
2490	1 30 56.8	30 19 29	1278	139	20.41	-0.39	...	0.11	0.03	...
2491	1 30 57.3	30 19 28	1282	166	18.65	-0.06	-0.83	0.02	0.01	0.03
2492	1 31 01.8	30 19 30	1282	414	19.62	-0.21	-1.20	0.02	0.01	0.03
2493	1 31 06.3	30 19 31	1283	658	20.80	0.38	...	0.05	0.05	...
2494	1 31 02.7	30 19 30	1283	459	20.89	-0.21	-0.99	0.06	0.03	0.04
2495	1 30 57.2	30 19 28	1284	162	19.93	-0.18	-1.01	0.04	0.03	0.04
2496	1 31 07.4	30 19 31	1284	720	20.38	0.22	-0.97	0.04	0.03	0.03
2497	1 31 03.8	30 19 30	1285	523	19.80	0.20	...	0.03	0.02	...
2498	1 31 04.3	30 19 30	1285	551	19.43	-0.06	-0.95	0.03	0.01	0.03
2499	1 30 51.4	30 19 26	1285	-159	19.72	-0.05	-0.81	0.03	0.03	0.05
2500	1 31 06.3	30 19 30	1285	659	21.00	0.08	...	0.06	0.04	...

TABLE 2 (cont.)

Number	α(1950)	δ(1950)	X	Y	V	B-V	U-B	σ_V	σ_B	σ_U
2501	1 31 07.4	30 19 31	1285	720	20.38	0.09	-0.95	0.04	0.02	0.04
2502	1 30 50.0	30 19 24	1288	-231	20.74	-0.46	...	0.09	0.03	...
2503	1 30 56.5	30 19 26	1288	120	18.83	-0.14	-1.02	0.07	0.03	0.05
2504	1 30 57.0	30 19 26	1290	149	19.75	-0.18	...	0.03	0.03	...
2505	1 31 13.8	30 19 32	1290	1071	20.98	-0.02	-1.23	0.09	0.05	0.03
2506	1 30 56.4	30 19 26	1290	119	18.53	0.07	...	0.02	0.02	...
2507	1 30 50.9	30 19 24	1291	-187	20.50	-0.22	-0.98	0.27	0.03	0.05
2508	1 31 07.0	30 19 29	1291	696	20.57	0.09	...	0.04	0.04	...
2509	1 30 56.9	30 19 26	1291	142	17.11	0.23	-0.07	0.02	0.02	0.05
2510	1 31 07.7	30 19 29	1292	733	20.87	0.28	...	0.04	0.03	...
2511	1 30 50.6	30 19 24	1292	-201	17.88	0.28	-0.14	0.02	0.02	0.05
2512	1 30 56.7	30 19 26	1292	131	19.11	-0.12	-1.21	0.51	0.35	0.07
2513	1 31 07.0	30 19 29	1293	696	20.82	-0.23	-0.96	0.06	0.03	0.04
2514	1 30 56.7	30 19 25	1293	130	19.46	0.18	...	0.18	0.22	...
2515	1 30 56.4	30 19 25	1293	117	20.13	-0.50	...	0.09	0.04	...
2516	1 30 56.3	30 19 25	1294	113	20.93	0.02	...	0.22	0.06	...
2517	1 30 50.0	30 19 23	1295	-237	20.23	0.38	...	0.03	0.03	...
2518	1 30 56.0	30 19 24	1297	95	19.06	-0.24	-1.08	0.03	0.01	0.01
2519	1 30 56.7	30 19 24	1298	133	20.13	0.04	-1.07	0.04	0.03	0.06
2520	1 30 56.7	30 19 24	1299	133	20.51	-0.14	...	0.05	0.03	...
2521	1 30 55.2	30 19 23	1301	52	20.02	-0.17	-0.98	0.02	0.11	0.02
2522	1 31 02.0	30 19 25	1302	421	20.70	0.10	-0.89	0.06	0.06	0.07
2523	1 30 47.1	30 19 19	1306	-392	20.70	0.25	...	0.04	0.04	...
2524	1 30 50.0	30 19 20	1306	-233	18.88	0.08	-0.81	0.02	0.03	0.05
2525	1 31 08.3	30 19 26	1307	769	20.57	0.22	...	0.04	0.04	...
2526	1 30 56.8	30 19 22	1308	135	20.50	0.02	...	0.05	0.04	...
2527	1 30 51.4	30 19 20	1309	-156	20.75	0.03	...	0.05	0.05	...
2528	1 30 55.5	30 19 21	1312	65	19.99	0.01	...	0.06	0.05	...
2529	1 31 04.4	30 19 23	1312	556	20.38	0.12	...	0.04	0.03	...
2530	1 30 51.2	30 19 19	1312	-170	19.11	0.31	-0.58	0.03	0.03	0.05
2531	1 30 49.9	30 19 19	1313	-241	20.17	-0.02	...	0.03	0.03	...
2532	1 30 51.1	30 19 18	1316	-177	20.54	-0.16	...	0.05	0.05	...
2533	1 30 50.4	30 19 18	1316	-213	20.79	0.14	-0.68	0.04	0.03	0.05
2534	1 30 50.0	30 19 18	1316	-235	19.80	-0.04	...	0.03	0.02	...
2535	1 30 57.2	30 19 20	1317	157	20.93	0.35	...	0.09	0.06	...
2536	1 30 55.7	30 19 19	1318	75	20.11	0.05	-1.07	0.00	0.03	0.01
2537	1 30 50.7	30 19 17	1319	-199	20.45	0.06	...	0.04	0.03	...
2538	1 30 45.2	30 19 15	1320	-499	19.12	0.06	...	0.02	0.02	...
2539	1 31 06.4	30 19 22	1321	661	20.69	-0.07	...	0.05	0.03	...
2540	1 30 55.4	30 19 18	1321	60	20.31	0.04	-0.74	0.03	0.03	0.05
2541	1 31 05.0	30 19 21	1321	587	19.94	-0.25	-1.16	0.04	0.02	0.04
2542	1 31 04.9	30 19 21	1321	579	20.54	0.40	...	0.05	0.04	...
2543	1 31 05.7	30 19 21	1322	624	20.42	-0.02	-1.01	0.04	0.02	0.05
2544	1 31 07.1	30 19 22	1323	701	20.02	-0.14	...	0.03	0.02	...
2545	1 30 55.1	30 19 18	1323	44	20.85	-0.01	...	0.07	0.04	...
2546	1 31 01.6	30 19 20	1324	402	20.50	-0.16	...	0.03	0.02	...
2547	1 30 46.2	30 19 15	1325	-441	19.92	-0.11	-1.06	0.03	0.03	0.05
2548	1 30 55.6	30 19 17	1328	69	19.99	-0.07	...	0.11	0.07	...
2549	1 30 50.5	30 19 15	1329	-209	20.99	0.16	-0.79	0.06	0.06	0.06
2550	1 30 49.6	30 19 15	1329	-255	20.51	0.10	0.74	0.06	0.03	0.08

TABLE 2 (cont.)

Number	α(1950)	δ(1950)	X	Y	V	B-V	U-B	σ_V	σ_B	σ_U
2551	1 30 55.6	30 19 16	1329	70	19.33	-0.14	...	0.03	0.02	...
2552	1 31 05.2	30 19 19	1330	596	19.68	-0.10	...	0.03	0.02	...
2553	1 30 55.0	30 19 16	1331	41	20.67	-0.48	...	0.05	0.04	...
2554	1 31 07.1	30 19 19	1334	700	19.22	0.08	...	0.02	0.01	...
2555	1 31 06.5	30 19 18	1337	670	20.74	-0.01	...	0.05	0.03	...
2556	1 30 55.1	30 19 14	1338	44	20.17	-0.05	...	0.09	0.04	...